Author:
Dunkley, Sam

Title:
Understanding actin-dependent chromosome cohesion in mammalian eggs

Understanding actin-dependent chromosome cohesion in mammalian eggs

Samuel Dunkley

University of Bristol

School of Biochemistry

University Walk

Bristol

UK

A dissertation submitted to the University of Bristol in accordance with the requirements of the degree of Doctor of Philosophy in the Faculty of Life Sciences, School of Biochemistry, December 2022

Abstract

Female meiosis is a specialised form of cell division responsible for the creation of a haploid egg containing 23 chromosomes. Of concern, ageing is accompanied by aneuploidy (incorrect chromosome numbers) in mammalian eggs, an underlying factor for an increased incidence of pregnancy failures seen in reproductively older females. This is consistent with an age-related decline in centromeric cohesion proteins leading to premature separation of sister chromatids during meiosis. Such a progressive loss of cohesion cannot however explain a sharp rise in aneuploidy recorded in older female eggs. Recent studies have highlighted an emerging role for the actin cytoskeleton in ensuring faithful segregation during meiosis. Here, the relationship between cohesion and actin is explored in reproductively young and aged eggs.

In this work F-actin is shown to help keep most sister chromatids together after centromeric cohesion has been lost in aged eggs. F-actin disruption caused premature separation in young eggs, whilst further exacerbating separation in aged eggs. Interestingly, F-actin loss did not affect canonical cohesion complexes, suggesting that F-actin disruption no longer limits spindle-microtubule pulling forces. Furthermore, experimentally reducing cohesion caused accelerated separation when F-actin was disrupted. Conversely, enriching F-actin within the meiotic spindle when cohesion complexes had been fully degraded, significantly reduced premature separation, suggesting that microtubule pulling forces are limited by F-actin. Finally, quantitative super-resolution microscopy revealed a spindle-specific decline in F-actin in aged eggs, stipulating its importance in preventing aneuploidy. These findings suggest that: actin limits premature sister chromatid separation, which would normally arise from centromeric cohesion decline, by limiting microtubule-based pulling forces and that loss of spindle F-actin may underlie the exponential increase in aneuploidy recorded in aged eggs.

Acknowledgements

First and foremost, I would like to thank my supervisor Dr Binyam Mogessie for his support, encouragement and guidance throughout the duration of my PhD. I would also like to thank members of the Mogessie Lab past and present, especially Kathleen for her unwavering help in all things technical, statistical and generally confusing to me. Big shoutouts go to Federica, Tom and Sabrina for making everyday lab life thoroughly enjoyable, as well as all those wholesome evenings at the pub!

I would like to thank all the members of C20 & C50 past and present, notably Giuliana and Jack as well as my thesis committee David & Mark for the guidance over the past 4 years. Special thanks go to Adam Grieve and Nicola Stevenson for reviewing sections of my thesis. I would like to thank my funding, The Wellcome Trust, for their financial support over my PhD and for their generous funding extension due to pandemic closures. Special shoutouts go to my fellow cohort Juma, Katy & Tiah for being in it together from the start, belated birthday celebrations, scientific moans, extra-curricular festivities and being an all-round top bunch. As well as the rest of the Wellcome bunch past and present.

I would like to thank my family for their huge support over the last few years and throughout my university stint, supporting me both mentally and financially during this time. Lastly and most importantly, I would like to thank my now fiancé Louisa for her unwavering support over the past 4 years and for reminding me to have a life outside of the lab. It has been a long road and certainly not the smoothest, but it has flown by in a blur.

Covid-19 Impact and Lab move statement

Between March 2020 – September 2020 lab access was prohibited by the University of Bristol, due to the UK governments COVID-19 restrictions. Lab access was reinstated in September 2020 however maximum occupancy rules were enforced until the Summer of 2021. Due to occupancy restrictions, animal work was not resumed until October 2020, at a reduced rate. This meant progress slowed due to reduced face-to-face training, experiments, access to microscope facilities and other equipment. The Wellcome Trust, generously granted a funded 3-month extension changing the submission date to December 2022. However, additional experimental time was effectively nullified with the movement of the majority of equipment from my host lab to Yale in April 2022.

Declaration

Declaration - I declare that the work in this dissertation was carried out in accordance with the requirements of the *University's Regulations and Code of Practice for Research Degree Programmes* and that it has not been submitted for any other academic award. Except where indicated by specific reference in the text, the work is the candidate's own work. Work done in collaboration with, or with the assistance of, others, is indicated as such. Any views expressed in the dissertation are those of the author.

SIGNED: Samuel Dunkley DATE: 1st December 2022

Contents

Index of Figures

Index of Movies

Movies for related figures can be found appended to the following publication:

Dunkley, S. & Mogessie, B. **Actin limits egg aneuploidies associated with female reproductive aging**. bioRxiv, 2022.2005.2018.491967doi:10.1101/2022.05.18.491967 (2022).

Movie	Description	Related Figure
S1.	Single confocal sections, Z-stack projection, showing Rec8 (magenta) and chromosomes (grey) - DMSO	**3.14**
S2.	Single confocal sections, Z-stack projection, showing Rec8 (magenta) and chromosomes (grey) – CytoD D	**3.14**
S3.	Time lapse movie of partial separation of chromatids (magenta) in a metaphase II-arrested mouse egg with partially degraded Rec8.	**4.2**
S4.	3D isosurface reconstruction of chromatids for bounding box analysis of chromatid scattering.	**4.3**
S5.	Time-lapse movie of partially degraded Rec8 inducing modest separation in a DMSO-treated egg.	**4.4**
S6.	Time-lapse movie of minor separation realignment events (arrows) of chromatids in a partial Rec8 degraded DMSO-treated egg	**4.5**
S7.	Time-lapse movie of partially degraded Rec8 inducing excessive separation in a CytoD-treated egg - 1	**4.4**
S8.	Time-lapse movie of partially degraded Rec8 inducing excessive separation in a CytoD-treated egg - 2	**4.4**
S9.	Time-lapse movie of completely degraded Rec8 inducing excessive separation.	**4.2**
S10.	Time-lapse movie of complete separation in a DMSO-treated egg with complete Rec8 degradation.	**4.6**
S11.	Time-lapse movie of restricted separation in a SiR-Actin-treated egg with complete Rec8 degradation.	**4.6**
S12.	Time-lapse movie of complete separation in a DMSO-treated egg with complete Rec8 degradation.	**4.7**
S13.	Time-lapse movie of restricted separation in a SiR-Tubulin-treated egg with complete Rec8 degradation.	**4.7**
S14.	Time-lapse movie of modest separation in a DMSO-treated egg with partially Rec8 degradation.	**4.8**
S15.	Time-lapse movie of modest separation in a CytoD-treated egg with partially Rec8 degradation.	**4.8**
S16.	Time-lapse movie of restricted separation in a SiR-Tubulin-treated egg with partial Rec8 degradation.	**4.8**
S17.	Time-lapse movie of restricted separation in a SiR-Tubulin and CytoD D-treated egg with partial Rec8 degradation.	**4.8**

List of Abbreviations

µg – Microgram

µl – Microlitre

µM – Micromolar

ACF7 – Actin Cross Linking Factor 7

ADP – Adenosine Diphosphate

aMTOCs – acentriolar Microtubule Organising Centres

ANOVA – Analysis of Variance

Arp2/3 – Actin-related protein 2/3

ATP – Adenosine Triphosphate

AU – Airy Unit

BSA – Bovine Serum Albumin

C57BL/6 – C57 Black 6

CD1 - Cluster of Differentiation 1

CENP-A – Centromere protein A

CPE – Cyclic polyadenylation elements

CPEB – CPE-binding protein

CytoD – Cytochalasin D

dbcAMP – N6,2′-O-Dibutyryladenosine 3′,5′-cyclic monophosphate sodium salt

DMSO – Dimethyl sulfoxide

DNA – Deoxyribonucleic Acid

DTT – Dithiothreitol

EDTA – Ethylene diamine tetra acetic acid

EGFP – Enhanced green fluorescent protein

EGTA – Egtazic acid

ERM – Ezrin, Radixin and Moesin

F-actin – Filamentous actin

FISH – Fluorescent *in situ* Hybridization

Fmn2 – Formin-2

FSH – Follicle Stimulating Hormone

G-actin – Globular actin

GDP – Guanosine-5’-diphosphate

GFP – Green Fluorescent Protein

GTP – Guanosine-5’-triphosphate

GV – Germinal Vesicle

H2B – Histone 2B

HEPES – N-2-Hydroxyethylpiperazine-N'-2-Ethanesulfonic Acid

IKD – Inter-Kinetochore Distance

IVF – *in vitro* Fertilisation

K-fibres – Kinetochore-fibres

Lat B – Latrunculin B

MAP4 – Microtubule Associated Protein 4

$MgSO_4$ – Magnesium Sulfate

ml – Millilitre

MPS1 – Monopolar Spindle Kinase 1

mRFP – mouse Red Fluorescent Protein

mRNA – messenger Ribonucleic Acid

MTB – Microtubule Binding

MW – Molecular Weight

NA – Numeric Aperture

NaOH – Sodium Hydroxide

NEBD – Nuclear Envelope Breakdown

Nipbl – Nipped B-like protein

Noco – Nocodazole

NTP – Nucleoside Triphosphate

PBS – Phosphate Buffered Saline

PFA – Paraformaldehyde

PLK1 – Polo-like Kinase 1

PP2A – Protein phosphatase 2A

PSSC – Premature Separation of Sister Chromatids

RAD21 – Recombinase 21

RAD21L – RAD21 Cohesin Complex Component Like 1

RCF – Relative Centrifugal Force

Rec8 –Meiotic recombination protein 8

RNA – Ribonucleic Acid

ROI – Region of Interest

SAC – Spindle Assembly Checkpoint

SD – Standard Deviation

Sgo2 – Shugoshin-2

siRNA – small interfering Ribonucleic acid

SMC1β – Structural Maintenance of Chromosome Protein 1β

SMC3 – Structural Maintenance of Chromosome Protein 3

ssRNA – single stranded Ribonucleic acid

STAG3 – Stromal Antigen 3

TALEN – Transcription Activator-Like Effector Nuclease

TBE – Tris Borate EDTA

TMT – Tandem Mass Tag

Topo II – Topoisomerase-II

TRIM - Tripartite motif containing protein

TRIM21 – Tripartite motif containing protein 21

UTR – Untranslated Region

v/v – Volume per volume

w/v – Weight per volume

ZP – Zona Pellucida

List of Publications

Dunkley, S. & Mogessie, B. **Actin limits egg aneuploidies associated with female reproductive aging**. *Science Advances* **9**, eadc9161, doi:10.1126/sciadv.adc9161 (2023).

Dunkley, S. & Mogessie, B. **Actin limits egg aneuploidies associated with female reproductive aging**. bioRxiv, 2022.2005.2018.491967doi:10.1101/2022.05.18.491967 (2022).

Dunkley, S., Scheffler, K. & Mogessie, B. **Cytoskeletal form and function in mammalian oocytes and zygotes.** Curr Opin Cell Biol 75, 102073, doi:10.1016/j.ceb.2022.02.007 (2022).

Preface

The majority of experimental results presented and discussed here are available in Dunkley and Mogessie, bioRxiv, 2022 (appendix 7.5 [3]). Additional experimental figures 3.5, 3.7, 7.1 and 7.2 found here are not in this manuscript.

All experiments and analyses in Chapter 3 – '*Actin limits egg aneuploidies associated with female reproductive ageing'* - were performed by Sam Dunkley.

All experiments in Chapter 4 – '*F-actin dampens microtubule-based pulling forces to prevent ageing-like premature chromatid separation'* were performed by Sam Dunkley. Analyses of instantaneous chromosome speeds (Figures 4.5c, 4.6e, 4.7e, 4.8e) and realignment events (Figures 4.5d) were performed by Binyam Mogessie. All other analyses were performed by Sam Dunkley.

Chapter 1 – Introduction

1.1 Background

Fertilisation combines the haploid genomes of a maternal egg and a paternal sperm. Unification of parental genomes sparks the beginning of mammalian life through formation of a unique embryo. Haploid genomes are produced via a specialised form of cell division, termed meiosis, composed of two asymmetric segregation events. Female meiosis is highly error prone and can lead to the production of eggs with incorrect chromosome numbers (aneuploid), which are often not viable for life. Unravelling the intricate mechanisms responsible for faithful chromosome segregation during meiosis holds clinical importance, as it will shed light on how their shortcomings lead to aneuploidy.

Microtubules and actin are structural components of the eukaryotic cytoskeleton that have been shown independently to be key players in accurately segregating chromosomes during meiosis. This thesis explores an interplay between actin and microtubules within the meiotic spindle and how their dysregulation leads to chromosome segregation errors in advancing reproductive age.

In this chapter, first the stages of meiosis will be outlined, highlighting important demonstrated roles for the actin and microtubule-based cytoskeleton. Secondly, the new and emerging functions of actin during meiosis will be discussed. Finally, the mechanisms attributed to the productions of aneuploid eggs will be explored.

1.1.1 Meiosis

Meiosis in male and female germline cells occurs in two distinct stages – meiosis I and meiosis II. Meiosis I is composed of prophase I, metaphase I and anaphase I (see Figure 1.1 for an overview). Metaphase II and anaphase II comprise meiosis II prior to embryo formation. For female mammals, germline cell development results in the production of precursor oocytes that mature into haploid egg cells during meiosis I. Progenitor oocytes are found within mammalian ovaries in the prophase I stage of meiosis, whereby 23 bivalent homologous chromosome pairs are recombined within the germinal vesicle (GV, nucleus) of the oocyte [4]. Meiotic resumption is stimulated by the release of an oocyte from the ovary. Following release,

the nuclear envelope breaks down (NEBD) and condensed chromosomes are captured by the microtubule-based spindle machinery (Figure 1.1). The first meiotic spindle is created by dynamic microtubules capturing condensed chromosomes at their centromeric regions. Stable interactions are mediated by microtubule bundles termed kinetochore fibres (K-fibres) [5]. K-fibres combine with a collection of proteins termed the kinetochore which is found at the centromeric region of chromosomes [5]. K-fibre chromosome interactions coordinate the correct alignment of chromosomes at the centre of the spindle known as the metaphase plate, which concludes the progression from prophase I to metaphase I (Figure 1.1). The spindle then migrates to the cell periphery, where the first segregation event occurs asymmetrically. One set of homologous chromosomes is eliminated from the main cell body into a smaller cell termed the polar body. The separation of chromosomes concludes anaphase I, which is followed by the formation of the second meiotic spindle which captures and organises the remaining chromosomes at metaphase II (Figure 1.1). Metaphase II signifies that the progenitor oocyte has now transitioned into a haploid egg (one set of chromosomes) that is ready for fertilisation by the sperm (Figure 1.1). Eggs will remain arrested in metaphase II until fertilisation. Fertilisation and introduction of the haploid paternal genome triggers the second asymmetric division of meiosis. The second spindle once more migrates to the cell periphery and eliminates half of the sister chromatids to a second polar body; this represents the completion of anaphase II [6] (Figure 1.1). This second division concludes the transition from an egg to a zygote containing both maternal and paternal haploid genomes. Zygote development begins through the formation of maternal and paternal pronuclei. Maternal and Paternal DNA then replicates before migration of the pronuclei to the centre of the cell. Next, the pronuclei breakdown and the mitotic spindle machinery assembles to capture and faithfully segregate sister chromatids into two daughter cells (Figure 1.1). This first symmetrical division highlights the first mitotic division and the beginning of the developing embryo [7]. The progression through Meiosis I and II is depicted in Figure 1.1.

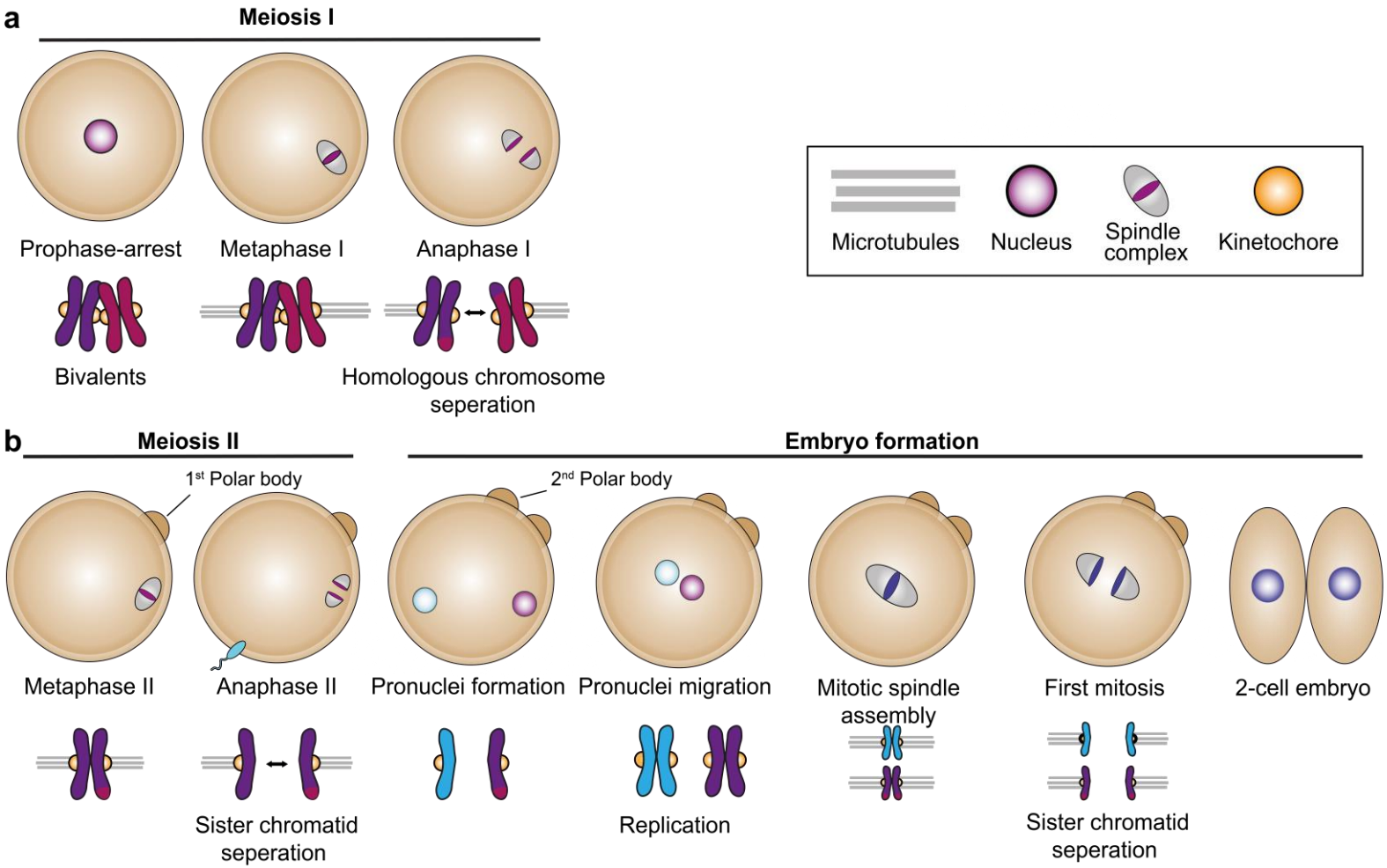

Figure 1.1 Oocyte maturation produces a fertilizable egg for subsequent embryo development (a) Meiosis I. Prophase-I arrested oocytes containing recombined homologous bivalent chromosome pairs. Ovary release stimulates nuclear envelop breakdown and capture of chromosomes by the microtubule-based spindle (Metaphase I). Correctly aligned spindles transmigrate to the cell periphery to undergo the first division, where half of the chromosomes are eliminated into the polar body (Anaphase I) – signalling the formation of a haploid egg. **(b)** Meiosis II. Capture of the remaining chromosomes to form the second metaphase spindle (Metaphase II). Anaphase II triggered by fertilization causing chromosomes to be split into chromatids, with one set being eliminated to a second polar body. Subsequent pronuclei migration and mitotic spindle assembly leads to the formation of a 2-cell embryo.

1.1.2 Actin and Microtubule polymerization dynamics

The cytoskeleton is developed during oocyte maturation in the ovary. Both microtubules and actin have key mechanical roles in mammalian meiosis but have differing mechanisms for assembly and disassembly. Microtubule polymers are composed of globular alpha- and beta-protein heterodimer subunits that assemble into protofilaments (Figure 1.2a). In mammalian cells, 13 protofilaments, assemble into cylindrical microtubules [8,9]. Generally, microtubules are considered to be hollow and around 25 nm in diameter, however more recently actin filaments were found inside the microtubule lumen through *in situ* cryo-electron tomography techniques [8,10,11]. Each tubulin monomer has the capacity to bind Guanosine-5'-triphosphate (GTP), with GTP-bound α-tubulin becoming fixed in a non-hydrolysable form upon heterodimerization with β-tubulin [12]. Upon protofilament formation, GTP-bound β-tubulin is hydrolysed to GDP-bound β-tubulin through the activation domain of α-tubulin [8]. For the most part, microtubule filaments exist in a GDP-bound state, except at the growing tip known as the GTP-cap. Microtubule polymerisation dynamics are dependent on the ability to cycle between growth and shrinkage – a process termed dynamic instability [13]. The GTP-cap promotes growth through heterodimerisation, whereas GTP hydrolysis to GDP results in rapid depolymerisation known as catastrophe [8,13]. The directionality of microtubules is determined by the terminating monomer. Terminal β-tubulin highlights the rapidly growing plus end, whereas minus ends terminate with α-tubulin (Figure 1.2b) [8]. In meiosis, microtubule-plus ends originate from the meiotic spindle poles, nucleating from acentriolar microtubule organising centres (aMTOCs) [14]. Microtubule polarity is important for the directionality of molecular motors such as dyneins (generally move towards the minus end) and kinesins (generally move towards the plus end), which carry cargo (organelles, vesicles, chromosomes [15]) along the microtubules [16]. Whilst most motor proteins have a consistent directionality, there are exceptions to the rule. For example, Kinesin-14 moves towards the minus end of microtubules to perform its function [17]. Much like microtubules, actin filaments assemble from individual monomers. Globular-actin (G-actin) is a 43 kDa (kilodalton) protein containing two tight binding sites which coordinate head-to-tail interactions with other free G-actin molecules [18,19]. Actin filament nucleation begins with three G-actin subunits aggregating into a trimeric form. Polymerization proceeds

spontaneously through addition of G-actin to each end of the growing filament. Growing filamentous actin (F-actin) is characterized by a double-stranded helical form, with a faster polymerizing plus end and a slower polymerizing minus end (Figure 1.2c) [19]. Akin to microtubules, actin monomers bind adenosine triphosphate (ATP), which hydrolyses to ADP after incorporation into the growing filament. F-actin polymers exist in an equilibrium, with dissociation of ADP-actin from the minus end (pointed end) of the filament [18]. The concentration of free monomers defines the rate at which F-actin is able to polymerize with high concentrations of ATP-bound G-actin favouring accelerated growth as they bind to the plus end (barbed end) [20]. Actin filaments can then form secondary structures such as bundles and networks through the actions of a cohort of actin binding proteins and nucleators, such as Fimbrin and the Arp2/3 complex [21,22]. The dynamicity of microtubules and actin coordinate their involvement in many aspects of meiosis. Microtubule based mechanisms are highly characterised in both meiosis and mitosis, however, exciting new roles for the actin cytoskeleton are being discovered and explored.

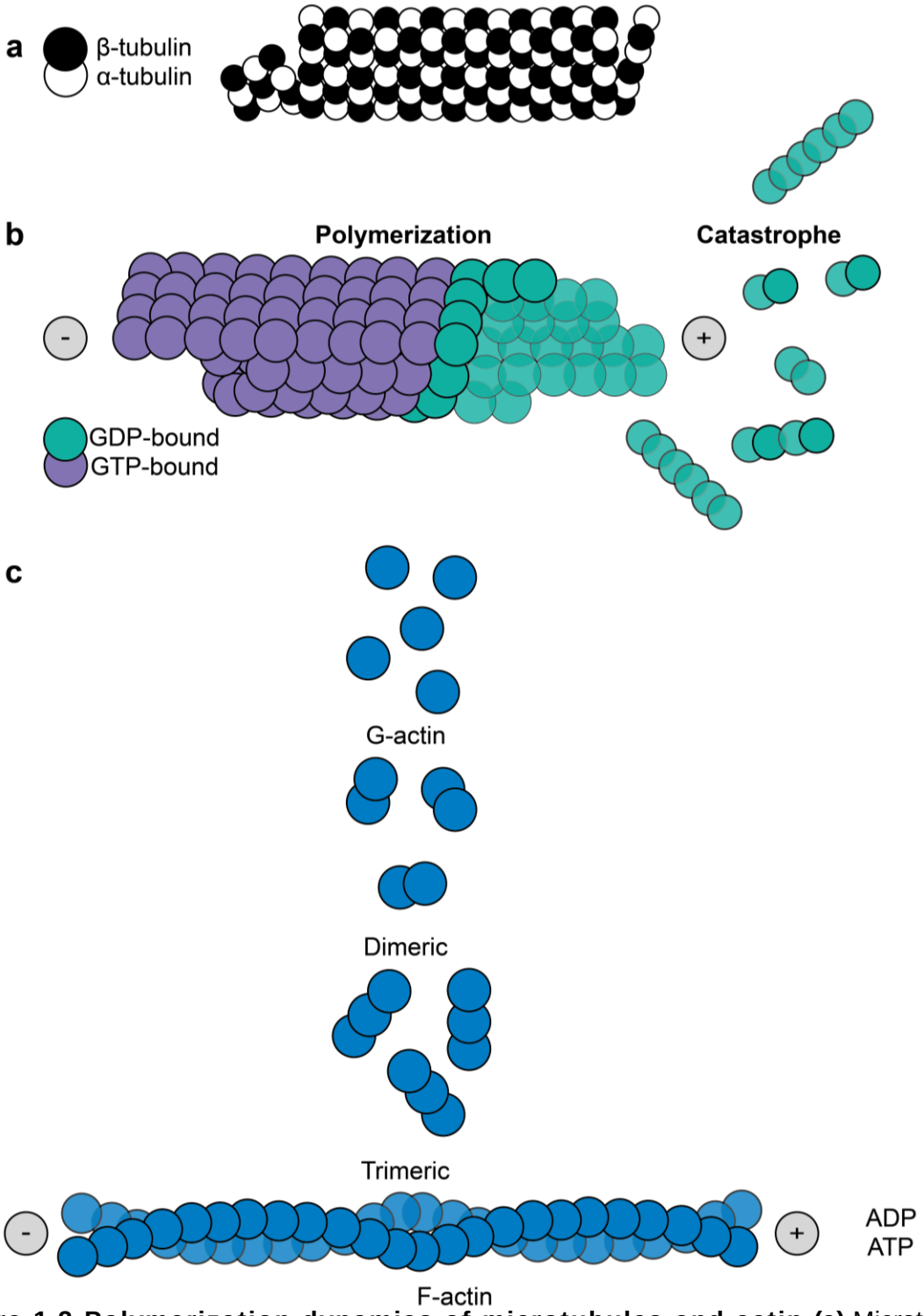

Figure 1.2 Polymerization dynamics of microtubules and actin (a) Microtubule filament schematic – assembled from alpha and beta tubulin dimers. **(b)** A schematic of Microtubule polymerization and catastrophe depicting the addition of GTP-bound tubulin dimers to the growing plus end. Hydrolysed GDP-bound monomers make up the already formed microtubule filament. Upon catastrophe, dimers and higher order structures are lost from the plus end, which then break down into GTP-bound monomers for re-addition to the growing plus end. **(c)** Actin polymerization schematic. Globular-actin (G-actin) self-assembles into dimeric and trimeric forms through ATP hydrolysis, which creates a 'pointed' ADP bound minus end and a growing ATP-bound 'barbed' plus end filament.

1.2 Pre-oocyte development and maturation

Ovaries contain both germ cells and somatic cells that work in concert to develop primordial follicles into mature prophase I arrested oocyte (primary follicles) cells ready for ovulation and subsequent maturation into egg cells. Puberty stimulates folliculogenesis, a mechanism which results in the maturation of primordial follicles into primary oocytes [23-25]. Granulosa cells surround the developing oocyte and release oestrogen in response to Follicle-Stimulating Hormone (FSH) secreted by the anterior pituitary gland [25]. Oestrogen stimulates folliculogenesis and the development of the zona pellucida around the developing oocyte [23]. The zona pellucida is a thick extracellular matrix composed of glycosylated proteins that acts to protect the oocyte. The zona pellucida is penetrated by the sperm during fertilization [23]. Oocyte development concludes with a zona pellucida encapsulated cell arrested in prophase I of meiosis, which contains a centralised germinal vesicle (nucleus). During this maturation, maternal mRNAs are expressed and translated to provide the proteins that are essential for meiotic spindle assembly and chromosome segregation in the latter stages of meiosis [26]. Other maturation events include the development of organelles such as cortical granules (important for fertilization [27]) and mitochondria as well as the functioning cytoskeleton [26]. Meiotic arrest is maintained within the ovary through high levels of cyclic adenosine 3,5-monophosphate (cAMP) produced by the surrounding granulosa cells [28]. Following ovulation, cAMP levels within the oocyte drops allowing meiosis to resume and the development of an egg to begin [26]. Meiotic resumption causes cessation of transcription and translation until the later stages of fertilization [26,29,30].

1.3 Prophase I

Meiosis I is comprised of three key stages: prophase I, metaphase I and anaphase I. Prophase I involves the reorganisation of chromatin into condensed chromosomes that are suitable for their segregation in the latter stages of meiosis [31]. Genome reorganization in prophase I can be further subdivided into Leptotene, Zygotene, Pachytene, Diplotene and Diakinesis (Figure 1.3) [32]. Leptotene follows pre-meiotic replication and is characterized by uncondensed chromosomes that begin to condense and pair [33,34]. Zygotene follows Leptotene and involves

further pairing of chromosomes in which double-stranded-breaks initiate homology search and linkages between homologous axes of chromosomes [33,35]. Pairing is initiated through the synaptonemal complex – a protein structure, comprised of SYC proteins. The synaptonemal complex assembles at double-stranded-breaks (DSBs) which aids in recombining chromosomes together, through a 'zippering' like mechanism along the axis of the chromosomes. Next, Pachytene, concludes synapsis of paired homologous chromosomes [33]. Pachytene is the longest stage of prophase I, resulting in paired condensed bivalent chromosome pairs [33]. Diplotene is characterized by the separation of homologs from each other through breakdown of the synaptonemal complex. However, these homologous pairs remain in proximity through chiasmata – regions of cross over generated from DSB induced recombination during synapsis [33,36]. Oocytes arrest in Diplotene of prophase I until ovulation. Diplotene is considered to be the most stable chromosome conformation, due to the chiasmata linking homologous pairs and is maintained for many months and years within prophase I arrested oocytes in the ovary [33,37]. Diakinesis marks the resumption of meiosis I and the release from prophase I arrest following ovulation. Diakinesis involves the breakdown of the nuclear envelope, chromosome contraction and a further separation of homologous chromosomes from each other [33].

Nuclear envelope breakdown (NEBD) is initiated through Cdk1/cyclin B phosphorylation of the nuclear pore complex leading to its break down [38-40]. Next, the nuclear lamina, responsible for structural organisation of the nucleus is depolymerized [41]. Mechanical forces then begin to break down the nuclear envelope. Dynein-coupled microtubules cause stretching and tearing of the nuclear membrane [42]. In oocytes, where nuclei are often larger than somatic cells, microtubule based tearing is often insufficient [40]. Research in starfish oocytes has identified a novel role for the actin cytoskeleton in disassembling meiotic nuclei [43]. Here, an Arp2/3 (Actin Related Protein 2/3 complex) dependent F-actin 'shell' is polymerised underneath the nuclear envelope prior to NEBD [43,44]. Interestingly, in regions of newly polymerized actin, nuclear fragmentation occurs due to spike-like actin filaments protruding into the nuclear envelope [43]. Additionally, these actin spikes appear important for limiting onward aneuploidy. When

formation of the actin shell was blocked, and breakdown of the nuclear envelope was slower, the microtubule based spindle struggled to capture chromosomes as they dissipated from the central region of the oocyte, leading to onward aneuploidy [43].

Whether this actin shell is present and important in other species, such as rodents or humans, remains to seen. However recent findings have shown filamentous actin structures in the nuclei of mouse oocytes, the abundance of which wanes with advancing age (discussed in section 1.9.3) [45]. Whether this nuclear actin and its reduction holds functions in NEBD and preventing aneuploidy remains to be investigated.

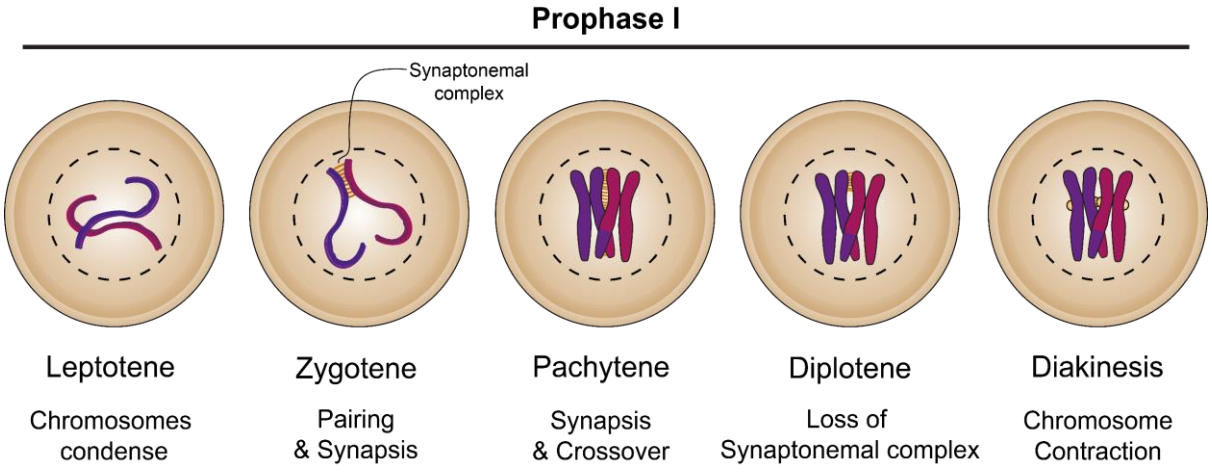

Figure 1.3 Stages of Prophase I Chromosome condensation in Leptotene, followed by establishment of the synaptonemal complex and the beginning of chromosome pairing in Zygotene. Further synapsis and crossover events creating chiasmata in Pachytene. Followed by dissolvement of the synaptonemal complex in Diplotene and movement of the chromosomes in Diakinesis.

1.4 Chromosome segregation in meiosis I

Female meiotic spindles in human, mice, *C.elegans*, *Drosophila* and many other species lack canonical centrosomes [46]. Acentrosomal microtubule organising centres (aMTOCs) act as substitutes to canonical MTOCs for spindle assembly [14]. Whilst lacking centrosomes, aMTOCs contain constitutive components such as: γ-tubulin, pericentrin, CEP170, Myosin-10 amongst others as well as minus-end binding proteins such as CAMSAP3 and dynein-related proteins like HOOK3 [14,47,48]. This cohort of proteins is complemented by microtubule nucleating proteins and factors which contribute to microtubule stability [48]. Chromosome capture by microtubules is initiated following nuclear envelope breakdown (NEBD). However, microtubule formation begins prior to NEBD. aMTOCs begin microtubule nucleation on the nuclear envelope and throughout the oocyte cytoplasm, following oocyte release from prophase I arrest [14,49,50]. Cytoplasmic aMTOCs transition to the nuclear envelope, where following NEBD they fragment and are redistributed by the kinesin-5 motor KIF11 [51]. Fragmentation occurs in a stepwise manner. First, PLK1 (polo-like kinase 1) triggers de-condensation of the aMTOCs [51]. Next, the aMTOCs are stretched by dyneins along the nuclear envelope prior to NEBD, producing fragmented 'ribbon-like' structures [51]. Finally, fragmentation is completed by KIF11 mediated re-localisation of the aMTOC material [51]. Next, chromosomes initiate further microtubule nucleation through localised Ran activation, which switches on nucleation and motor proteins – culminating in the formation of a 'microtubule ball' [14,52]. Chromatin-initiated microtubule nucleation has been documented in both mitosis and meiosis. Ran (Ras-related nuclear protein) is a small GTPase. Bound to chromatin is a guanine nucleotide exchange factor called RRC1 (Regulator of chromosome condensation 1) which switches Ran into its GTP bound state, generating a localised Ran-GTP gradient following NEBD [52]. Ran-GTP in turn induces the activation of microtubule-associated proteins such as TPX2, which recruits the tubulin ring complex to initiate microtubule nucleation in the proximity of the chromosomes to create a 'microtubule ball' [14,52,53]. KIF11 microtubule sliding then causes aMTOCs to be clustered into two distinct poles, forming the basis of the bipolar meiotic spindle [14]. Centrosome clustering has also been reported in drosophila oocytes, wherein clustering is dependent on Kinesin-1, for re-localisation to the posterior of the nucleus [54]. Clustering of MTOCs is not unique to

meiosis. Indeed, clustering of centrosomes in cancer cells, which often have increased MTOCs, is essential in limiting the formation of multipolar spindles [55,56]. The transition to metaphase I involves the organisation of the chromosomes within the first meiotic spindle. Initial organisation involves the transition of chromosomes to the surface of the 'microtubule ball' through molecular motors such as chromokinesins [15,50]. The chromosomes then localise around the forming spindle as the aMTOCs move outwards to create poles. This localisation of the chromosomes is termed the 'prometaphase belt.' The chromosomes then congress to form the metaphase-plate at the equator of the spindle [57].

Microtubule-based organisation of chromosomes involves interactions with the centromere associated kinetochore proteins. The kinetochore builds around the histone H3 protein CENP-A found at the centromeres of chromatids [58,59]. CENP-A is essential for the recruitment of an extensive array of other kinetochore proteins including: CENP-C, KNL1, MIS12 and NDC80 [58]. Characterization of the kinetochore and its ever-increasing array of proteins is still an ongoing avenue of research in the field. Of note, NDC80 is responsible for microtubule-kinetochore attachments in combination with other microtubule binding factors and motor proteins [58,60]. In meiosis I, bivalent chromosome pairs are orientated to face opposite poles, whilst sister kinetochores face the same spindle pole[50]. Sister kinetochore orientation requires the meiosis specific kinetochore associated protein, MEIKIN, and occurs following bipolarization and congression [57,61]. Following correct orientation the spindle migrates to the cell periphery, where the spindle elongates and k-fibres (kinetochore-fibres) shorten driving the first segregation event of meiosis, anaphase I [50,62]. Asymmetric division (at the cortex) in meiosis is important to limit the amount of cytoplasm that is lost with each anaphase [50]. Elimination of half the homologous chromosomes to the first polar body also eliminates cytoplasmic proteins, maternal mRNAs and ATP sources. Therefore, spindle positioning and asymmetric division limits the loss of essential factors for onwards meiosis II [63].

1.5 Cohesion

In both mitosis and meiosis, chromosomes and chromatids are held together by a ring-like protein complex located on the arms and at centromeric regions, known as the cohesin

complex [64]. Cohesion has many differing roles including transcriptional regulation [65], ensuring genome stability [66], facilitating DNA repair [67] and most importantly here, maintaining chromosome integrity during division [68]. Cohesin complexes are essential for chromosome alignment within the spindle and for generating centromeric tension by counteracting microtubule-based pulling forces[69]. Cohesion regulation is incredibly important for spatio-temporal control of bivalent chromosome segregation in anaphase I and sister chromatid segregation in anaphase II of mammalian meiosis[69].

1.5.1 Cohesion components and structure

Cohesion is maintained by a ring-like structure comprised of four canonical subunits. In meiotic chromosomes cohesin proteins SMC1β, SMC3, RAD21/L and REC8, which assemble with a stoichiometry of 1:1:1:1, maintain chromosome integrity by lining both the arms of chromosomes and the centromeric regions (Figure 1.4b) [69-71]. Additional proteins STAG3 (Stromal Antigen 3) [70], found at arm loci only, and SGO2-PP2A (Shugoshin-2, Protein-Phosphatase-2A) [69,72-75] pairings found only at centromeric regions, complete meiotic specific cohesion complexes.

SMC (Structural Maintenance of Chromosome) proteins are comprised of coiled-coil domains at the N- and C- termini that are linked through central flexible hinge domains to an ATPase head [76]. Anti-parallel SMC1-SMC3 proteins act to connect two DNA molecules [76,77]. SMC1β (Structural Maintenance of Chromosome Protein 1β) is a meiosis specific isoform of SMC1 which complexes with SMC3 (Structural Maintenance of Chromosome Protein 3) to form the ring-like structure [76,78]. Here in meiosis, SMC1-SMC3 antiparallel interactions encapsulate two sister chromatids or two homologous chromosomes.

Kleisin subunits interact with SMC proteins through their N and C terminal domains in order to complete the ring like structure of cohesion that encapsulates DNA molecules [77,79]. Kleisin subunit proteins RAD21 (Recombinase 21), RAD21L (RAD21 Cohesin Complex Component Like 1) and REC8 (Meiotic recombination protein 8) differ in their spatiotemporal distribution throughout meiosis [80]. The meiosis-specific kleisin subunit REC8 can be found along the chromosomes prior to meiotic DNA replication. It is then cleaved from chromosome arms

during anaphase I, whilst being maintained at the centromeres until cleavage at anaphase II (Figure 1.4b) [80-82]. RAD21L localises to cohesion complexes following DNA replication, accumulating until the Zygotene stage and subsequently dissociating during pachytene [83]. RAD21 links SMC proteins in distinct stages of meiosis when compared to RAD21L and REC8. RAD21 is absent between leptotene and zygotene, until its re-emergence in late pachytene when it replaces RAD21L cohesion complexes [80,84,85]. Interestingly, RAD21 is found at different sites to RAD21L or REC8 linked cohesion complexes, suggesting specificity or replacement of the other kleisin complexes [84-86].

STAG proteins interact with cohesion complexes through the kleisin subunit [70]. STAG3 is found localised at chromosome arms only during meiosis. STAG3-RAD21L and STAG3-REC8 partners are important for chromosome axis organisation, whilst STAG3-REC8 further influences synapsis and the fidelity of meiotic recombination during prophase I [87].

The final component of the centromeric cohesin ring is the SGO2-PP2A complex. Shugoshin-2 partners with protein-phosphatase 2A through extension of a coiled-coil into the active site of PP2A [75]. SGO2-PP2A is essential for protecting REC8 at centromeric cohesion complexes and is maintained at centromeric loci until metaphase II [73]. Localization of this complex is essential for limiting phosphorylation dependent cleavage of REC8 as discussed below (section 1.5.3).

1.5.2 Cohesion Loading

Cohesion complexes are loaded onto chromatin prior to DNA replication in S phase [88]. Nipbl-Mau2 cohesin-loader partners interact with the SMC heads to initiate their ATPase activity [88-90]. ATP hydrolysis causes a conformational change in the cohesin ring that allow it to open for DNA to pass through [88]. The Nipbl protein is sufficient for the association of the ring-loading complex with the DNA [88]. The location of loading can be broadly generalised into two chromosomal loci – at centromeres and arms. Centromeric cohesion loading is dependent on interactions with the kinetochore complex, whereas arm cohesion is less-well characterized [88,91]. One suggested possibility for arm cohesion loading is redistribution of cohesion

complexes through ATP-dependent translocation, which has been visualised through *in vitro* single molecule assays [88].

1.5.3 Regulation of chromosome segregation by Cohesin

During anaphase I of meiosis, bivalent chromosomes are separated by the microtubule-based spindle, leading to the elimination of one set of chromosomes to the polar body (Figure 1.1a). Prior to separation, chromosomes are correctly aligned and attached to microtubule filaments at their centromeric regions. The chiasmata (crossover events) created between homologous chromosome pairs (bivalents) during prophase I creates tension between the kinetochores upon microtubule capture [92]. Bipolar attachment (to each spindle pole) and the resulting tension is sensed by the spindle machinery. Correct attachment of bivalent chromosome pairs to opposite spindle poles satisfies the Spindle Assembly Checkpoint (SAC) and allows for segregation to proceed [93]. For separation to occur, cohesion complexes linking the arms of bivalent chromosomes must first be cleaved, whilst importantly maintaining centromeric cohesion complexes (Figure 1.1a, 1.4a). Cohesin cleavage is mediated by Seperase, an endopeptidase that severs the kleisin-subunit of REC8, causing the cohesin ring to open and allow separation to occur in a timely manner [82]. In order for cleavage to occur REC8 must be phosphorylated by polo-like kinase 1 (PLK1, in mice, MPS1, in humans) [82,94]. Upon phosphorylation by PLK1, Rec8 is cleaved by Seperase, which initiates dissolution of the cohesin ring. Importantly meiotic fidelity is ensured by protection of centromeric cohesion complexes from cleavage during anaphase I by the SGO2-PP2A partnership (Figure 1.4b) [73,95]. PP2A removes phosphate groups added to centromeric localised Rec8 by PLK1, to ensure Seperase does not prematurely cleave centromeric cohesion complexes during anaphase I [96]. Following fertilization during anaphase II of meiosis II, the remaining centromeric cohesion complexes are cleaved in order for sister chromatids to be separated (Figure 1.1b, 1.4b). At this point, one set of sister chromatids is eliminated into a second polar body [80,97,98]. SGO2-PP2A governance in anaphase II is thought to be relieved by a tension-dependent re-localisation as chromosomes are bi-orientated in the second meiotic spindle [73,96,99]. Indeed, tension-less spindles in anaphase of mitosis still show colocalization of

shugosin with centromeric cohesion complexes [73]. Unprotected centromeric REC8 is subsequently phosphorylated and cleaved to allow anaphase II to occur (Figure 1.4b) [82].

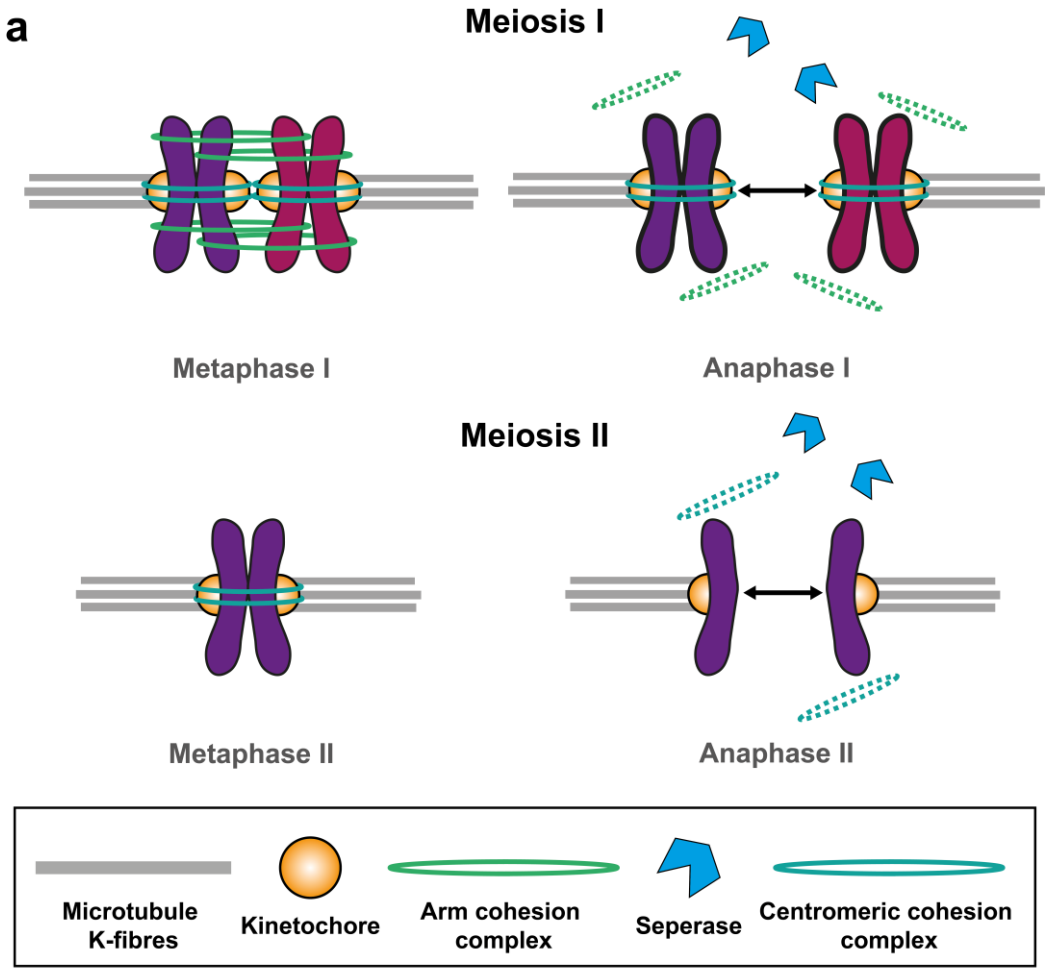
a
Meiosis I
Metaphase I
Anaphase I
Meiosis II
Metaphase II
Anaphase II
Microtubule K-fibres
Kinetochore
Arm cohesion complex
Seperase
Centromeric cohesion complex

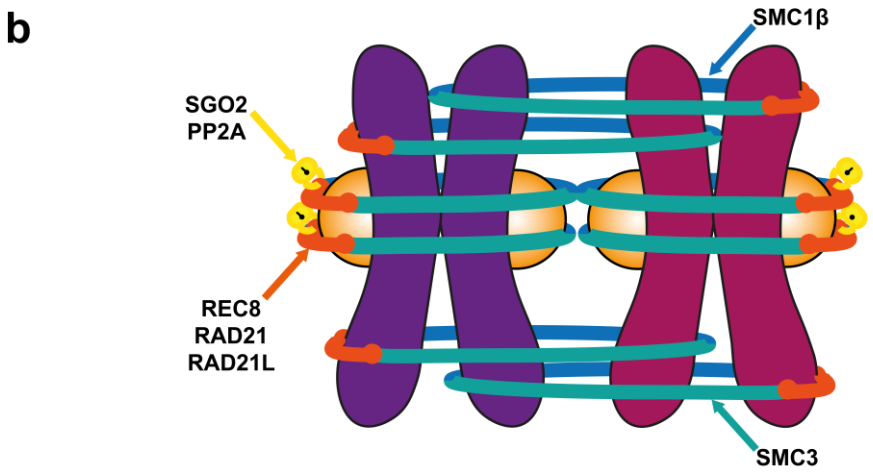
b
SMC1β
SGO2
PP2A
REC8
RAD21
RAD21L
SMC3

Figure 1.4 Chromosome cohesion ensures faithful segregation during meiosis I and meiosis II (a) Timely resolution of cohesion prior to anaphase I and II. Separase mediated cleavage of Rec8 prior to anaphase I cause arm cohesion loss and dissolution of bivalent chromosome pairs. Centromeric cohesion complexes are cleaved by seperase following fertilization by the sperm to allow sister chromatids to separate during anaphase II. **(b)** Components of the centromeric and arm cohesion complexes. SGO2-PP2A protects centromeric cohesion complexes from phosphorylation during anaphase I in order to main sister chromatid pairs. Tension dependent re-localisation leaves centromeric Rec8 vulnerable for Separase cleavage during anaphase II.

1.6 Fertilisation initiates mammalian meiosis II

Fertilisation starts with the binding of a sperm to the zona pellucida through ZP glycoproteins (zona pellucida sperm-binding proteins) [23,100,101]. Upon binding to the zona pellucida, the sperm releases a secretory vesicle known as the acrosome [100]. The acrosome releases proteolytic enzymes that allow disruption of the pellucida and plasma membrane fusion between the egg and sperm [102]. Fusion triggers an increase in calcium levels within the metaphase II arrested egg leading to a signalling cascade that culminates with the activation of the anaphase promoting complex (APC/C) [100]. Subsequently, centromeric Rec8 is cleaved by Separase, and sister chromatids are segregated by the second meiotic spindle, with one set being eliminated to the second polar body (Figure 1.1b).

1.7 Pronuclear Migration

After introduction of the paternal genome through fertilization, maternal and paternal pronuclei form in the embryo's periphery [100]. These pronuclei contain haploid genomes that must be unified prior to the first mitotic division [103]. Unification of these two genomes requires actin and microtubule-mediated migration to the centre of the zygote in order for a single spindle to form [104,105]. Migration in mouse zygotes is thought to rely primarily on the actin cytoskeleton, even though an extensive microtubule network and acentriolar microtubule organising centres (aMTOCs) are available [104,106]. However, until recently the mechanisms by which haploid genomes unite in mouse zygotes was poorly understood. Investigations by Scheffler, et al. [104] characterized two mechanisms that induce pronuclear migration in mouse embryos. Broadly these two mechanisms can be split by their site of action - with one mechanism responsible for fast pronuclear migration at the periphery of the zygote and the second mechanism for slower central movement [104]. The first mechanism involves inward propulsion primarily of the paternal pronuclei inwards from the cell cortex independently of vesicle mediated pressure gradients (discussed below, section 1.9.1). First, the fertilization cone is flattened which forces the pronuclei inwards. This flattening event is driven by a Spire2 ring [104]. Prior to flattening, an enrichment of Rab11a-positive vesicles was recorded behind the paternal pronucleus. Rab11a-positive vesicles enrich Spire2 at the plasma membrane [104,107]. Spire2 is aided by

Formin-2 in the synthesis of new actin filaments [108]. As the cone flattens, the Spire2 ring at the base of the cone contracts, which propels the paternal pronucleus inwards [104]. Localized actin nucleation by formin-2 and Spire2 behind the male pronuclei then accelerates the pronucleus into the cytoplasm further [104]. The second slower mechanism is driven primarily through microtubules and dynein, although the actin cytoskeleton is also crucial for this migration stage. As pronuclei form, zygotes create a dynamic microtubule network from aMTOCs [109]. Both maternal and paternal genomes require this microtubule network to be moved via dynein transport to the centre of the zygote [104]. Interestingly, whilst microtubule dependent, if actin is depolymerized then the second slower phase of pronuclei migration is halted [104,110]. Scheffler, et al. [104] demonstrated that the presence of an actin cortex was essential for slower migration, as microtubules and aMTOCs use the cortex to push the pronuclei inwards and transport them to the centre of the zygote.

1.8 Meiosis to Mitosis – Embryo development

The transition from meiotic to mitotic chromosomes segregation requires the switch from acentrosomal spindle formation to centrosomal spindle assembly. Prior to fertilization centrioles in oocytes are eliminated and reassembled *de novo* in the early embryo [50]. Centriole elimination has been recorded in many different species, including humans, mice, flies and worms [46,111-114]. Additionally, during spermatogenesis, sperm centrioles are degenerated meaning that no paternal centrosomal material is provided to the developing embryo during fertilization [46,115]. Interestingly, the first three embryonic divisions are acentrosomal [100]. The mitotic spindle in these divisions are assembled in a similar manner to meiosis through aMTOCs [100]. In the following divisions, centrioles emerge and the spindle morphology transitions into a mitotic-like appearance – shorter with defined spindle poles [100,109,116]. As the embryo develops, all cells divide through canonical spindles that are nucleated from microtubule organising centres (MTOCs) [109].

The second major difference between meiotic and mitotic division is the switch from asymmetric to symmetric division. In meiosis, chromosomes are separated through two asymmetric divisions, designated by the spindle positioning at the cortex of the cell (discussed

previously, Section 1.5). For mitosis, the spindle must be redistributed to the centre of the cell for symmetric division to occur. As previously described (section 1.7), maternal and paternal pronuclei migrate to the centre of the zygote in a microtubule and actin dependent manner [104,109]. Localisation of pronuclei and subsequent nuclear envelope breakdown leads to the formation of the first mitotic spindle through aMTOCs and subsequent symmetric divisions [101].

1.8.1 Gene expression and Translational control during meiosis

Transcription stops towards the end of prophase I as the chromosomes become condensed in the germinal vesicle. Large reserves of maternal transcripts govern the transition through oocyte maturation in prophase I, meiosis I and II, through to fertilization. Recently, mRNAs in the oocytes were found to be stored in mitochondrial associated compartments [117]. ZAR1 (Zygotic arrest 1) is an RNA-binding protein that mediates this compartmentalization by clustering of mRNAs to protect them from degradation [117]. During meiosis, translation is controlled through regulation of maternal mRNAs. Differential expression allows proteins to be made for the multitude of cellular mechanisms at play during each stage of meiosis. A primary regulatory mechanism is through cytoplasmic polyadenylation elements (CPEs) which are found in the 3' untranslated regions (UTR) of oocyte mRNAs [100,118]. CPE-binding protein (CPEB) binds CPEs in combination with the protein Maskin to repress translation [100,118]. Phosphorylation of CPEB causes dissociation and initiation of translation by the initiation complex, providing a translational switch at different stages of meiosis [100,118]. One example is the activation of DAZL (Deleted in AZoospermia) upon CPEB dissociation [100]. DAZL subsequently induces expression of spindle associated proteins through RNA-binding [119].

Transition from egg to embryo requires degradation of the remaining maternal mRNA transcripts. Transcriptional degradation begins following prophase I, where growth and arrest transcripts are degraded [100]. Degradation continues throughout meiosis and fertilization once the relevant transcripts are not required [100]. Maternal mRNAs are predominantly eliminated by the 2-cell stage embryo in mice [120]. The RNA-binding protein MYS2 promotes mRNA stability in oocytes and eggs [121]. CDC2A mediated phosphorylation of MYS2 during meiosis inactivates

MYS2 causing a decrease in mRNA stability allowing their degradation [100,121,122].However, the regulation of mRNA destabilisation in meiosis is not well understood [100].

In the 2-cell embryo, transcription is reinitiated, which signifies the transition from maternal to embryonic gene expression [100,123]. For transcription to reinitiate, the chromatin must be remodelled into a more accessible euchromatic state. The maternal catalytic subunit of the SWI/SNF chromatin remodelling complex, BRG1, is required for the transition to transcriptionally active chromatin [100,124]. Indeed, BRG1 depleted embryos, have reduced H3K4 dimethylation, which is a euchromatic (active) marker [124]. Remodelling of chromatin is an essential step for the transition from a maternal to a zygotic genome.

1.9 Functions of actin in meiosis

At a glance, the mechanisms of chromosome segregation in meiosis seem predominately microtubule based. However, new roles for the actin cytoskeleton are emerging in this highly complex process. Actin has been described to hold many cellular functions during mammalian oocyte development and throughout meiosis I and meiosis II. Such roles include vesicle transport, nuclear regulation, nuclear and pronuclei migration, spindle anchorage and positioning, polar body extrusion and faithful chromosome segregation [125].

1.9.1 Actin-dependent vesicle transport

The cytoplasmic actin network is created by Formin-2 and Spire 1/2 nucleators found at the cortex of the oocyte and on Rab11a positive vesicles [125]. These nucleators initiate the formation of elongated actin filaments to create a dynamic actin network throughout the cytoplasm [49,108,126]. Vesicle-bound nucleators act as sites of production as well as sequestration of nucleators from the cytoplasm to the cortex [108]. Rab11a vesicles facilitate a dynamic cytoplasmic actin meshwork by recruiting myosin-5b to initiate movement along actin filaments [108]. Coordinated vesicle movement to the plasma membrane creates an emanating vesicle-actin network across the cell [127]. This network is essential for other processes including the transport of Rab27a-positive vesicles to the cortex which act to prevent polyspermy and contribute to centration of the oocyte nucleus [128,129].

1.9.2 Actin-mediated nuclear positioning

Recently actin was described to have a crucial role in pronuclear migration following fertilization (introduced in section 1.7) [104]. Cytoplasmic actin also appears crucial for centralisation of the germinal vesicle in mouse oocytes during the culmination of prophase I. In the final stages of folliculogenesis, the large oocyte nucleus termed the germinal vesicle is transported from the periphery of the cell to the center ready for the resumption of meiosis and nuclear envelope breakdown [125]. Oocytes with off-centre nuclei are considered to be immature. Actin nucleation is lost in *Fmn2*$^{-/-}$ (formin-2) oocytes resulting in predominately off-centred nuclei [49,126,130]. As previously described a vesicle-dependent gradient is important for nucleus centring (section 1.9.1) [129]. An increased presence of actin nucleating Rab11a vesicles at the oocyte cortex creates a positive inwards pressure. Inhibiting the actin-dependent motor myosin-5b and thus limiting vesicle dynamics, reduces the likelihood of nuclear centralisation [125]. As the vesicle gradient increases with higher pressures at the cortex, the nucleus is pushed to the lower pressure which is present at the centre of the cell [129]. This nuclear migration is expedited by an increased cytoplasmic fluidity introduced by vesicle movement [129].

1.9.3 Emerging roles of nuclear actin

The presence of F-actin within the nucleus has been controversial in the field for many years. Evidence of nuclear actin in other systems is abundant, however for a long-time actin filaments were only observed upon challenge with nonphysiologically high DNA damage [131-133]. However, recent technological advances in light microscopy techniques have allowed F-actin structures to be identified in oocyte nuclei [134]. Recently actin filaments were identified inside the nuclei of non-manipulated prophase I arrested oocytes from mice and sheep [45]. Interestingly these nuclear actin filaments were present but reduced in oocytes from reproductively older mice. This indicated that F-actin within the nucleus maybe important for chromatin maintenance [131] in prophase oocytes, and it's reduction with advancing age may hold consequences for infertility. Furthermore, this study demonstrated that disrupting cytoplasmic F-actin caused a shift in G-actin import into the nucleus and the subsequent polymerization of nuclear actin. High levels of nuclear actin were associated with onwards

segregation defects (discussed further in section 1.11.2) [45]. These findings shed new light on nuclear actin filaments and their implications for prophase I of meiosis [45,135].

1.9.4 F-actin drives spindle migration

Spindle migration in mitosis is dependent on astral microtubules initiating from centrosomes at the spindle poles, which push and pull against the cortex to move the spindle [136]. Saliently, oocytes in many species lack centrioles and have few astral microtubules [14,125]. Rather than using an astral microtubule driven mechanism, meiotic spindle migration in mice depends on an F-actin driven mechanism. This is achieved by myosin-2, found at spindle poles, which pulls on the actin network to aid in relocation of the spindle [49]. Interestingly, spindle migration is perturbed if myosin-5b is blocked, which implicates the vesicle-actin network gradient in the movement of the spindle [107]. Pushing, as well as myosin-2 mediated pulling of the spindle has also been proposed to aid spindle migration. Formin-2 has been found at the lagging pole of the meiotic spindle, suggesting that a polarized production of actin-filaments may produce a pushing momentum to drive localisation of the spindle [137,138].

1.9.5 Cortical actin polarization

Oocytes in prophase I are composed of an unpolarized uniform actin cortex, surrounded by microvilli membrane projections. These projections promote the binding and fusion of the sperm during fertilization [139]. The cortex of the oocyte becomes polarised as a result of spindle migration during metaphase, during which a thickened actin cap forms in the proximity of the spindle. This actin cap is thought to be required for spindle anchorage in the latter stages of meiosis II [140]. Microvilli in the vicinity of the actin cap are subsequently lost, preventing the likelihood of paternal chromosome capture by the maternal spindle in meiosis II[141]. Interestingly, the formation of the actin cap is dependent on the chromosomal DNA rather than the microtubules [142]. A concentrated gradient of the small GTPase Ran forms around the chromosomes and recruits the actin nucleator Arp2/3 to create the actin cap at the site of the metaphase II spindle [125,143].

1.9.6 Polar body extrusion requires actin

Polar body extrusion occurs in both meiosis I and II, which signifies the elimination of chromosomes and chromatids from the main cell body. Extrusion requires an enrichment of myosin-2 and actin within the actin-cap [144]. Differences in polar body extrusion are present during meiosis I and meiosis II. In meiosis I a membrane protrusion is formed by the actin nucleators, Arp2/3, Spire 1/2 and formin-2, around the cortical chromosomes and actin cap [108,145,146]. An actomyosin ring forms with aid from Ran GTPases around the membrane protrusion [147]. Contraction of this ring is mediated by RhoA and Ect2 in order to eliminate half of the meiotic spindle from the main cell body [148]. For meiosis II, the actomyosin ring formation requires Ran, Cdc42 and Mos proteins and forms around a membrane furrow located at the spindle midzone before contraction and chromatid elimination [125,148].

1.9.7 A cytoplasmic actin flow coordinates spindle anchorage

Following polar body extrusion after the first division, the remaining chromosomes are captured by the second metaphase spindle. The second meiotic spindle is anchored to the cortex in the vicinity of the actin cap until fertilization by the sperm [125,149,150]. For localisation of the second spindle to the cortex, a cytoplasmic actin flow is created by Arp2/3 mediated actin nucleation [151]. Polymerisation of actin from the actin cap around the cell periphery to the opposite side of the egg and into the centre of the cell - creates a 'cytoplasmic streaming' force [151]. 'Cytoplasmic streaming' is thought to oppose myosin-2 driven pushing towards the egg center [151]. This balance in forces causes anchorage of the second metaphase spindle at the cortex until fertilization by the sperm.

1.9.8 Chromosome capture and segregation

Chromosome segregation has been generally considered to rely on microtubules dynamics alone [7]. Recently F-actin was found in meiotic spindles from mouse, human, pig and sheep eggs, indicating its involvement in chromosomes capture and segregation, and that its function is evolutionarily conserved [152]. Technological advances in fluorescent probes and imaging techniques enabled actin structures to be visualised alongside microtubules within the meiotic spindle [134]. High-resolution imaging showed assembly of spindle F-actin over the course of

the first division. Intensities of spindle actin filaments peaked prior to anaphase I, which highlighted a potential role for actin in chromosome segregation. Indeed, actin disruption through genetic modulation (Formin-2, *Fmn2*$^{-/-}$) or through actin depolymerising agents (Cytochalasin D [153,154]) produced segregation defects during the first anaphase. A high proportion of chromosomes lagged between the two separating parties [152]. These lagging chromosomes were apparent independently of disruption to actin-vesicle and spindle transport as well as cytokinesis.

Spindle F-actin was also visualised prior to anaphase II, with actin disruption causing alignment defects within the metaphase II spindle. Changes in alignment and separation suggested an interplay between microtubules and actin within the meiotic spindle. Interestingly the formation of K-fibres was disrupted by actin changes [152]. K-fibre intensities dropped when actin was disrupted in *Fmn2*$^{-/-}$ or cytochalasin D-treated eggs. Conversely, overexpressing the K-fibre regulating protein CLASP1 (cytoplasmic linker-associated protein 1) in *Fmn2*$^{-/-}$ eggs caused an increased abundance of K-fibres [152,155]. Stabilising actin through the introduction of high concentrations of SiR-Actin[156], however, did not lead to increasing levels of K-fibre formation, suggesting that dynamic actin is essential for K-fibre formation [152]. These data highlighted the importance of actin in promoting functional K-fibres in mouse eggs. Actin's role in mammalian meiosis was further emphasised in human oocytes. Roeles and Tsiavaliaris [157] confirmed the presence of spindle actin within the meiotic spindle in human oocytes as well as a role in organising spindle microtubules into functional fibres for segregating chromosomes

1.10 Mechanisms of Aneuploidy

Incorrect chromosome numbers, termed aneuploidy arises from inaccurate segregation during meiosis. Aneuploid embryos can be primarily attributed to female meiosis, with <5% of errors resulting from male meiosis [2]. Indeed, ~2% of sperm contain monosomies (single chromosomes) or trisomies (triplicate chromosomes) [2]. Often defects in the homologous pairing of sperm chromosomes results in spermatocyte death during pachytene of prophase I or during metaphase I. Female meiosis however is highly error-prone as oocytes progress

through meiosis with uncorrected defects, with 20-40% of all resulting conceptions thought to have abnormal chromosome numbers [2]. Most segregation errors are not compatible with life and those that progress tend to prematurely terminate or produce embryos with genetic syndromes. Trisomies of chromosomes including 13, 15 and 21 (the latter being the most common) produce genetic syndromes such as Down's syndrome [158,159], whilst trisomy 16 has the highest incidence of miscarriage [160].

1.10.1 Types of aneuploidies

Errors in female meiosis primarily occur during meiosis I, with chromosomes being separated incorrectly during anaphase I. 'True' non-disjunction involves the segregation of both homologous chromosomes to the same pole, which could result in both copies being eliminated to the polar body or both being retained (Figure 1.5) [2,160]. 'Achiasmate' non-disjunction occurs when chiasmata (crossover events, see section 1.5) either resolve prematurely or fail to form in the first place. During anaphase I these chromosomes are pulled by the same pole and are either eliminated to the polar body or retained (Figure 1.5) [2,160]. Premature separation of sister chromatids is an additional form of non-disjunction in which chromatids are disengaged prematurely and move to opposing poles during meiosis I (Figure 1.5). 'True' non-disjunction is also apparent during meiosis II, in which upon anaphase, sister chromatids fail to disengage and are pulled towards the same spindle pole. It has been suggested that differences in the type of non-disjunction varies between chromosomes and the age of the oocyte/egg [2]. Dysregulation of the homologous recombination pathway or location of recombination events has implications for the likelihood of some non-disjunction phenotypes. Recombination in the proximity of the centromere or further upstream may causes non-disjunction phenotypes more readily [2].

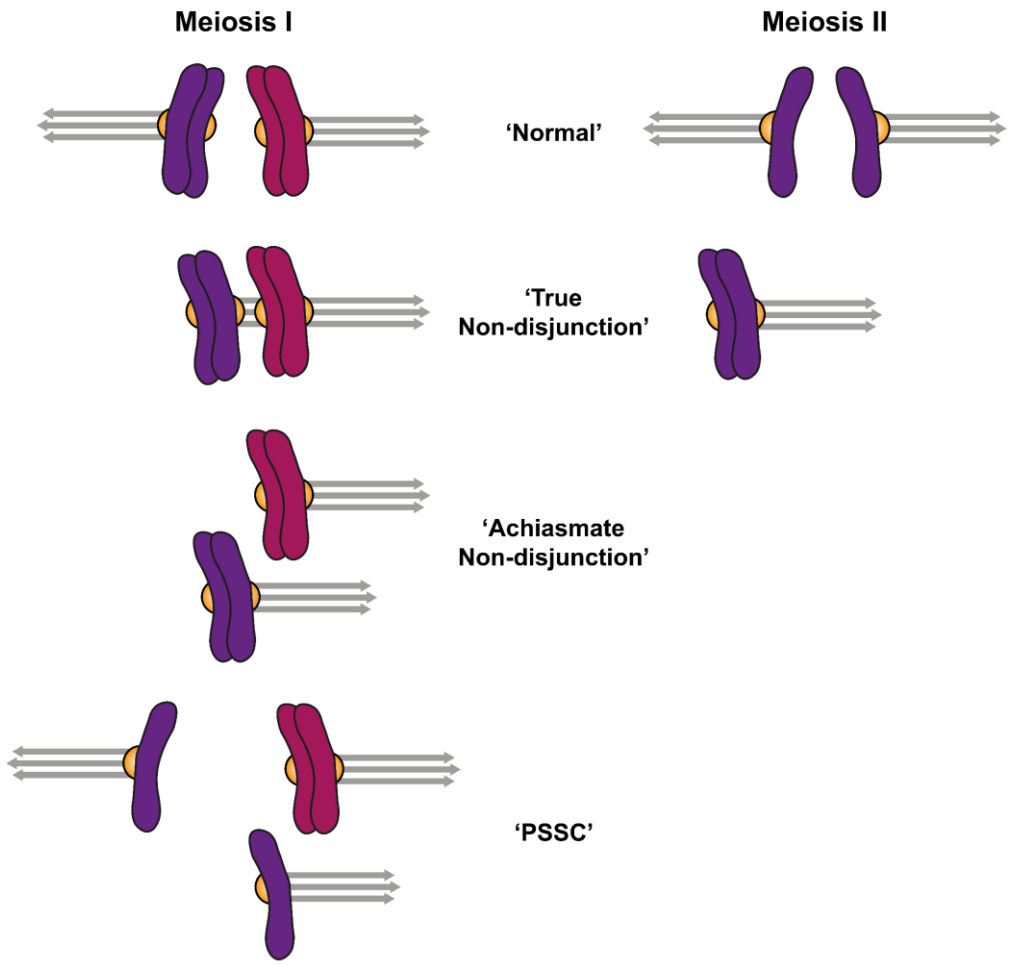

Figure 1.5 Types of Aneuploidy in meiosis I and II. Normal bivalent segregation in meiosis I and normal sister chromatid separation in meiosis II. 'True' non-disjunction, whereby both homologous chromosomes are separated to the same pole in meiosis I, and where both sister chromatids are separated to the same pole during meiosis II. 'Achiasmate' non-disjunction wherein prematurely resolved crossovers cause chromosomes to be pulled by the same pole. PSSC, premature separation of sister chromatids, in which sister chromatids segregate to opposite poles during anaphase I. Diagram adapted from Hassold and Hunt [2]

1.10.2 Spindle assembly checkpoint astringency leads to aneuploidy

Aneuploidy can arise from misfiring of the error checking mechanisms in meiosis [161]. The spindle assembly checkpoint (SAC) prohibits the initiation of anaphase until correct and stable bipolar chromosome/chromatid attachments have been made. Unattached kinetochores are the result of poorly formed spindles [162] or via Aurora kinase sensing of incorrect attachments, resulting in microtubule depolymerization [163]. Incorrect attachments include, merotelic, whereby a kinetochore is attached to both spindle poles and syntelic, wherein chromosome pairs are both attached to the same pole. Unattached kinetochores initiate an MPS1 (monopolar spindle 1) response causing activation of the SAC and the recruitment of the mitotic checkpoint complex (MCC). MCC components (MAD2, BUBR1, BUB3, CDC20) inhibit the anaphase-promoting complex (APC, an E3 ubiquitin ligase), by accumulating at kinetochores until they have been correctly attached to K-fibre microtubules and limit cell cycle progression through CDC20 sequestration [93]. Upon correct attachment SAC components dissociate and inhibitory cyclin B and securin are ubiquitinated by APC leading to degradation by the proteosome and seperase mediated cleavage of REC8[164]. This SAC-APC mechanism is conserved in both mitosis and meiosis [158]. For mitosis, a single unattached kinetochore has been shown to activate the SAC [165]. Mammalian oocytes have a functional SAC; however, they often fail to detect incorrect kinetochore-microtubule attachments in meiosis I [158,166-170]. Indeed, univalent chromosomes (unpaired homologous chromosomes) are often mis-segregated in human oocytes, which would normally activate the spindle assembly checkpoint due to a lack of microtubule-based tension [158]. In fact, univalents have been shown to activate the SAC in mouse oocytes allowing segregation to proceed [166,171]. SAC astringency leads to activation of the APC and incorrect segregation at anaphase, furthering the likelihood of aneuploid mammalian embryos.

1.10.3 Spindle instability in humans causes aneuploidy

Most meiotic studies are conducted in organisms other than humans. This is primarily due to difficulties in obtaining oocytes and eggs from human donors. Furthermore, studies are often conducted on oocytes that are incompatible for *in vitro* fertilisation (IVF), meaning

investigations are performed on atretic oocytes (follicles). Follicular atresia involves the degeneration and subsequent reabsorption of follicles during their maturation [172,173]. Atretic oocyte-based studies are therefore confounded by this major limitation. Whilst mouse and other organisms display chromosome segregation defects and resulting aneuploidy, the incidence in human is significantly higher [47,162]. Mouse meiosis I is completed within ~12-14 hours, whereas initial spindle formation and organisation to metaphase-I takes ~16 hours in humans [162]. Often the establishment of a bipolar spindle is hampered by spindle instability events. Holubcová, et al. [162] recorded apolar and multipolar spindle instability lasting an average of ~8 hours before adjustment to correct bipolar spindles in human oocytes. In comparison, mouse spindles rarely showed polarity defects. Concurringly, the instability in human oocytes correlated well with segregation errors, with increased prevalence of lagging chromosomes recorded in spindles with severe defects [162]. These findings from Holubcová, et al. [162], should be confirmed in mature healthy human oocytes provided by donors. More recently an underlying factor for spindle instability in humans was identified. Human spindles were found to be lacking the motor protein KIFC1, which appears to be essential for spindle stability [47]. Indeed, selective depletion of KIFC1 in mouse oocytes caused instability in the spindle [47]. As previously, these findings from So, et al. [47] should be confirmed in healthy oocytes from human donors.

1.10.4 Sister kinetochore splitting leads to misalignment

In mice, sister kinetochores appear as single foci on each chromatid [74,174,175]. Recent work with human oocytes observed sister chromatids split into one or more fragments in both young and aged oocytes [176]. The likelihood for spilt kinetochores was shown to increase with advancing maternal age, with the majority of chromosomes having 3-4 distinct kinetochores [176]. As anticipated, fragmented kinetochores often showed aberrant attachment to microtubule K-fibres from both spindle poles (merotelic). Additionally, chromosomes were often improperly orientated within the meiotic spindle. Live imaging analysis described a prolonging of chromosome congression and reorganization of misaligned chromosomes [176]. Misaligned or

improperly attached chromosomes would result in aneuploidy following anaphase if efforts are not made by the spindle to correct these defects.

1.11 The 'Maternal age effect'

A confounding factor for increased levels of misegregation and resulting aneuploid eggs is advancing maternal age [158]. It has been estimated that women harbour 400,000 – 600,000 oocytes when they start puberty [158]. Precursor oocyte cells can be held within the ovary in prophase I arrest for decades before ovulation and resumption of meiosis I. Ageing oocytes have an increased likelihood of chromosome misegregation and development into aneuploid eggs, with the incidence of trisomy climbing rapidly beyond 35 years of age [158,160].

When viable for life, only 0.3% births with aneuploid chromosome numbers are live, with the majority resulting in still births or miscarriage [1]. Live offspring often have genetic syndromes, with Down's syndrome being the most common (1/1000). Other syndromes with high incidences resulting from chromosome abnormality include Patau syndrome (triplication of chromosome 13) and Mosaicism resulting from trisomy of chromosome 15. There is a documented increase in the likelihood for aneuploidy in women over the age of 25, with a 33% increase in trisomy recorded from cohort studies (Figure 1.6) [1,2]. The first incidence of maternal age associated aneuploidy was recorded in 1933 [177]. Interestingly, as discussed below, 90% of all age-related aneuploidies resulting in genetic syndromes or embryo deaths can be attributed to weakened chromosome cohesion [1,97,158].

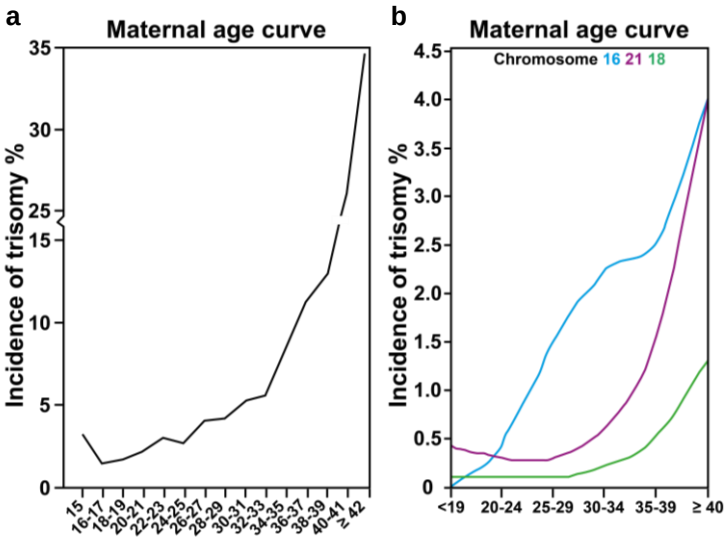

Figure 1.6 Incidences of trisomy with advancing reproductive age (a) The maternal age curve, generated by combining individual trisomies (from b), showing an exponential rise in the likelihood for trisomy as maternal age increases, adapted from Hassold [1]. **(b)** Individual chromosome trisomy contribution to the maternal age effect. Chromosomes 16, 18 and 21 all increase in incidence as reproductive age approaches 40 years of age, adapted from Hassold [1].

1.11.1 Cohesion is lost with advancing reproductive age

Whilst it was known that advancing reproductive age increased the likelihood for misegregation and aneuploidy, why meiosis mechanisms were disturbed was unknown. Chiang, et al. [174] identified that a weakening of the cohesion complex, crucial for spatio-temporal control of segregation, was a key factor in age-related aneuploidies. They found an increased spacing between sister centromeres (inter-kinetochore-distance, IKD) in both metaphase I and metaphase II chromosomes from aged mice, suggesting centromeric cohesion had been weakened [174]. Further analysis showed the meiosis-specific kleisin subunit REC8 was significantly reduced in chromosome spreads from aged mice [174]. Interestingly, total REC8 levels within aged oocytes and eggs were not reduced, when compared to young populations, inferring that Rec8 is not reloaded onto chromosomes after it has been lost [174]. Furthermore, following studies indicated that cohesion complexes in aged populations were more susceptible to seperase mediated cleavage [178]. A weakening of cohesion was found in human eggs by Duncan, et al. [97]. Inter-kinetochore distances grew with advancing reproductive age correlating with an increased susceptibility to chromosome segregation errors[97]. Collectively these studies highlighted an age-related decrease in Rec8 at sister centromeres as a causative factor for increased aneuploidy.

1.11.2 Actin and microtubule disruption in aged oocytes and eggs

The gradual loss of cohesion with advancing maternal age goes some way to explaining how premature sister chromatid separation (PSSC) increases over the age of 30. However, it was previously unknow how ‘true’ non-disjunctions of whole chromosomes occurred in meiosis I and how these events increased with age (Figure 1.5). Recent work from Nakagawa and FitzHarris [179] demonstrated that aged mouse oocytes have aberrant microtubule dynamics that result in misegregation of chromosomes during meiosis I. It was shown that a large proportion of aged oocytes develop multipolar spindles following nuclear envelope breakdown. Interestingly, these multipolar spindles were corrected and became bipolar after a number of hours. Microtubule dynamics were altered in aged oocytes, with filaments polymerizing at differing rates and forming fewer stabilised K-fibre attachments than their young

counterparts[179]. Multipolar spindle formation caused misalignment of chromatid pairs as well as lagging chromosomes during anaphase I. Alignment and timing defects induced by aberrant microtubule dynamics increased the likelihood for non-disjunction of chromatid pairs in aged oocytes [179].

Age-related lagging chromosomes in meiosis I was furthered explored by Mihajlovic, et al. [180] who identified two distinct classes arise with advancing reproductive age. 'Classical' class-I lagging chromosomes were characterized by slower poleward movement, most likely due to aberrant microtubule dynamics, as described previously [179]. The second, class-II lagging chromosomes were discerned as mildly misaligned on the metaphase plate. Upon initiation of anaphase, class-II chromosomes moved at similar speeds to others but lagged behind other chromosomes[180]. Of note, class-II lagging chromosomes often separated correctly whereas class-I lagging often resulted in misegregation and aneuploidy. As microtubule dynamics become dysregulated with age, the likelihood for class-I nondisjunction in meiosis I increases [179,180].

Actin dysregulation has also been implicated in chromosome misalignment and segregation defects. As previously discussed nuclear actin was recently shown in mouse oocytes to have involvement in chromatin mobility and the maintenance of the cytoplasmic actin network [45]. Clinically relevant, actin mutants have been shown to produce excessive nuclear actin filaments in interphase nuclei [181]. Scheffler, et al. [45] created excessive nuclear filaments within prophase I oocytes through introduction of these actin mutants [181]. These actin mutants were found to cause misaligned and lagging chromosomes as a result of excessive nuclear actin filaments obstructing the meiotic spindle.

As discussed previously, actin filaments were recently identified in the meiotic spindle both in metaphase I and metaphase II [152]. Importantly actin was shown to be essential for preventing lagging chromosomes during anaphase I and anaphase II. Actin's role extended to correct alignment and the organisation of microtubules into functional K-fibres for faithful segregation. Whilst we know microtubule dynamics are disrupted in ageing populations, leading to

misalignment and misegregation defects, changes to spindle F-actin populations with advancing reproductive age are yet to be explored [179].

1.12 Understanding actin-dependent cohesion in mammalian eggs

Whilst an age-related decline of cohesion complexes provides basis for an increased likelihood of aneuploidy, it cannot fully explain the exponential rise in segregation errors recorded in reproductively aged eggs [74,158,174,178]. Other factors may contribute directly or indirectly to cohesion loss in these aged eggs. As discussed, the actin cytoskeleton is a key functional component of the meiotic segregation machinery [50,134,152,182]; in this thesis the hypothesis that actin's dysfunction in mammalian eggs contributes to the exponential rise in age-related aneuploidy was explored.

To this end, the aim of this thesis was to explore the relationship between cohesion complexes and the actin cytoskeleton in female meiosis. This involved investigating the following aims:

Aim 1: Discover whether actin disruption affects canonical chromosome cohesion mechanism. To do so, the following objectives were investigated:

- Understanding how actin disruption and/or microtubule perturbation affect premature separation of sister chromatids in young and aged mice.
- Quantifying changes in meiotic cohesion complex proteins in response to actin disruption.

Aim 2: Investigate whether actin-enrichment prevents premature separation of sister chromatids caused by progressive ageing-like weakening of cohesion. To do so, the following objectives were investigated:

- Create an acute system for ageing-like weakening of cohesion.
- Enrich actin in a system of ageing-like weakened cohesion.

The following chapters explore these questions by combining gain/loss of functions assays with advanced imaging techniques in a mouse model of mammalian meiosis.

Chapter 2 – Materials and Methods

2.1 Mouse oocyte isolation, culturing and maturation

Animal work throughout this study was performed at the University of Bristol following guidelines and approval of the Animal Welfare and Ethical Review Body (AWERB). Mice were housed in a pathogen-free environment, according to UK Home Office regulations and the guidelines provided by the University of Bristol's Animal Services Unit (ASU). Female mice were sacrificed by cervical dislocation according to UK Home Office guidelines. Ovaries were isolated and excess tissue including a protective fat layer and the connecting oviduct were removed using tweezers under a stereomicroscope, performed in M2 medium (section 7.2.1) containing 250 nM non-hydrolysable cyclic AMP analogue dbcAMP 250 nM (N6,2′- O-Dibutyryladenosine 3′,5′-cyclic monophosphate sodium) (D0627, Sigma). dbcAMP maintains prophase I arrest by inhibiting second messenger signalling [24,134]. M2 medium was made in house in embryo tested water (for details see appendix, section 7.2.1). Mature oocytes were released from ovaries by puncturing with 13 mm gauge hypodermic needles (BD303800, BD Microlance™). Oocytes were collected using a mouth aspiration tube assembly complemented with a glass micropipette and a 0.22 µm membrane filter (GSWP04700, MF-Millipore™) [134]. Oocytes were cleaned by washing through 9 droplets of M2 media supplemented with dbcAMP, to remove excess cellular debris. For meiotic resumption, oocytes were washed through 9 droplets of M2 media alone, to remove prophase inhibition by dbcAMP.

Oocytes were isolated from the ovaries of 8–12-week-old C57BL/6 or CD1 mice, defined as 'young'. 'Aged' oocytes were collected from 8–9-month-old CD1 or 13–14-month-old C57BL/6 mice. Most experiments were performed in wild type CD1 outbred females. C57BL/6 (inbred) were used for comparison of spindle and cytoplasmic F-actin populations between young and ageing egg populations (Figures 3.1, 3.2, 3.3) due to pandemic-associated supply chain issues of aged CD1 mouse strains.

2.2 Cytoskeletal drug addition experiments

Drug addition experiments were performed by washing oocytes/eggs through 9 droplets of drug supplemented M2 medium. Metaphase II arrested eggs (>4 hours post polar body extrusion) were treated for 4 hours with either: Cytochalasin D (C8273-1MG, Merck) diluted in M2 medium at a final concentration of 5 µg/ml or Latrunculin B (428020-1MG, Merck) diluted to a final concentration of 5 µM to disrupt F-actin. To stabilise F-actin, 10 µM SiR-Actin (SC001, Spirochrome) was used, for 4 hours. For live imaging experiments, the Docetaxel-derivative compound SiR-Tubulin (SC002, Spirochrome) was used at a final concentration of 1 µM, for 4 hours to stabilise microtubules. For combinatory microtubule stabilisation and F-actin disruption live-imaging experiments, eggs were treated with 1 µM SiR-Tubulin for 2 hours then 5 µg/ml Cytochalasin D and 1 µM SiR-Tubulin for 2 hours. For TRIM-Away experiments, drug treatment was implemented prior to antibody microinjection, maintained throughout the injection, and imaging timeline.

For metaphase I, meiotic resumption was induced by washing through 9 droplets of M2 medium to allow maturation to begin. Metaphase I oocytes were fixed/spread ~6 hours after nuclear envelope breakdown (NEBD). For actin disruption maturing oocytes were treated with Cytochalasin D (C8273-1MG, Merck) diluted in M2 medium at a final concentration of 5 µg/ml. For Monopolar Spindle Kinase 1 (MPS1) inhibition, maturing oocytes were treated with Reversine (CAY10004412-5 mg, Cambridge Bioscience) diluted in M2 medium at a final concentration of 0.5 µM.

All drugs were dissolved in Dimethyl Sulfoxide (DMSO, D2650-5X5ML, Merck). For control conditions, DMSO was diluted identically to the corresponding experimental conditions in M2 medium.

2.3 Fixation and immunostaining of mouse oocytes and eggs

Oocytes were fixed in meiosis I after metaphase I spindle assembly (6 hours after nuclear envelope breakdown) or in meiosis II (~12-14 hours after meiosis resumption). Cells were fixed in 2% formaldehyde (v/v), 10mM $MgSO_4$, 0.5% Triton X-100 (v/v), 100 mM HEPES (N-2-Hydroxyethylpiperazine-N'-2-Ethanesulfonic Acid) and 50mM EGTA at 37°C for 30 minutes,

then extracted and blocked overnight in 3% Bovine Serum Albumin (BSA) (w/v) and 0.3% Triton X-100 (v/v) supplemented Phosphate Buffered Saline (PBS) at 4°C. For CENP-A immunostaining experiments, eggs were fixed at room temperature for 20 minutes prior to extraction in PBS supplemented with 0.25% Triton X-100 (v/v) at room temperature for 10 minutes. Eggs were then incubated at 4°C in 3% BSA-PBS (w/v) (11483823, Fisher-Scientific) overnight. In Rec8 immunostaining experiments, cells were treated with Tyrode's acidic solution (T1788-100ML, Merck) to remove the zona pellucida prior to fixation [183,184]. For both Rec8 and CENP-A immunostaining experiments, fixed cells were incubated in a solution of λ-phosphatase (P0753S, NEB) at 30°C for 2 hours before immunostaining. Primary antibodies were: Rec8 rabbit antiserum [174] produced by Michael Lampson (1:2000 dilution, incubation for 3 hours at room temperature in 5% BSA-PBT), CENP-A (2048S, Cell Signalling Technology, 1:200 dilution, incubation for 1.5 hours at 37°C in 5% BSA-PBS), Topoisomerase II (ab52934, Abcam, 1:200 dilution, incubation for 1 hour at room temperature in 5% BSA-PBS) and Tubulin (MCA78G, Bio-Rad, 1:200 dilution, incubation for 1 hour at room temperature in 5% BSA-PBS). Secondary antibodies and stains were Alexa-Fluor-488-labelled anti-rabbit (A11034, Molecular Probes, 1:500 dilution, incubation for 1.5 hours at room temperature), Alexa-Fluor-568-labelled anti-rabbit (A11011, Molecular Probes, 1:500 dilution, incubation for 1.5 hours at room temperature), Alexa-Fluor-647-labelled anti-rat (A21247, Molecular Probes, 1:1000 dilution, incubation for 1 hour at room temperature), Alexa-488 phalloidin (A12379, Molecular Probes, 1:20 dilution, incubation for 1 hour at room temperature) and Hoechst 33342 (62249, Molecular Probes, 1:400 dilution, incubation for 1 hour at room temperature). For the same primary species, antibodies and corresponding secondary antibodies were incubated sequentially. Oocytes and eggs were imaged in glass-bottom dishes (P35G-0-14-C, MatTek Corporation) in PBS under mineral oil. Images in both control and experimental conditions were acquired using identical imaging settings.

2.4 Metaphase chromosomal spreading, fixation, and immunostaining

For chromosomal spreading, the zona pellucida was digested from metaphase I oocytes or metaphase II arrested eggs through washing in droplets of Tyrode's acid solution (T1788-100ML, Merck) under mineral oil (M8410, Sigma) [183,184]. Cells were recovered in M2 medium for 15 minutes at 37°C following zona removal. For chromosomal spreading, 2-3 cells were transferred via mouth-pipetting onto a well of a 15-well multi-test slide (096041505, MP Biomedicals) containing a water-based spreading solution of 1% paraformaldehyde (v/v), 3 mM DTT, 0.15% Triton-X100 (v/v) adjusted to a pH of 9.2-9.4 with 1 M NaOH. Slides were incubated at room temperature overnight in a humidified non-transparent box before airdrying at room temperature. Dried wells were then incubated with a solution of λ-phosphatase (P0753S, NEB) at 30°C for 2 hours. Spreads were then blocked in 3% BSA-PBS (w/v) (11483823, Fisher-Scientific) for 10 minutes at room temperature. Immunostaining was performed through sequential incubation of primary antibodies and secondary antibodies with three intervening washes of slides in 1X PBS of 10 minutes in glass Coplin jars (MIC6000, Scientific Labs). Primary antibodies were: Rec8 rabbit antiserum [174] produced by Michael Lampson (1:2000 dilution, incubation for 3 hours at room temperature in 3% BSA-PBS) and CENP-A (2048S, Cell Signalling Technology, 1:200 dilution, incubation for 1.5 hours at 37°C in 3% BSA-PBS). Secondary antibodies were Alexa-Fluor-488-labelled anti-rabbit (A11034, Molecular Probes, 1:500 dilution, incubation for 1.5 hours at 37°C) and Hoechst 33342 (62249, Molecular Probes, 1:400 dilution, incubation for 1 hour at room temperature). Slides were readied for imaging by covering wells with Vectashield antifade mounting medium (H-1000-10, 2B Scientific) and mounting with 22x22 mm glass coverslips (631-0124, VWR) before sealing with clear nail varnish.

2.5 Confocal, super-resolution and widefield immunofluorescence microscopy

Confocal immunofluorescence images were acquired through a Zeiss LSM 800 confocal microscope using a 40x C-Apochromat 1.2 NA water immersion objective (421767-9971-790, Zeiss). Z-stacks were composed of 0.3 µm optical sections covering a range of 15 µm to capture the entirety of the meiotic spindle, allowing spindle microtubules, single chromatids,

their centromeres and whole chromosomes to be captured. Likewise, for Rec8 fluorescence quantification, 0.5 µm optical sections were imaged over a range of 30 µm, to enable chromosomes to be distinguished from one another.

Super-resolution 3D images of fluorescently labelled phalloidin spindle F-actin structures were acquired using the Airyscan module of a Zeiss LSM 800 microscope through a 40x Apochromat 1.2 NA water immersion objective. The Airyscan module is composed of 32 GaAsP detector elements [185]. Each detector can be considered as a single pinhole, displaced from the central optical axis, allowing light to be collect from different phases of the sample. When compared to a conventional confocal with a pinhole set at 0.2 AU (Airy Units), Airyscan modules collect 95% more light from 6 of the detector elements (1.25 AU) [185]. This vastly increases the signal to noise ratio as light is not obscured by a closed pinhole [185]. F-actin filaments were acquired from the middle of the meiotic spindle in 0.5 µm optical-sections over a range of 2.5 µm. Post-acquisition processing in ZEN2 software (Zeiss) (Airyscan processing module) produced super-resolution images.

For cytoplasmic F-actin imaging, single optical sections of fluorescently labelled phalloidin F-actin structures were acquired at super-resolution through the Airyscan module of a Zeiss LSM 800 microscope equipped with a 40x Apochromat 1.2 NA water immersion objective. 0.5 µm single sections were captured at the equator of each individual egg. Post-acquisition processing in ZEN2 software (Zeiss) (Airyscan processing module) produced super-resolution images.

To image metaphase II chromosomal spreads, 3D fluorescent images were acquired at 0.5 µm optical sections across a range of 5 µm using a Leica DMI6000 inverted widefield microscope equipped with a 100x HCX PL APO CS oil immersion objective (506211, Leica Microsystems). For figure quality images of metaphase II chromosomal spreads, 3D fluorescent images were acquired at 0.5 µm optical sections across a range of 5 µm using Leica SP8X confocal microscope equipped with a 63x HC PL APO CS2 water immersion objective (506361, Leica Microsystems).

Oocytes and eggs were imaged in glass-bottom dishes (P35G-0-14-C, MatTek Corporation) in PBS for fixed samples or in appropriate M2 supplemented media under mineral oil. Images in both control and experimental conditions were acquired using identical imaging settings.

2.6 Quantification of cytoplasmic and spindle F-actin fluorescence intensity in young and ageing mouse eggs

The ratio of cytoplasmic F-actin to spindle F-actin intensity was determined from sum-intensity projection of Z-stacks over a range of 2.5 µm in Image J [186,187], centred around the equator of the spindle. Spindle-actin filament intensities were measured by drawing five identical square regions of interest (ROI) inside the spindle at random. Intensities were then averaged from these regions. Likewise, cytoplasmic F-actin intensities were measured by averaging five ROIs within the areas surrounding the spindle. Care was taken to avoid large patches devoid of signal which are a common finding in C57BL/6 eggs. Ratios of spindle-cytoplasmic actin were determined in each egg by dividing the average mean intensity of the spindle F-actin by the average mean intensity of the cytoplasmic actin (equation 1).

To measure global F-actin fluorescent intensities single-slice Airyscan images were acquired from the equator of the egg. As before five identical square ROIs were drawn within the cytoplasm. Care was taken to avoid spindle f-actin and large patches devoid of signal which are a common finding in C57BL/6 eggs. The five fluorescent intensities were then averaged for each egg. Background removal was performed by subtracting the average mean intensities of five ROIs outside of the cell, in regions containing no obvious phalloidin signal, from the average cytoplasmic F-actin fluorescent intensity (equation 2).

Mean fluorescence intensities for spindle and cytoplasmic f-actin were normalized by dividing individual values from young and aged eggs by the average mean fluorescence intensity of young (control) groups.

Equation 1

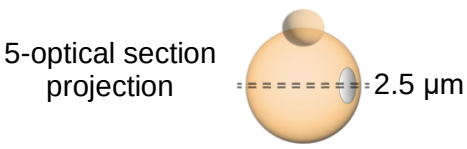

$$\textbf{Spindle: Cytoplasmic F} - \textbf{actin mean intensity} = \frac{\left(\frac{\sum \text{Spindle ROIs}}{5}\right)}{\left(\frac{\sum \text{Cytoplasmic ROIs}}{5}\right)}$$

Equation 2

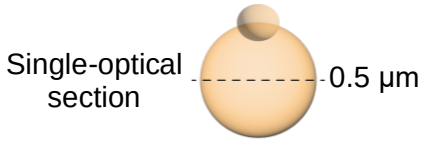

$$\textbf{Cytoplasmic F} - \textbf{actin mean intensity} = \left(\frac{\sum \text{Cytoplasmic ROIs}}{5}\right) - \left(\frac{\sum \text{Background ROIs}}{5}\right)$$

2.7 Quantification of spindle microtubule fluorescence intensity in young and ageing mouse eggs

Spindle microtubule intensity was measured from sum intensity projection of 0.5 µm Z-slices over a range of 2.5 µm. Sum intensity projections were performed in ImageJ. Fluorescence intensity for each spindle was acquired by averaging the mean fluorescence intensity from five identical ROIs within the spindle. Background intensity removal was performed by subtracting the average mean intensity of five identically sized square regions of interest taken from the cytoplasmic regions that did not contain any obvious microtubule filaments, from the average mean intensity of the spindle microtubules (equation 3). Mean fluorescent spindle microtubule intensities were then normalized by dividing each individual value in both young and ageing eggs by the average mean fluorescence intensity of the young groups.

Equation 3

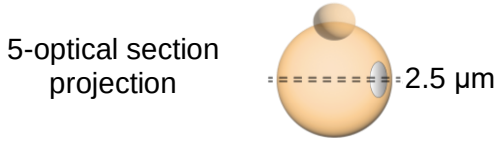

$$\textbf{Spindle} - \textbf{microtubule mean intensity} = \left(\frac{\sum \text{Spindle ROIs}}{5}\right) - \left(\frac{\sum \text{Background ROIs}}{5}\right)$$

2.8 Identification and quantification of prematurely separated sister chromatids in intact spindles and chromosomal spreads

Chromosomes and chromatids from control and experimentally treated metaphase II arrested eggs were identified by reconstructing their 3D volume using the surfaces module of Imaris software (Bitplane). Reconstruction was based on the immunofluorescence signal of Topoisomerase II (an enzyme that localises to the pericentromeric regions of DNA [188]). Kinetochores were then identified using the immunofluorescence signal of CENP-A with the spot detection module of Imaris. Spots were defined with subpixel accuracy from the central regions (maximum signal) of the CENP-A signal [176]. Kinetochores of the same bivalent were defined by the centromeric volume and spots in consecutive z-planes encapsulating the entire centromeric region of the bivalent [176]. This was performed manually allowing single chromatids in which no neighbouring kinetochores were present to be identified. These single chromatids were counted as prematurely separated chromatids in both control and experimental groups. Similarly, chromosomes and chromatids were identified via Hoechst labelling and spot detection of the immunofluorescence signal of CENP-A in metaphase II chromosomal spreads. As before single chromatids were recorded as having no neighbouring sister-kinetochore signal in both control and experimental chromosomal spreads.

2.9 Quantification of inter-kinetochore distances in intact spindles and chromosomal spreads

Measuring the inter-kinetochore distance (IKD) in F-actin disrupted eggs required the development of an imaging analysis pipeline in intact spindles and chromosomal spreads. 3D immunofluorescence images were captured, with centromeres, chromosomes, and spindle microtubules (intact only) labelled. As previously described (section 2.8), the 3D volume of chromosomes and chromatids was reconstructed using the surface module of Imaris (Bitplane). Centromeres were also identified as before using the spot detection module of Imaris. Kinetochores of the same bivalent were defined by the centromeric volume and identified spots in consecutive z-planes encapsulating the entire centromeric region of the bivalent[176]. To measure the inter-kinetochore distance between sister chromatids, the distance between the center of each centromeric spot (maximum signal intensity) and its corresponding

sister centromere was recorded using the measurement of points function in Imaris. This provided a measurement between the centre of each kinetochore to its corresponding pair in µm. Single chromatids with no corresponding sister, did not provide an inter-kinetochore distance and therefore are not included in a whole chromosome analysis of inter-kinetochore distance between control and experimentally treated eggs. In chromosome spreads, as before chromosomes and chromatids were labelled with Hoechst stain and kinetochores were identified using the spot detection module using CENP-A as a reference. The inter-kinetochore distance was measured using the measurements of points function, recording the distance between the center of each kinetochore and its corresponding pair in µm. The development of this pipeline was then used to quantify changes in the IKD that might arise from actin disruption.

2.10 Quantification of fluorescent intensities of cohesion complexes in intact spindles and chromosomal spreads

In intact metaphase I spindles, 3D volumes of metaphase I chromosomes were reconstructed using the surface module of Imaris software (Bitplane), using the Hoechst 3342 immunofluorescence signal as a reference. Reconstructed 3D volumes were subsequently used to create individual chromosome masks in Imaris. Chromosomal masks allowed the fluorescence intensity of Rec8 within the chromosome mask to be isolated from background signal outside of the chromosome. Individual Rec8 mean fluorescent intensities could then be ascertained from each chromosome in control and experimentally treated conditions.

For chromosomal spreads, sum-intensity projections of Z-stacks were performed in ImageJ. Subsequently, mean Rec8 fluorescence intensity in metaphase I chromosomal spreads were quantified by manually drawing a region of interest around each chromosome using the polygon tool in Image J. This analysis allowed the mean fluorescence intensity to be recorded for each metaphase I chromosome.

For both intact spindles and chromosomal spreads, mean intensity measurements were normalized by division of experimental and control groups by the average mean intensity of the values from each control group.

2.11 Generation of expression constructs and mRNA synthesis

To label chromosomes, H2B-mRFP mRNA was transcribed from the readily available expression construct pGEM-H2B-mRP (cloning strategy as described here [14,45]) (Map, appendix figure 7.3). To label spindle microtubules, MAP4-eGFP was transcribed from the readily available expression construct pGEM-MAP4-MTB-eGFP (cloning strategy as described here [14,189]) (Map, appendix figure 7.4). For TRIM-Away experiments mRNA was transcribed from pGEM-SNAP-TRIM21 constructs (cloning strategy as described here [3]) (Map, appendix figure 7.5).

mRNA for microinjections were transcribed from linearised pGEM vectors (cut using *AscI* (R0558, NEB)) according to the protocol of the mMESSAGE mMACHINETM T7 Transcription Kit (AM1344, Thermo Fisher Scientific). Linearised DNA and transcribed mRNA was purified using a phenol/chloroform-based extraction protocol. 10-15 µg of plasmid DNA was combined with 5 µl of *AscI* and rCutSmart™ Buffer (B6004S, NEB) in a total volume of 200 µl. Reactions were placed at 37°C overnight for linearisation of vectors. Equal volumes of phenol were added to the reactions, vortexed and centrifuged to isolate the upper phase. Equal volumes of Chloroform were then added to the upper phase and vortexed and centrifuged as before. 2.5 volumes of 100% ethanol and 0.1 volumes of 3M sodium acetate were then added to the upper phase. Reactions were then centrifuge at 21,300 RCF (Relative Centrifugal Force) for 15 minutes. DNA pellets were washed with 70% ethanol before airdrying and dissolving in 5 µl of RNase free water. The concentrations of linearised DNA were then attained via a NanoDrop Lite spectrophotometer (reading at 260 nm) (ND-LITE-PR, Thermo Fisher Scientific). For mRNA synthesis, 1 µg of linearised DNA was combined with 1X NTP/CAP, 1X reaction buffer, 2 µl of enzyme mix and RNase free water in a final volume of 20 µl (mMESSAGE mMACHINETM T7 Transcription Kit (AM1344, Thermo Fisher Scientific)). mRNA reactions were placed at 37 °C for 2 hours before addition of 1 µl DNase for 15 minutes at 37 °C. Following mRNA synthesis, 115 µl of RNase free water and 15 µl of Ammonium acetate stop solution was added. Equal volumes of phenol-chloroform were added to each reaction, vortexed and centrifuged to isolate the upper phase. Equal volumes of chloroform

were then added to the upper phase, vortexed and centrifuged as before. One volume of Isopropanol was then added to the second upper phase before incubation at -20 °C overnight. Reactions were then centrifuged at 4 °C ~21,300 RCF. mRNA pellets were then airdried and resuspended in RNase free water. Purity and concentrations of mRNA were assessed through gel electrophoresis and spectrophotometry.

To assess mRNAs via gel electrophoresis, 1 µl of mRNA was supplemented with 1 µl of RNase free water and 8 µl of RNA loading dye (NEB N0362S). Size was assessed by comparison to a mix of 2 µl of ssRNA ladder (NEB N0362S) with 8 µl of RNA loading dye. Both ladder and mRNA mixes were denatured at 70 °C for 10 minutes, before being cooled and loaded onto 1% agarose gels in 1X TBE.

2.12 Microinjection of mRNA and protein

Microinjection was used to introduce *in vitro* transcribed mRNA and/or protein into prophase I arrested oocytes or metaphase II arrested eggs. Microinjections were performed using mercury back-filled needles, pulled using a brown flame micropipette puller described further here[134]. Needle tips were varied in diameter (0.3-0.7 µm) as well as in taper, to optimise injections for increased survival and ease of injection. Oocytes or eggs were placed into a shelf constructed from glass coverslips (Figure 2.1) and injected with 6-8 picolitres of *in vitro* transcribed mRNA. mRNA was diluted in RNAse free water to an optimised concentration prior to injection. Following injection oocytes were recovered and allowed to translate at 37°C for 3 hours. Subsequently, oocytes were released from prophase-arrest through washout of dbcAMP. For protein, antibodies were introduced to metaphase II arrested eggs via microinjection of 2-3 picolitres of antibody diluted in PBS supplemented with 0.05% (v/v) NP40 85124, Pierce™) and Alexa Fluor 488 Dextran 10,000 MW (Molecular Probes, D22910; 1:40 dilution). Alexa Fluor 488 Dextran was utilized to validate antibody injection via fluorescence.

2.13 High-resolution confocal live cell microscopy

Confocal time-lapse sequences of meiosis maturation and metaphase II arrested mouse eggs were acquired using a LSM 800 microscope equipped with a 40X C-Apochromat 1.2 NA water-immersion objective (421767-9971-790, Zeiss). Images were obtained within an

environmental chamber maintained at 37 °C for the entirety of acquisition. Images were acquired across a range of 30-40 μm of 1.5 μm thick z-sections. Acquisition through ZEN2 software allowed Z-stacks to be collected every five minutes for the duration of the time-lapse. Laser power was reduced in contrast to fixed sample imaging to minimise the risk of damage and cell death. Cells were imaged in M2 medium supplemented with/without cytoskeletal drugs (described previously, section 2.2) under mineral oil in glass-bottom imaging dishes (P35G-0-14-C, MatTek Corporation).

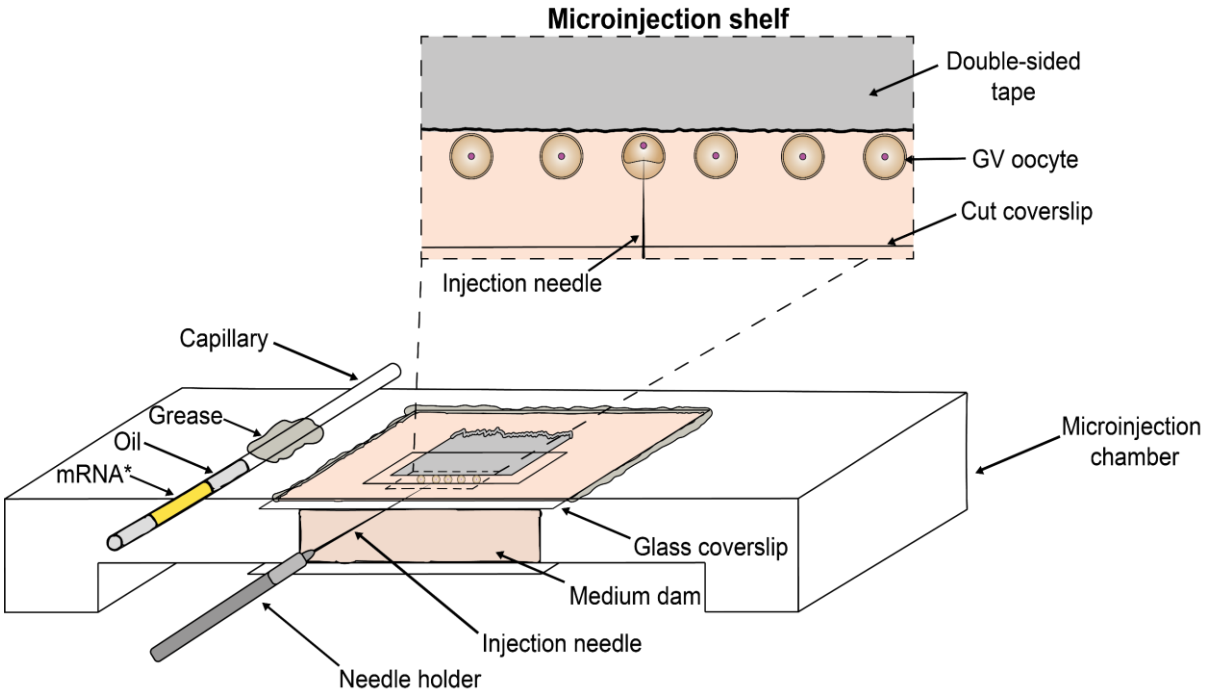

Figure 2.1 Microinjection set-up for injections of mRNA and protein into oocytes/eggs Cells are injected with mercury-filled needles connected to oil-filled hydraulic pumps, visualised on calibrated microscopes with measurement binoculars (allows quantitative injection). Microinjection needles are pulled with a micropipette puller, where heat, velocity, time, pull and pressure parameters can be optimised to improve efficiency and cell viability post injection. In a U-shaped microinjection chamber, cells are loaded into a glass shelf - created by spacing two sterilised coverslips between double-sided tape. ***mRNA or protein is loaded into RNase free glass capillaries, between oil phases, and held by grease in a groove on the microinjection chamber. mRNA and oil are collected through negative pressure and injected into oocytes/eggs by penetrating the cell membrane. Microinjections are conducted in a medium dam supplemented with drug additions where appropriate.

2.14 Complete and partial targeted degradation of cohesion complexes through TRIM-away

For complete cohesion TRIM-away experiments, TRIM21 expressing metaphase II arrested eggs were microinjected with 2-3 picolitres of Rec8 antiserum[174] at a dilution of 1:1 in PBS. Rec8 antiserum dilutions were supplemented with 0.05% (v/v) NP40-PBS and Alexa-Fluor 488 Dextran 10,000 MW (D22910, Molecular Probes) at a dilution of 1:40. For partial cohesion TRIM-away experiments, metaphase II arrested eggs expressing TRIM21 were injected as before with 2-3 picolitres of Rec8 antiserum at a dilution of 1:30-1:50 in combination with Alexa-Fluor 488 Dextran 10,000 MW (D22910, Molecular Probes) at a dilution of 1:40 and 0.05% (v/v) NP40-PBS. Control and experimental conditions were injected sequentially with the same Rec8 antiserum solution. In combinatory Rec8 degradation and cytoskeletal manipulation experiments, TRIM-away microinjection experiments were undertaken in M2 medium supplemented with individual or cytoskeletal drug combinations as appropriate.

2.15 3D chromatid surface reconstruction and chromatid scatter volume quantification

Chromatid surfaces were reconstructed from time-lapse sequences, using the H2B-mRFP signal as reference. Reconstruction was performed using the surfaces module of Imaris (Bitplane). Manual background removal was performed for each time frame and time-lapse movie to erase volumes that were not chromatid based, or signal from the chromosomes within the polar body. Object orientated bounding box analysis was subsequently performed in Imaris to provide the minimal cuboidal volume which encloses all the surfaces in each period. This analysis provides a measurement in XYZ which can be multiplied to determine the volume for each time frame. This bounding box analysis provides a ‘chromatid scatter volume’ for each time point. For each individual egg, normalization was achieved by dividing the chromatid scatter volume at each time point by the starting volume when the time-lapse was started (T = 0 mins) (equation 4). Normalized values were then visualized as individual traces or averaged to show trends between control and experimental groups.

$$\textbf{Normalised Chromatid Scatter Volume (CSV)} = \frac{(\mathrm{X} \times \mathrm{Y} \times \mathrm{Z} \text{ at } \mathrm{Tn})}{(\mathrm{X} \times \mathrm{Y} \times \mathrm{Z} \text{ at } \mathrm{T0})}$$

Equation 4

2.16 Quantification of 3D chromatid realignment and movement speed

The proportion of realigned chromatids returning to the spindle equator was analysed using the 3D chromatid surfaces previously described (section 2.15). A realignment event was defined as a misaligned chromatid re-joining the central chromosome mass for a period of at least 10 minutes. The proportion of realignment for control and experimental conditions was recorded in each individual egg where premature separation occurred.

The 3D chromatid surfaces previously acquired (described section 2.15) were used to quantify chromatid movement speeds for control and experimental conditions. Chromatids that migrated away from the main chromosome mass at the spindle equator were recorded in these analyses. Frame-to-frame movement was measured by recording the position of each individual chromatid's leading pole with the Measurements of Points function in Imaris (Bitplane). Cumulative displacement of each chromatid (μm) was then divided by the total duration of movement (minutes) to calculate 'instantaneous chromatid movement' speeds.

Equation 5

$$\textbf{Instaneous chromatid movement speed} = \frac{\text{Displacement (μm)}}{\text{Movement time (mins)}}$$

2.17 Statistical data analyses

Histograms, box plots and scatter plots were generated using Prism (GraphPad) software. Box plots show 5th, 95th (whiskers), 25th and 75th percentiles (box) enclosing 50% of the data, as well as means (line). Box plots are overlaid with individual data points. Details of statistical test can be found in the figure legends for each graph and test. Normality tests were performed in Prism on data sets before significance tests, to determine if the date was normally distributed. Appropriate statistical significance tests (parametric or nonparametric), one-way or two-way analysis of variances (ANOVA) were then performed in Prism software. Non-significant values are indicated as N.S., with significance values detailed as * P<0.05, ** P<0.005 and *** P<0.0005.

Chapter 3 – Actin limits egg aneuploidies associated with female reproductive ageing

3.1 Introduction

Chromosome cohesion is essential for the spatio-temporal control of chromosome segregation in meiosis I and meiosis II. Cohesion complexes located along chromosome arms maintain association between homologs until they are separated during anaphase I of meiosis I (Figure 1.3) [88,174,178]. Thereafter, cohesion between sister centromeres holds chromatids together until they are separated during anaphase of meiosis II (Figure 1.3). Reproductive age-related cohesion depletion generally results in egg and embryo aneuploidy, a cellular state of incorrect chromosome numbers. Embryo aneuploidy is a leading cause of pregnancy failure and genetic disorders, which highlights the importance of chromosome cohesion for healthy mammalian development. An exponential increase in aneuploidy in eggs and embryos from reproductively older women cannot be fully explained by a gradual loss of chromosome cohesion. Dysfunction of other key factors in mammalian meiosis must be contributing to the incidence of aneuploidy with advancing reproductive age. More recently, the actin cytoskeleton has emerged as a key player for ensuring accurate chromosome segregation in mammalian eggs [152,157]. This led to the development of a hypothesis that changes to the actin cytoskeleton contribute to aneuploidy as maternal age increases. An age-related dysfunction in F-actin could be an additive factor to the effects of gradual cohesion loss, leading to an exponential rise in aneuploidy. In this chapter, the relationship between the actin cytoskeleton and canonical chromosome cohesion was probed, importantly in young and ageing mammalian eggs.

3.2 Female reproductive ageing is accompanied by spindle-specific F-actin loss in eggs

The actin cytoskeleton is an essential component of the meiosis-specific chromosome segregation machinery [152,157]. To investigate whether age-dependent actin dysfunction can explain an exponential rise in aneuploidy, fluorescently labelled F-actin structures in eggs of young (6–12-week-old) and reproductively aged (58–62-week-old) mice were visualised by super-resolution microscopy (Figure 3.1a,b). Visualisation of phalloidin labelled F-actin showed that spindle F-actin populations in aged eggs were significantly reduced (Figure 3.1a,b, 3.2e). Aged eggs appear to have more disorder in their spindle F-actin populations when compared to young eggs which have consistent long filaments running through the microtubule-based spindle (Figure 3.1b). Quantification of F-actin fluorescence intensity ratios between the spindle and cytoplasm (method described in section 2.6) confirmed a significant spindle-specific F-actin loss in aged eggs (Figure 3.1c,d, 3.2e). This significant reduction indicates that reproductive ageing in female mammalian eggs is accompanied by a spindle-specific reduction of F-actin in metaphase-II spindles. To further confirm that F-actin loss in aged eggs is localised to the spindle, the cytoplasmic F-actin content of young and aged eggs was measured directly by super resolution microscopy. Single optical sections of fluorescently labelled F-actin structures were collected from young (6–12-week-old) and reproductively aged (58–62-week-old) eggs (Figure 3.2a,b). Quantification of the mean cytoplasmic F-actin intensity (method described in section 2.6, Figure 3.2c) revealed no significant difference between young and aged cytoplasmic F-actin levels (Figure 3.2d). These data (Figure 3.1 and Figure 3.2) collectively indicate a spindle-specific reduction in F-actin population in aged mammalian eggs.

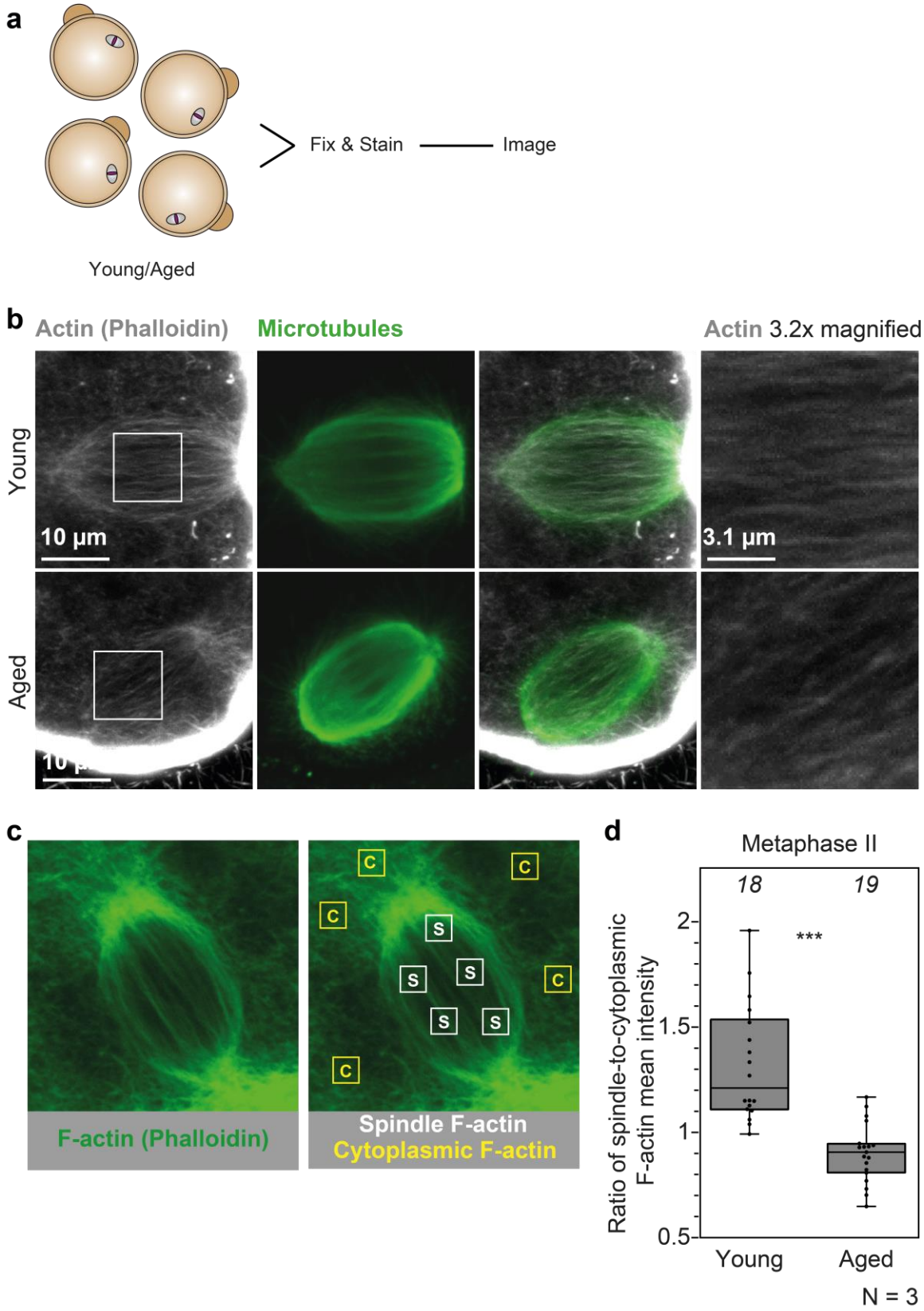
a
Fix & Stain
Image
Young/Aged
b
Actin (Phalloidin)
Microtubules
Actin 3.2x magnified
Young
Aged
10 µm
3.1 µm
c
F-actin (Phalloidin)
Spindle F-actin
Cytoplasmic F-actin
C
S
d
Metaphase II
18
19
***
Ratio of spindle-to-cytoplasmic F-actin mean intensity
2
1.5
1
0.5
Young
Aged
N = 3

Figure 3.1 Female reproductive ageing is accompanied by spindle-specific F-actin loss in eggs (a) Experimental design schematic. Oocytes were collected and allowed to progress through meiosis I to metaphase II arrest, characterized by the first polar body protrusion. Eggs were then fixed and stained for F-actin (phalloidin, grey) and Microtubules (tubulin, green) before imaging. **(b)** Sum intensity projections of phalloidin labelled spindle F-actin and microtubules in young and aged metaphase II-arrested eggs. Boxes mark regions that are magnified in insets. **(c)** Regions of interest used for quantification of the ratio of spindle: cytoplasmic F-actin intensity (described in methods section 2.6) **(d)** Quantification of ratio of spindle-to-cytoplasmic F-actin mean fluorescence intensity in young (1.00 $\pm$ 0.58) and aged (0.58 $\pm$ 0.27) metaphase II-arrested eggs. Data are from three independent experiments, numbers in italics represent the number of eggs analysed per condition. Statistical significance,*** $p<0.0001$ was evaluated using Mann-Whitney t-test. N.B $\bar{x} \pm SD$

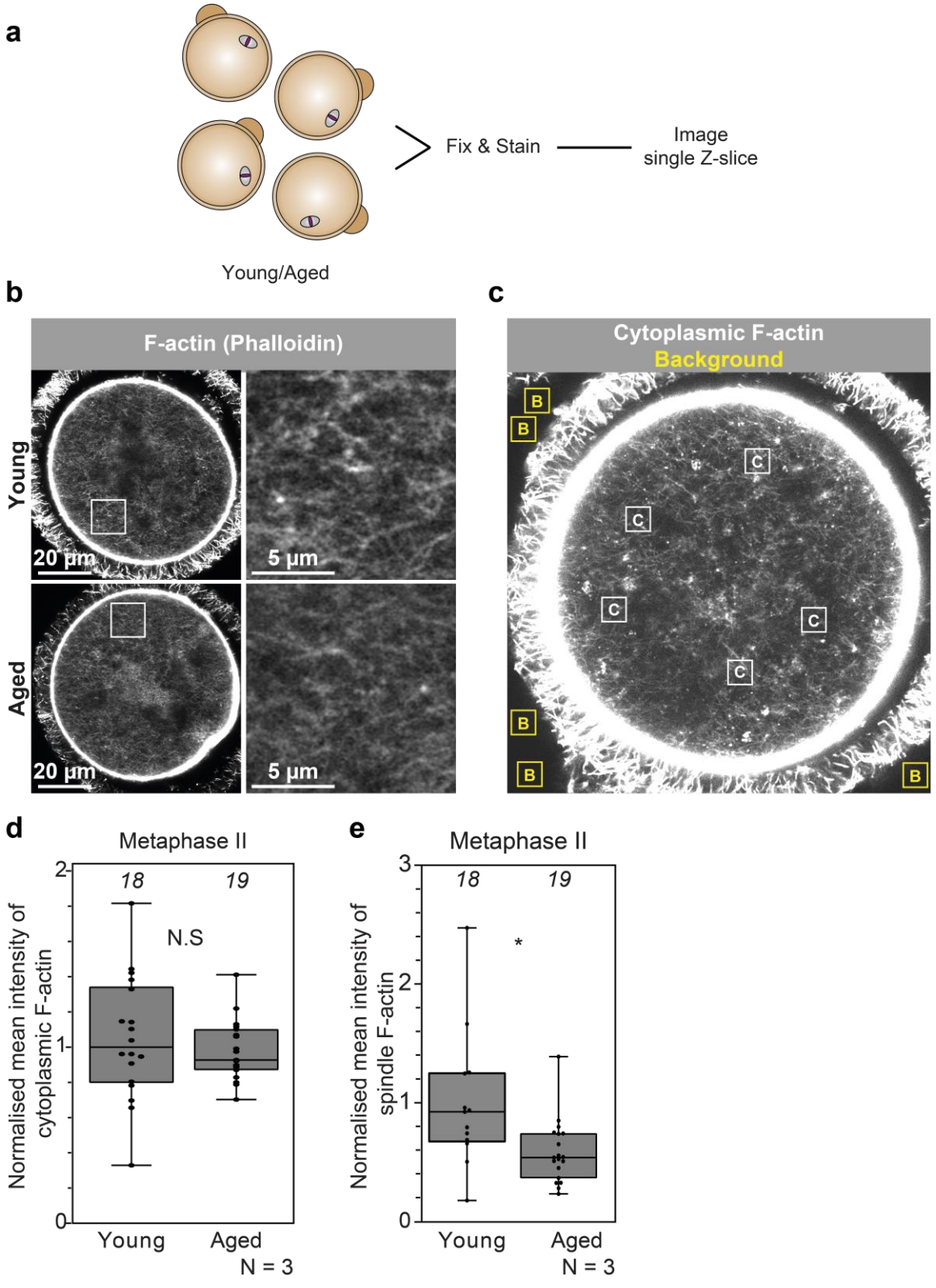
a
Fix & Stain
Image
single Z-slice
Young/Aged
b
F-actin (Phalloidin)
Young
Aged
20 µm
5 µm
20 µm
5 µm
c
Cytoplasmic F-actin
Background
B
C
d
Metaphase II
18
19
N.S
Normalised mean intensity of cytoplasmic F-actin
Young
Aged
N = 3
e
Metaphase II
18
19
*
Normalised mean intensity of spindle F-actin
Young
Aged
N = 3

Figure 3.2 Cytoplasmic F-actin intensity does not decrease with reproductive age (a) Experimental design schematic. Oocytes were collected and allowed to progress through meiosis I to metaphase II arrest, characterized by the first polar body protrusion. Eggs were then fixed and stained for F-actin (phalloidin, grey) before imaging. **(b)** Representative single section Airyscan images of phalloidin labelled cytoplasmic F-actin structures in metaphase II-arrested eggs of reproductively young or aged mice. Boxes mark regions that are magnified in insets. **(c)** Regions of interest used for quantification of cytoplasmic F-actin intensity (described in Materials and Methods 2.6) **(d)** Normalised cytoplasmic F-actin mean fluorescence intensities in young (1.05 ± 0.35) and aged (0.98 ± 0.17) metaphase II-arrested eggs. Data are from three independent experiments, numbers in italics represent the number of eggs analysed per group. Statistical significance, N.S p = 0.4564 was evaluated using Mann-Whitney t-test. N.B $\bar{x}$ ± SD **(e)** Normalised spindle F-actin mean fluorescence intensities in young (1.05 ± 0.35) and aged (0.98 ± 0.17) metaphase II-arrested eggs. Data are from three independent experiments, numbers in italics represent the number of eggs analysed per group. Statistical significance, * P<0.05 was evaluated using Mann-Whitney t-test. N.B $\bar{x}$ ± SD

3.3 Spindle microtubule filaments do not significantly decrease with reproductive age

An interplay between microtubules and actin has been identified in many systems [152,190-195]. Indeed, acute nocodazole mediated depolymerization of meiotic spindles in eggs causes rapid dissipation of spindle F-actin [152]. Microtubule disruption in aged eggs could therefore explain spindle-specific F-actin loss during female reproductive aging. To examine this possibility, spindle microtubule populations were assessed in young (6–12-week-old) and reproductively aged (58-62-week-old) mouse eggs (Figure 3.3 a, b). Quantification of the mean fluorescent intensities (see methods section 2.7 for details) showed that spindle microtubules do not decrease with advancing reproductive age (Figure 3.3 c, d). These results indicate that a spindle-specific reduction in F-actin is not because of a decrease in microtubules within metaphase II meiotic spindles in aged eggs.

Spindle microtubules are not reduced in aged eggs, so it is unlikely that spindle F-actin is disrupted due to defective microtubule dynamics as previously reported by Nakagawa and FitzHarris [179]. These data suggest that ageing may be accompanied by loss of F-actin-microtubule crosstalk proteins [190]. Interestingly, aged eggs have a significantly increased microtubule intensity, when compared with young eggs (Figure 3.3d). It would be expected therefore that spindle F-actin would increase in line with increased microtubules, emphasising the extent of the defects recorded here.

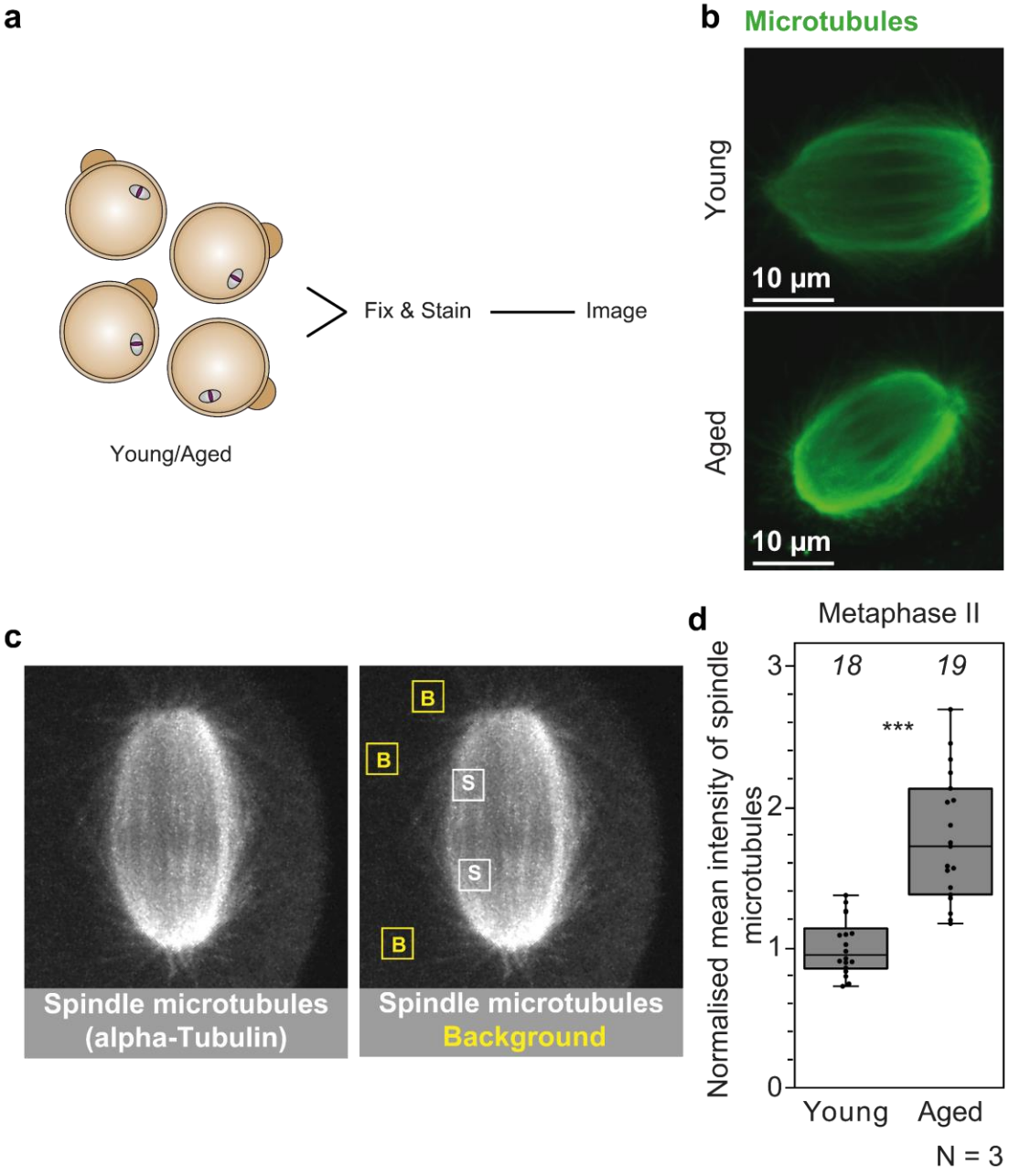
a
Young/Aged
Fix & Stain
Image
b
Microtubules
Young
Aged
10 µm
10 µm
c
Spindle microtubules
(alpha-Tubulin)
B
B
S
S
B
Spindle microtubules
Background
d
Metaphase II
18
19
***
Normalised mean intensity of spindle microtubules
3
2
1
0
Young
Aged
N = 3

Figure 3.3 Microtubule density is not reduced with reproductive ageing (a) Experimental design schematic. Oocytes were collected and allowed to progress through meiosis I to metaphase II arrest, characterized by the first polar body protrusion. Eggs were then fixed and stained for microtubules (tubulin, green) before imaging. **(b)** Sum intensity projections of microtubules in young and aged metaphase II-arrested eggs. **(c)** Example of method (described in section 2.7) for quantification, background correction and normalisation of spindle microtubule mean fluorescence intensities in eggs of reproductively young (1.00 ± 0.20) or aged (1.78 ± 0.45) mice. **(d)** Normalised spindle microtubule mean fluorescence intensities in young and aged metaphase II-arrested eggs. Data are from 3 independent experiments, numbers in italics represent the number of eggs analysed per group. Statistical significance, *** $p<0.0001$ was evaluated using Mann-Whitney t-test. N.B $\bar{x}$ ± SD

3.4 Quantitative microscopy pipeline for identification of prematurely separated chromatids

To examine how reproductive age-related F-actin disruption affects chromosomal organization, quantitative immunofluorescence microscopy was coupled with the spot detection module of Imaris software (Bitplane). High-resolution 3D microscopy (Figure 3.4, top panel) (details methods section 2.3, 2.5) allowed identification of centromeres (labelled with CENP-A) on sister chromatids labelled with Topoisomerase II (an enzyme that localises to the pericentromeric regions of DNA [188]) in the meiotic spindle (tubulin). Developing this pipeline allowed separated chromatids to be identified and counted in differing treatment conditions. Further analysis details can be found in methods section 2.8.

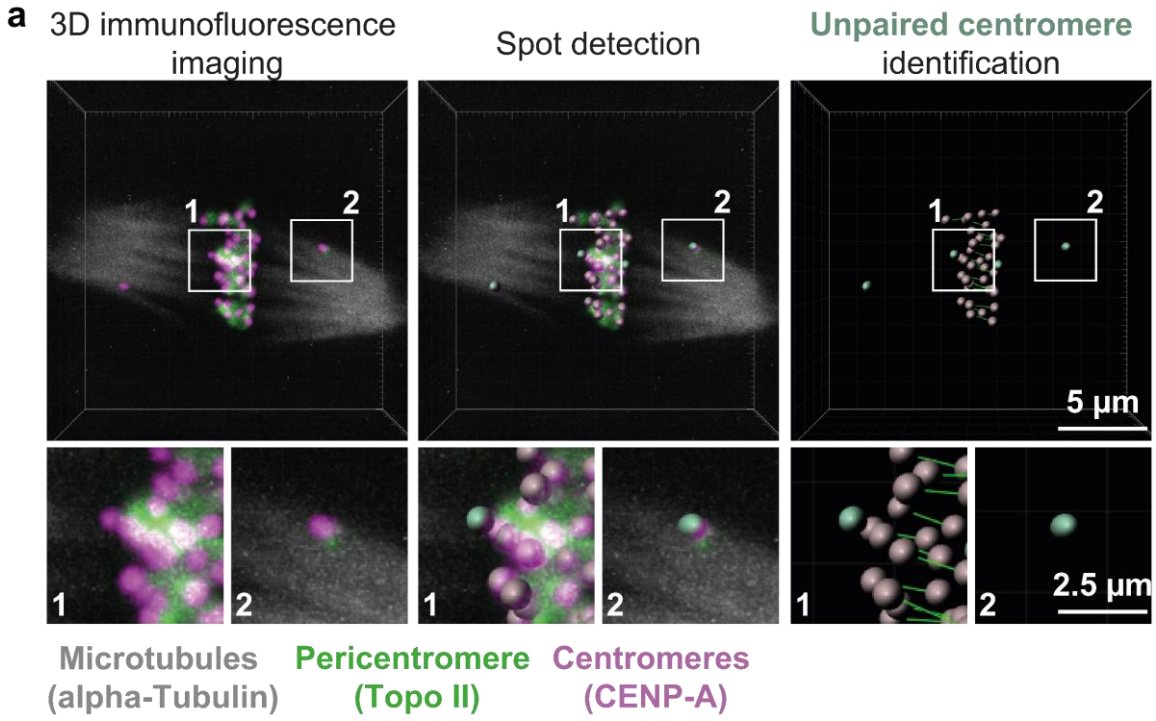

Figure 3.4 Imaging analysis pipeline for quantification of PSSC in mammalian eggs (**a)** Unpaired chromatid identification pipeline from maximum intensity projected immunofluorescence images of CENP-A, Topoisomerase-II, and microtubules. Pipeline begins with 3D immunofluorescence imaging, followed by spot detection in Imaris and unpaired centromere identification (highlighted as green spots). Green lines between centromeres indicate manual pairings to highlight prematurely separated sister chromatids. Boxes mark regions magnified in insets, 1. Showing a separated single chromatid within the main chromosome mass, 2. Highlighting a single chromatid that has been pulled towards the spindle poles.

3.5 F-actin loss exacerbates reproductive age-related premature chromatid separation in mammalian eggs

To understand whether reproductive age-related disruption of F-actin impacts chromosome organization, the actin-depolymerizing pharmacological compound Cytochalasin D [153,154] was used to disrupt F-actin in mammalian eggs. Cytochalasin D is a cell permeable agent that directly binds to the barbed end of actin filaments inhibiting new association or dissociation of monomeric subunits [196]. In contrast to control eggs where the cytoplasm was filled with a network of F-actin structures, Cytochalasin D treated eggs rarely contained filamentous actin-structures (Figure 3.5a, b). Although filaments are dissembled, the total level (measured by mean intensity) of actin is not diminished within the cell (Figure 3.5c). These results validated that Cytochalasin D treatment of mammalian eggs can be used successfully to remove intracellular F-actin networks.

Next, 3D high-resolution microscopy was conducted in reproductively young (6–12-week-old) and reproductively old (35-39-week-old) mouse eggs. Meiotic cold-stable treated spindles centromeres and chromosomes were imaged to assay whether actin-disruption exacerbates premature sister chromatid separation in ageing eggs. The cold-stable assay was used to selectively depolymerise non-kinetochore bound, dynamic microtubules [197]. Removal of non-k-fibres allows more precise imaging of sister chromatid interactions by removing background tubulin signal. Typically, cold exposure (through placement on ice) details prominent gaps within the spindle where non-kinetochore microtubules have been depolymerised and k-fibre interactions have been emphasised (Figure 3.6a). In DMSO-treated control aged eggs, 10/26 (~38%) showed at least two prematurely separated sister chromatids (Figure 3.6b,c). This observation is consistent with numerous studies of ageing-related cohesion loss, resulting in premature separation of sister chromatids [74,174,178]. In comparison to control aged eggs that showed moderate levels of separation, 17/21 (~80%) Cytochalasin D-treated eggs had a significantly high incidence of premature separation (Figure 3.6b,c). Together with the finding that spindle F-actin is disrupted during female reproductive ageing (Figure 3.1), these data suggest that F-actin limits the extent of premature chromatid splitting in cohesion-deficient aged eggs. Overall, these results are consistent with a hypothesis that spindle-associated

actin filaments counteract age-related aneuploidy by restricting the movement of prematurely separated sister chromatids.

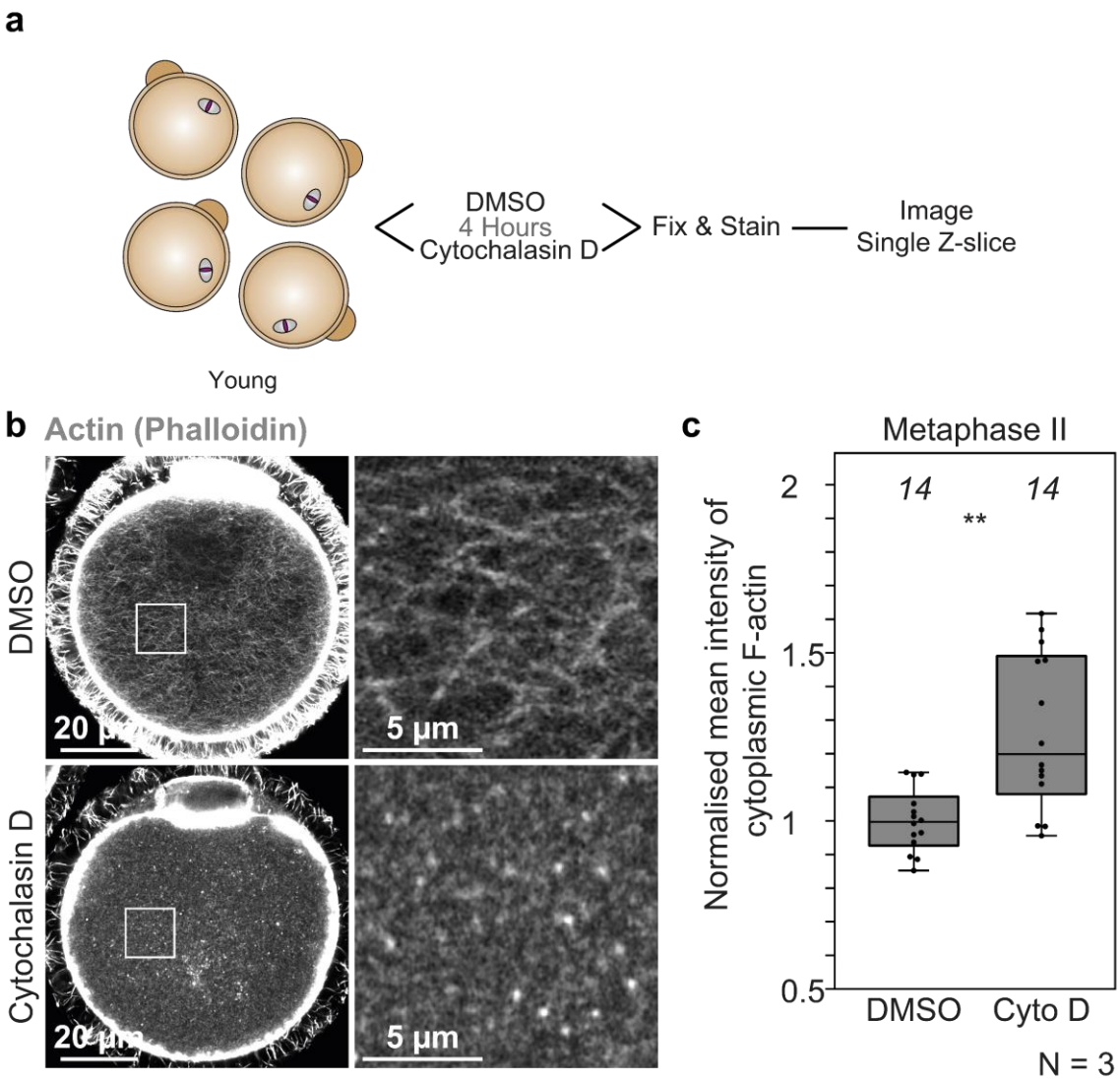

Figure 3.5 Cytochalasin D efficiently disrupts F-actin structures in mammalian eggs (a) Experimental design schematic. Oocytes were collected and allowed to progress through meiosis I to metaphase II arrest, characterized by the first polar body protrusion. Eggs were then incubated in media supplemented with either DMSO or Cytochalasin D (5 µg/ml) for 4 hours, then fixed and stained for F-actin (phalloidin, grey) before imaging. **(b)** Representative single-slice Airyscan immunofluorescence images of F-actin in DMSO- or Cytochalasin D-treated young and aged metaphase II-arrested eggs **(c)** Normalised cytoplasmic F-actin mean fluorescence intensities in DMSO (1.00 ± 0.09) and Cytochalasin D (1.27 ± 0.23) treated metaphase II-arrested eggs. Data are from three independent experiments, numbers in italics represent the number of eggs analysed per group. Statistical significance, ** p = 0.0017 was evaluated using Mann-Whitney t-test. N.B $\bar{x}$ ± SD II-arrested eggs.

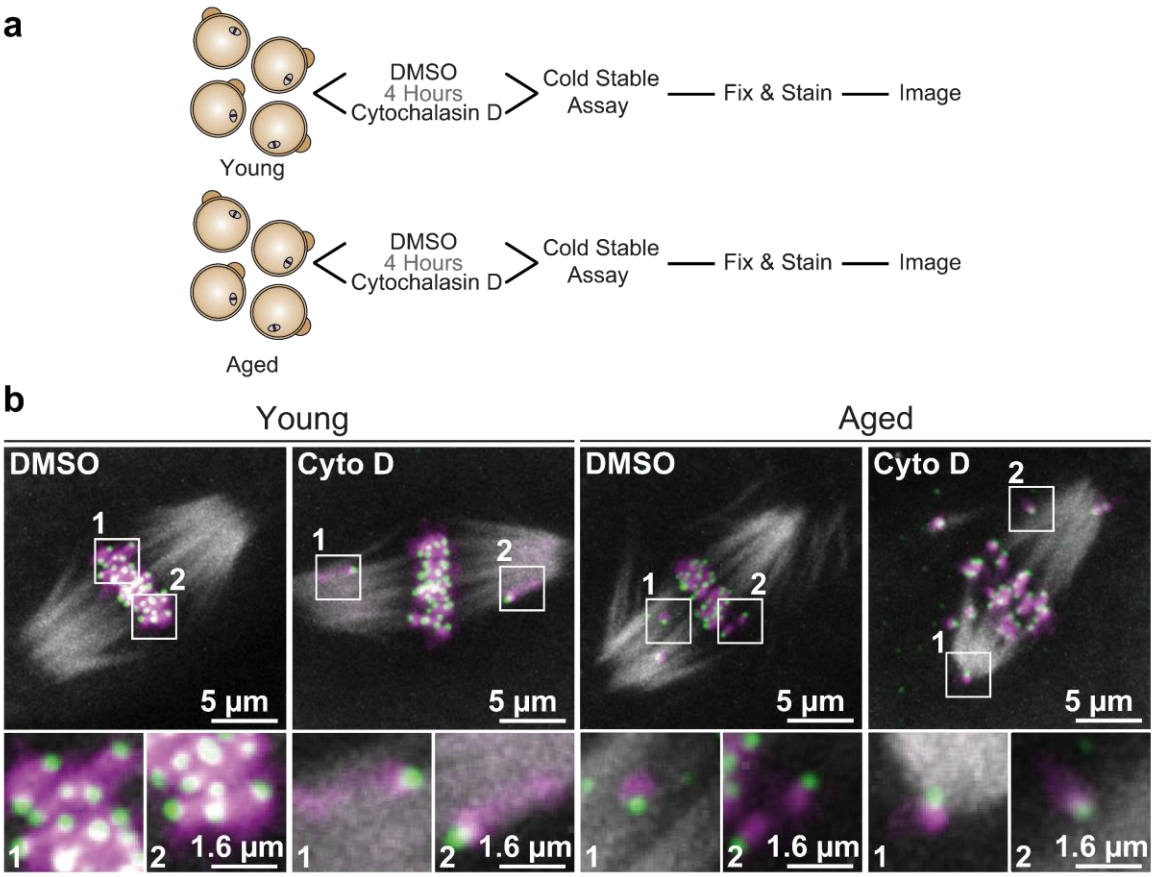
a
DMSO
4 Hours
Cytochalasin D
Cold Stable
Assay
Fix & Stain
Image
Young
Aged
b
Young
Aged
DMSO
Cyto D
5 µm
1.6 µm
Pericentromere (Topo II)
Centromeres (CENP-A)
Microtubules (alpha-Tubulin)
c
Metaphase II
Number of single chromatids per egg
20
25
26
21
N.S
**
*
***
DMSO
Cyto D
Young
Aged
N = 3

Figure 3.6 F-actin loss exacerbates reproductive age-related premature chromatid separation in mammalian eggs (a) Experimental design schematic. Oocytes were collected and allowed to progress through meiosis I to metaphase II arrest, characterized by the first polar body protrusion. Eggs were then incubated in media supplemented with either DMSO or Cytochalasin D (5 μg/ml) for 4 hours. Eggs were then placed on ice for 15 minutes to depolymerise non-kinetochore bound microtubules, before fixation, staining and imaging **(b)** Representative maximum intensity projected immunofluorescence images of microtubules, centromeres, chromatid pairs and single chromatids in DMSO- or Cytochalasin D-treated young and aged metaphase II-arrested eggs.**(c)** Quantification of the number of single chromatids in DMSO- or Cytochalasin D-treated young and aged metaphase II-arrested eggs. Data are from three independent experiments, numbers in italics represent the number of eggs analysed per group. Statistical significance was evaluated using Mann-Whitney t-test. Aged D:C ** $p<0.0069$, Young D:C ** $p=0.009$, Young C: Aged D N.S $p=0.5771$

3.6 F-actin disruption in young eggs induces ageing-like premature chromatid separation

In aged eggs actin disruption resulted in increasing numbers of prematurely separated chromatids. Similar experiments were performed in young eggs, to address whether loss of actin can predispose to prematurely separated chromatids. To this end, 3D high-resolution microscopy was employed to examine whether F-actin impacted chromosome cohesion in young eggs. These imaging assays where similarly combined with Cytochalasin D mediated actin disruption in reproductively young (6-12-weeks-old) eggs. In DMSO-treated control eggs, 2/20 had at least two prematurely separated sister chromatids (Figure 3.6b, c). In contrast, Cytochalasin D-mediated disruption of F-actin caused significant untimely chromatid splitting, with 12/25 eggs displaying at least two prematurely separated sister chromatids (Figure 3.6 b,c). Importantly, the likelihood of premature chromatid separation in Cytochalasin D treated young eggs is statistically comparable to the incidence of untimely chromatid splitting in control aged eggs (Figure 3.6 b,c). This suggests that F-actin disruption could be sufficient to induce egg aneuploidies comparable with female reproductive ageing.

To independently confirm that F-actin loss exacerbates premature separation of sister chromatids, metaphase II-arrested young eggs were treated with Latrunculin B, a mechanistically distinct F-actin disrupting compound that blocks actin polymerization by sequestration of unbound monomeric G-actin [154,157]. The incidence of prematurely separated chromatids in Latrunculin B-treated eggs was similar to that seen in Cytochalasin D-treated eggs, with 12/20 having two or more single chromatids (Figure 3.7 b,c). As before, this was a significant increase to young DMSO control treated eggs (Figure 3.7c).

Collectively, these data demonstrate that disruption of F-actin is sufficient to induce high incidence of premature chromatid separation in young eggs that is reminiscent of common sister chromatid splitting events that accompany female reproductive aging.

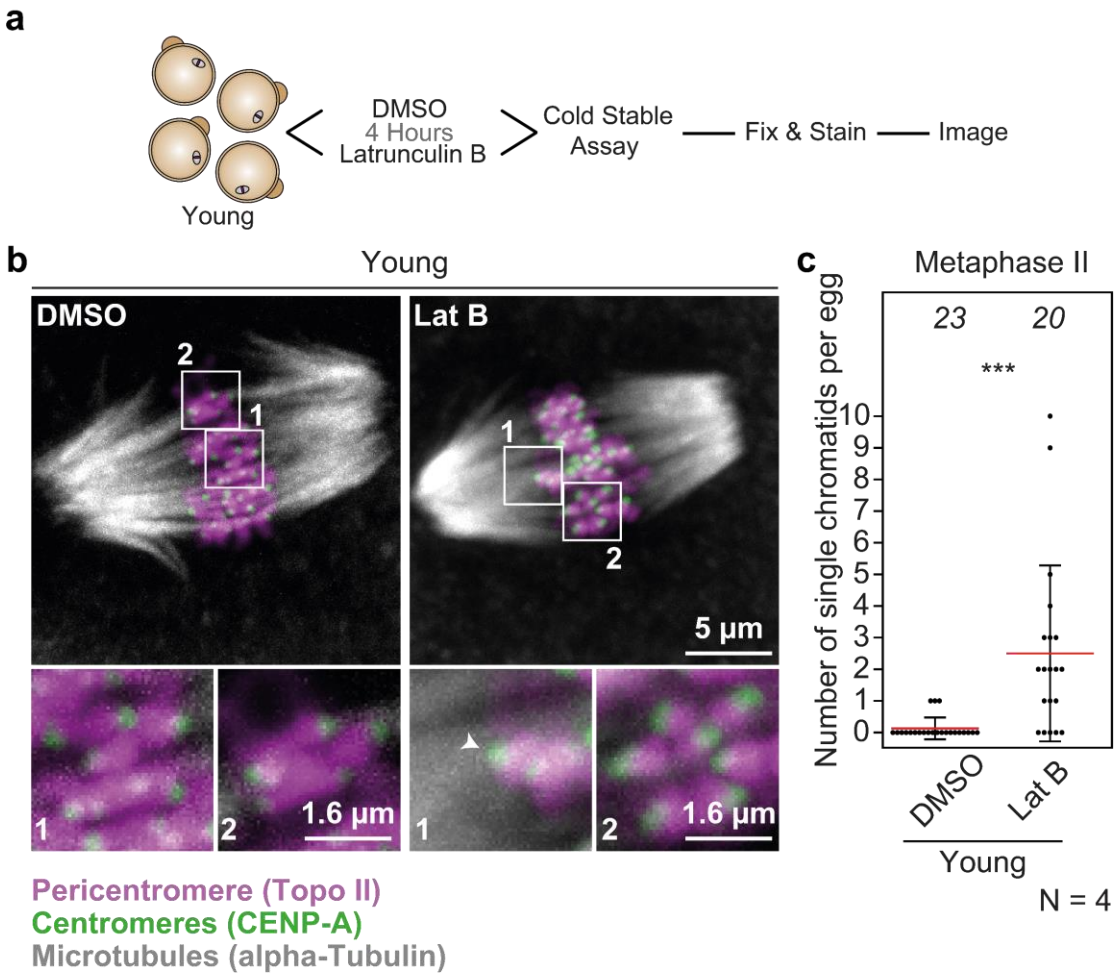

Figure 3.7 F-actin loss exacerbates premature chromatid separation in mammalian eggs (a) Experimental design schematic. Oocytes were collected and allowed to progress through meiosis I to metaphase II arrest, characterized by the first polar body protrusion. Eggs were then incubated in media supplemented with either DMSO or Latrunculin B (5 µM) for 4 hours. Eggs were then placed on ice for 15 minutes to depolymerise non-kinetochore bound microtubules, before fixation, staining and imaging **(b)** Representative maximum intensity projected immunofluorescence images of microtubules, centromeres, chromatid pairs and single chromatids in DMSO- or Latrunculin B-treated young metaphase II-arrested eggs. **(c)** Quantification of the number of single chromatids in DMSO- or Latrunculin B-treated young metaphase II-arrested eggs. Data are from four independent experiments, numbers in italics represent the number of eggs analysed per group. Statistical significance, *** p<0.0001, was evaluated using Mann-Whitney t-test.

3.7 Quantitative microscopy assays to measure premature chromatid separation in chromosomal spreads

To further confirm the finding that F-actin disruption predisposes eggs to premature chromatid separation, chromosomal spreading techniques were optimised and performed to visualise single chromatids outside of the meiosis spindle. Often in intact spindles, chromosomes are tightly bunched in the main chromosome mass making it hard to distinguish prematurely separated sister chromatids. High-resolution 3D-immunfluorescence microscopy (Figure 3.8, top panel) (detailed in methods section 2.4, 2.5) allowed identification of centromeres (magenta, CENP-A) and chromosomes (grey, Hoechst) in chromosomal spreads. Kinetochores were then identified using an automated spot detection algorithm in Imaris and sister kinetochores were related to each other (Figure 3.8, bottom panel). Developing this pipeline allowed separated chromatids to be identified and counted in differing treatment conditions. Further analysis details can be found in methods section 2.8

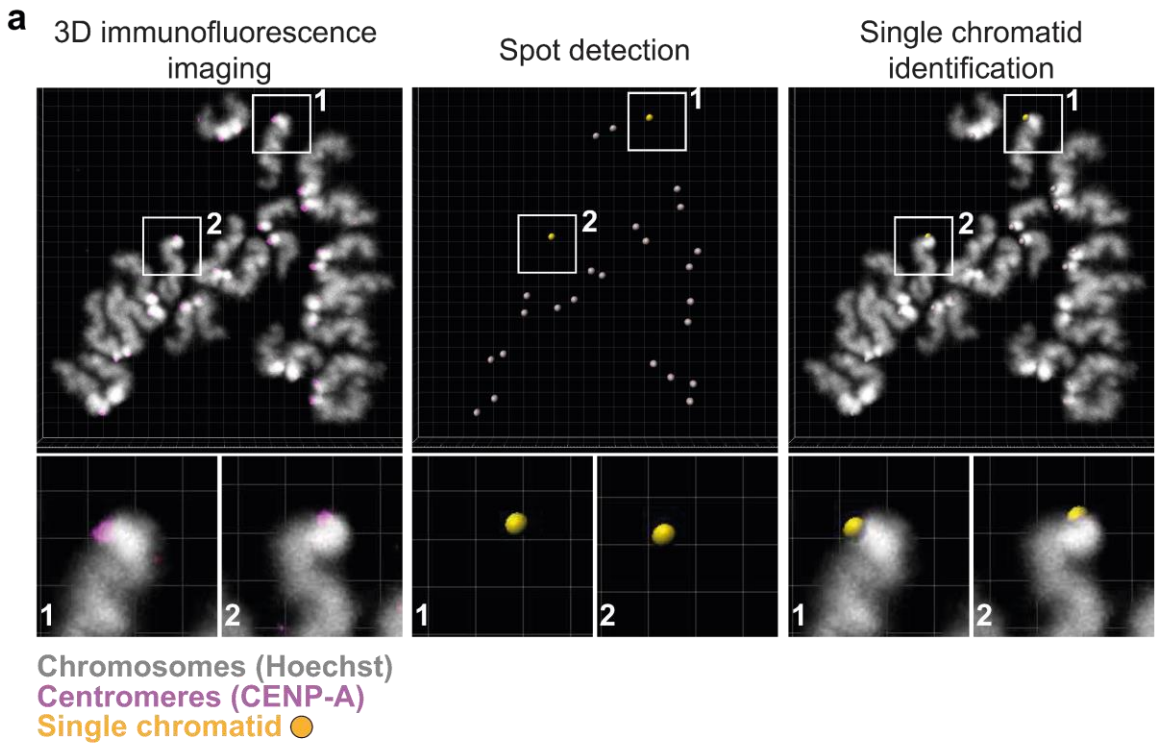

Figure 3.8 Quantitative microscopy pipeline reproducibly identifies prematurely separated chromatids in chromosomal spreads (a) First maximum intensity projected immunofluorescence images of CENP-A and Hoechst from metaphase-II chromosome spreads were acquired. Next spot detection allowed identification of sister kinetochores within a pair – defined as two proximal centromeres spanning consecutive optical sections. Single chromatids were then readily identifiable as having no corresponding pair.

3.8 Chromosomal spread analyses reveal that F-actin disruption impacts chromatid association

3D immunofluorescence imaging was conducted on metaphase-II chromosomal spreads from 6-12-weeks-old eggs. In DMSO control spreads, 3/19 showed two or more prematurely separated single chromatids, whereas 14/19 contained completely undisturbed chromosome pairs (Figure 3.9b,d). As in intact spindles, Cytochalasin D treatment caused a significant increase in untimely chromatid splitting with 8/19 chromosomal spreads displaying two or more single chromatids (Figure 3.9b,d). These results were confirmed by performing chromosomal spreads of metaphase II-arrested eggs that were treated with Latrunculin B, which disrupts actin via a distinct mechanism of action from Cytochalasin D [154]. 8/15 of chromosomal spreads from Latrunculin B-treated eggs had two or more prematurely separated single chromatids. This was a significant increase in chromatid splitting, with control treated spreads showing little separation (Figure 3.9c,e). Often odd numbers of single chromatids were recorded in chromosome spread analyses. This could be due to prematurely separated single chromatids being lost during the spreading process or through the numerous washing stages required to produces quantifiable immunofluorescence images. Data obtained using these independent chromosomal spread approaches confirm that acute disruption of F-actin in metaphase II predisposes young eggs to high incidence of premature chromatid separation.

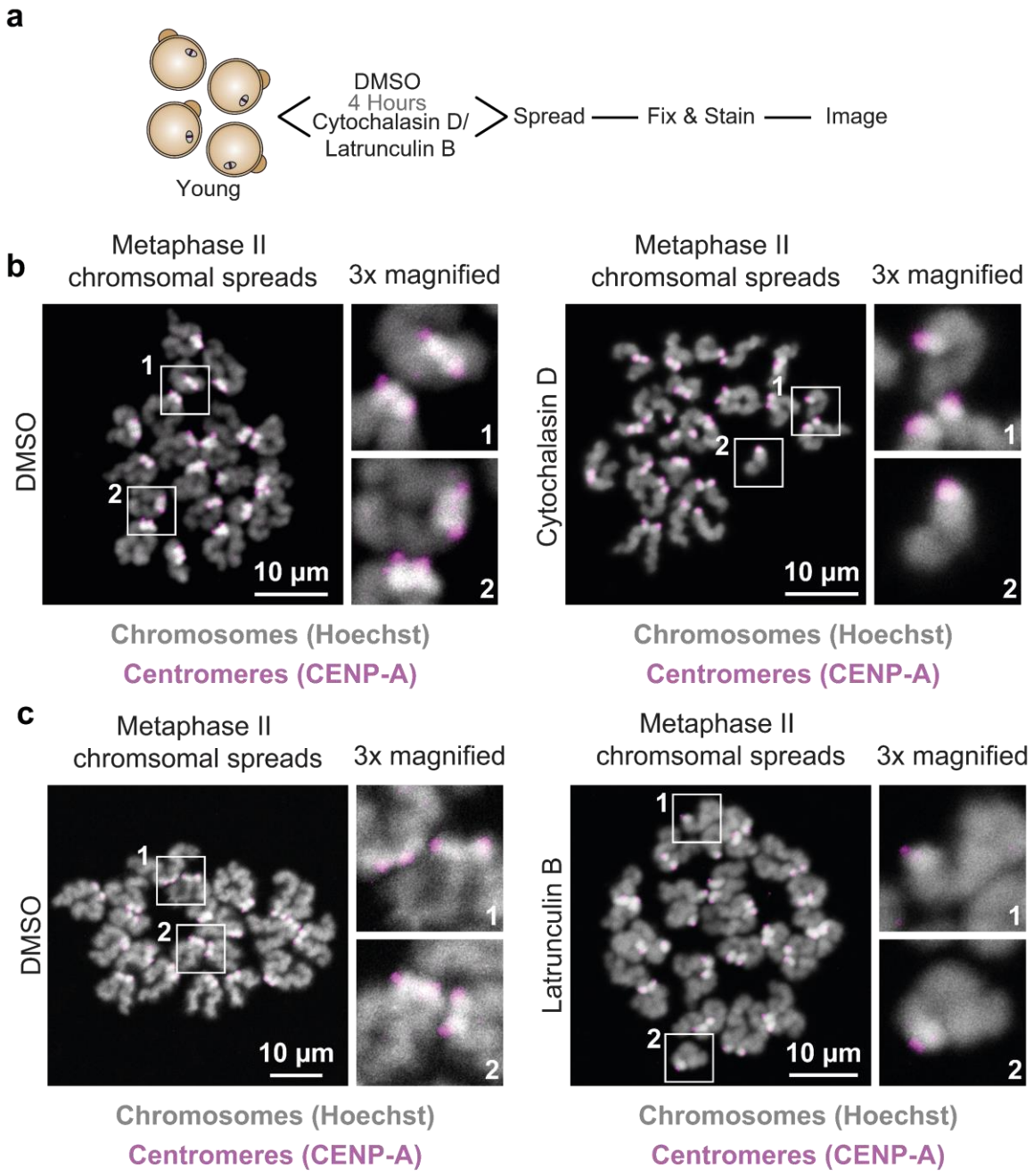
a
Young
DMSO
4 Hours
Cytochalasin D/
Latrunculin B
Spread
Fix & Stain
Image
b
Metaphase II
chromsomal spreads
3x magnified
DMSO
Cytochalasin D
10 µm
Chromosomes (Hoechst)
Centromeres (CENP-A)
c
Latrunculin B

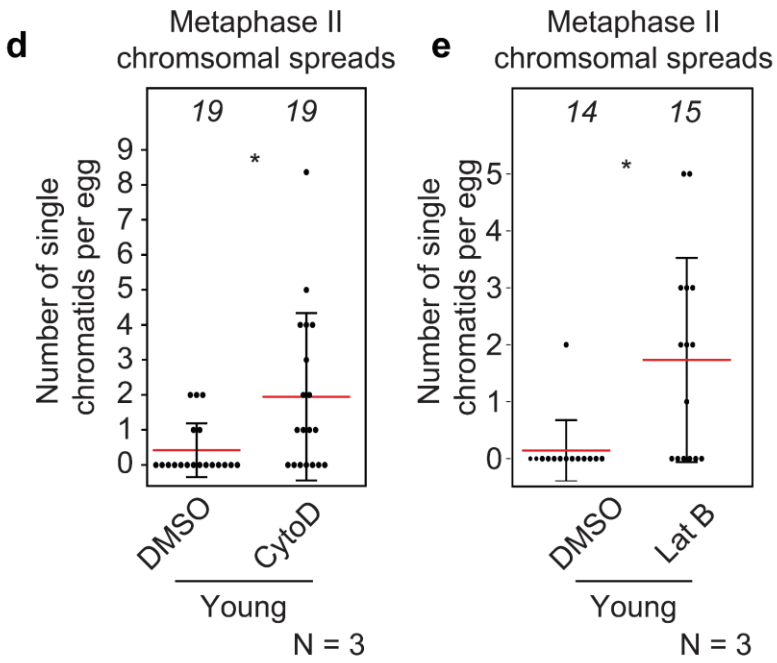

Figure 3.9 F-actin loss exacerbates premature chromatid separation in chromosome spreads (a) Experimental design schematic. Oocytes were collected and allowed to progress through meiosis I to metaphase II arrest, characterized by the first polar body protrusion. Eggs were then incubated in media supplemented with either DMSO, Cytochalasin D (5 µg/ml) or Latrunculin B (5 µM) for 4 hours. The zona was then removed before spreading onto glass slides, fixation, staining and imaging **(b)** Representative maximum intensity projected immunofluorescence images of centromeres and chromatids in metaphase II chromosomal spreads of DMSO- or Cytochalasin D-treated young eggs. **(c)** Representative maximum intensity projected immunofluorescence images of centromeres and chromatids in metaphase II chromosomal spreads of DMSO- or Latrunculin B-treated young eggs. **(d)** Quantification of the number of single chromatids in metaphase II chromosomal spreads of DMSO- or Cytochalasin D-treated young eggs. Data are from three independent experiments numbers in italics represent the number of spreads analysed per group. Statistical significance, * p=0.0131 was evaluated using Mann-Whitney t-test. **(e)** Quantification of the number of single chromatids in metaphase II chromosomal spreads of DMSO- or Latrunculin B-treated eggs. Data are from three independent experiments numbers in italics represent the number of spreads analysed per group. Statistical significance, * p=0.0031 was evaluated using Mann-Whitney t-test.

3.9 F-actin loss does not increase inter-kinetochore distance in intact eggs

F-actin disruption in both young and aged eggs caused an increase in untimely separation of sister chromatids eluding to a weakening of chromosome cohesion. A readout for weakened cohesion is an increase in the inter-kinetochore distance (IKD) – essentially the spacing between sister chromatids created by bipolar microtubule attachment [174]. An increase in IKD and therefore a weakening of chromosome cohesion has been previously reported in reproductively aged mouse and human eggs [97,174,178]. Inter-kinetochore distances were measured from 6-12-week-old metaphase II eggs treated with either DMSO or Cytochalasin D. To measure the distance between sister kinetochores, cold-treated metaphase II spindles, predominantly composed of kinetochore-bound microtubules, were imaged using high-resolution immunofluorescence microscopy (Figure 3.10a, methods section 2.9). In control DMSO-treated eggs, the average inter-kinetochore distance (IKD) of 1.35 ± 0.30 µm was statistically comparable to the average IKD of 1.32 ± 0.26 µm found between sister chromatids from Cytochalasin D-treated eggs (Figure 3.10b). These results suggest that actin-disruption does not appear to cause weakened cohesion and that microtubule-based tension, created by bipolar kinetochore attachment, is generally maintained across sister-kinetochores.

These results were further investigated by measuring the inter-kinetochore distances of metaphase II-arrested eggs that were treated with Latrunculin B [154]. In control DMSO-treated eggs, inter-kinetochore distances averaged at 1.43 ± 0.35 µm between sister chromatids (Figure 3.10c), which is similar to DMSO controls in Cytochalasin D treatment experiments. However, in Latrunculin B treated eggs the mean IKD significantly reduced to 1.22 ± 0.36 µm (Figure 3.10c). This suggests microtubule tension across sister-kinetochores was lost when actin was depolymerized using Latrunculin B. Consistently, however, Latrunculin B did not cause an increase in the IKD, confirming a notion that actin disruption does not appear to influence a weakening of chromosome cohesion.

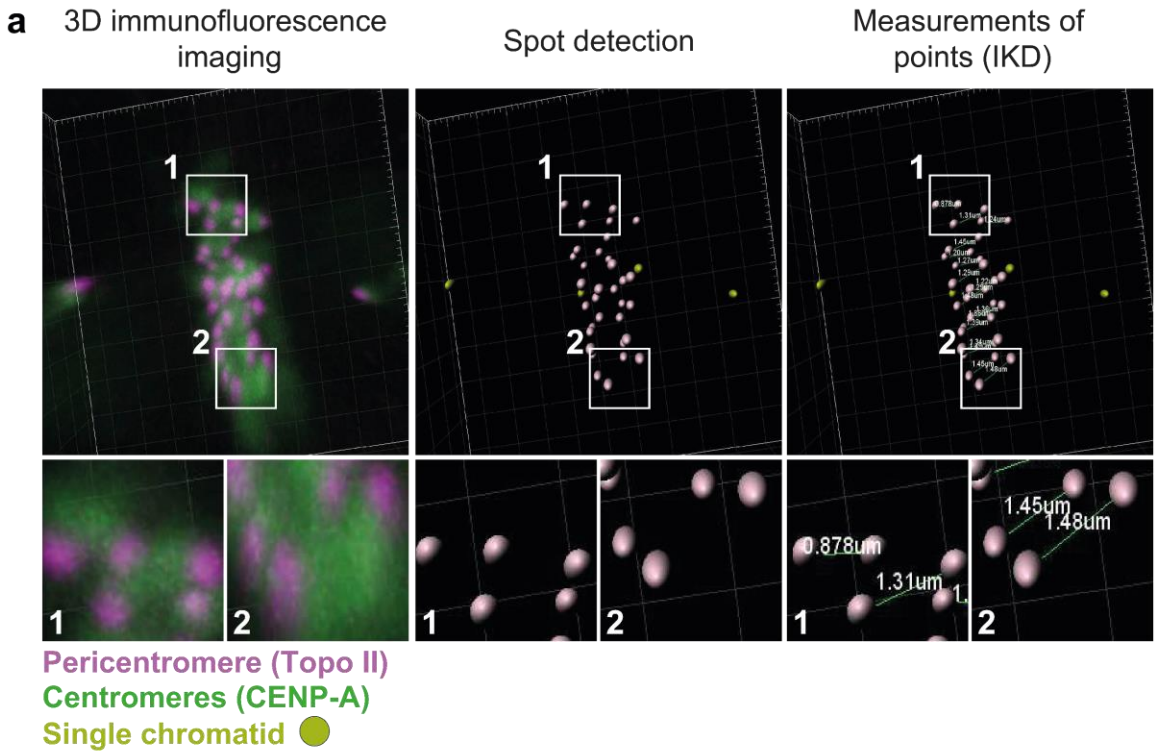
a
3D immunofluorescence imaging
Spot detection
Measurements of points (IKD)
1
2
0.878um
1.31um
1.45um
1.48um
Pericentromere (Topo II)
Centromeres (CENP-A)
Single chromatid

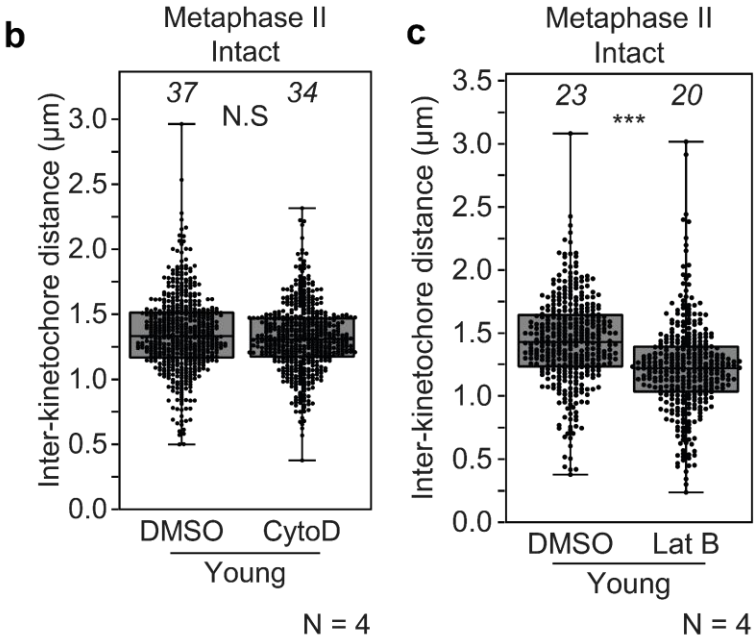
b
Metaphase II
Intact
37
N.S
34
Inter-kinetochore distance (µm)
3.0
2.5
2.0
1.5
1.0
0.5
0.0
DMSO
CytoD
Young
N = 4

c
Metaphase II
Intact
23
***
20
Inter-kinetochore distance (µm)
3.5
3.0
2.5
2.0
1.5
1.0
0.5
0.0
DMSO
Lat B
Young
N = 4

Figure 3.10 F-actin loss does not globally affect inter-kinetochore distance in intact spindles (a) IKD measurement pipeline from maximum intensity projected immunofluorescence images of CENP-A and Topoisomerase II from metaphase II intact eggs. Spot detection with manual correction allowing pairing and measurements of IKD in Imaris software (Bitplane). **(b)** Quantification of Inter-Kinetochore distance in DMSO- or Cytochalasin D-treated young metaphase II-arrested eggs (5 µg/ml, 4 hours). For DMSO groups, the total number of kinetochore pairs analysed was 544, For Cytochalasin D groups, the total number of kinetochore pairs analysed was 540 **(c)** Quantification of Inter-Kinetochore distance in DMSO- or Latrunculin B-treated young metaphase II-arrested eggs (5 µM, 4 hours). For DMSO groups, the total number of kinetochore pairs analysed was 380 whereas for Latrunculin B groups, the total number of kinetochore pairs analysed was 355. Data are from four independent experiments, numbers in italics represent the number of eggs analysed per group. Statistical significance was evaluated using Mann-Whitney t-test. N.B $\bar{x} \pm SD$

3.10 F-actin loss does not globally increase inter-kinetochore distance in chromosomal spreads

In intact metaphase II eggs, cytoskeletal forces influence sister-chromatids through biorientation, and the tension generated from microtubule-based pulling forces [92,198]. Changes in inter-kinetochore distances maybe masked by tension created by opposing microtubule pulling forces. Inter-kinetochore distances (IKD) were therefore measured in chromosomal spreads of DMSO and Cytochalasin D treated metaphase II-arrested young eggs (Figure 3.11a, methods section 2.9). The average IKD in control DMSO of 1.83 ± 0.56 was statistically comparable to the average IKD of 1.89 ± 0.78 recorded between sister kinetochores in Cytochalasin D-treated chromosomal spreads (Figure 3.11b). As before, Latrunculin B was used as a mechanistically distinct actin depolymeriser. There was a marginally significant increase in IKD when actin-was disrupted with Latrunculin-B, which could be attributed to the inclusion of prematurely separated sister chromatids that remain near to each other within the analysis (Figure 3.11c). Generally, these data concur with Cytochalasin D-treated intact eggs suggesting that actin disruption does not globally cause a weakening of cohesion between sister chromatids.

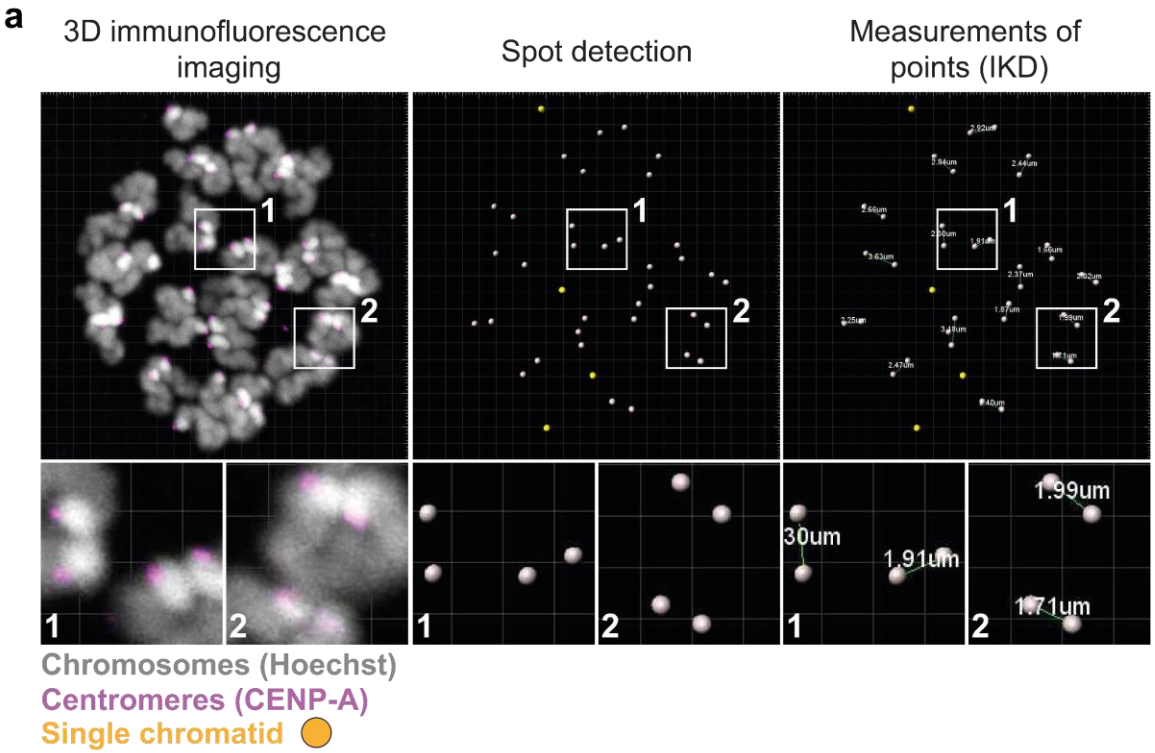
a
3D immunofluorescence imaging
Spot detection
Measurements of points (IKD)
1
2
1.99um
30um
1.91um
1.71um
Chromosomes (Hoechst)
Centromeres (CENP-A)
Single chromatid

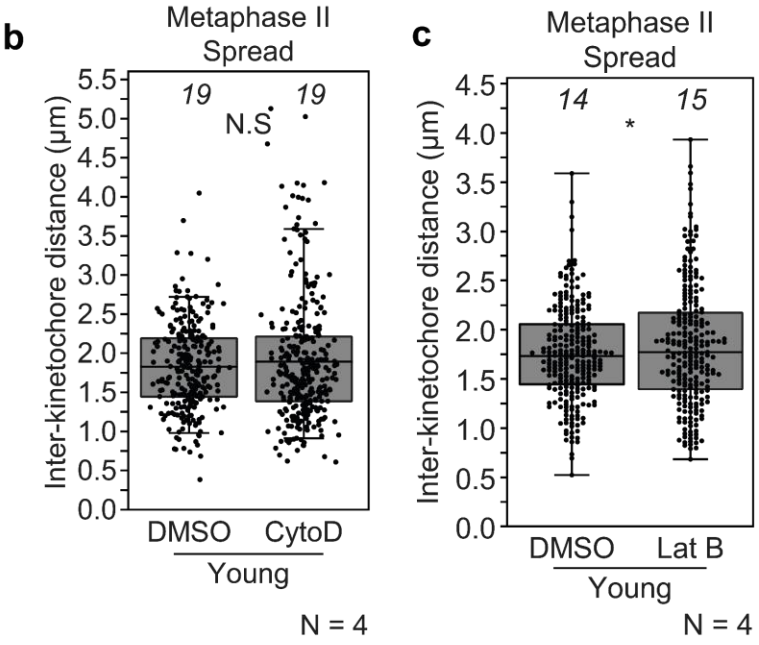
b
Metaphase II Spread
19
19
N.S
Inter-kinetochore distance (µm)
5.5
5.0
4.5
4.0
3.5
3.0
2.5
2.0
1.5
1.0
0.5
0.0
DMSO
CytoD
Young
N = 4

c
Metaphase II Spread
14
15
*
Inter-kinetochore distance (µm)
4.5
4.0
3.5
3.0
2.5
2.0
1.5
1.0
0.5
0.0
DMSO
Lat B
Young
N = 4

Figure 3.11 F-actin loss does not globally increase inter-kinetochore distance in chromosome spreads (a) IKD measurement pipeline from maximum intensity projected immunofluorescence images of CENP-A and Hoechst from metaphase II chromosomal spreads. Spot detection with manual correction and pairing for measurements of IKD in Imaris software (Bitplane). For both single chromatids are highlighted in a different colour, see key. **(b)** Quantification of Inter-Kinetochore distance in DMSO- or Cytochalasin D-treated young metaphase II-arrested eggs (5 µg/ml, 4 hours). **(c)** Quantification of Inter-Kinetochore distance in DMSO- or Latrunculin B -treated young metaphase II-spreads (5 µM, 4 hours). Data are from four independent experiments, numbers in italics represent the number of eggs/spreads analysed per group. Statistical significance was evaluated using Mann-Whitney t-test. N.B $\bar{x} \pm SD$

3.11 F-actin disruption does not impact classical mechanisms of centromeric cohesion in intact eggs

Previous data from intact metaphase II eggs suggested that when actin was disrupted, the inter-kinetochore distance did not increase, indicating that cohesion had not been weakened in a whole chromosome analysis. To expand on this observation, it was important to visualise cohesion complexes in intact spindles, to discern if cohesion was indeed affected. To visualise how actin disruption impacts cohesion, a 3D immunofluorescence microscopy approach was developed. This entailed immunostaining of the meiosis specific protein Rec8 which is found lining the chromosome arms and centromeres in meiosis I oocytes prior to anaphase I (methods section 2.3). Figure 3.12a shows maximum intensity projections of a mouse metaphase I spindle, depicting chromosomes (Hoechst) and Rec8. Magnified regions (boxed), clearly showing Rec8 positive cohesion complexes at centromeric and arm loci. When combined with 3D volume reconstruction in Imaris, this approach provided a method for selectively measuring fluorescence intensity of cohesion proteins on individual chromosomes (Figure 3.12b, methods section 2.10).

As a proof-of-concept experiment to confirm that this imaging pipeline can reproducibly measure reduced cohesion levels, metaphase I oocytes were treated with Reversine, an inhibitor of monopolar spindle kinase 1 (Mps1) [199] which leads to the loss of Shugosin-2 at the centromeres, exposing Rec8 to Seperase mediated cleavage [72]. The Rec8 intensity should therefore decrease in oocytes treated with Reversine. Quantification of cohesion levels using this approach revealed that Rec8 fluorescence intensity was significantly reduced in Reversine-treated oocytes when compared to control DMSO-treated oocytes (Figure 3.13b,c,)

To visualise if actin disruption caused changes to established cohesion complexes, metaphase I oocytes were matured in DMSO or actin destabilising Cytochalasin D supplemented media. 3D immunofluorescence images were then obtained from each group to visualise Rec8 positive cohesion complexes along the arms and at the centromeres of chromosomes (Figure 3.14b,c, Supplementary movie S1 and S2). Quantification of the normalised Rec8 mean intensity showed no significant difference between control and

Cytochalasin D treated oocytes (Figure 3.14d). These data demonstrate that it is unlikely that loss of F-actin disrupts classical cohesion mechanisms, and that premature separation likely arises from alternative sources.

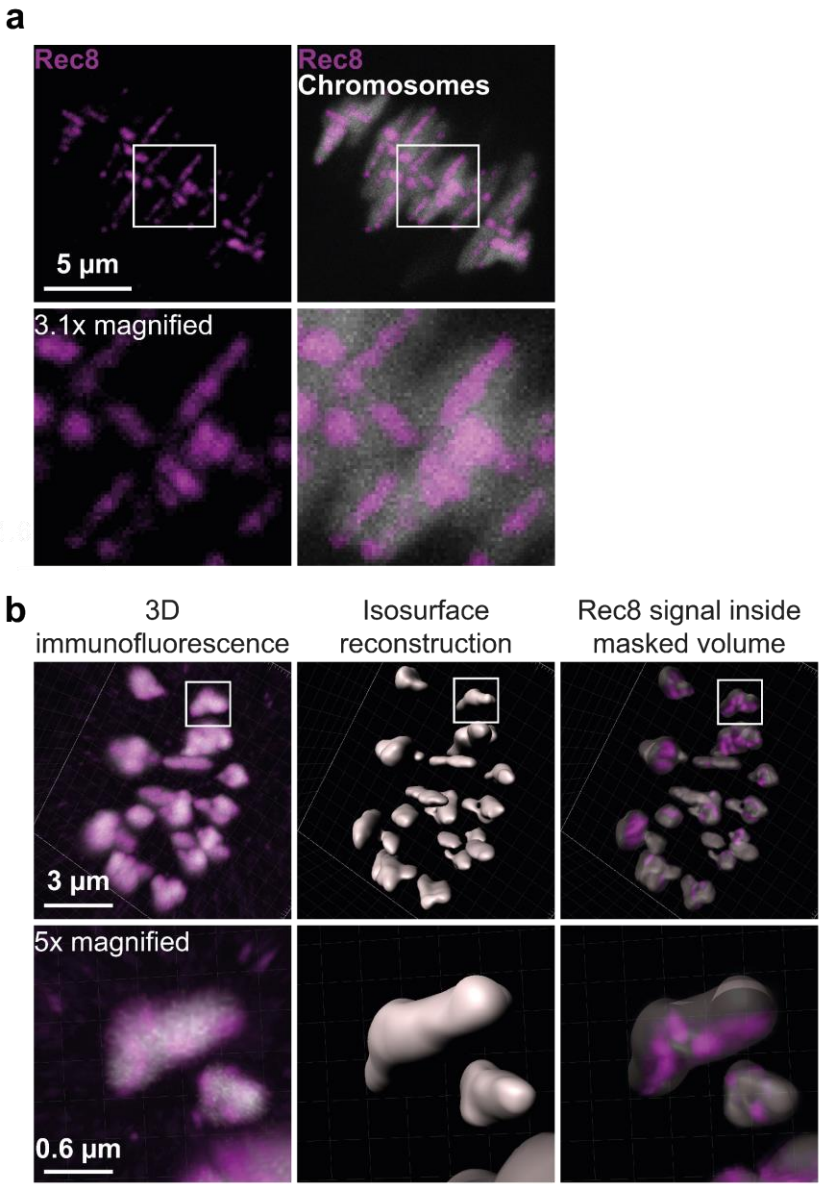

Figure 3.12 Imaging cohesion complexes and quantifying intensities in mammalian eggs (a) Maximum intensity projected high-resolution immunofluorescence images of Rec8 cohesin complexes (magenta) and homologous chromosomes (grey) in a mouse oocyte. Chromosome arm cohesion complexes are cleaved prior to anaphase-I ~5-6 hours after nuclear envelope breakdown (NEBD). Oocytes were therefore fixed once a metaphase-I spindle had formed and bivalent chromosomes were organised in a metaphase-plate, prior to cohesion cleavage. **(b)** Rec8 immunofluorescence intensity quantification pipeline for intact oocytes. This pipeline was established from 3D immunofluorescence images showing Rec8 (magenta) and bivalent homologous chromosome pairs (grey) Isosurface reconstruction allowed individual chromosome volumes to be attained. Chromosome volumes allowed the Rec8 signal to be masked; Rec8 mean fluorescent intensities were then recorded for each chromosome. Further details of this analysis pipeline can be found in methods section 2.10.

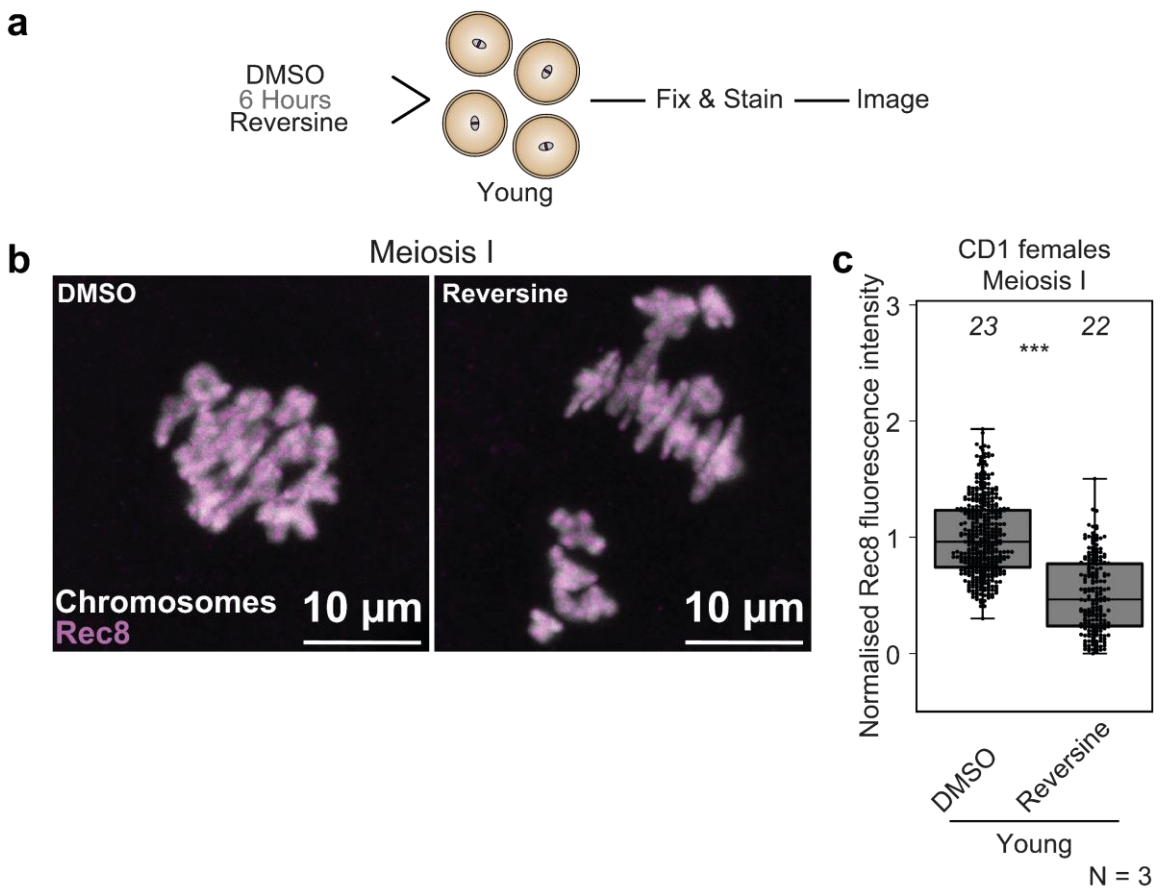

Figure 3.13 Changes in Rec8 intensity can be quantified in metaphase-I eggs

(a) Experimental design schematic. Oocytes were collected and allowed to progress to metaphase I, in media supplemented with either DMSO or Reversine (0.5 µM). The zona was then removed before fixation, staining and imaging **(b)** Representative maximum intensity projections from immunofluorescence images of Rec8 and chromosomes in DMSO and Reversine-treated mouse oocytes. **(c)** Normalised Rec8 mean fluorescence intensities in DMSO- or Reversine-treated mouse oocytes. Data are from three independent experiments, numbers in italics represent the number of oocytes analysed per group. Statistical significance, *** $p<0.0001$ was evaluated using Mann-Whitney t-test. N.B $\bar{x} \pm SD$

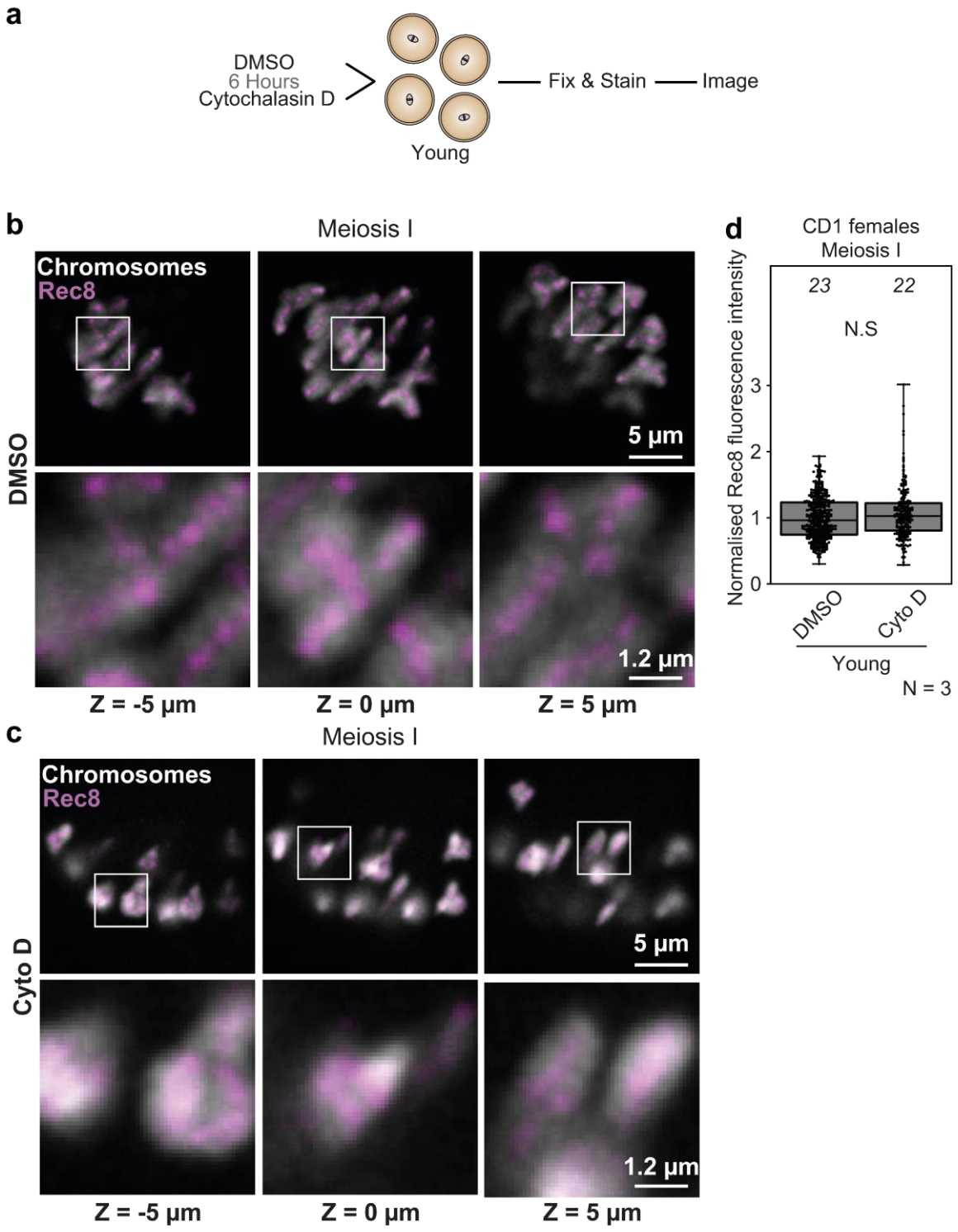
a
DMSO
6 Hours
Cytochalasin D
Young
Fix & Stain
Image
b
Meiosis I
Chromosomes
Rec8
DMSO
5 µm
1.2 µm
Z = -5 µm
Z = 0 µm
Z = 5 µm
c
Meiosis I
Chromosomes
Rec8
Cyto D
5 µm
1.2 µm
Z = -5 µm
Z = 0 µm
Z = 5 µm
d
CD1 females
Meiosis I
Normalised Rec8 fluorescence intensity
23
22
N.S
0
1
2
3
DMSO
Cyto D
Young
N = 3

Figure 3.14 F-actin disruption does not impact classical mechanisms of cohesion in intact oocytes (a) Experimental design schematic. Oocytes were collected and allowed to progress to metaphase I, in media supplemented with either DMSO or Cytochalasin D (5 µg/ml). The zona was then removed before fixation, staining and imaging **(b)** Representative single confocal section from immunofluorescence images of Rec8 and chromosomes – spaced 5 µm apart – in DMSO and Cytochalasin D-treated mouse oocytes. **(c)** Normalised Rec8 mean fluorescence intensities in DMSO- or Cytochalasin D-treated mouse oocytes. Data are from three independent experiments, numbers in italics represent the number of oocytes analysed per group. Statistical significance, N.S p=0.0862 was evaluated using Mann-Whitney t-test. N.B $\bar{x}$ ± SD

3.12 F-actin disruption does not impact classical mechanisms of centromeric cohesion in metaphase I chromosome spreads

Intact metaphase I oocytes showed no significant changes in Rec8 mean intensity levels when actin was disrupted. These results were further investigated with an independent approach by measuring Rec8 cohesion levels in metaphase I chromosomal spreads. Figure 3.15a depicts an exemplar sum intensity projection of metaphase I chromosomes (Hoechst) and Rec8 positive cohesion complexes. From these sum intensity projections, manual polygon drawing was performed to record the Rec8 mean intensity for each chromosome (Figure 3.15b, Methods section 2.10). As a proof-of-concept experiment to confirm that this imaging pipeline can reproducibly measure reduced cohesion levels, metaphase I oocytes were treated with Reversine before spreading, to disturb cohesion complexes [199]. Quantification of cohesion levels using this approach revealed that Rec8 fluorescence intensity was significantly reduced in Reversine-treated oocytes when compared to control DMSO-treated oocytes (Figure 3.15d,e). To confirm the effect of F-actin observed in intact oocytes using this quantitative microscopy assay, Rec8 fluorescence intensity was measured in chromosomal spreads from DMSO or Cytochalasin D-treated metaphase I oocytes. These analyses revealed that disruption of F-actin did not significantly affect Rec8 fluorescence intensities on chromosomes (Figure 3.16b,c). It is therefore unlikely that premature separation of sister chromatids in Cytochalasin D-treated eggs arise from cohesion loss.

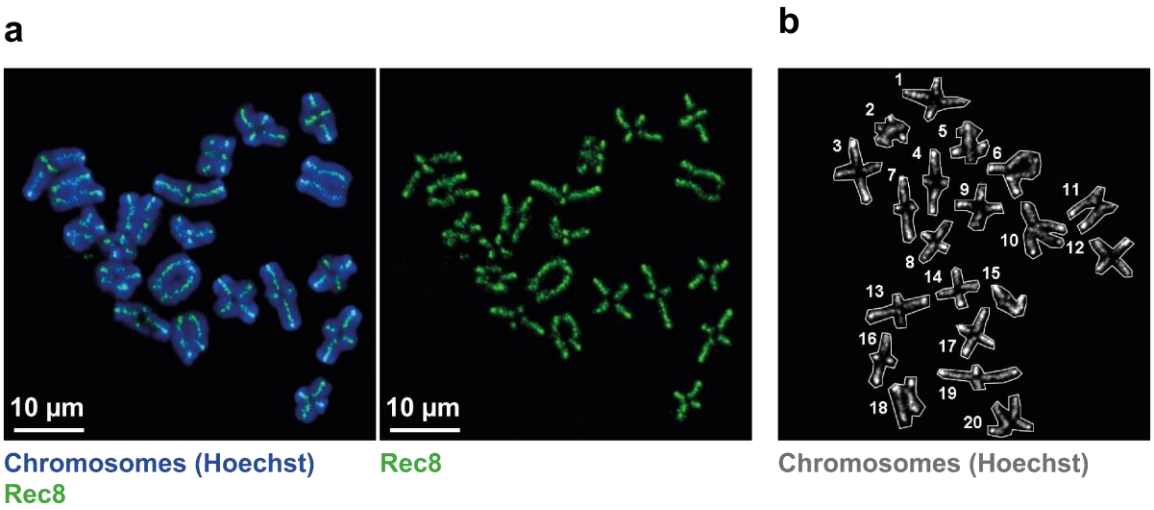
a
b
10 µm
10 µm
Chromosomes (Hoechst)
Rec8
Rec8
Chromosomes (Hoechst)

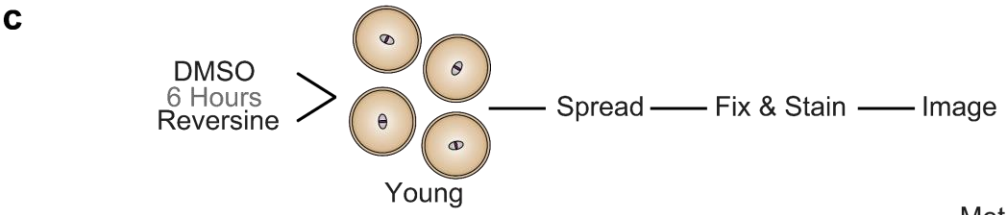
c
DMSO
6 Hours
Reversine
Young
Spread
Fix & Stain
Image

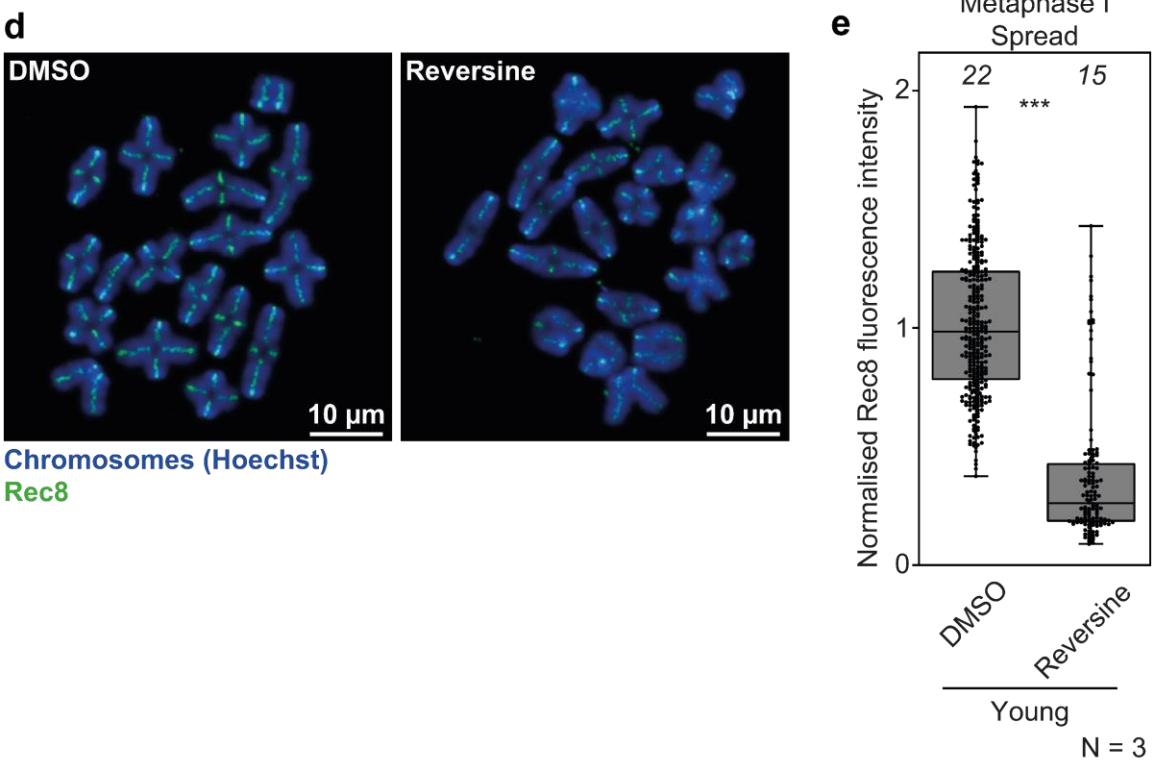
d
DMSO
Reversine
10 µm
10 µm
Chromosomes (Hoechst)
Rec8
e
Metaphase I
Spread
22
15
***
Normalised Rec8 fluorescence intensity
2
1
0
DMSO
Reversine
Young
N = 3

Figure 3.15 Changes in Rec8 intensity can be quantified in metaphase I chromosomal spreads (a) Maximum intensity projected immunofluorescence images of Rec8 cohesin complexes and homologous chromosomes in a metaphase I spreads. **(b)** Rec8 immunofluorescence intensity quantification pipeline for chromosome spreads. Sum intensity projections, followed by manual polygon drawing around Rec8 signal and measurement of the mean intensity on a chromosome-by-chromosome level. **(c)** Experimental design schematic. Oocytes were collected and allowed to progress to metaphase I, in media supplemented with either DMSO or Reversine (0.5 μM). The zona was then removed before spreading, fixation, staining and imaging **(d)** Maximum intensity projected immunofluorescence images of Rec8 cohesin complexes and homologous chromosomes in DMSO and Reversine-treated metaphase I spreads. **(e)** Normalised Rec8 mean fluorescence intensities in DMSO- or Reversine-treated metaphase I spreads. Data are from three independent experiments, numbers in italics represent the number of spreads analysed per group. Statistical significance, *** $p<0.0001$ was evaluated using Mann-Whitney t-test. N.B $\bar{x} \pm SD$

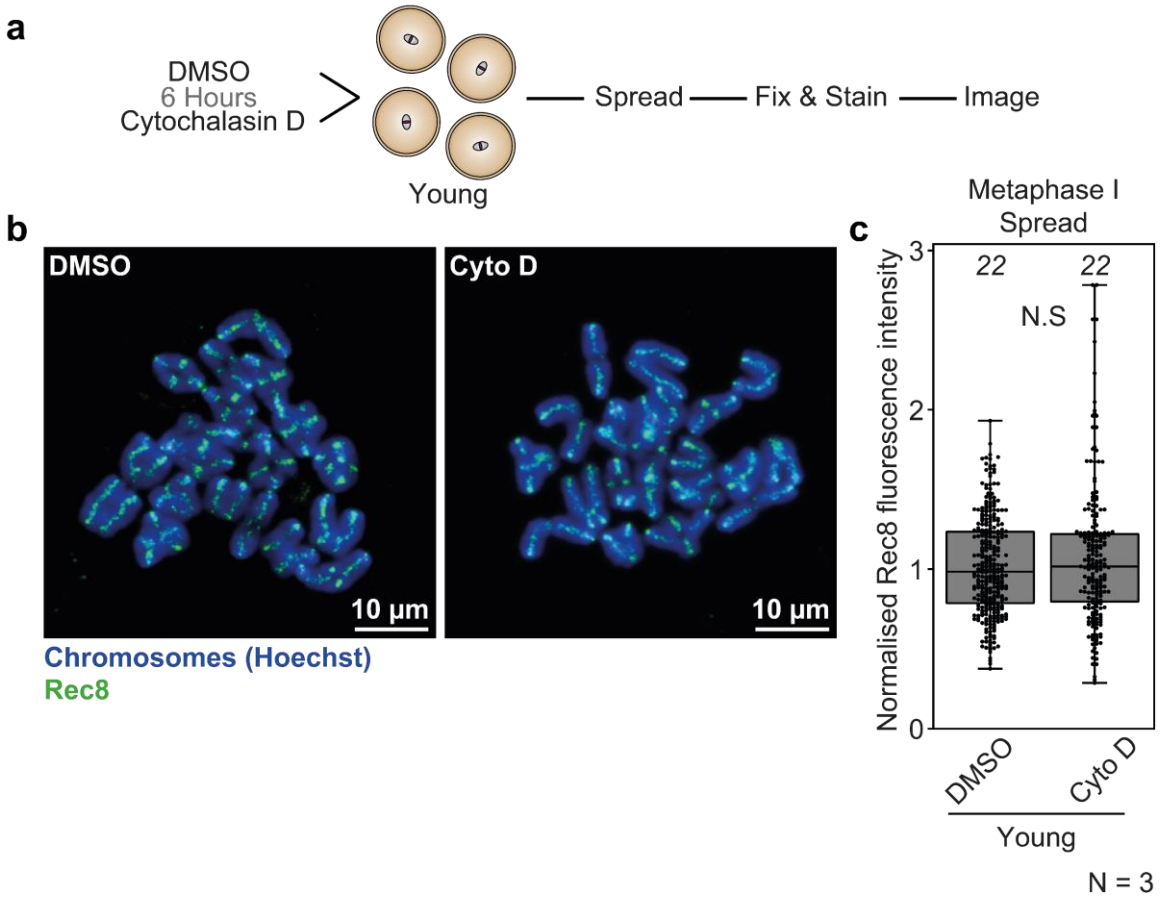

Figure 3.16 F-actin disruption does not impact classical mechanisms of cohesion in metaphase-I chromosome spreads (a) Experimental design schematic. Oocytes were collected and allowed to progress to metaphase I, in media supplemented with either DMSO or Cytochalasin D (5 µg/ml). The zona was then removed before spreading, fixation, staining and imaging **(b)** Maximum intensity projected immunofluorescence images of Rec8 cohesin complexes and homologous chromosomes in DMSO and Cytochalasin D-treated metaphase-I spreads. **(c)** Normalised Rec8 mean fluorescence intensities in DMSO- or Cytochalasin D-treated metaphase I spreads. Data are from three independent experiments, numbers in italics represent the number of spreads analysed per group. Statistical significance, N.S p=0.1796 was evaluated using Mann-Whitney t-test. N.B $\bar{x} \pm SD$

3.13 Chapter Summary

Initial insights influenced a working hypothesis that actin disruption in ageing eggs may be an additive factor to gradual cohesion weakening [97,174,178] and would result in an increased risk of misegregation and aneuploidy in mammalian eggs. Indeed, spindle-actin is reduced with advancing reproductive age and its disruption causes an increased prevalence of premature sister chromatid separation (PSSC) in aged eggs. Importantly, global actin levels are not reduced as a result of age, which highlights a spindle-specific reduction of F-actin. Additionally, this is not as a result of microtubules changes within the meiotic spindle, in fact, microtubule intensities increased in aged spindles. Of importance, F-actin disruption in young eggs is sufficient to induce 'ageing-like' levels of PSSC independently of canonical cohesion loss. Mimicking 'ageing-like' premature separation in young eggs in hours as opposed to months by destabilising F-actin, provides a tool for exploring actin's role in the context of untimely sister chromatid splitting. The following chapter explores the interplay between actin and microtubules within the meiotic spindle through gain/loss of function assays and high-resolution live imaging.

Chapter 4 – F-actin dampens microtubule-based pulling forces to prevent ageing-like premature chromatid separation

4.1 Introduction

Female meiosis is a dynamic process, which requires spatiotemporal control of spindle assembly and chromosome segregation to ensure the production of haploid eggs with the correct number of chromosomes. Premature separation of sister chromatids (PSSC) in oocytes or eggs arising from cohesion depletion results in embryo aneuploidies which are generally not compatible with life. The actin cytoskeleton was recently found to prevent chromosome segregation errors in mammalian eggs by promoting robust kinetochore-microtubule interactions [152]. However, the role of F-actin in limiting the incidence of PSSC is unknown. Here, actin disruption increased the likelihood for untimely sister chromatid splitting in young eggs, independently of canonical cohesion mechanisms. However, these experiments were performed in fixed oocytes, eggs and chromosomal spreads. In this chapter, the role of F-actin in maintaining sister chromatid association was investigated by combining advanced live imaging assays with rapid protein degradation methods.

4.2 High-resolution live imaging of meiosis in mouse oocytes

Meiosis progression can be visualized through high-resolution live imaging from prophase I arrest to the extrusion of the first polar body and formation of the second meiotic spindle. To image this process, germinal vesicle (GV) prophase I arrested oocytes are microinjected with H2B-mRFP and MAP4-eGFP mRNA to label chromosomes and spindle microtubules, respectively (see methods section 2.11). After release from prophase I arrest, the stages of meiosis I can be observed and tracked including spindle formation, anaphase I, and polar body extrusion (Figure 4.1). Labelling *in vitro* synthesized mRNAs with fluorescent tags allows mechanisms and dynamics to be unravelled in mammalian oocytes and eggs. These high-resolution live imaging assays were taken forward to investigate the role of F-actin in maintaining sister chromatid association.

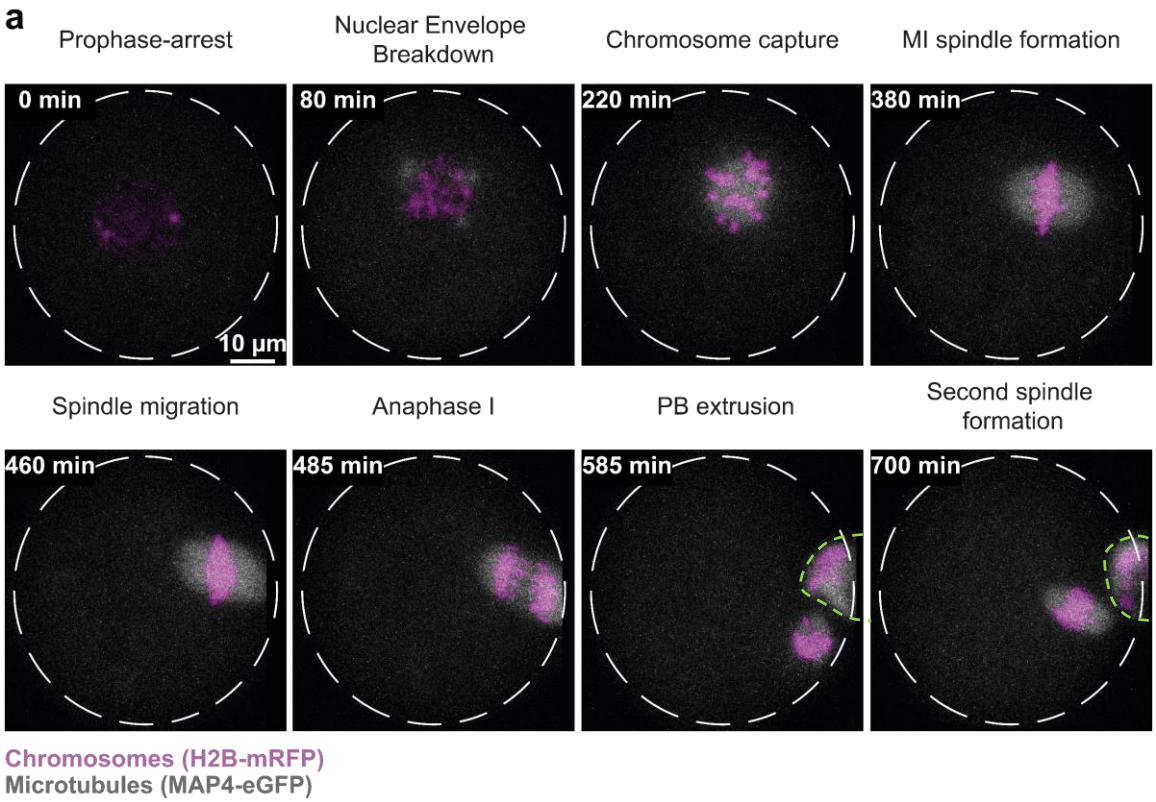

Figure 4.1 High-resolution live imaging of meiosis I (a) Visualisation of meiotic events from prophase I to second spindle formation in mammalian eggs. Chromosomes (magenta, H2B-mRFP) and microtubules (grey, MAP4-eGFP) interact throughout meiosis. Time is indicated in minutes; dashed white line outlines the border of the main cell body, dashed green line indicates the polar body (identified using transmitted light). Scale 10 µm, timelapse every 5 minutes until completion of meiosis I.

4.3 Rapid cohesion degradation for induction of 'ageing-like' PSSC in mouse eggs

Quantitative immunofluorescence microscopy data in figure 3.6 indicated that F-actin within the meiotic spindle limits premature separation of sister chromatids (PSSC) in ageing mammalian eggs. It would be difficult to investigate cytoskeletal dynamics in aged eggs due to their limited number and fragility, making them inappropriate for microinjection-based gain/loss of function assays. Directly evaluating the role of the actin cytoskeleton in limiting age-related PSSC therefore required a method to prematurely uncouple sister chromatids in young eggs. Here, TRIM-away, a method for rapid degradation of endogenous proteins, was used to acutely deplete the meiosis-specific cohesin subunit Rec8, thereby prematurely separating sister chromatids in metaphase II-arrested young eggs. The TRIM-away system utilises TRIM21 (Tripartite motif-containing protein 21), which is a physiological regulator of the innate immune response [200]. TRIM21 is a cytosolic E3 ubiquitin ligase that recognizes the Fc domain of antibodies, and in doing so stimulates immune signalling and antigen degradation through ubiquitin-based proteasomal degradation [200,201]. Experimentally, this innate immune pathway can be adapted by introducing into a cell antibodies against a protein of interest (Figure 4.2a). Subsequently, antibody binding to the target protein causes association of TRIM21 to the Fc domain. Antibody-antigen-TRIM21 complexes are then polyubiquitinated and targeted for proteasomal protein degradation. Importantly, this mechanism allows acute proteasomal degradation of a protein of interest often within minutes to hours [200]. This is particularly beneficial in mammalian eggs where meiotic proteins are generally long-lived and reserve mRNA transcripts are abundant, meaning conventional knockdown methods such as siRNAs are ineffective [200,202]. To mimic 'ageing-like' premature separation of sister chromatids low concentrations of Rec8 antiserum ('Partial') [178] were microinjected into metaphase II-arrested young eggs already expressing H2B-mRFP and TRIM21 mRNA (methods section 2.11) (Figure 4.2b,c). Low concentrations were introduced to only partially degrade Rec8, akin to reduced cohesion recorded with advancing maternal age [174,178]. High-resolution live imaging of chromosomes and chromatids showed modest separation and dispersion of single chromatids when Rec8 was partially degraded (Figure 4.2d, Supplementary movie S3). This 'ageing-like' system of cohesion loss was taken forward

to dissect the role of actin in PSSC. For further investigations where the cytoskeleton was challenged, high concentrations of Rec8 antiserum (‘Complete’) were microinjected into metaphase II-arrested young eggs already expressing H2B-mRFP and TRIM21 mRNA (methods section 2.11) (Figure 4.2b,c). Comparatively to ‘partial,’ ‘complete’ Rec8 degradation produced phenotypically higher levels of premature disengagement (Figure 4.2d, Supplementary movie S9). Tuneable levels of cohesion loss were used to dissect the contributions of the actin and microtubule cytoskeletons in PSSC.

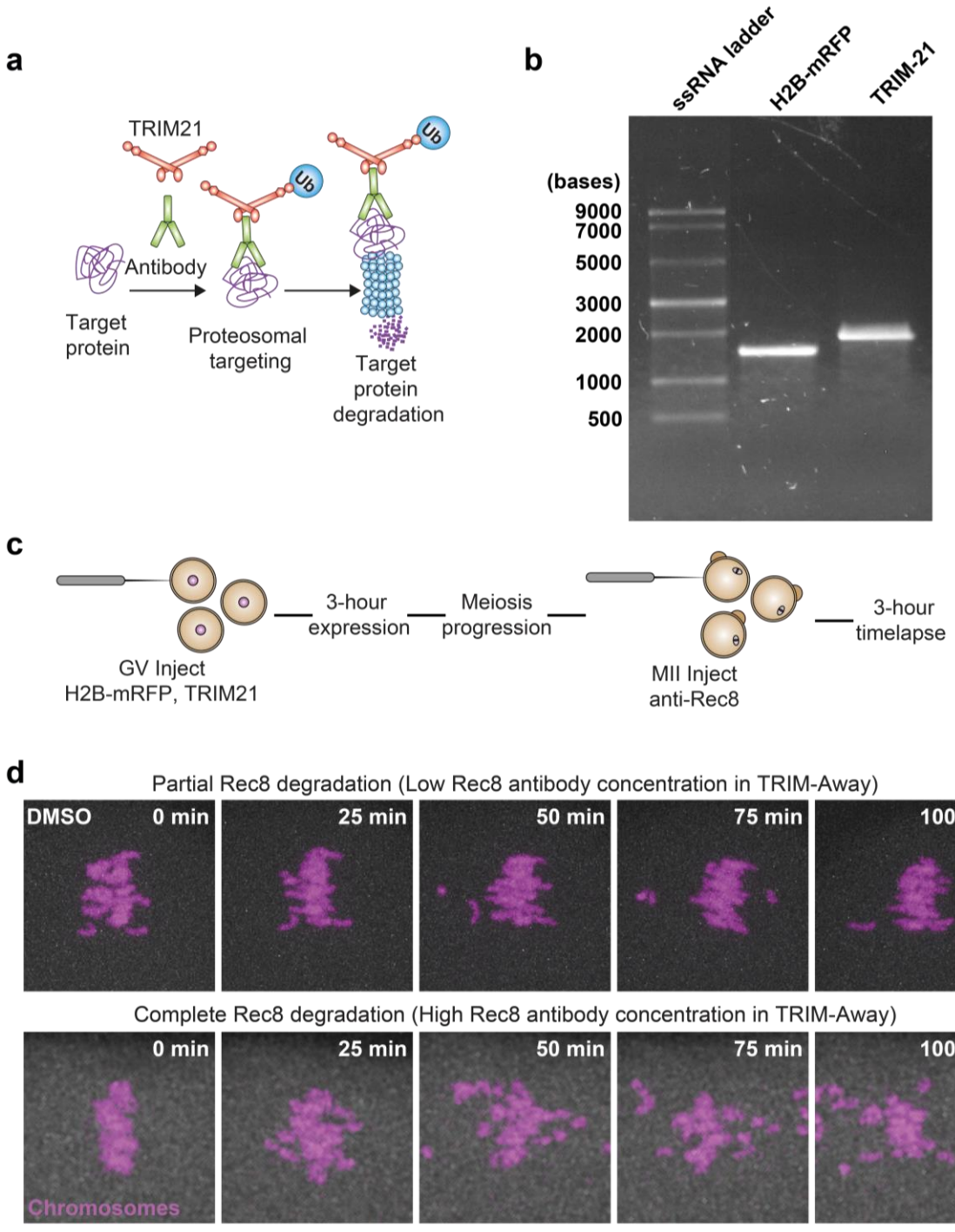

Figure 4.2 Acute partial degradation of Rec8 in mammalian eggs. I (a) TRIM-away mechanism schematic. **(b)** Exemplar 1% agarose gel image of in-vitro transcribed mRNAs. First lane ssRNA ladder (left to right), numbers relate to base pair of reference band, lane two in vitro-transcribed H2B-mRFP, lane three on vitro-transcribed mouse-TRIM21. **(c)** Experimental design schematic for Rec8 TRIM-away and imaging. **(d)** Stills from time lapse movie of chromosomes (H2B-mRFP, magenta) in a metaphase II-arrested egg with partial (upper panel) and fully degraded Rec8 (lower panel), scale bar 5 µm. Extensive scattering and reduced realignment events clearly distinguishes complete and partial Rec8 degradation.

4.4 Quantitative analysis of chromatid disengagement using Bounding Box measurements

Rec8 cleavage via TRIM-away visually causes premature separation events to occur in a short timescale. To quantify separation events, an imaging analysis pipeline for quantifying the amount of separation caused by Rec8 TRIM-away was created. For this, 3D surface reconstruction of chromosomes and chromatids, using the surfaces module of Imaris, were utilised to quantify the amount of premature separation and the generation of single chromatids caused by Rec8 cleavage (Figure 4.3b, Supplementary movie S4). Following reconstruction, the object-orientated bounding box output in Imaris allowed the calculation of the minimal cuboidal volume, which contained the entire chromosome/chromatid volume at each time-point throughout the time-lapse window (Figure 4.3a,b, Supplementary movie S4) (methods section 2.15). This volume was termed the 'chromatid scatter volume' (CSV) and it was plotted for each time point over the entire period, either as its raw volume or normalised to the initial timepoint as a read-out of deviation from the starting volume. This analysis provided a quantification for scattering of single chromatids that had prematurely separated as a result of Rec8 degradation by TRIM-Away.

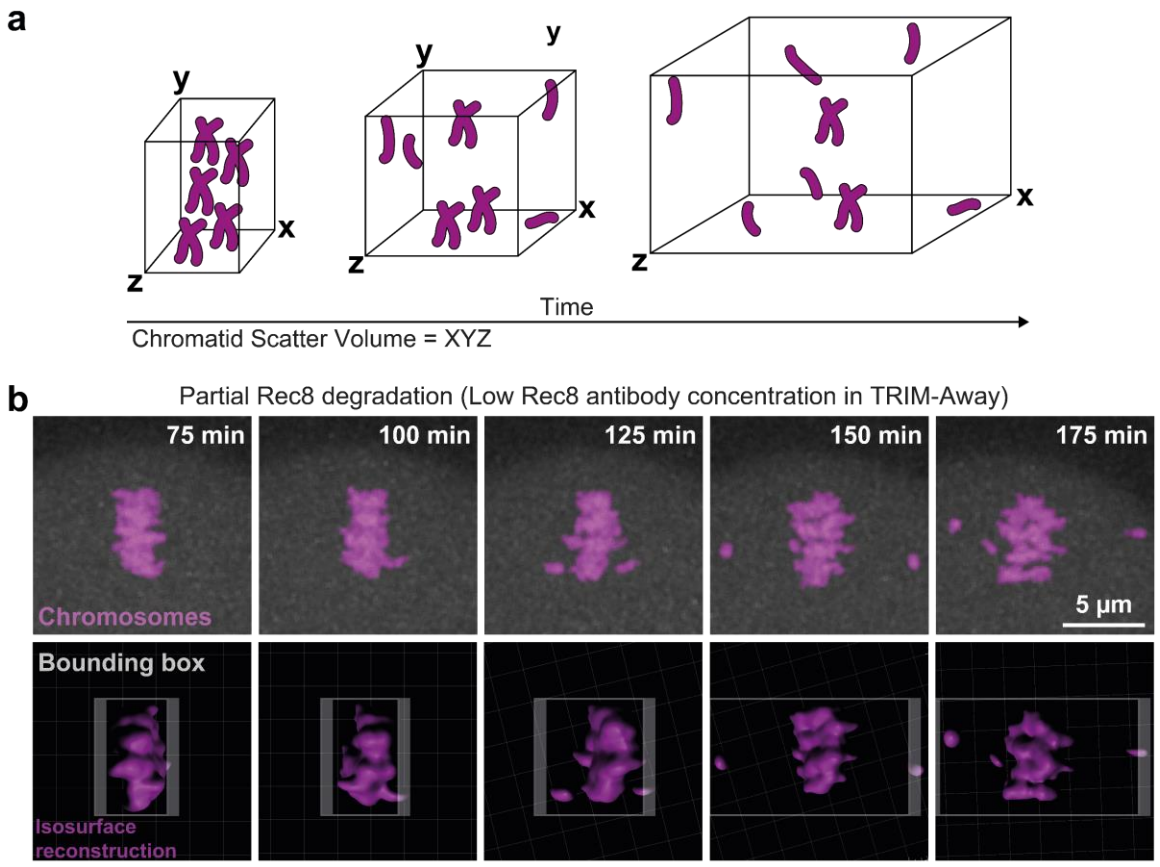

Figure 4.3 Bounding-box analysis of chromatid scatter. (a) Bounding-box analysis schematic, encapsulating the minim cuboidal volume **(b)** Time-lapse movie analysis pipeline – upper panel reference stills from a time lapse movie of chromosomes (H2B-mRFP, magenta) in a metaphase II egg (scale bar 5 µm) – lower panel pseudo-object-orientated bounding box encapsulating chromosomes, showing an increase of the minimal cuboidal volume as the time-lapse progresses and the chromatids move further from the main chromatid mass – output chromatid scatter volume (CSV).

4.5 F-actin disruption in young eggs accelerates premature chromatid separation and reduces realignment events

Figure 3.6 indicated that F-actin within the meiotic spindle limits premature separation of sister chromatids (PSSC) in ageing populations of mammalian eggs. To interrogate this phenotype in real time, metaphase II-arrested young eggs were partially depleted of Rec8 in the absence of actin. DMSO-treated control eggs showed gradual sister chromatid separation ~40 minutes after microinjection (Figure 4.4b, upper panel, Supplementary movie S5). Few single chromatids moved away from the main chromosome mass, but often realigned at the spindle equator after ~2 hours (Figure 4.4b, upper panel, Supplementary movie S6). Actin disruption through Cytochalasin D-treatment exacerbated premature separation events, with partial cohesion degradation causing extensive scattering of single chromatids (Figure 4.4b, lower panel, Supplementary movie S7 and S8). After ~ 40 minutes chromatids separated from the main spindle mass and often failed to realign at the spindle equator. Comparisons between chromatid scatter volume plots (CSV) showed a significantly increased amount of scatter in Cytochalasin-treated eggs when compared to control DMSO-treated eggs (Figure 4.4c,d). These insights demonstrate that when F-actin is disrupted, 'ageing-like' cohesion loss via partial Rec8 TRIM-away, is more likely to induce PSSC and subsequent aneuploidy.

F-actin disruption caused an increased likelihood for premature separation, with single chromatids often appearing to move faster and realign less frequently. To analyse this increase in chromatid acceleration, separated chromatids were reconstructed from high-resolution movies, in Imaris and their frame-to-frame movement was tracked (Figure 4.5b, methods section 2.16 for further details). In DMSO-treated control eggs with partial cohesion depletion, prematurely separated single chromatids accelerated on average at speeds of 0.50±0.32 µm/min (Figure 4.5c). Single chromatids in Cytochalasin D-treated eggs moved at significantly greater speeds, with average displacement measured at 0.71±0.37 µm/min (Figure 4.5c). This could be explained by spindle microtubule pulling forces being greater when F-actin is disrupted. Additionally, this analysis allowed scoring of the proportion of single chromatids that displaced but subsequently realigned to the main chromosome mass (Figure 4.5a, methods section 2.16 for further details). In control eggs, ~62% of prematurely separated

single chromatids returned to the main chromosome mass within the 3-hour time lapse (Figure 4.5d). Conversely, in Cytochalasin D-treated eggs, a significant reduction of only ~31% of prematurely separated chromatids realigned at the spindle equator (Figure 4.5d). These data, suggest that actin functions in two ways to prevent chromatid scattering: firstly, it opposes microtubule based pulling forces and reduces the acceleration of prematurely separated chromatids. Secondly, F-actin promotes the realignment of single chromatids back to the spindle equator.

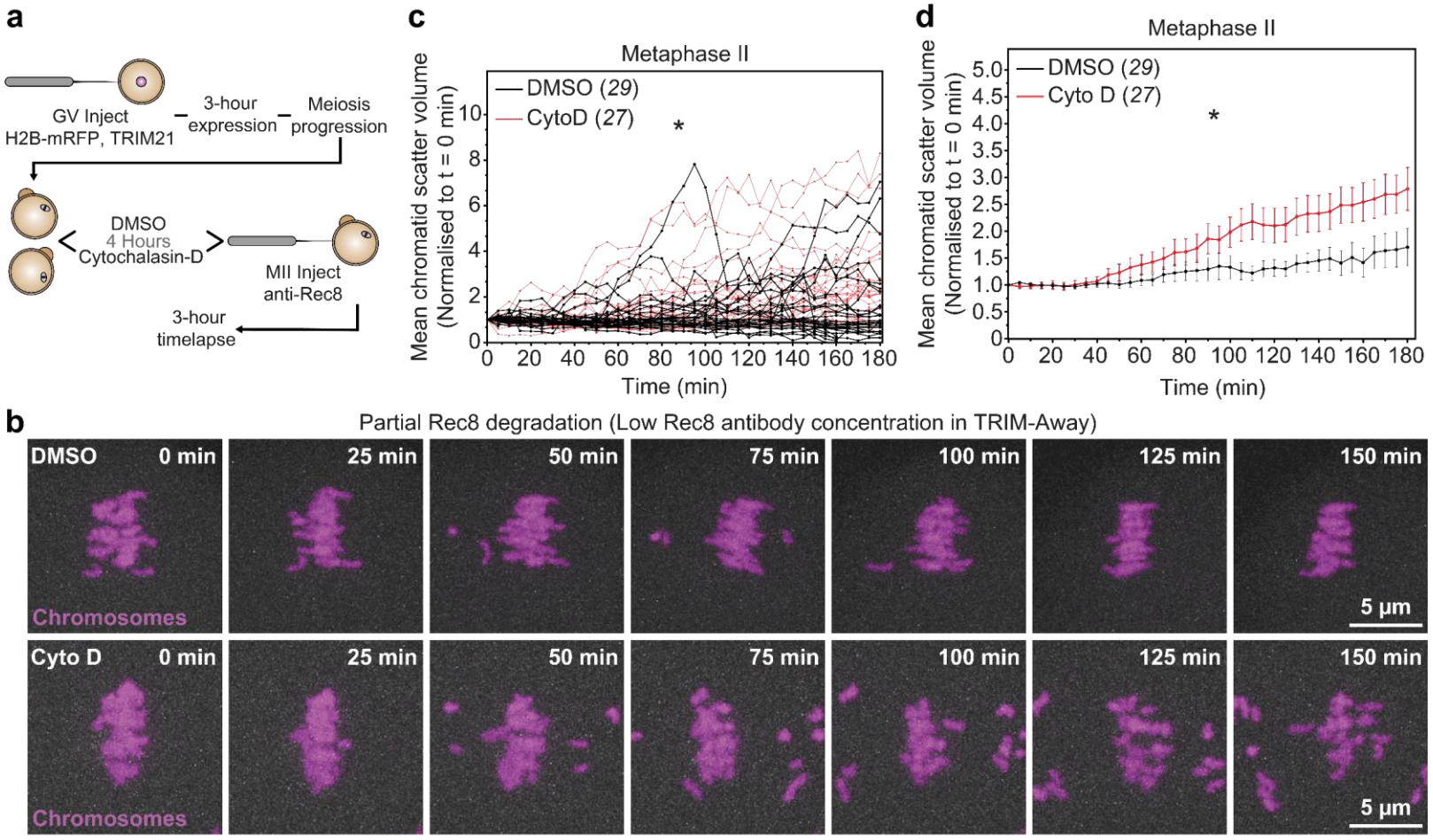
a
GV Inject
H2B-mRFP, TRIM21
3-hour
expression
Meiosis
progression
DMSO
4 Hours
Cytochalasin-D
MII Inject
anti-Rec8
3-hour
timelapse
c
Metaphase II
DMSO (29)
CytoD (27)
*
Mean chromatid scatter volume
(Normalised to t = 0 min)
Time (min)
d
Metaphase II
DMSO (29)
Cyto D (27)
*
Mean chromatid scatter volume
(Normalised to t = 0 min)
Time (min)
b
Partial Rec8 degradation (Low Rec8 antibody concentration in TRIM-Away)
DMSO
Cyto D
0 min
25 min
50 min
75 min
100 min
125 min
150 min
Chromosomes
5 µm

Figure 4.4 F-actin disruption in young eggs accelerates ageing-like premature chromatid separation (a) Experimental design schematic – GV injections, mRNA expression and prophase release, drug treatment (Cytochalasin D, 5 µg/ml, 4 hours) and Rec8 TRIM-away. **(b)** Stills from representative time lapse movies of chromosomes (H2B-mRFP, magenta) in DMSO (upper panel) - or Cytochalasin D-treated (lower panel) metaphase II-arrested eggs with partially degraded Rec8. Scale bar 5 µm). **(c)** Normalised to T=0 mins chromatid scatter volumes measured over 3 hours in DMSO (black)- or Cytochalasin D-treated (red) metaphase II-arrested eggs with partially degraded Rec8. Split plots can be seen in appendix figure 7.1a,b. Data are from three independent experiments, numbers in parentheses correspond to the total number of eggs analysed in each group,* p=0.0300 (One-way ANOVA). **(d)** Mean normalised chromatid scatter volumes measured over 3 hours in DMSO (black)- or Cytochalasin D-treated (red) metaphase II-arrested eggs with partially degraded Rec8. Data are from three independent experiments, numbers in parentheses correspond to the total number of eggs analysed in each group,* p=0.0300 (One-way ANOVA). N.B $\bar{x} \pm SD$

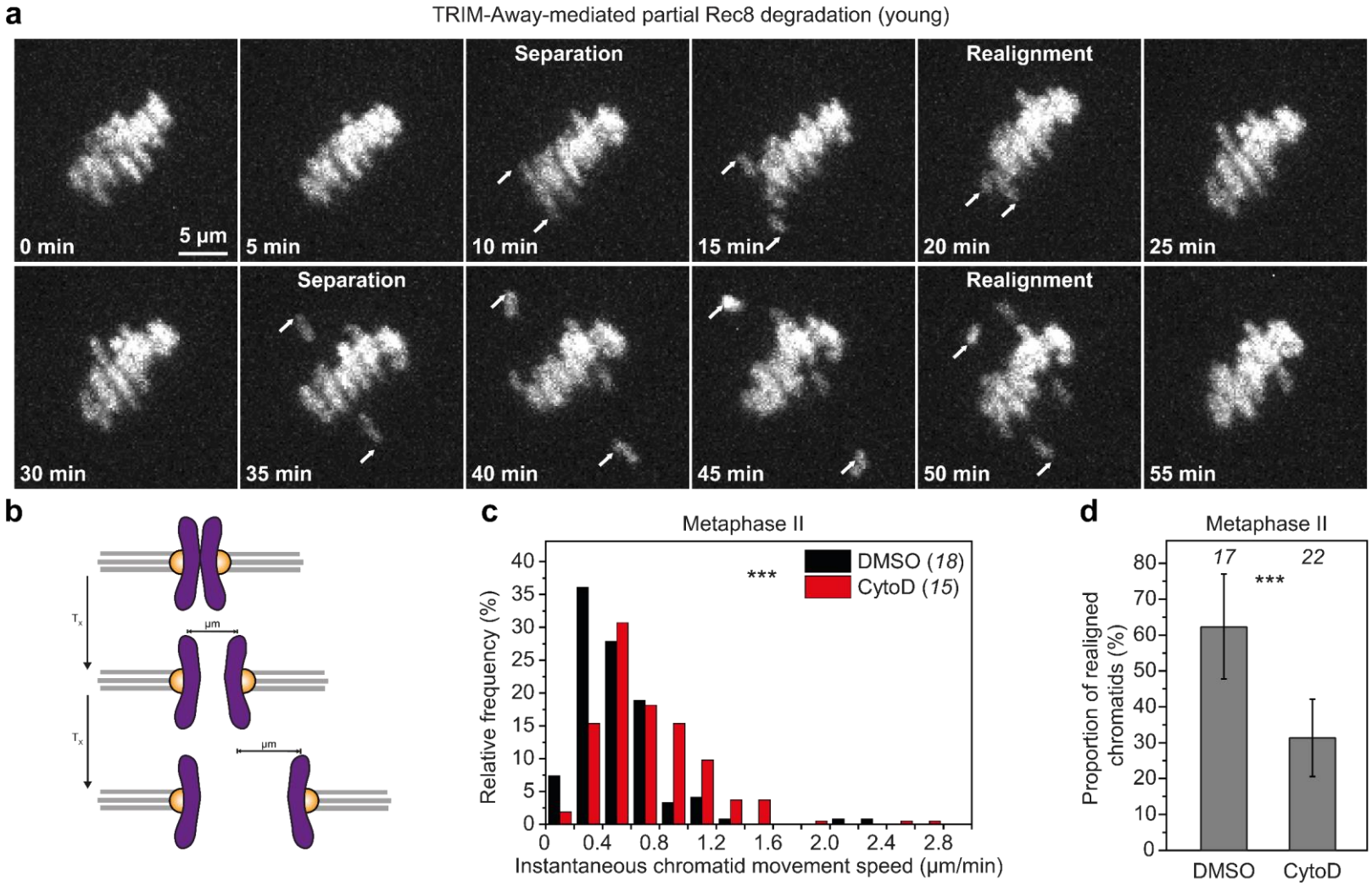
a
TRIM-Away-mediated partial Rec8 degradation (young)
0 min
5 µm
5 min
Separation
10 min
15 min
Realignment
20 min
25 min
30 min
Separation
35 min
40 min
45 min
Realignment
50 min
55 min
b
Tx
µm
Tx
µm
c
Metaphase II
***
DMSO (18)
CytoD (15)
Relative frequency (%)
0
5
10
15
20
25
30
35
40
0
0.4
0.8
1.2
1.6
2.0
2.4
2.8
Instantaneous chromatid movement speed (µm/min)
d
Metaphase II
17
22
***
Proportion of realigned chromatids (%)
0
10
20
30
40
50
60
70
80
DMSO
CytoD

Figure 4.5 F-actin disruption in young eggs accelerates premature chromatid separation and reduces realignment events (a) Representative maximum intensity projected high-resolution confocal images of sister chromatids in a metaphase II-arrested mouse egg with partially degraded Rec8 indicating modest chromatid separation and subsequent realignment events. Arrows highlight separation and realignment events. **(b)** Instantaneous chromatid movement speed schematic. Measurements were recorded as distances travelled per timepoint for separated chromatids, see materials and methods section 2.16 for further details. **(c)** Distribution of instantaneous chromatid movement speeds (µm/min) in DMSO (black)- or Cytochalasin treated (red) metaphase II-arrested eggs (5 µg/ml, 4 hours) with partially degraded Rec8. Data are displayed as box and whiskers plot in appendix figure 7.2a. Data are from three independent experiments, numbers in parentheses correspond to the total number of events analysed in each group, *** $p<0.0001$ (Mann-Whitney corrected, unpaired T-Test). **(d)** Proportion of scattered chromatids that re-established alignment to the spindle equator in DMSO- or Cytochalasin D-treated metaphase II-arrested eggs with partially degraded Rec8. Data are from three independent experiments, numbers in parentheses correspond to the total number of events analysed in each group, *** $p<0.0001$ (Mann-Whitney corrected, unpaired T-Test). N.B $\bar{x} \pm SD$

4.6 F-actin stabilisation limits chromatid scattering in the absence of centromeric cohesion

F-actin disruption predisposes weakly-linked sister chromatids, to premature separation (Figure 3.6, 3.7, 3.9), which in turn is likely to lead to chromosome misegregation and aneuploidy. Next, F-actin stabilisation was introduced to see whether chromatid scattering could be limited in cohesion depleted eggs. Furthermore, complete cohesion degradation was introduced here, by microinjecting higher concentrations of Rec8 antibody into eggs (methods 2.1). Complete degradation caused more extensive separation of sister chromatids when compared to partial degradation (Supplementary movie S9). SiR-actin (a fluorescently labelled derivative of Jasplakinolide [203]) was used at a high concentration to stabilise F-actin filaments, prior to complete cohesion degradation. In DMSO-treated eggs, complete cohesion degradation caused extensive PSSC and chromatid scattering, with realigning chromatids often displacing again (Figure 4.6b, Supplementary movie S10). Despite a complete lack of cohesion, single chromatids in SiR-Actin stabilised spindles were largely retained within the main chromosome mass at the spindle equator for the duration of the 3-hour timelapse (Figure 4.6b, Supplementary movie S11). Comparisons between chromatid scatter volume plots (CSV) showed significant scattering in DMSO treated eggs when compared to SiR-Actin treated eggs (Figure 4.6c,d). Instantaneous chromatid movement analysis detailed prematurely separated chromatids accelerated at a significantly slower rate in SiR-Actin-treated spindles (0.42±0.33 µm/min) in comparison to DMSO-treated eggs (0.85±0.49 µm/min) (Figure 4.6e). Collectively these data support a model wherein F-actin limits accelerated separation and restricts poleward movement of single chromatids in eggs with depleted centromeric cohesion, highlighting the importance of F-actin loss in the context of reproductive aging where cohesion is weakened, and microtubule dynamics are defective [179].

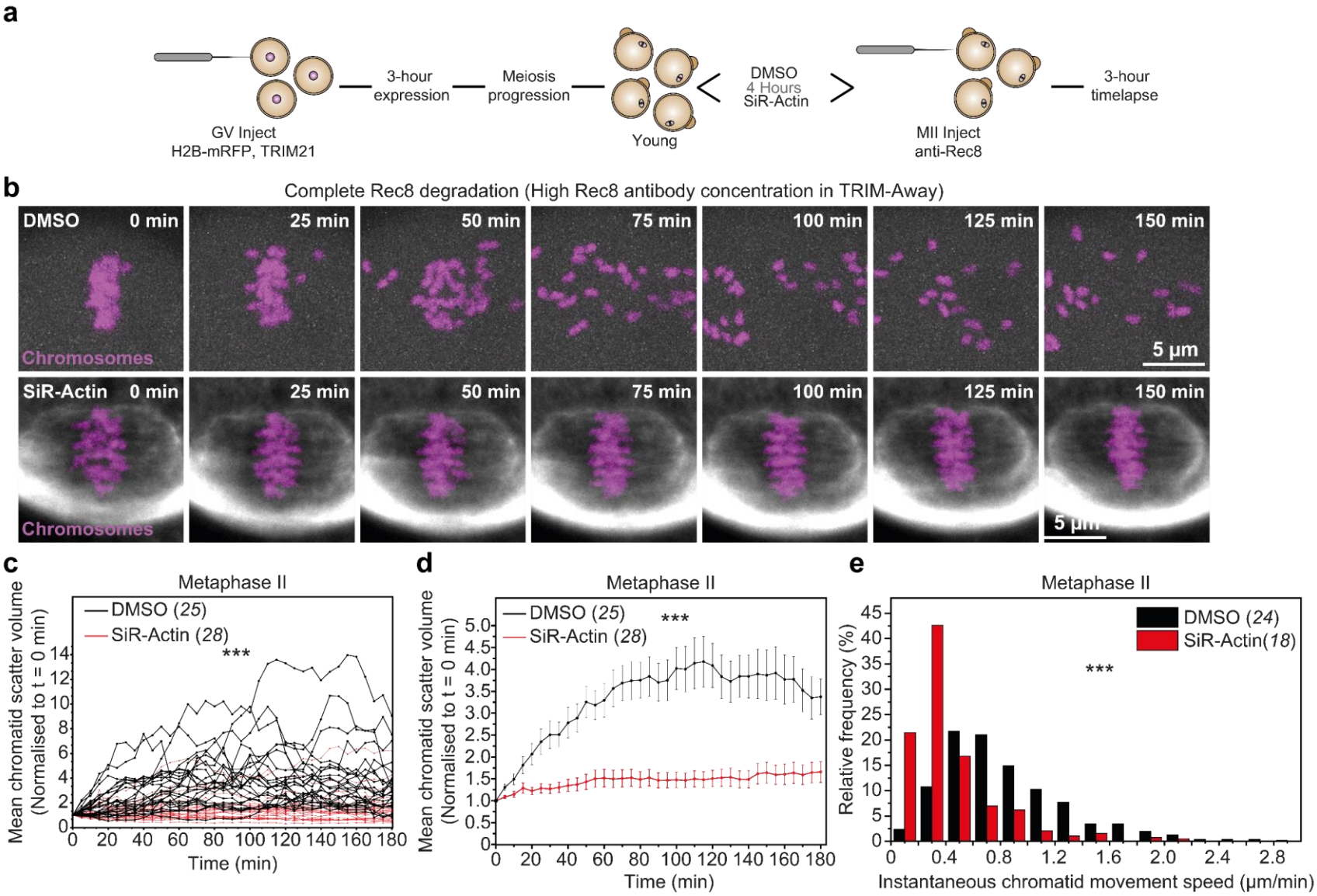
a
GV Inject
H2B-mRFP, TRIM21
3-hour
expression
Meiosis
progression
Young
DMSO
4 Hours
SiR-Actin
MII Inject
anti-Rec8
3-hour
timelapse
b
Complete Rec8 degradation (High Rec8 antibody concentration in TRIM-Away)
DMSO
SiR-Actin
0 min
25 min
50 min
75 min
100 min
125 min
150 min
Chromosomes
5 µm
c
Metaphase II
DMSO (25)
SiR-Actin (28)
***
Mean chromatid scatter volume
(Normalised to t = 0 min)
Time (min)
d
Metaphase II
DMSO (25)
SiR-Actin (28)
***
Mean chromatid scatter volume
(Normalised to t = 0 min)
Time (min)
e
Metaphase II
DMSO (24)
SiR-Actin(18)
***
Relative frequency (%)
Instantaneous chromatid movement speed (µm/min)

Figure 4.6 F-actin enrichment blocks premature chromatid separation in the absence of centromeric cohesion (a) Experimental design schematic – GV injections of H2B-mRFP and TRIM21, 3-hour mRNA expression before prophase-I release and progression through meiosis I, drug treatment and complete Rec8 TRIM-away. **(b)** Stills from representative time lapse movies of chromosomes (H2B mRFP, magenta) in DMSO (upper panel)- or SiR-Actin-treated (10 µM, 4 hours, grey, lower panel) metaphase II-arrested eggs with fully degraded Rec8 (Scale bar 5 µm). **(c)** Normalised to T=0 mins chromatid scatter volumes measured over 3 hours in DMSO (black)- or SiR-Actin-treated (red) metaphase II-arrested eggs with completely degraded Rec8. Split plots can be seen in appendix figure 7.1c,d. Data are from three independent experiments, numbers in parentheses correspond to the total number of eggs analysed in each group,*** $p<0.0001$ (One-way ANOVA). **(d)** Mean normalised chromatid scatter volumes measured over 3 hours in DMSO (black)- or SiR-Actin-treated (red) metaphase II-arrested eggs with completely degraded Rec8. Data are from three independent experiments, numbers in parentheses correspond to the total number of eggs analysed in each group,*** $p<0.0001$ (One-way ANOVA). **(e)** Distribution of instantaneous chromatid movement speeds (µm/min) in DMSO (black)- or SiR-Actin-treated (red) metaphase II-arrested eggs with completely degraded Rec8. Data are displayed as box and whiskers plot in appendix figure 7.2b. Data are from three independent experiments, numbers in parentheses correspond to the total number of events analysed in each group, *** $p<0.0001$ (Mann-Whitney corrected, unpaired T-Test). N.B $\bar{x} \pm SD$

4.7 Blocking microtubule dynamics prevents separation of sister chromatids

Microtubule polymerisation and depolymerisation generate pushing and pulling forces that move chromosomes and chromatids [204-214] as well as other cellular objects such as the nucleus [215-220]. During anaphase, the spindle elongates as microtubule k-fibres shorten driving separation of chromosomes and chromatids [50,62]. Interestingly, defects in microtubule dynamics have been identified as a risk for chromosomal aneuploidies in aged eggs [179]. It was therefore important to understand whether microtubules are powering chromatid movement in eggs with experimentally disrupted cohesion. Here, the role of microtubule dynamics was assessed by treating metaphase II eggs with high concentrations of the live imaging probe SiR-Tubulin (a fluorogenic derivative of docetaxel (Taxol based compound)) to limit their movement [156]. Consistently, DMSO-treated eggs displayed extensive separation of single chromatids after complete Rec8 degradation had been introduced (Figure 4.7, Supplementary movie S12). In contrast SiR-Tubulin-treated eggs had reduced scattering of single chromatids (Figure 4.7b, Supplementary movie S13). Comparisons between chromatid scatter volume plots (CSV) show a significantly increased amount of scatter in DMSO-treated eggs when compared to SiR-Tubulin-treated eggs (Figure 4.7c,d). Additionally, instantaneous chromatid movement analysis showed prematurely separated chromatids significantly slowed in SiR-Tubulin-treated spindles (0.61±0.40 µm/min) in comparison to DMSO-treated eggs (0.88±0.46 µm/min) (Figure 4.7e). These data agree that microtubules are responsible for driving the movement of single chromatids once centromeric cohesion is experimentally reduced in this system.

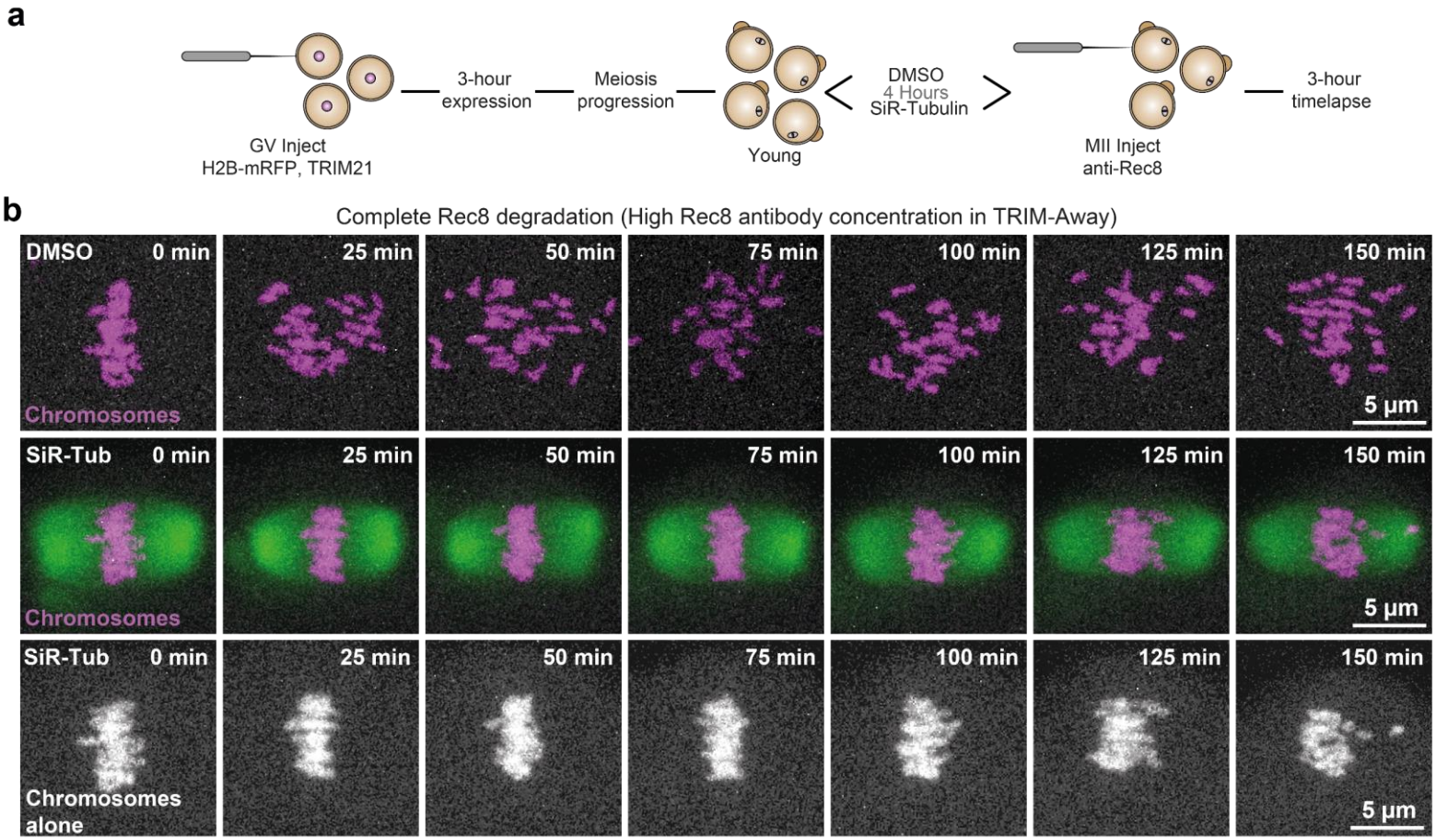
a
GV Inject
H2B-mRFP, TRIM21
3-hour
expression
Meiosis
progression
Young
DMSO
4 Hours
SiR-Tubulin
MII Inject
anti-Rec8
3-hour
timelapse
b
Complete Rec8 degradation (High Rec8 antibody concentration in TRIM-Away)
DMSO
SiR-Tub
Chromosomes
Chromosomes
alone
0 min
25 min
50 min
75 min
100 min
125 min
150 min
5 µm

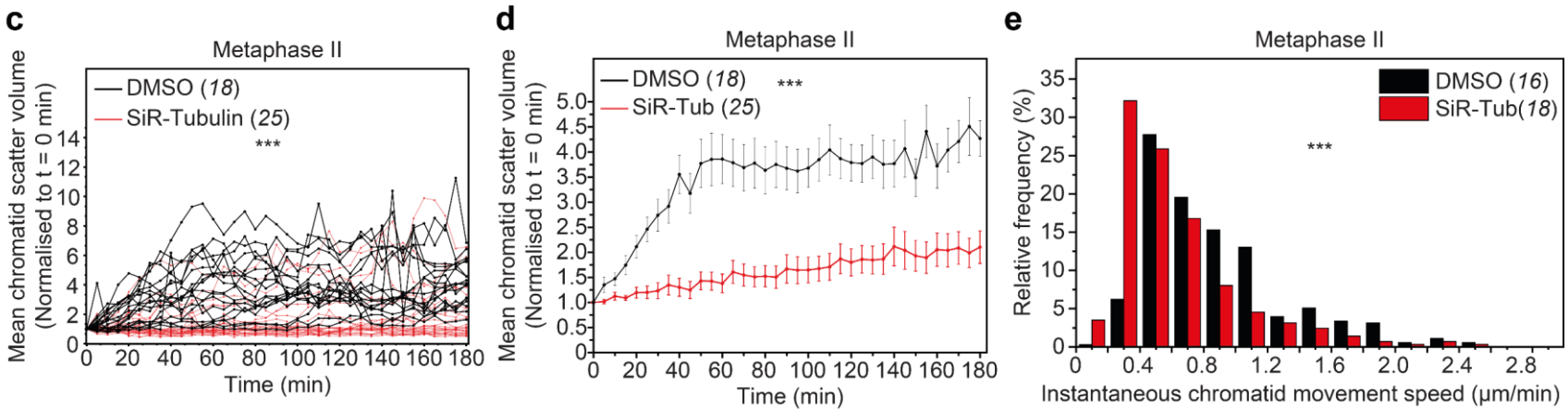

Figure 4.7 Microtubule stabilisation blocks premature chromatid separation in the absence of centromeric cohesion **(a)** Experimental design schematic – GV injections of H2B-mRFP and TRIM21, 3-hour mRNA expression before prophase-I release and progression through meiosis I, drug treatment (SiR-Tubulin, 1 µM, 4 hours) and complete Rec8 TRIM-away. **(b)** Stills from representative time lapse movies of chromosomes (magenta, H2B-mRFP) in DMSO (upper-panel)- or SiR-Tubulin-treated (green, middle panel) (lower panel shows chromosomes only from SiR-tubulin treated stills) metaphase II-arrested eggs with fully degraded Rec8. Scale bar 5 µm. **(c)** Normalised to T=0 mins chromatid scatter volumes measured over 3 hours in DMSO (black)- or SiR-Tubulin-treated (red) metaphase II-arrested eggs with completely degraded Rec8. Split plots can be seen in appendix figure 7.1e,f. Data are from three independent experiments, numbers in parentheses correspond to the total number of eggs analysed in each group,*** $p<0.0001$ (One-way ANOVA). **(d)** Mean normalised chromatid scatter volumes measured over 3 hours in DMSO (black)- or SiR-Tubulin-treated (red) metaphase II-arrested eggs with partially degraded Rec8. Data are from three independent experiments, numbers in parentheses correspond to the total number of eggs analysed in each group,*** $p<0.0001$ (One-way ANOVA). **(e)** Distribution of instantaneous chromatid movement speeds (µm/min) in DMSO (black)- or SiR-Tubulin-treated (red) metaphase II-arrested eggs with completely degraded Rec8. Data are displayed as box and whiskers plot in appendix figure 7.2c. Data are from three independent experiments, numbers in parentheses correspond to the total number of events analysed in each group, *** $p<0.0001$ (Mann-Whitney corrected, unpaired T-Test). N.B $\bar{x} \pm SD$

4.8 Blocking microtubule dynamics limits chromatid separation exacerbated by F-actin loss

Figures 4.4 and 4.6 suggested that F-actin opposes microtubule based pulling forces once centromeric cohesion begins to weaken. To further investigate this, Cytochalasin D and SiR-Tubulin treatments were combined with partial centromeric cohesion depletion to understand whether unopposed microtubule pulling underlies premature separation of sister chromatids in cohesion deficient mammalian eggs. In line with previous results (Figure 4.4), F-actin disrupted eggs showed extensive chromatid scattering when Rec8 was partially degraded via TRIM-away (Figure 4.8a, Supplementary movie S15). Consistently, control DMSO-treated eggs had modest scattering and realignment events (Figure 4.8a, Supplementary movie S14). Blocking of microtubule dynamics using SiR-Tubulin consistently limited poleward relocation of separated single chromatids (Figure 4.8a, Supplementary movie S16). As expected, blocking microtubule dynamics in eggs lacking F-actin, limited the extent of chromatid scattering, which would normally be seen when actin was disrupted (Figure 4.8a, Supplementary movie S17). Chromatid scatter plots revealed no significant differences between combination treatments (SiR-Tubulin and Cytochalasin D) and DMSO or SiR-Tubulin alone groups (Figure 4.8c,d). SiR-Tubulin and Cytochalasin D-treated eggs had significantly reduced chromatid scatter to eggs treated with Cytochalasin D alone (Figure 4.8c,d). Additionally, the acceleration of chromatids was significantly reduced in SiR-Tubulin and Cytochalasin D-treated eggs when compared to F-actin disrupted eggs (Figure 4.8e). Collectively these results suggest that in an ‘ageing-like’ system of weakened cohesion microtubule based pulling forces are normally insufficient to separate the majority of weakly linked chromatids when F-actin is present. F-actin appears to oppose the separation of sister chromatids reducing their acceleration and promoting their realignment to the spindle equator. These microtubule-pulling forces would be unopposed in aged eggs where spindle-actin is depleted (Figure 3.1).

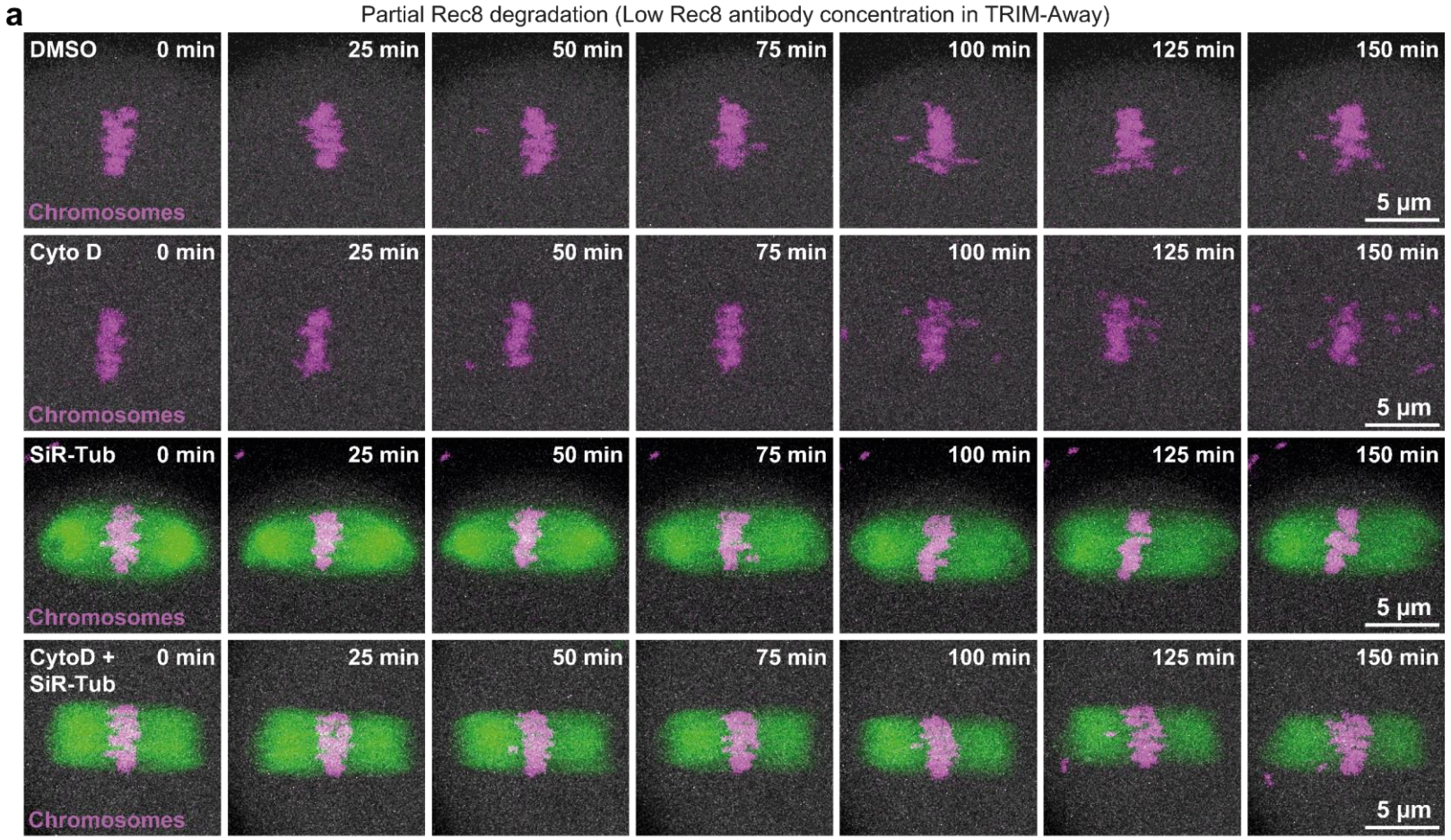
a
Partial Rec8 degradation (Low Rec8 antibody concentration in TRIM-Away)
DMSO
Cyto D
SiR-Tub
CytoD +
SiR-Tub
0 min
25 min
50 min
75 min
100 min
125 min
150 min
Chromosomes
5 µm

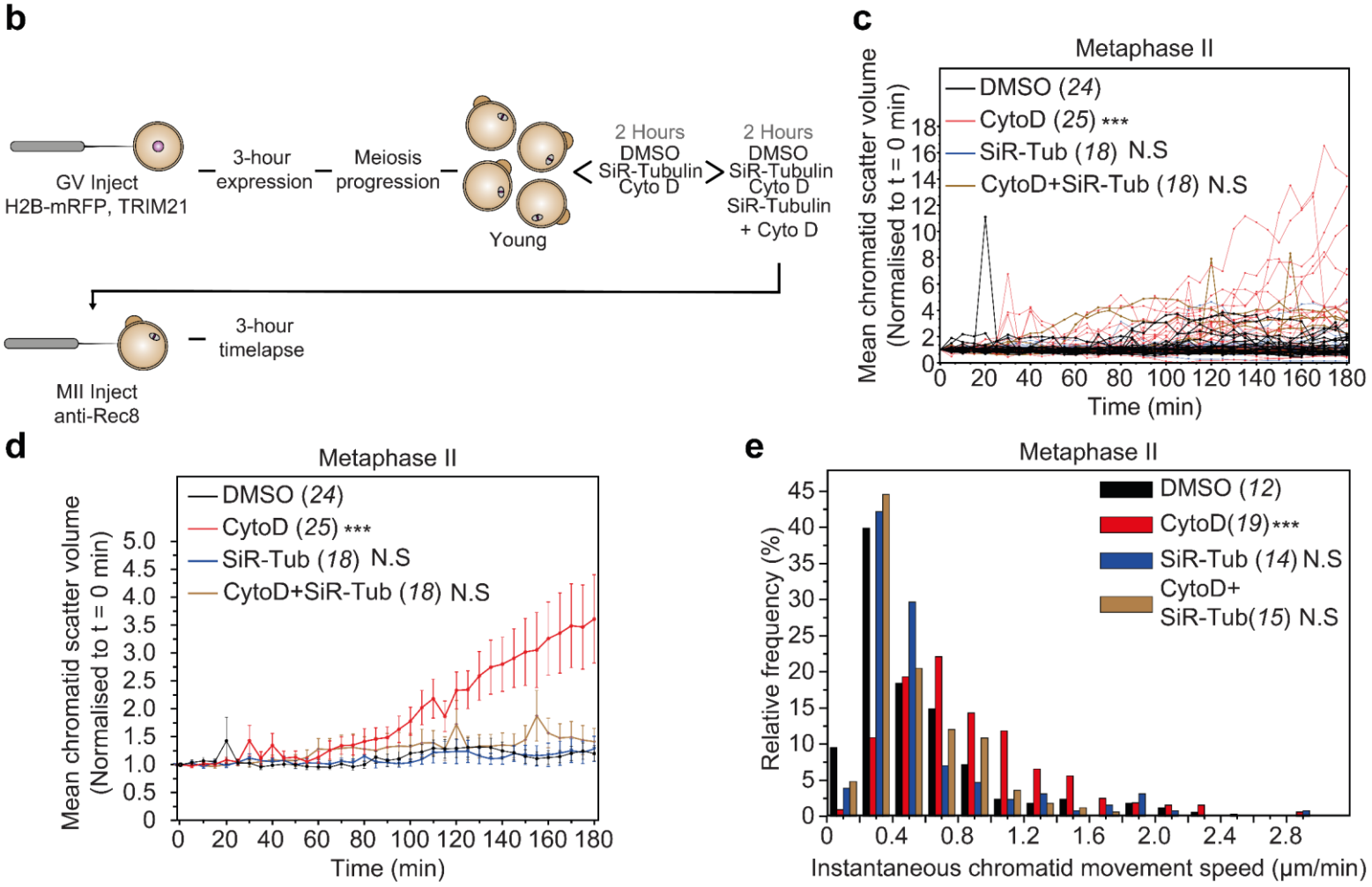
b
GV Inject
H2B-mRFP, TRIM21
3-hour
expression
Meiosis
progression
Young
2 Hours
DMSO
SiR-Tubulin
Cyto D
2 Hours
DMSO
SiR-Tubulin
Cyto D
SiR-Tubulin
+ Cyto D
MII Inject
anti-Rec8
3-hour
timelapse
c
Metaphase II
DMSO (24)
CytoD (25) ***
SiR-Tub (18) N.S
CytoD+SiR-Tub (18) N.S
Mean chromatid scatter volume
(Normalised to t = 0 min)
Time (min)
d
Metaphase II
DMSO (24)
CytoD (25) ***
SiR-Tub (18) N.S
CytoD+SiR-Tub (18) N.S
Mean chromatid scatter volume
(Normalised to t = 0 min)
Time (min)
e
Metaphase II
DMSO (12)
CytoD(19)***
SiR-Tub (14) N.S
CytoD+
SiR-Tub(15) N.S
Relative frequency (%)
Instantaneous chromatid movement speed (µm/min)

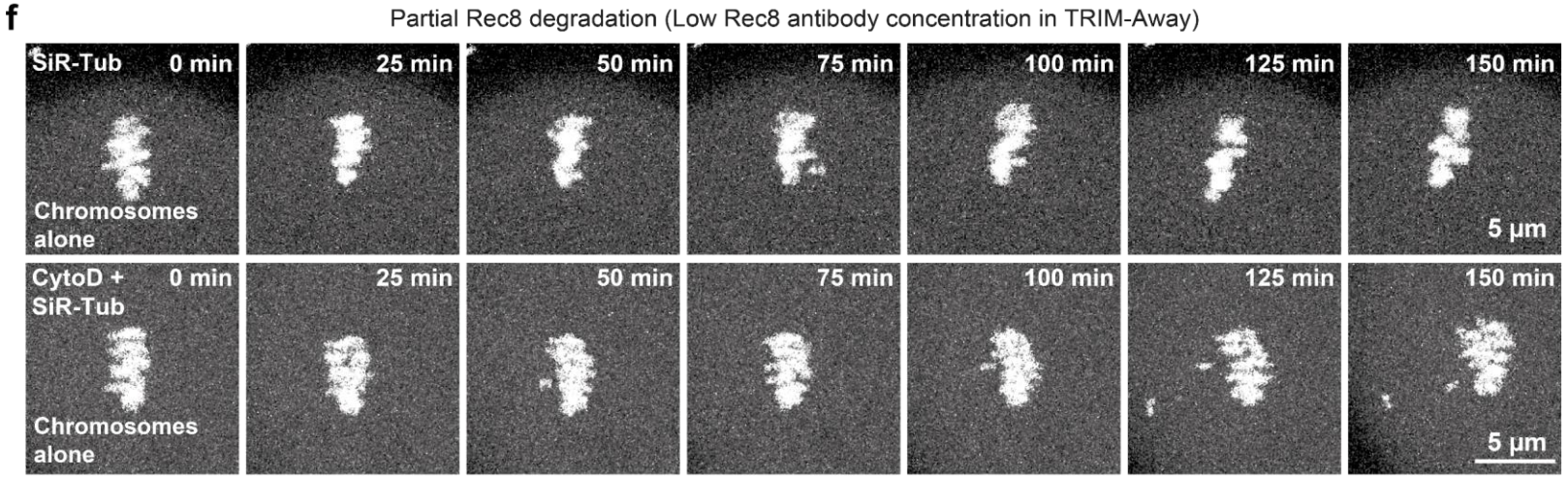
f
Partial Rec8 degradation (Low Rec8 antibody concentration in TRIM-Away)
SiR-Tub
0 min
25 min
50 min
75 min
100 min
125 min
150 min
Chromosomes alone
5 µm
CytoD + SiR-Tub
0 min
25 min
50 min
75 min
100 min
125 min
150 min
Chromosomes alone
5 µm

Figure 4.8 F-actin dampens microtubule-based pulling forces to prevent ageing-like premature chromatid separation **(a)** Stills from representative time lapse movies of chromosomes (magenta, H2B-mRFP) in DMSO (upper-panel)- or Cytochalasin D-treated (second panel), SiR-Tubulin-treated (green, third panel), Cytochalasin D and SiR-Tubulin treated (green, bottom panel) metaphase II-arrested eggs with partially degraded Rec8. Scale bar 5 µm. **(b)** Experimental design schematic – GV injections of H2B-mRFP and TRIM21, 3-hour mRNA expression before prophase-I release and progression through meiosis I, drug treatment (Cytochalasin D, 5 µg/ml, SiR-Tubulin 1 µM) and complete Rec8 TRIM-away. **(c)** Normalised to T=0 mins chromatid scatter volumes over 3 hours in DMSO- (black), Cytochalasin D- (red), SiR-Tubulin (blue)- or Cytochalasin D and SiR-Tubulin-treated (brown) metaphase II arrested eggs with partially degraded Rec8. Split plots can be seen in appendix figure 7.1g,h. Data are from three independent experiments, numbers in parentheses correspond to the total number of eggs analysed in each group,*** $p<0.0001$ (One-way ANOVA). **(d)** Mean normalised chromatid scatter volumes measured over 3 hours in DMSO- (black), Cytochalasin D- (red), SiR-Tubulin- (blue) or Cytochalasin D and SiR-Tubulin-treated (brown) metaphase II arrested eggs with partially degraded Rec8. Data are from three independent experiments, numbers in parentheses correspond to the total number of eggs analysed in each group,*** $p<0.0001$. **(e)** Distribution of instantaneous chromatid movement speeds (µm/min) in DMSO- (black), Cytochalasin D- (red), SiR-Tubulin- (blue) or Cytochalasin D and SiR-Tubulin-treated (brown) metaphase II-arrested eggs with partially degraded Rec8. Data are displayed as box and whiskers plot in appendix figure 7.2d. Data are from three independent experiments, numbers in parentheses correspond to the total number of events analysed in each group, *** $p<0.0001$ (One-way ANOVA). N.B $\bar{x} \pm SD$ **(f)** Stills from representative time lapse movies from (a), showing only chromosomes (magenta, H2B-mRFP) in SiR-Tubulin-treated (upper panel) and Cytochalasin D and SiR-Tubulin treated (bottom panel) metaphase II-arrested eggs with partially degraded Rec8. Scale bar 5 µm.

4.9 Chapter Summary

The contribution of actin in limiting premature separation of sister chromatids was explored by partial or complete degradation of the meiotic cohesion protein Rec8. Tuneable degradation of Rec8 allowed an 'ageing-like' system of PSSC to be created in which the contributions of the actin and microtubule cytoskeletons could be observed. High-resolution live imaging assays uncovered increased and accelerated chromatid separation in actin-disrupted eggs, with actin stabilisation rescuing these splitting events. Actin appears crucial for chromatid realignment and for restricting poleward chromatid movement driven by microtubule based-pulling forces when cohesion is degraded. Taken together, a model, whereby spindle-specific F-actin loss seen with advancing reproductive age coupled with progressive cohesion loss, creates unchallenged microtubule-based pulling forces that lead chromosomes to split prematurely, can be proposed.

Chapter 5 – Discussion

5.1 Actin limits egg aneuploidies associated with female reproductive ageing

5.1.1 A spindle-specific reduction in F-actin with advancing maternal age

Advancing reproductive age leads to an exponential rise in cases of incorrect chromosome segregation, resulting in the formation of aneuploid eggs [1,2,74,158,160]. A gradual weakening of cohesion complexes has been recorded in mice and humans which often leads to premature separation of sister chromatids and onwards misegregation [97,174,178]. Such an exponential rise however cannot be explained fully by one factor. Here, a reduction in spindle F-actin, essential for organising microtubules into functional fibres for faithful chromosome segregation [152], was hypothesised to be altered or reduced in ageing eggs. A change in spindle F-actin could be an additive factor to cohesion decline, responsible for further separation of sister chromatids. Super-resolution microscopy was performed in young and aged mouse eggs to assess cellular F-actin integrity [134]. As hypothesised, in ageing mouse eggs, the intensity of spindle f-actin filaments reduced relative to control young eggs (Figure 3.1). Reduced spindle F-actin, with no changes in global cytoplasmic actin filaments, suggests changes to actin regulators such as Arp2/3 [221] or proteins associated with actin-microtubule crosstalk declining with advancing reproductive age [190,222]. Actin-microtubule crosstalk has been previously recorded in meiotic spindles in which recovery from pharmacological actin disruption involved new actin filaments being pulled into and aligning with the microtubule spindle [152]. These insights suggest the presence of spindle associated proteins that mediate interactions between the microtubule and actin cytoskeleton in mammalian eggs. Interestingly, here, the intensity of microtubules within the meiotic spindle did not decrease with advancing reproductive age when spindle actin filaments declined (Figure 3.3). Microtubules and actin have been previously described to regulate each other at centrosomes [223-225]. Initial *in vitro* investigations demonstrated that microtubule nucleating centrosomes directly promote the assembly of actin filaments [223]. In lymphocytes, low microtubule densities are correlated with high levels of actin filaments nucleated at the centrosomes [226]. Interestingly, when actin was disassembled in lymphocytes microtubule abundance conversely increased [226]. This contradictory regulation is also present during mitosis. During mitotic anaphase, actin filaments nucleate around centrosomes, leading

to a reduction in centrosomal microtubule abundance [224]. Spindle microtubule intensity appeared to increase in aged oocytes, whilst spindle-actin filaments decreased (Figure 3.1, 3.3). Whilst oocytes are acentrosomal [14], the contradictory regulation of microtubules and actin at centrosomes in other systems could explain the increase in microtubule intensity in aged meiotic spindles (Figure 3.3). Further investigations should aim to identify microtubule-actin regulators within the meiotic spindle and whether these spindle associated proteins are compromised with advancing maternal age. These data conclude an age-related decline in spindle F-actin which could be attributed to dysregulation of actin regulators within mammalian eggs.

5.1.2 F-actin mitigates PSSC in female meiosis

As hypothesised, spindle-actin filaments declined with advancing maternal age. Eggs were further challenged with actin depolymerisers, to evaluate whether actin loss exacerbates aneuploidy resulting from ageing-related cohesin decline. Actin disruption in aged eggs lead to extensive untimely separation of sister chromatids (Figure 3.6). These results suggested that F-actin reduces premature separation of sister chromatids (PSSC) in ageing eggs. Often, misaligned chromosomes are improperly segregated in anaphase II when actin is disrupted[152]. In combination with an age-related decline in spindle F-actin, it can therefore be suggested that F-actin loss is a contributing factor to the exponential rise in aneuploidy recorded in embryos as maternal age increases. Consistently, actin removal in young eggs introduced modest untimely sister chromatid separation (Figure 3.6). The presence of single chromatids is surprising as young oocytes will have a much stronger complement of cohesion complexes at their centromeres [97,174,178]. Interestingly, the number of single chromatids recorded in actin disrupted eggs was akin to the number present in control ageing eggs (Figure 3.6). Highlighting that F-actin disruption in young eggs is sufficient to produce an ‘ageing-like’ incidences of PSSC, that would usually accumulate over many decades. Mimicking ‘ageing-like’ PSSC in young eggs in such an acute timescale (4 hours), was important for future experiments where gain/loss of function assays were performed.

5.1.3 F-actin loss leads to sister chromatid separation independent of chromosome cohesion

The presence of single chromatids in actin depleted eggs, suggested a weakening or loss of cohesion complexes found at the centromeres of chromosomes. Metaphase chromosomal spreads are performed following cell lysis and therefore in the absence of spindle microtubules [184]. As microtubule-based pulling forces create tension across sister centromeres [92,227], it is not possible to conclude the effects of actin disruption on inter-kinetochore spacing using spreading techniques alone. Actin disruption did not globally increase inter-kinetochore distances in both intact eggs and chromosomal spreads (Figure 3.10). These data were independently confirmed through the use of a mechanistically distinct actin disrupting agent, Latrunculin B [154]. In fact, Latrunculin B treatment did not mirror the IKDs recorded in Cytochalasin D treated eggs. A marginal increase in IKD was recorded in Latrunculin B treated chromosomal spreads (Figure 3.11), which could be due to the inclusion of separated single chromatids within the analysis. Completely separated single chromatids generated by actin loss should not be recorded and therefore should not contribute to a whole-chromosome IKD analysis. However, manual identification of chromatid pairs by the user could provide error, with some prematurely separated chromatids thought to be paired due to their proximity. To account for this, an automatic pairing algorithm could be developed to eliminate user bias. Nonetheless, these data suggest a chromosome specific disruption to cohesion caused by actin loss, resulting in certain chromosomes separating prematurely. Chromosome specific defects would lead to chromosome specific aneuploidies if viable embryos formed. Chromosome-specific changes are interesting when considering meiotic drive, whereby at anaphase particular chromosomes/chromatids are more likely to be retained in the main cell body than others, which are segregated into the polar body[228-230]. Further experiments should aim to characterize which chromosomes are most affected by actin disruption. Chromosomes 21,18 and 16 which have high incidences of trisomy could likely be most affected by actin loss [160].

To further investigate the effect of actin disruption on chromosome cohesion, imaging protocols were developed to visualise whether canonical cohesion proteins were dysregulated

as a result of actin loss. For this, Rec8, the meiotic-specific kleisin subunit of the cohesion complex was probed to visualise centromeric and arm based cohesin [82]. Optimization of a serum-based antibody for Rec8 [174], kindly provided by Michael Lampson, took many iterations in order to produce quantifiable images. For both intact and chromosomal spreads, post-fixation dephosphorylation was required to reduce signal to noise during subsequent imaging. Lambda phosphatase removes phosphate groups from threonine, serine and tyrosine residues and has catalytic similarities to PP2A [231] (which is abundant at centromeric cohesion complexes prior to anaphase [75,96,232]). To decide if quantifiable changes in Rec8 were feasible in both intact and chromosomal spreads; Reversine was used as a positive control. Reversine, an Mps1 inhibitor, causes disassociation of shugoshin-2-PP2A pairs from the cohesin ring, leading to seperase-mediated Rec8 cleavage [72,199]. Significant decreases in Rec8 mean intensity were recorded in intact and metaphase I chromosomal spreads following Reversine treatment (Figure 3.13, 3.15), confirming that quantifiable changes in cohesion complexes could be recorded. Consistently with inter-kinetochore measurements, metaphase I oocytes did not have significant changes in cohesion as a result of actin disruption (Figure 3.14, 3.16). IKD and Rec8 intensity measurements suggest that F-actin disruption leads to premature chromatid separation independently of canonical chromosome cohesion pathways. Gradual cohesion loss with advancing maternal age, does not appear to be as a consequence of the age-related decline in spindle-actin recorded here [97,174]. Chiang, et al. [174] showed no significant differences in total Rec8 protein expression between young and aged oocytes. It is conceivable that an absence of cohesin reloading to chromosomes is not as a result of actin decline in aged eggs [233,234]. Instead, cohesion complex reloading could be as a result of defective microtubule dynamics in aged eggs [179].

5.2 F-actin dampens microtubule-based pulling forces to prevent ageing-like premature chromatid separation

5.2.1 Fine-tuning cohesion loss – modulating Rec8 TRIM-away

The TRIM-away system was first published in 2017 and proof of function experiments focused on acutely degrading histone 2B, the kinesis-5 motor protein Eg5 and Rec8 amongst other targets [200]. These experiments were performed in somatic cells as well as in mouse oocytes

and eggs. Since, the TRIM-away system has been used to examine the contributions of proteins in many different systems and scenarios [45,235-241]. Rec8 TRIM-away experiments performed in this body of work mimic the results produced by Clift, et al. [200], with separation events occurring after 10 minutes as a result of concentrated anti-Rec8 introduction (Figure 4.2). Importantly phenotypes are consistent even though a different antibody was used here. In this work, Rec8 antibody concentrations were varied in order to induce differing levels of cohesion degradation. High concentrations were microinjected in order to cause complete degradation of cohesion complexes, where extensive separation events were observed akin to those seen in the original publication. Lower concentrations were introduced in order to mimic 'ageing-like' separation of sister chromatids, with fewer separation events occurring compared to high concentrations. Partial depletion aided in assessing the effects of actin-disruption on a more physiological level, whereas complete degradation challenged stabilised microtubules and stabilised actin to limit premature separation events. Whilst recently, studies have used the TRIM-away to degrade other targets through antibody or nanobody introduction, the work performed here is the first-time the amount of degradation has been modulated successfully [45,240,241]. Cohesion in young eggs has not been experimentally modulated in a way that resembles reproductive ageing until this point.

5.2.2 Chromatid Scatter volume – using volume reconstruction to measure scatter, acceleration, and realignment

Analysing the effects of Rec8 TRIM-away from high-resolution live imaging timelapses required careful consideration. Volume reconstructions in Imaris allowed chromatid densities that separated from the central chromosome mass to be detected. Combined with object orientated bounding box outputs, chromatid scatter volumes could be recorded. The object-orientated bounding box (OO) was chosen over the axis-aligned bounding box (AA) [242]. AA-bounding boxes produce measurements of the difference between the maximum and minimum coordinate from each axis. For example, AA length X is equal to the difference between the maximum X value and the minimum X value parallel to the axis. Whereas OO-bounding records the minimal XYZ values relative to the object itself rather than the set axis, making it more appropriate to account for the differing angles of the meiotic spindle. One

limitation of this analysis was the manual removal of background signal or signal from the separated chromosomes in the polar body. This meant manually deleting surfaces the algorithm had identified during each movie, which was time consuming. Additionally, this analysis did not consider the number of separation events. Often single separation events would occur, with single chromatids being dragged poleward by microtubules. This meant larger chromatid scatter volumes were recorded as the chromatid moved from the main chromosome mass. For partially depleted DMSO control and stabilised actin or microtubule conditions these single separation events were few, meaning only slight skewing of the mean volumes occurred, at a level insufficient to alter data trends.

To measure chromatid acceleration, manual recording of frame-to-frame displacement, tracking the tip of a reconstructed chromatid volume, generated instantaneous acceleration reads. This analysis produced individual accelerations for each time-point. One limitation of this analysis was only eggs with obvious chromatid movement were recorded. Fewer accelerations were recorded in control conditions compared with drug addition groups as a result. Additionally, this analysis is manual and therefore may introduce unconscious bias. Volume reconstruction also aided in quantifying realignment events. Again, only eggs with single chromatid poleward movement were included in this analysis, meaning control conditions had fewer data points. Chromatid volume reconstruction using the surfaces module algorithm in Imaris (Bitplane) provides a powerful tool for measuring chromatid scatter, acceleration and realignment.

5.2.3 Actin opposes microtubule based pulling forces and promotes realignment of scattered single chromatids

Figure 3.6 highlighted an unexpected increase in single chromatids when actin was disrupted in both young and aged eggs. This finding was explored further in a system of ageing-like centromeric cohesion loss by utilising Rec8 TRIM-away. Initial optimisation of the concentration of anti-Rec8 allowed mimicry of an ageing-like proportion of premature separation events. Modulating cohesion degradation induced a modest number of separation events akin to the numbers seen in aged *in vitro* matured eggs (Figure 4.2). ‘Partial’ and

‘Complete’ Rec8 degradation is the first example of how tuneable the TRIM-away system is. Consistently with aged eggs where actin was reduced, ‘ageing-like’ Rec8 depleted young eggs showed more extensive chromatid separation events when actin was disturbed (Figure 4.4). Additionally, realignment events reduced in concert with increased chromatid acceleration, likely as a result of unhindered microtubule dynamics [6] (Figure 4.5). Actin’s involvement in opposing microtubule-based forces has been recorded previously in organelle transport [243]. From this data it appears actin has two key roles within the meiotic spindle. Firstly, a brake to acceleration induced by microtubule based pulling forces and secondly as a governor for realignment of prematurely separated single chromatids. Actin’s role in limiting lagging chromosomes/chromatids has already been shown previously during metaphase I [152].

Prematurely separated chromatids are generated during metaphase II arrest following successful anaphase I completion. High-resolution live imaging showed that following separation single chromatids are frequently positioned to opposing sides of the spindle equator in control eggs. Further, actin loss disturbed realignment, meaning single chromatids cycled across opposite sides of the spindle, increasing the likelihood for misegregation at anaphase II. This is consistent with previous work, where actin disruption in meiosis I caused misaligned and lagging chromosomes in metaphase II which cycled across opposing sides of the spindle and resulted in misegregation during anaphase II [152]. Visualizing whether prematurely separated chromatids randomly misalign and subsequently result in loss/gain of chromatid during anaphase II in the context of cohesion loss, will require the development of imaging assays and time-dependent degradation of Rec8 in the earliest stages of meiosis II. Expansion into acute degradation of cohesion complexes in aged eggs will further our understanding of F-actins role in promoting alignment and reducing PSSC.

The actin cytoskeleton holds many function in mammalian meiosis including, vesicle transport, nuclear migration, spindle positioning and faithful chromosome segregation [125,126,236,243]. Currently there are no experimental assays that specifically disrupt spindle F-actin populations. However, previously developed pharmacological assays were used here, that originally characterized the functions of spindle actin in chromosome segregation [134,152]. These

experimental assays excluded the contribution of the cytoplasmic actin network, vesicle trafficking and cytokinesis, confirming spindle F-actins' importance for faithful chromosome segregation.

5.2.4 F-actin enrichment restricts poleward movement of prematurely separated single chromatids

F-actin enrichment within the meiotic spindle causes stabilisation of kinetochore bound microtubule fibres [152]. Here, F-actin stabilisation using SiR-Actin, a fluorescent derivative of Jasplakinolide [134,152,156,203], limited sister chromatid movement despite complete loss of cohesion from centromeric regions (Figure 4.6) and also caused separating chromatids to slow. This data adds to previous ideas that actin limits premature separation and promotes realignment. However, it is expected that spindle F-actin needs to be dynamic to limit chromosome segregation errors in physiological conditions. Mogessie and Schuh [152] noted that highly stabilised F-actin caused chromosome misalignment and segregation defects in both meiosis I and II. This appears to not be an issue during metaphase II arrest where stabilised actin does not seem to be highly dynamic when cohesion is lost. This is not to say stabilisation is producing undynamic F-actin, as filament movement can be seen following complete cohesion loss (Supplementary movie S11).

Importantly, this is considered to be a spindle-specific F-actin affect. As previously discussed, the use of SiR-Actin does not appear to limit cytoplasmic actin process such as actin-dependent vesicle transport [127,152]. Furthermore, the concentration of SiR-Actin required to limit separation in cohesion deficient eggs, required optimisation. Whilst lower concentrations, stabilised cytoplasmic actin and some spindle-actin populations, this level of stabilisation was not sufficient to limit chromatid scattering (data not shown). Additionally, all Rec8 TRIM-away experiments included the co-injection of high molecular weight fluorescently tagged Dextran molecules. These were co-injected as a proxy for successful antibody introduction. The introduction of dextran would increase cytoplasmic crowding in both control and drug addition conditions [244,245]. As no restricted chromatid movement was observed in control dextran-injected eggs, it can be concluded that changing the cytoplasmic biophysical properties does

not have a visible effect on chromatid dynamics. These data demonstrate a new function for F-actin in restricting prematurely separated chromatids from being pulled poleward in metaphase II eggs when cohesion is degraded.

5.2.5 Microtubules drive segregation and scattering following cohesion degradation

Microtubules are well-characterised drivers of chromosome segregation in many systems [50,204-220,246]. Recently a decline in microtubule function in aged eggs, resulting in aberrant microtubule dynamics was shown to result in egg aneuploidy and chromosomal abnormalities [179]. Age-related changes in microtubule dynamics, causes meiotic segregation errors independently of cohesion [180]. This is consistent with PSSC independently of cohesion changes shown here in figures 3.14, 3.16. To confirm whether microtubule-based pulling forces were responsible for chromatid acceleration in a cohesion depleted system, microtubule dynamics were restricted. The fluorogenic derivative of Docetaxel [156,179], SiR-Tubulin was introduced to stabilise microtubule filaments prior to Rec8 cleavage. Stabilised microtubule filaments significantly slowed prematurely separated single chromatids, restricting their location to the spindle equator (Figure 4.8). This data confirmed, in a system of induced cohesion loss, that microtubules drive sister chromatid scattering. Once more, this is not to say stabilised microtubules completely lose their dynamics. Movement can still be seen within the stabilised filaments (Supplementary movie S13). Whether these relate to newly formed polymers or movement in existing k-fibres, interpolar microtubules or astral microtubules, remains to be discerned [247]. Importantly, these stabilisation experiments allowed refinement of SiR-Tubulin concentrations for further studies where actin and microtubules were challenged in combination.

5.2.6 Microtubule pulling forces pull apart chromosomes when actin is disturbed

Given that F-actin is important for organising microtubules into functional K-fibres that are able to separate chromosomes faithfully [152], and an age-related decrease in spindle actin was recorded here (Figure 3.1), it was hypothesized that blocking microtubule dynamics when actin was pharmacologically disrupted would not result in premature separation events in an ‘ageing-like’ system of cohesion loss. In contrast to eggs with dynamic microtubules, following

partial Rec8 TRIM-away, SiR-Tubulin and Cytochalasin D-treated eggs had minimal premature chromatid separation events (Figure 4.10). This experiment highlights that F-actin may hold a previously uncharacterized role in opposing microtubules. It would be difficult to reproducibly measure microtubule dynamics in cohesion deficient eggs due to the excessive nature of chromatid scattering when F-actin is disrupted. Whilst we know that spindle F-actin is essential for stabilising kinetochore-bound microtubules, and its enrichment nullifies microtubule dynamics, the exact relationship between microtubules and actin within the meiotic spindle is yet to be clarified [152]. In young eggs, with strong cohesion actin may supplement resistance to microtubule based pulling forces, creating the correct amount of centromeric tension. Actin opposition would become more crucial in aged eggs as cohesion begins to wane, explaining why F-actin disruption in aged eggs leads to further separation of sister chromatids. Consistently aberrant microtubule dynamics have been recorded in aged mouse eggs, which were proposed to be cohesion-independent causes of aneuploidy [179,180].

5.2.7 Actin-microtubule crosstalk in meiotic spindles

Premature chromatid separation independently of changes to canonical chromosome cohesion pathways, points toward changes in the cytoskeletal forces exerted on chromosomes. Dynamic microtubule k-fibres constantly pull and push the kinetochores within the spindle in order to create tension [204-220,227]. Surprisingly here, Latrunculin B treatment in metaphase II eggs caused a significant decrease in inter-kinetochore distances (Figure 3.10). In these eggs tension across the kinetochores appears to be lost, potentially due to changes in the meiotic spindle. Latrunculin B treatment also caused an increased prevalence for untimely sister chromatid splitting (Figure 3.7). One explanation for this phenotype is the loss of tension dependent localisation of Sgo2-PP2A complexes from the centromeres. Removal of Sgo2-PP2A complexes would allow Rec8 mediated cleavage by seperase [70,248]. In *in vitro* assays, mitotic shugosin was shown to strongly associate with microtubules to aid kinetochore-microtubule stability [249]. When microtubules tension is lost, it could be conceived that Sgo2 is lost from the centromeres as a result of k-fibre instability.

Actin-microtubule crosstalk has been identified in many process of cell biology[190,222]. Interplay between microtubules and actin through mediating factors can function as guidance for microtubule plus end growth [192], coordinate microtubule sliding [193], anchoring in mitotic cell rounding [194] and influence division in many species [126,135,145,152,157,250,251]. Such crosstalk in prominent cellular mechanisms provides basis for actin-microtubule interaction in meiotic spindles. Influences of actin on k-fibre microtubule stability and faithful segregation have already been demonstrated [152].

Here stabilising actin filaments, prior to cohesion loss, limited the number of premature separation events (Figure 4.6). Visually, chromosomes were maintained in proximity to one another in SiR-Actin treated eggs, suggesting that stabilisation of F-actin within the spindle or in the surrounding meshwork limits scattering through steric interaction [126,157,252]. The reduction of spindle F-actin filaments with advancing reproductive age could be influencing a shift in microtubule-based forces on chromosomes, skewing the tension exerted on sister kinetochores. In the presence of microtubules, actin disruption caused premature separation of some sister chromatids in young eggs (Figure 3.6). When actin is lost microtubule based pulling forces on some chromosomes could appear too great causing them to be pulled apart. Why all chromosomes do not separate furthers an idea of chromosome specific aneuploidies existing in meiosis [59].

5.3 Model

From this data, it can be proposed that actin is a key factor in limiting premature separation of sister chromatids, especially in advancing reproductive age. F-actin reduction within the meiotic spindle could be an additional factor contributing to the exponential rise in age-related aneuploidy recorded in reproductively older women. Here a model, wherein spindle F-actin in young eggs, coupled with strong cohesion complexes is sufficient to limit microtubule based pulling forces on chromosomes (Figure 5.1a). As cohesion wanes, actin filaments in young eggs, dampen pulling forces from the meiotic spindle in order to limit premature separation events. In aged eggs, as a result of both cohesion loss and F-actin reduction, microtubule-based pulling forces are unchallenged and separate chromosomes prematurely. This model

was based on modulated cohesion degradation using the Trim-Away system in the presence, stabilisation, or absence of F-actin as well as combinatory experiments where microtubule dynamics were blocked (Figure 5.1b,c,d).

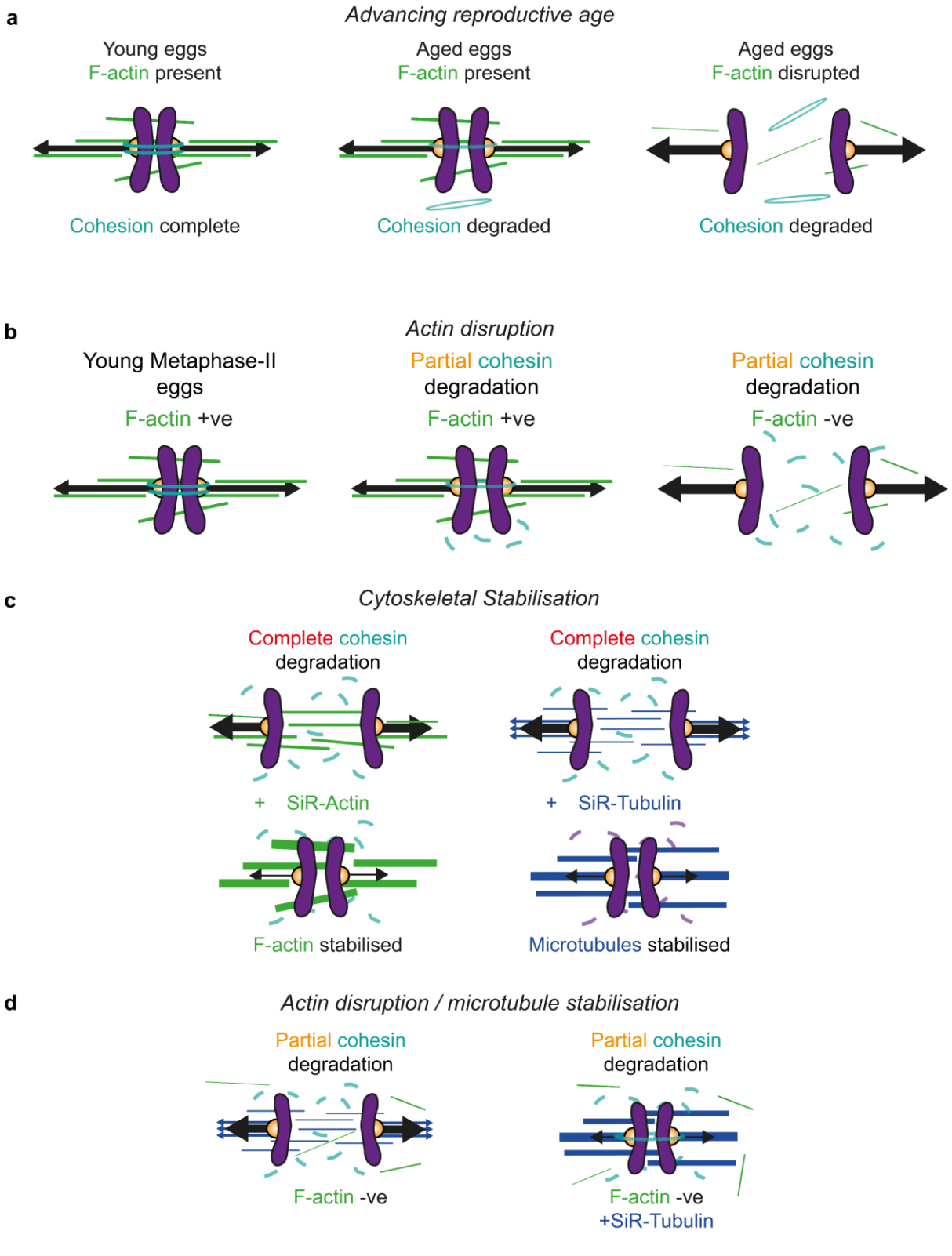
a
Advancing reproductive age
Young eggs
F-actin present
Cohesion complete
Aged eggs
F-actin present
Cohesion degraded
Aged eggs
F-actin disrupted
Cohesion degraded
b
Actin disruption
Young Metaphase-II eggs
F-actin +ve
Partial cohesin degradation
F-actin +ve
Partial cohesin degradation
F-actin -ve
c
Cytoskeletal Stabilisation
Complete cohesin degradation
+ SiR-Actin
F-actin stabilised
Complete cohesin degradation
+ SiR-Tubulin
Microtubules stabilised
d
Actin disruption / microtubule stabilisation
Partial cohesin degradation
F-actin -ve
Partial cohesin degradation
F-actin -ve
+SiR-Tubulin

Figure 5.1 Model (a) Advancing reproductive age schematic. As F-actin (green) and cohesion (turquoise) reduces with increasing age, microtubules (black) separate chromosomes prematurely. **(b)** Actin disruption in combination with partial Rec8 TRIM-Away schematic. **(c)** Cytoskeletal stabilisation diagram using SiR-Actin and SiR-Tubulin in combination with complete Rec8 TRIM-away. **(d)** Combinatory microtubule stabilisation and actin disruption diagram in combination with partial Rec8 TRIM-away.

5.4 Questions Raised

- How does actin influence microtubule dynamics in the meiotic spindle?
    - Are there microtubule-actin crosslinkers within the spindle?
    - Does actin directly oppose microtubules or is its function on chromosomes themselves?
- How is spindle-actin dysregulated with advancing maternal age?
    - Are actin associated factors disrupted?
    - Are microtubule associated factors disrupted?
- Are microtubule k-fibres affected by actin loss with advancing reproductive age?
- Does actin disruption cause premature separation of sister chromatids in other species?
- Which chromosomes are more likely to prematurely separate as a result of actin loss?
- Are centromeric cohesion complexes specifically affected by actin loss?
    - Could cohesion be affected on a chromosome specific level?

5.5 Future investigations

5.5.1 Quantifying cohesion complexes in metaphase II eggs

There was no significant change in arm and centromeric cohesion complex abundance as a result of actin disruption in both intact metaphase I oocytes and metaphase I chromosomal spreads. Positive control Reversine treated oocytes did however show a significant reduction in Rec8 positive cohesion complexes, confirming that changes could be attained and quantified in imaging assays. However, most experiments were performed in metaphase II-arrested eggs where arm cohesion has been cleaved (prior to anaphase I) and only centromeric cohesion remains [50,158]. It will therefore be interesting to also quantify changes in cohesion complexes as a result of actin disruption in metaphase II eggs. Imaging centromeric cohesion is difficult due to the compacted nature of the centromere in metaphase II, the reduction in cohesion complexes, as well as obscuring kinetochore-microtubule interactions [253]. Super-resolution imaging techniques, such as Airyscan, Stimulated Emission Depletion (STED) or expansion microscopy imaging may be required in order to image quantifiable centromeric cohesion complexes in intact and chromosome spreads from metaphase II eggs [185,254,255]. These imaging techniques would allow insights into whether centromeric cohesion is specifically altered by actin disruption.

5.5.2 Chromosome specific aneuploidy identification using fluorescence *in situ* hybridization (FISH)

Most eggs treated with actin disrupting agents, Cytochalasin D or Latrunculin B contained prematurely separated sister chromatids which could be visualised in intact spindles and chromosomal spreads. However, there was no global change to cohesion, inter-kinetochore distance and not every chromosome was affected by actin disruption. It appears that actin disruption affects a specific population of chromosomes. These prematurely separated chromosomes will not have contributed to whole-chromosome analysis of inter-kinetochore distance. It will therefore be interesting to characterize which chromosomes are being affected most by actin disruption. Preliminary attempts were made to characterise separated chromatids through volume reconstructions in Imaris (Bitplane), with the aim of gaining insights into whether different sized chromosome were more likely to split prematurely.

However, it was difficult to dissect chromatid volumes from the main chromosome mass in intact eggs and to relate single chromatids to their separated sister. In chromosomal spreads, whilst it was clearer to distinguish single chromatids, relating which single chromatid belonged to its sister was difficult. Further investigations should aim to characterize chromosome-specific aneuploidies through fluorescent *in situ* hybridization (FISH) karyotyping[256]. Optimising FISH would allow characterization of size-specific or chromosome specific aneuploidies, for example chromosome 21 (frequently mis-segregated in Down's syndrome [257]).

5.5.3 Dissecting actin-dependent cohesion at the arms and centromeres of chromosomes

Actin may influence cohesion or microtubule buffering at the chromosome arms, centromeres or globally. Indeed, it has been shown that actin nucleation occurs on chromosomes in order to organise microtubule capture [252]. Targeted actin gain/loss of function assays, in combination with Rec8 TRIM-away, at chromosome arms and centromeres would discern if different sub-populations of actin have differing roles within mammalian eggs. Centromeric targeting of actin populations could employ TALEN (Transcription Activator-Like Effector Nuclease) [258] based constructs locating to the major satellite repeat sequences found at chromosome centromeres [45,259]. For targeting of chromosome arms, constructs could be fused to Histone 2B (H2B) to allow incorporation in the chromatin. Actin-nanobody based TRIM-away could then be implemented to degrade actin at these target regions [200]. Degrading actin in these regions may shed further light on where actin is functioning in respect to differing chromosome loci. Once an understanding of actin's localised function has been developed, modifications to constructs can be made to incorporate actin stabilisation at each locus. For stabilisation, the actin stabilising domain Utrophin (UtrCH, calponin homology domain) could be targeted using TALENs or H2B to the chromosomes and centromeric regions [7]. These stabilisation constructs could then be used in combination with Rec8 TRIM-away to further characterise actin's role in buffering microtubule based pulling forces on chromosomes in mammalian eggs.

5.5.4 Proteomics in aged eggs – are changes in actin related proteins present?

Here, high-resolution imaging showed a spindle-specific reduction in F-actin filaments in ageing mouse eggs. Spindle-filaments also appeared disordered and more fragmented when compared to control young eggs. It will be interesting to follow up on these findings by investigating the proteomics profiles of young and aged mammalian eggs. For this, Tandem-Mass-Tag (TMT) proteomics would be employed [260], primarily looking for expression changes of actin nucleators and regulators such as Formin-2 and Arp2/3 which are involved in filament assembly and branching [22,145,221,252]. Downregulation of actin-related protein in aged populations will allow further *in vivo* experiments to be developed to understand why there is a spindle-specific reduction in F-actin filaments in aged eggs. One limitation to these studies would be the number of eggs required for TMT. Often aged mice produce very few oocytes for isolation, meaning many mice would be needed to provide enough protein for TMT analysis. One alternative avenue would be to investigate changes in actin related proteins in young and aged porcine eggs. Porcine eggs are an ideal candidate for proteomics studies due to their large volumes and genome similarities to humans [261]. Using porcine eggs from young and aged sows would overcome protein abundance issues limiting the use of mouse eggs.

An additional option for investigating age-related changes in actin/microtubule regulatory proteins would be to explore population health studies. Collaborations with population health specialists, or clinical departments could provide information on gene, RNA or protein level changes in actin/microtubule regulating proteins with advancing reproductive age. For example, a recent study identified 290 genetic loci determinants of ovarian ageing in 200,000 European women, with genetic variants of DNA damage response (DDR) featuring amongst others [262]. Changes in actin/microtubule regulating proteins could provide molecular clues for investigation, as to why spindle actin is dysregulated with advancing reproductive age.

5.5.5 Metaphase II for Rec8 TRIM-away

One limitation of using metaphase II-arrested eggs for Rec8 TRIM-away studies is that sister kinetochores have established stable K-fibre interactions [6]. This means that even if premature separation has occurred sister chromatids are likely to be directed to the appropriate pole by

microtubule K-fibres, akin to the correct segregation that would occur in anaphase II. Theoretically the result would be an egg with the correct chromosome numbers and not aneuploid. To account for this, Rec8 TRIM-away would need to be performed before stable attachments have been made, during the transition from anaphase I to metaphase II. Cohesion loss would then likely result in incorrect attachments and aneuploidy. Performing these experiments in combination with cytoskeletal manipulation would further expand on actin's role in limiting misegregation in an ageing-like system of cohesion depletion.

5.5.6 Comparisons to other mammalian species

Previous studies identified novel roles for actin in mammalian eggs in many different species. Actin was found to protect mammalian eggs from chromosome segregation errors in mouse, pig and sheep as well as importantly, human oocytes and eggs [152,157]. Further nuclear actin, thought to have links to age-related infertility, was found in mouse, pig and sheep prophase I -arrested oocytes [45]. It will therefore be interesting to explore the phenotypes found here in other mammalian species. Conserved reductions of age-related spindle-actin, especially in humans, would help to inform screening protocols and education. Further, exploring the relationship between actin and microtubule forces in the meiotic spindle in other mammalian species or *in vitro* assays would help to provide clarity on these mechanisms.

5.6 Limitations of this study

One key limitation of this study was the use of mice as a model organism. Whilst, mouse eggs are similar to human, obvious differences are present. Physiological, structural, genomic, and mechanistic differences distinguish mouse from human. Importantly for this study, weakened cohesion is seen in both human and mouse eggs with advancing reproductive age, as well as the presence of spindle F-actin important for accurate chromosome segregation in both species [97,152,174]. Similarities between these species made the use of mouse oocytes a viable option for investigating actin-dependent cohesion mechanisms.

5.6.1 Analysing spindle actin

This study highlighted a decrease in spindle F-actin in aged eggs. Intensities were collected through averaged regions of interest (ROIs) within the meiotic spindle and compared to the

cytoplasmic intensity. Ideally, the entire spindle-F-actin volume would have been quantified. Attempts were made to quantify spindle-actin by volume reconstruction of the entire meiotic spindle, using the tubulin signal. Spindles were reconstructed using the surfaces module of Imaris allowing a mask to be created to only quantify intensities within the spindle. However due to the proximity of the spindle to the cortex of the egg, masked volumes often included high intensity cortical actin populations [126]. These high intensity populations would significantly skew spindle-F-actin intensity measurements. Additionally, variation in the position of the spindle within the egg volume meant that no overall background subtraction could be made, as the densities of cortical actin being quantified varied.

5.6.2 Analysing global actin

Here, whilst spindle actin filaments decreased with advancing reproductive age, global cytoplasmic intensities did not significantly decrease when compared to young eggs, highlighting a spindle specific reduction in F-actin. Global actin intensities were collected through averaged ROIs within the cytoplasm. C57BL/6 mice consistently have large patches devoid of phalloidin signal within their cytoplasm. ROIs were collected away from these patches in order to quantify intensity of the cytoplasm. This meant whole slice-intensities could not be gathered as these patches varied between eggs. Single Z-slices were acquired at the centre of each egg, sometimes including the spindle-actin filaments. The presence of spindle-actin filaments in images also meant whole-slice intensities could not be gathered as the enrichment from the spindle would confound mean intensities.

5.6.3 ‘Partial’ and ‘Complete’ Rec8 TRIM-Away

Here, the contributions of the actin and microtubule cytoskeletons to premature sister chromatid separation were dissected by varying the levels of cohesion degradation. ‘Partial’ and ‘Complete’ Rec8 degradation showed phenotypically distinct levels of premature chromatid separation in high-resolution imaging assays. However, the levels of cohesion degradation were not quantified. Further experiments should aim to compare the levels of Rec8 degradation produced through microinjection of high and low concentrations of Rec8 antiserum by western blotting or immunofluorescence techniques.

5.7 Therapeutic applications

An age-related reduction in spindle F-actin structures furthers our understanding of female meiosis and may harbour clinical importance. Perhaps, restoring F-actin to the meiotic spindle would aid in reducing aneuploidy rates associated with progressive cohesion loss in aged eggs. Enriching spindle F-actin populations pharmacologically through SiR-Actin treatment seems illogical as it has been shown to cause chromosome segregation defects in young eggs [152]. As previously discussed, further investigations should focus on characterising the causes underlying an age-related decline in spindle F-actin, whether this is dependent on dysregulation of actin- or microtubule-related proteins in aged eggs. Further experiments could then explore whether re-introduction of these proteins is sufficient to rescue faithful chromosome segregation in aged eggs with cohesion deficiency.

5.8 Summary

New roles for F-actin in promoting microtubule stability and organisation have been identified in many cellular mechanisms as well as in female meiosis [125,152,157,191,222,226,250,263-267]. F-actin has more recently been shown to be a component of the mitotic spindle machinery and is important for accurately separating sister chromatids [132,268]. The findings in this thesis suggest that spindle-specific actin filaments are important for mitigating microtubule-based pulling forces on sister centromeres. This mitigation becomes ever more important with advancing reproductive age. Spindle F-actin therefore might act similarly in mitotic cell division, where aneuploidies associated with ageing have been identified [269-273]. Future explorations should focus on the interactions of microtubules and actin within the meiotic spindle. Investigations into the dysregulation of F-actin within the spindle with advancing reproductive age should also be emphasised.

Chapter 6 – References

1 Hassold, T. a. C., D. Maternal age-specific rates of numerical chromosome abnormalities with special reference to trisomy. *Human Genetics*, 11-17 (1985).

2 Hassold, T. & Hunt, P. To err (meiotically) is human: the genesis of human aneuploidy. *Nat Rev Genet* **2**, 280-291 (2001). https://doi.org:10.1038/35066065

3 Dunkley, S. & Mogessie, B. Actin limits egg aneuploidies associated with female reproductive aging. *bioRxiv*, 2022.2005.2018.491967 (2022). https://doi.org:10.1101/2022.05.18.491967

4 Sanders, J. R. & Jones, K. T. Regulation of the meiotic divisions of mammalian oocytes and eggs. *Biochem Soc Trans* **46**, 797-806 (2018). https://doi.org:10.1042/BST20170493

5 Patel, J., Tan, S. L., Hartshorne, G. M. & McAinsh, A. D. Unique geometry of sister kinetochores in human oocytes during meiosis I may explain maternal age-associated increases in chromosomal abnormalities. *Biol Open* **5**, 178-184 (2015). https://doi.org:10.1242/bio.016394

6 Bennabi, I., Terret, M. E. & Verlhac, M. H. Meiotic spindle assembly and chromosome segregation in oocytes. *J Cell Biol* **215**, 611-619 (2016). https://doi.org:10.1083/jcb.201607062

7 Ohkura, H. Meiosis: an overview of key differences from mitosis. *Cold Spring Harb Perspect Biol* **7** (2015). https://doi.org:10.1101/cshperspect.a015859

8 Desai, A. & Mitchison, T. J. Microtubule polymerization dynamics. *Annu Rev Cell Dev Biol* **13**, 83-117 (1997). https://doi.org:10.1146/annurev.cellbio.13.1.83

9 Evans, L., Mitchison, T. & Kirschner, M. Influence of the centrosome on the structure of nucleated microtubules. *J Cell Biol* **100**, 1185-1191 (1985). https://doi.org:10.1083/jcb.100.4.1185

10 Paul, D. M. *et al.* In situ cryo-electron tomography reveals filamentous actin within the microtubule lumen. *Journal of Cell Biology* **219** (2020). https://doi.org:10.1083/jcb.201911154

11 Schur, F. K. M. Toward high-resolution in situ structural biology with cryo-electron tomography and subtomogram averaging. *Current Opinion in Structural Biology* **58**, 1-9 (2019). https://doi.org:https://doi.org/10.1016/j.sbi.2019.03.018

12 Spiegelman, B. M., Penningroth, S. M. & Kirschner, M. W. Turnover of tubulin and the N site GTP in Chinese hamster ovary cells. *Cell* **12**, 587-600 (1977). https://doi.org:10.1016/0092-8674(77)90259-8

13 Mitchison, T. & Kirschner, M. Dynamic instability of microtubule growth. *Nature* **312**, 237-242 (1984). https://doi.org:10.1038/312237a0

14 Schuh, M. & Ellenberg, J. Self-organization of MTOCs replaces centrosome function during acentrosomal spindle assembly in live mouse oocytes. *Cell* **130**, 484-498 (2007). https://doi.org:10.1016/j.cell.2007.06.025

15 Almeida, A. C. & Maiato, H. Chromokinesins. *Curr Biol* **28**, R1131-r1135 (2018). https://doi.org:10.1016/j.cub.2018.07.017

16 Ross, J. L., Shuman, H., Holzbaur, E. L. & Goldman, Y. E. Kinesin and dynein-dynactin at intersecting microtubules: motor density affects dynein function. *Biophys J* **94**, 3115-3125 (2008). https://doi.org:10.1529/biophysj.107.120014

17 Cross, R. A. Kinesin-14: the roots of reversal. *BMC Biology* **8**, 107 (2010). https://doi.org:10.1186/1741-7007-8-107

18 Brieher, W. Mechanisms of actin disassembly. *Molecular Biology of the Cell* **24**, 2299-2302 (2013). https://doi.org:10.1091/mbc.e12-09-0694

19 Oosterheert, W., Klink, B. U., Belyy, A., Pospich, S. & Raunser, S. Structural basis of actin filament assembly and aging. *Nature* (2022). https://doi.org:10.1038/s41586-022-05241-8

20 Shekhar, S., Pernier, J. & Carlier, M.-F. Regulators of actin filament barbed ends at a glance. *Journal of Cell Science* **129**, 1085-1091 (2016). https://doi.org:10.1242/jcs.179994

21 Bretscher, A. Fimbrin is a cytoskeletal protein that crosslinks F-actin in vitro. *Proc Natl Acad Sci U S A* **78**, 6849-6853 (1981). https://doi.org:10.1073/pnas.78.11.6849
22 Goley, E. D. & Welch, M. D. The ARP2/3 complex: an actin nucleator comes of age. *Nature Reviews Molecular Cell Biology* **7**, 713-726 (2006). https://doi.org:10.1038/nrm2026
23 Wassarman, P. M. & Litscher, E. S. Female fertility and the zona pellucida. *Elife* **11** (2022). https://doi.org:10.7554/eLife.76106
24 Wang, Y. *et al.* Cyclic AMP in oocytes controls meiotic prophase I and primordial folliculogenesis in the perinatal mouse ovary. *Development* **142**, 343-351 (2015). https://doi.org:10.1242/dev.112755
25 Zhao, Y. *et al.* Current Understandings of Core Pathways for the Activation of Mammalian Primordial Follicles. *Cells* **10** (2021). https://doi.org:10.3390/cells10061491
26 He, M., Zhang, T., Yang, Y. & Wang, C. Mechanisms of Oocyte Maturation and Related Epigenetic Regulation. *Front Cell Dev Biol* **9**, 654028 (2021). https://doi.org:10.3389/fcell.2021.654028
27 Liu, M. The biology and dynamics of mammalian cortical granules. *Reproductive Biology and Endocrinology* **9**, 149 (2011). https://doi.org:10.1186/1477-7827-9-149
28 Mehlmann, L. M., Jones, T. L. & Jaffe, L. A. Meiotic arrest in the mouse follicle maintained by a Gs protein in the oocyte. *Science* **297**, 1343-1345 (2002). https://doi.org:10.1126/science.1073978
29 De La Fuente, R. & Eppig, J. J. Transcriptional activity of the mouse oocyte genome: companion granulosa cells modulate transcription and chromatin remodeling. *Dev Biol* **229**, 224-236 (2001). https://doi.org:10.1006/dbio.2000.9947
30 Zuccotti, M., Bellone, M., Longo, F., Redi, C. A. & Garagna, S. Fully-mature antral mouse oocytes are transcriptionally silent but their heterochromatin maintains a transcriptional permissive histone acetylation profile. *J Assist Reprod Genet* **28**, 1193-1196 (2011). https://doi.org:10.1007/s10815-011-9562-4
31 Grey, C. & de Massy, B. Chromosome Organization in Early Meiotic Prophase. *Front Cell Dev Biol* **9**, 688878 (2021). https://doi.org:10.3389/fcell.2021.688878
32 Borum, K. Oogenesis in the mouse. A study of the meiotic prophase. *Exp Cell Res* **24**, 495-507 (1961). https://doi.org:10.1016/0014-4827(61)90449-9
33 Wang, X. & Pepling, M. E. Regulation of Meiotic Prophase One in Mammalian Oocytes. *Front Cell Dev Biol* **9**, 667306 (2021). https://doi.org:10.3389/fcell.2021.667306
34 Hernández-Hernández, A. *et al.* The central element of the synaptonemal complex in mice is organized as a bilayered junction structure. *Journal of Cell Science* **129**, 2239-2249 (2016). https://doi.org:10.1242/jcs.182477
35 Kim, K. P. *et al.* Sister cohesion and structural axis components mediate homolog bias of meiotic recombination. *Cell* **143**, 924-937 (2010). https://doi.org:10.1016/j.cell.2010.11.015
36 Bolcun-Filas, E. & Schimenti, J. C. Genetics of meiosis and recombination in mice. *Int Rev Cell Mol Biol* **298**, 179-227 (2012). https://doi.org:10.1016/b978-0-12-394309-5.00005-5
37 Hartshorne, G. M., Lyrakou, S., Hamoda, H., Oloto, E. & Ghafari, F. Oogenesis and cell death in human prenatal ovaries: what are the criteria for oocyte selection? *Mol Hum Reprod* **15**, 805-819 (2009). https://doi.org:10.1093/molehr/gap055
38 Solc, P. *et al.* Multiple Requirements of PLK1 during Mouse Oocyte Maturation. *PLOS ONE* **10**, e0116783 (2015). https://doi.org:10.1371/journal.pone.0116783
39 Dultz, E. *et al.* Systematic kinetic analysis of mitotic dis- and reassembly of the nuclear pore in living cells. *Journal of Cell Biology* **180**, 857-865 (2008). https://doi.org:10.1083/jcb.200707026
40 Mogessie, B. & Schuh, M. Nuclear Envelope Breakdown: Actin' Quick to Tear Down the Wall. *Current Biology* **24**, R605-R607 (2014). https://doi.org:https://doi.org/10.1016/j.cub.2014.05.059

41 Gerace, L. & Blobel, G. The nuclear envelope lamina is reversibly depolymerized during mitosis. *Cell* **19**, 277-287 (1980). https://doi.org:https://doi.org/10.1016/0092-8674(80)90409-2
42 Beaudouin, J., Gerlich, D., Daigle, N., Eils, R. & Ellenberg, J. Nuclear Envelope Breakdown Proceeds by Microtubule-Induced Tearing of the Lamina. *Cell* **108**, 83-96 (2002). https://doi.org:https://doi.org/10.1016/S0092-8674(01)00627-4
43 Mori, M. *et al.* An Arp2/3 Nucleated F-Actin Shell Fragments Nuclear Membranes at Nuclear Envelope Breakdown in Starfish Oocytes. *Current Biology* **24**, 1421-1428 (2014). https://doi.org:https://doi.org/10.1016/j.cub.2014.05.019
44 Lénárt, P. *et al.* A contractile nuclear actin network drives chromosome congression in oocytes. *Nature* **436**, 812-818 (2005). https://doi.org:10.1038/nature03810
45 Scheffler, K., Giannini, F., Lemonnier, T. & Mogessie, B. The prophase oocyte nucleus is a homeostatic G-actin buffer. *J Cell Sci* **135** (2022). https://doi.org:10.1242/jcs.259807
46 Manandhar, G., Schatten, H. & Sutovsky, P. Centrosome reduction during gametogenesis and its significance. *Biol Reprod* **72**, 2-13 (2005). https://doi.org:10.1095/biolreprod.104.031245
47 So, C. *et al.* Mechanism of spindle pole organization and instability in human oocytes. *Science* **375**, eabj3944 (2022). https://doi.org:10.1126/science.abj3944
48 So, C. *et al.* A liquid-like spindle domain promotes acentrosomal spindle assembly in mammalian oocytes. *Science* **364** (2019). https://doi.org:10.1126/science.aat9557
49 Schuh, M. & Ellenberg, J. A new model for asymmetric spindle positioning in mouse oocytes. *Curr Biol* **18**, 1986-1992 (2008). https://doi.org:10.1016/j.cub.2008.11.022
50 Mogessie, B., Scheffler, K. & Schuh, M. Assembly and Positioning of the Oocyte Meiotic Spindle. *Annu Rev Cell Dev Biol* **34**, 381-403 (2018). https://doi.org:10.1146/annurev-cellbio-100616-060553
51 Clift, D. & Schuh, M. A three-step MTOC fragmentation mechanism facilitates bipolar spindle assembly in mouse oocytes. *Nat Commun* **6**, 7217 (2015). https://doi.org:10.1038/ncomms8217
52 Carazo-Salas, R. E. *et al.* Generation of GTP-bound Ran by RCC1 is required for chromatin-induced mitotic spindle formation. *Nature* **400**, 178-181 (1999). https://doi.org:10.1038/22133
53 Namgoong, S. & Kim, N.-H. Meiotic spindle formation in mammalian oocytes: implications for human infertility†. *Biology of Reproduction* **98**, 153-161 (2018). https://doi.org:10.1093/biolre/iox145
54 Loh, M. *et al.* Kinesin-1 promotes centrosome clustering and nuclear migration in the Drosophila oocyte. *bioRxiv*, 2022.2002.2016.480671 (2022). https://doi.org:10.1101/2022.02.16.480671
55 Krämer, A., Maier B Fau - Bartek, J. & Bartek, J. Centrosome clustering and chromosomal (in)stability: a matter of life and death.
56 Milunović-Jevtić, A., Mooney, P., Sulerud, T., Bisht, J. & Gatlin, J. C. Centrosomal clustering contributes to chromosomal instability and cancer.
57 Kitajima, T. S., Ohsugi, M. & Ellenberg, J. Complete kinetochore tracking reveals error-prone homologous chromosome biorientation in mammalian oocytes. *Cell* **146**, 568-581 (2011). https://doi.org:10.1016/j.cell.2011.07.031
58 Musacchio, A. & Desai, A. A Molecular View of Kinetochore Assembly and Function. *Biology (Basel)* **6** (2017). https://doi.org:10.3390/biology6010005
59 Dumont, M. *et al.* Human chromosome-specific aneuploidy is influenced by DNA-dependent centromeric features. *EMBO J* **39**, e102924 (2020). https://doi.org:10.15252/embj.2019102924
60 Umbreit, N. T. *et al.* The Ndc80 kinetochore complex directly modulates microtubule dynamics. *Proceedings of the National Academy of Sciences* **109**, 16113-16118 (2012). https://doi.org:doi:10.1073/pnas.1209615109
61 Kim, J. *et al.* Meikin is a conserved regulator of meiosis-I-specific kinetochore function. *Nature* **517**, 466-471 (2015). https://doi.org:10.1038/nature14097

62 FitzHarris, G. Anaphase B Precedes Anaphase A in the Mouse Egg. *Current Biology* **22**, 437-444 (2012). https://doi.org:https://doi.org/10.1016/j.cub.2012.01.041
63 Schmerler, S. & Wessel, G. M. Polar bodies--more a lack of understanding than a lack of respect. *Mol Reprod Dev* **78**, 3-8 (2011). https://doi.org:10.1002/mrd.21266
64 Ishiguro, K.-i. & Watanabe, Y. Chromosome cohesion in mitosis and meiosis. *Journal of Cell Science* **120**, 367-369 (2007). https://doi.org:10.1242/jcs.03324
65 Dorsett, D. & Merkenschlager, M. Cohesin at active genes: a unifying theme for cohesin and gene expression from model organisms to humans. *Current Opinion in Cell Biology* **25**, 327-333 (2013). https://doi.org:https://doi.org/10.1016/j.ceb.2013.02.003
66 Mannini, L. & Musio, A. The dark side of cohesin: The carcinogenic point of view. *Mutation Research/Reviews in Mutation Research* **728**, 81-87 (2011). https://doi.org:https://doi.org/10.1016/j.mrrev.2011.07.004
67 Mehta, G. D., Kumar, R., Srivastava, S. & Ghosh, S. K. Cohesin: Functions beyond sister chromatid cohesion. *FEBS Letters* **587**, 2299-2312 (2013). https://doi.org:https://doi.org/10.1016/j.febslet.2013.06.035
68 Mannini, L. *et al.* SMC1B is present in mammalian somatic cells and interacts with mitotic cohesin proteins. *Scientific Reports* **5**, 18472 (2015). https://doi.org:10.1038/srep18472
69 Brooker, A. S. & Berkowitz, K. M. The roles of cohesins in mitosis, meiosis, and human health and disease. *Methods Mol Biol* **1170**, 229-266 (2014). https://doi.org:10.1007/978-1-4939-0888-2_11
70 Winters, T., McNicoll, F. & Jessberger, R. Meiotic cohesin STAG3 is required for chromosome axis formation and sister chromatid cohesion. *EMBO J* **33**, 1256-1270 (2014). https://doi.org:10.1002/embj.201387330
71 Matityahu, A. & Onn, I. It's all in the numbers: Cohesin stoichiometry. *Front Mol Biosci* **9**, 1010894 (2022). https://doi.org:10.3389/fmolb.2022.1010894
72 El Yakoubi, W. *et al.* Mps1 kinase-dependent Sgo2 centromere localisation mediates cohesin protection in mouse oocyte meiosis I. *Nat Commun* **8**, 694 (2017). https://doi.org:10.1038/s41467-017-00774-3
73 Lee, J. *et al.* Unified mode of centromeric protection by shugoshin in mammalian oocytes and somatic cells. *Nat Cell Biol* **10**, 42-52 (2008). https://doi.org:10.1038/ncb1667
74 Lister, L. M. *et al.* Age-related meiotic segregation errors in mammalian oocytes are preceded by depletion of cohesin and Sgo2. *Curr Biol* **20**, 1511-1521 (2010). https://doi.org:10.1016/j.cub.2010.08.023
75 Xu, Z. *et al.* Structure and function of the PP2A-shugoshin interaction. *Mol Cell* **35**, 426-441 (2009). https://doi.org:10.1016/j.molcel.2009.06.031
76 Revenkova, E., Eijpe, M., Heyting, C., Gross, B. & Jessberger, R. Novel Meiosis-Specific Isoform of Mammalian SMC1. *Molecular and Cellular Biology* **21**, 6984-6998 (2001). https://doi.org:doi:10.1128/MCB.21.20.6984-6998.2001
77 Hirano, T. SMC protein complexes and higher-order chromosome dynamics. *Current Opinion in Cell Biology* **10**, 317-322 (1998). https://doi.org:https://doi.org/10.1016/S0955-0674(98)80006-9
78 Revenkova, E. *et al.* Cohesin SMC1β is required for meiotic chromosome dynamics, sister chromatid cohesion and DNA recombination. *Nature Cell Biology* **6**, 555-562 (2004). https://doi.org:10.1038/ncb1135
79 Schleiffer, A. *et al.* Kleisins: A Superfamily of Bacterial and Eukaryotic SMC Protein Partners. *Molecular Cell* **11**, 571-575 (2003). https://doi.org:https://doi.org/10.1016/S1097-2765(03)00108-4
80 Ishiguro, K. I. The cohesin complex in mammalian meiosis. *Genes Cells* **24**, 6-30 (2019). https://doi.org:10.1111/gtc.12652
81 Burkhardt, S. *et al.* Chromosome Cohesion Established by Rec8-Cohesin in Fetal Oocytes Is Maintained without Detectable Turnover in Oocytes Arrested for Months in Mice. *Curr Biol* **26**, 678-685 (2016). https://doi.org:10.1016/j.cub.2015.12.073

82 Kudo, N. R. *et al.* Role of cleavage by separase of the Rec8 kleisin subunit of cohesin during mammalian meiosis I. *J Cell Sci* **122**, 2686-2698 (2009). https://doi.org:10.1242/jcs.035287
83 Lee, J. & Hirano, T. RAD21L, a novel cohesin subunit implicated in linking homologous chromosomes in mammalian meiosis. *Journal of Cell Biology* **192**, 263-276 (2011). https://doi.org:10.1083/jcb.201008005
84 Ishiguro, K., Kim, J., Fujiyama-Nakamura, S., Kato, S. & Watanabe, Y. A new meiosis-specific cohesin complex implicated in the cohesin code for homologous pairing. *EMBO Rep* **12**, 267-275 (2011). https://doi.org:10.1038/embor.2011.2
85 Parra, M. a. T. *et al.* Involvement of the cohesin Rad21 and SCP3 in monopolar attachment of sister kinetochores during mouse meiosis I. *Journal of Cell Science* **117**, 1221-1234 (2004). https://doi.org:10.1242/jcs.00947
86 Xu, H. *et al.* A new role for the mitotic RAD21/SCC1 cohesin in meiotic chromosome cohesion and segregation in the mouse. *EMBO Rep* **5**, 378-384 (2004). https://doi.org:10.1038/sj.embor.7400121
87 Fukuda, T. *et al.* STAG3-mediated stabilization of REC8 cohesin complexes promotes chromosome synapsis during meiosis. *Embo j* **33**, 1243-1255 (2014). https://doi.org:10.1002/embj.201387329
88 Makrantoni, V. & Marston, A. L. Cohesin and chromosome segregation. *Curr Biol* **28**, R688-r693 (2018). https://doi.org:10.1016/j.cub.2018.05.019
89 Kuleszewicz, K., Fu, X. & Kudo, N. Cohesin loading factor Nipbl localizes to chromosome axes during mammalian meiotic prophase. *Cell division* **8**, 12 (2013). https://doi.org:10.1186/1747-1028-8-12
90 Parenti, I. *et al.* MAU2 and NIPBL Variants Impair the Heterodimerization of the Cohesin Loader Subunits and Cause Cornelia de Lange Syndrome. *Cell Rep* **31**, 107647 (2020). https://doi.org:10.1016/j.celrep.2020.107647
91 Hinshaw, S. M., Makrantoni, V., Harrison, S. C. & Marston, A. L. The Kinetochore Receptor for the Cohesin Loading Complex. *Cell* **171**, 72-84.e13 (2017). https://doi.org:10.1016/j.cell.2017.08.017
92 Vallot, A. *et al.* Tension-Induced Error Correction and Not Kinetochore Attachment Status Activates the SAC in an Aurora-B/C-Dependent Manner in Oocytes. *Curr Biol* **28**, 130-139 e133 (2018). https://doi.org:10.1016/j.cub.2017.11.049
93 Musacchio, A. & Salmon, E. D. The spindle-assembly checkpoint in space and time. *Nature Reviews Molecular Cell Biology* **8**, 379-393 (2007). https://doi.org:10.1038/nrm2163
94 Wengner, A. M. *et al.* Novel Mps1 Kinase Inhibitors with Potent Antitumor Activity. *Mol Cancer Ther* **15**, 583-592 (2016). https://doi.org:10.1158/1535-7163.Mct-15-0500
95 Rattani, A. *et al.* Sgol2 provides a regulatory platform that coordinates essential cell cycle processes during meiosis I in oocytes. *Elife* **2**, e01133 (2013). https://doi.org:10.7554/eLife.01133
96 Clift, D., Bizzari, F. & Marston, A. L. Shugoshin prevents cohesin cleavage by PP2A(Cdc55)-dependent inhibition of separase. *Genes Dev* **23**, 766-780 (2009). https://doi.org:10.1101/gad.507509
97 Duncan, F. E. *et al.* Chromosome cohesion decreases in human eggs with advanced maternal age. *Aging Cell* **11**, 1121-1124 (2012). https://doi.org:10.1111/j.1474-9726.2012.00866.x
98 Ishiguro, K. & Watanabe, Y. Chromosome cohesion in mitosis and meiosis. *J Cell Sci* **120**, 367-369 (2007). https://doi.org:10.1242/jcs.03324
99 Clift, D. & Marston, A. L. The role of shugoshin in meiotic chromosome segregation. *Cytogenet Genome Res* **133**, 234-242 (2011). https://doi.org:10.1159/000323793
100 Clift, D. & Schuh, M. Restarting life: fertilization and the transition from meiosis to mitosis. *Nature Reviews Molecular Cell Biology* **14**, 549-562 (2013). https://doi.org:10.1038/nrm3643
101 Wassarman, P. M. & Litscher, E. S. Mammalian fertilization: the egg's multifunctional zona pellucida. *Int J Dev Biol* **52**, 665-676 (2008). https://doi.org:10.1387/ijdb.072524pw

102 Wassarman, P. M., Jovine, L. & Litscher, E. S. A profile of fertilization in mammals. *Nature Cell Biology* **3**, E59-E64 (2001). https://doi.org:10.1038/35055178
103 Bianchi, E. & Wright, G. J. Sperm Meets Egg: The Genetics of Mammalian Fertilization. *Annual Review of Genetics* **50**, 93-111 (2016). https://doi.org:10.1146/annurev-genet-121415-121834
104 Scheffler, K. *et al.* Two mechanisms drive pronuclear migration in mouse zygotes. *Nature Communications* **12**, 841 (2021). https://doi.org:10.1038/s41467-021-21020-x
105 Reichmann, J. *et al.* Dual-spindle formation in zygotes keeps parental genomes apart in early mammalian embryos. *Science* **361**, 189-193 (2018). https://doi.org:doi:10.1126/science.aar7462
106 Schatten, G., Simerly, C. & Schatten, H. Microtubule configurations during fertilization, mitosis, and early development in the mouse and the requirement for egg microtubule-mediated motility during mammalian fertilization. *Proceedings of the National Academy of Sciences* **82**, 4152-4156 (1985). https://doi.org:doi:10.1073/pnas.82.12.4152
107 Holubcová, Z., Howard, G. & Schuh, M. Vesicles modulate an actin network for asymmetric spindle positioning. *Nature Cell Biology* **15**, 937-947 (2013). https://doi.org:10.1038/ncb2802
108 Pfender, S., Kuznetsov, V., Pleiser, S., Kerkhoff, E. & Schuh, M. Spire-Type Actin Nucleators Cooperate with Formin-2 to Drive Asymmetric Oocyte Division. *Current Biology* **21**, 955-960 (2011). https://doi.org:10.1016/j.cub.2011.04.029
109 Courtois, A., Schuh, M., Ellenberg, J. & Hiiragi, T. The transition from meiotic to mitotic spindle assembly is gradual during early mammalian development. *Journal of Cell Biology* **198**, 357-370 (2012). https://doi.org:10.1083/jcb.201202135
110 Chaigne, A. *et al.* F-actin mechanics control spindle centring in the mouse zygote. *Nature Communications* **7**, 10253 (2016). https://doi.org:10.1038/ncomms10253
111 SZOLLOSI, D., CALARCO, P. & DONAHUE, R. P. Absence of Centrioles in the First and Second Meiotic Spindles of Mouse Oocytes. *Journal of Cell Science* **11**, 521-541 (1972). https://doi.org:10.1242/jcs.11.2.521
112 Hertig, A. T. & Adams, E. C. Studies on the human oocyte and its follicle. I. Ultrastructural and histochemical observations on the primordial follicle stage. *J Cell Biol* **34**, 647-675 (1967). https://doi.org:10.1083/jcb.34.2.647
113 Pimenta-Marques, A. *et al.* A mechanism for the elimination of the female gamete centrosome in Drosophila melanogaster. *Science* **353**, aaf4866 (2016). https://doi.org:10.1126/science.aaf4866
114 Mikeladze-Dvali, T. *et al.* Analysis of centriole elimination during C. elegans oogenesis. *Development* **139**, 1670-1679 (2012). https://doi.org:10.1242/dev.075440
115 Manandhar, G., Sutovsky, P., Joshi, H. C., Stearns, T. & Schatten, G. Centrosome reduction during mouse spermiogenesis. *Dev Biol* **203**, 424-434 (1998). https://doi.org:10.1006/dbio.1998.8947
116 Gueth-Hallonet, C. *et al.* gamma-Tubulin is present in acentriolar MTOCs during early mouse development. *J Cell Sci* **105 (Pt 1)**, 157-166 (1993). https://doi.org:10.1242/jcs.105.1.157
117 Cheng, S. *et al.* Mammalian oocytes store mRNAs in a mitochondria-associated membraneless compartment. *Science* **378**, eabq4835 (2022). https://doi.org:doi:10.1126/science.abq4835
118 Oh, B., Hwang, S., McLaughlin, J., Solter, D. & Knowles, B. B. Timely translation during the mouse oocyte-to-embryo transition. *Development* **127**, 3795-3803 (2000). https://doi.org:10.1242/dev.127.17.3795
119 Chen, J. *et al.* Genome-wide analysis of translation reveals a critical role for deleted in azoospermia-like (Dazl) at the oocyte-to-zygote transition. *Genes Dev* **25**, 755-766 (2011). https://doi.org:10.1101/gad.2028911
120 Pikó, L. & Clegg, K. B. Quantitative changes in total RNA, total poly(A), and ribosomes in early mouse embryos. *Dev Biol* **89**, 362-378 (1982). https://doi.org:10.1016/0012-1606(82)90325-6

121 Medvedev, S., Pan, H. & Schultz, R. M. Absence of MSY2 in mouse oocytes perturbs oocyte growth and maturation, RNA stability, and the transcriptome. *Biol Reprod* **85**, 575-583 (2011). https://doi.org:10.1095/biolreprod.111.091710
122 Medvedev, S., Yang, J., Hecht, N. B. & Schultz, R. M. CDC2A (CDK1)-mediated phosphorylation of MSY2 triggers maternal mRNA degradation during mouse oocyte maturation. *Developmental Biology* **321**, 205-215 (2008). https://doi.org:https://doi.org/10.1016/j.ydbio.2008.06.016
123 Hamatani, T., Carter, M. G., Sharov, A. A. & Ko, M. S. Dynamics of global gene expression changes during mouse preimplantation development. *Dev Cell* **6**, 117-131 (2004). https://doi.org:10.1016/s1534-5807(03)00373-3
124 Bultman, S. J. *et al.* Maternal BRG1 regulates zygotic genome activation in the mouse. *Genes Dev* **20**, 1744-1754 (2006). https://doi.org:10.1101/gad.1435106
125 Uraji, J., Scheffler, K. & Schuh, M. Functions of actin in mouse oocytes at a glance. *J Cell Sci* **131** (2018). https://doi.org:10.1242/jcs.218099
126 Azoury, J. *et al.* Spindle positioning in mouse oocytes relies on a dynamic meshwork of actin filaments. *Curr Biol* **18**, 1514-1519 (2008). https://doi.org:10.1016/j.cub.2008.08.044
127 Schuh, M. An actin-dependent mechanism for long-range vesicle transport. *Nature Cell Biology* **13**, 1431-1436 (2011). https://doi.org:10.1038/ncb2353
128 Cheeseman, L. P., Boulanger, J., Bond, L. M. & Schuh, M. Two pathways regulate cortical granule translocation to prevent polyspermy in mouse oocytes. *Nature Communications* **7**, 13726 (2016). https://doi.org:10.1038/ncomms13726
129 Almonacid, M. *et al.* Active diffusion positions the nucleus in mouse oocytes. *Nat Cell Biol* **17**, 470-479 (2015). https://doi.org:10.1038/ncb3131
130 Azoury, J., Lee, K. W., Georget, V., Hikal, P. & Verlhac, M.-H. Symmetry breaking in mouse oocytes requires transient F-actin meshwork destabilization. *Development* **138**, 2903-2908 (2011). https://doi.org:10.1242/dev.060269
131 Caridi, C. P., Plessner, M., Grosse, R. & Chiolo, I. Nuclear actin filaments in DNA repair dynamics. *Nature Cell Biology* **21**, 1068-1077 (2019). https://doi.org:10.1038/s41556-019-0379-1
132 Plessner, M., Knerr, J. & Grosse, R. Centrosomal Actin Assembly Is Required for Proper Mitotic Spindle Formation and Chromosome Congression. *iScience* **15**, 274-281 (2019). https://doi.org:10.1016/j.isci.2019.04.022
133 Belin, B. J., Lee, T. & Mullins, R. D. DNA damage induces nuclear actin filament assembly by Formin -2 and Spire-(1/2) that promotes efficient DNA repair. [corrected]. *Elife* **4**, e07735 (2015). https://doi.org:10.7554/eLife.07735
134 Mogessie, B. Visualization and Functional Analysis of Spindle Actin and Chromosome Segregation in Mammalian Oocytes. *Methods Mol Biol* **2101**, 267-295 (2020). https://doi.org:10.1007/978-1-0716-0219-5_17
135 Dunkley, S., Scheffler, K. & Mogessie, B. Cytoskeletal form and function in mammalian oocytes and zygotes. *Curr Opin Cell Biol* **75**, 102073 (2022). https://doi.org:10.1016/j.ceb.2022.02.007
136 Kotak, S. & Gönczy, P. Mechanisms of spindle positioning: cortical force generators in the limelight. *Current Opinion in Cell Biology* **25**, 741-748 (2013). https://doi.org:https://doi.org/10.1016/j.ceb.2013.07.008
137 Li, H., Guo, F., Rubinstein, B. & Li, R. Actin-driven chromosomal motility leads to symmetry breaking in mammalian meiotic oocytes. *Nature Cell Biology* **10**, 1301-1308 (2008). https://doi.org:10.1038/ncb1788
138 Yi, K. *et al.* Sequential actin-based pushing forces drive meiosis I chromosome migration and symmetry breaking in oocytes. *Journal of Cell Biology* **200**, 567-576 (2013). https://doi.org:10.1083/jcb.201211068
139 Runge, K. E. *et al.* Oocyte CD9 is enriched on the microvillar membrane and required for normal microvillar shape and distribution. *Developmental Biology* **304**, 317-325 (2007). https://doi.org:https://doi.org/10.1016/j.ydbio.2006.12.041

140 Longo, F. J. & Chen, D.-Y. Development of cortical polarity in mouse eggs: Involvement of the meiotic apparatus. *Developmental Biology* **107**, 382-394 (1985). https://doi.org:https://doi.org/10.1016/0012-1606(85)90320-3
141 Luo, J., McGinnis, L. K. & Kinsey, W. H. Fyn kinase activity is required for normal organization and functional polarity of the mouse oocyte cortex. *Molecular Reproduction and Development* **76**, 819-831 (2009). https://doi.org:https://doi.org/10.1002/mrd.21034
142 Deng, M., Suraneni, P., Schultz, R. M. & Li, R. The Ran GTPase Mediates Chromatin Signaling to Control Cortical Polarity during Polar Body Extrusion in Mouse Oocytes. *Developmental Cell* **12**, 301-308 (2007). https://doi.org:10.1016/j.devcel.2006.11.008
143 Dumont , J. *et al.* A centriole- and RanGTP-independent spindle assembly pathway in meiosis I of vertebrate oocytes. *Journal of Cell Biology* **176**, 295-305 (2007). https://doi.org:10.1083/jcb.200605199
144 Simerly, C., Nowak, G., Lanerolle, P. d. & Schatten, G. Differential Expression and Functions of Cortical Myosin IIA and IIB Isotypes during Meiotic Maturation, Fertilization, and Mitosis in Mouse Oocytes and Embryos. *Molecular Biology of the Cell* **9**, 2509-2525 (1998). https://doi.org:10.1091/mbc.9.9.2509
145 Dumont, J. *et al.* Formin-2 is required for spindle migration and for the late steps of cytokinesis in mouse oocytes. *Dev Biol* **301**, 254-265 (2007). https://doi.org:10.1016/j.ydbio.2006.08.044
146 Sun, S.-C. *et al.* Arp2/3 Complex Regulates Asymmetric Division and Cytokinesis in Mouse Oocytes. *PLOS ONE* **6**, e18392 (2011). https://doi.org:10.1371/journal.pone.0018392
147 Dehapiot, B., Carrière, V., Carroll, J. & Halet, G. Polarized Cdc42 activation promotes polar body protrusion and asymmetric division in mouse oocytes. *Developmental Biology* **377**, 202-212 (2013). https://doi.org:https://doi.org/10.1016/j.ydbio.2013.01.029
148 Elbaz, J., Reizel, Y., Nevo, N., Galiani, D. & Dekel, N. Epithelial Cell Transforming Protein 2 (ECT2) Depletion Blocks Polar Body Extrusion and Generates Mouse Oocytes Containing Two Metaphase II Spindles. *Endocrinology* **151**, 755-765 (2010). https://doi.org:10.1210/en.2009-0830
149 Liu, L., Trimarchi, J. R., Oldenbourg, R. & Keefe, D. L. Increased Birefringence in the Meiotic Spindle Provides a New Marker for the Onset of Activation in Living Oocytes1. *Biology of Reproduction* **63**, 251-258 (2000). https://doi.org:10.1095/biolreprod63.1.251
150 Maro, B., Johnson, M. H., Pickering, S. J. & Flach, G. Changes in actin distribution during fertilization of the mouse egg. *J Embryol Exp Morphol* **81**, 211-237 (1984).
151 Yi, K. *et al.* Dynamic maintenance of asymmetric meiotic spindle position through Arp2/3-complex-driven cytoplasmic streaming in mouse oocytes. *Nature Cell Biology* **13**, 1252-1258 (2011). https://doi.org:10.1038/ncb2320
152 Mogessie, B. & Schuh, M. Actin protects mammalian eggs against chromosome segregation errors. *Science* **357** (2017). https://doi.org:10.1126/science.aal1647
153 Schliwa, M. Action of Cytochalasin D on Cytoskeletal Networks. *J. Cell Biology* **92**, 79-91 (1982).
154 Wakatsuki, T., Schwab, B., Thompson, N. C. & Elson, E. L. Effects of cytochalasin D and latrunculin B on mechanical properties of cells. *J Cell Sci* **114**, 1025-1036 (2001).
155 Maiato, H. *et al.* Human CLASP1 Is an Outer Kinetochore Component that Regulates Spindle Microtubule Dynamics. *Cell* **113**, 891-904 (2003). https://doi.org:https://doi.org/10.1016/S0092-8674(03)00465-3
156 Lukinavicius, G. *et al.* Fluorogenic probes for live-cell imaging of the cytoskeleton. *Nat Methods* **11**, 731-733 (2014). https://doi.org:10.1038/nmeth.2972
157 Roeles, J. & Tsiavaliaris, G. Actin-microtubule interplay coordinates spindle assembly in human oocytes. *Nat Commun* **10**, 4651 (2019). https://doi.org:10.1038/s41467-019-12674-9

158 Herbert, M., Kalleas, D., Cooney, D., Lamb, M. & Lister, L. Meiosis and maternal aging: insights from aneuploid oocytes and trisomy births. *Cold Spring Harb Perspect Biol* **7**, a017970 (2015). https://doi.org:10.1101/cshperspect.a017970
159 Antonarakis, S. E., Lyle, R., Dermitzakis, E. T., Reymond, A. & Deutsch, S. Chromosome 21 and down syndrome: from genomics to pathophysiology. *Nat Rev Genet* **5**, 725-738 (2004). https://doi.org:10.1038/nrg1448
160 Nagaoka, S. I., Hassold, T. J. & Hunt, P. A. Human aneuploidy: mechanisms and new insights into an age-old problem. *Nat Rev Genet* **13**, 493-504 (2012). https://doi.org:10.1038/nrg3245
161 Wartosch, L. *et al.* Origins and mechanisms leading to aneuploidy in human eggs. *Prenat Diagn* **41**, 620-630 (2021). https://doi.org:10.1002/pd.5927
162 Holubcová, Z., Blayney, M., Elder, K. & Schuh, M. Error-prone chromosome-mediated spindle assembly favors chromosome segregation defects in human oocytes. *Science* **348**, 1143-1147 (2015). https://doi.org:doi:10.1126/science.aaa9529
163 Vallardi, G., Cordeiro, M. H. & Saurin, A. T. A Kinase-Phosphatase Network that Regulates Kinetochore-Microtubule Attachments and the SAC. *Prog Mol Subcell Biol* **56**, 457-484 (2017). https://doi.org:10.1007/978-3-319-58592-5_19
164 Herbert, M. *et al.* Homologue disjunction in mouse oocytes requires proteolysis of securin and cyclin B1. *Nat Cell Biol* **5**, 1023-1025 (2003). https://doi.org:10.1038/ncb1062
165 Kuhn, J. & Dumont, S. Mammalian kinetochores count attached microtubules in a sensitive and switch-like manner. *J Cell Biol* **218**, 3583-3596 (2019). https://doi.org:10.1083/jcb.201902105
166 Nagaoka, S. I., Hodges, C. A., Albertini, D. F. & Hunt, P. A. Oocyte-specific differences in cell-cycle control create an innate susceptibility to meiotic errors. *Curr Biol* **21**, 651-657 (2011). https://doi.org:10.1016/j.cub.2011.03.003
167 Gui, L. & Homer, H. Spindle assembly checkpoint signalling is uncoupled from chromosomal position in mouse oocytes. *Development* **139**, 1941-1946 (2012). https://doi.org:10.1242/dev.078352
168 Kolano, A., Brunet, S., Silk, A. D., Cleveland, D. W. & Verlhac, M.-H. Error-prone mammalian female meiosis from silencing the spindle assembly checkpoint without normal interkinetochore tension. *Proceedings of the National Academy of Sciences* **109**, E1858-E1867 (2012). https://doi.org:doi:10.1073/pnas.1204686109
169 Lane, S. I. & Jones, K. T. Non-canonical function of spindle assembly checkpoint proteins after APC activation reduces aneuploidy in mouse oocytes. *Nat Commun* **5**, 3444 (2014). https://doi.org:10.1038/ncomms4444
170 Sebestova, J., Danylevska, A., Novakova, L., Kubelka, M. & Anger, M. Lack of response to unaligned chromosomes in mammalian female gametes. *Cell Cycle* **11**, 3011-3018 (2012). https://doi.org:10.4161/cc.21398
171 Kouznetsova, A., Lister, L., Nordenskjöld, M., Herbert, M. & Höög, C. Bi-orientation of achiasmatic chromosomes in meiosis I oocytes contributes to aneuploidy in mice. *Nature Genetics* **39**, 966-968 (2007). https://doi.org:10.1038/ng2065
172 Bukovsky, A., Caudle, M. R., Svetlikova, M. & Upadhyaya, N. B. Origin of germ cells and formation of new primary follicles in adult human ovaries. *Reproductive Biology and Endocrinology* **2**, 20 (2004). https://doi.org:10.1186/1477-7827-2-20
173 Vidal, J. D. & Dixon, D. in *Boorman's Pathology of the Rat (Second Edition)* (ed Andrew W. Suttie) 523-536 (Academic Press, 2018).
174 Chiang, T., Duncan, F. E., Schindler, K., Schultz, R. M. & Lampson, M. A. Evidence that weakened centromere cohesion is a leading cause of age-related aneuploidy in oocytes. *Curr Biol* **20**, 1522-1528 (2010). https://doi.org:10.1016/j.cub.2010.06.069
175 Shomper, M., Lappa, C. & FitzHarris, G. Kinetochore microtubule establishment is defective in oocytes from aged mice. *Cell Cycle* **13**, 1171-1179 (2014). https://doi.org:10.4161/cc.28046
176 Zielinska, A. P., Holubcova, Z., Blayney, M., Elder, K. & Schuh, M. Sister kinetochore splitting and precocious disintegration of bivalents could explain the maternal age effect. *Elife* **4**, e11389 (2015). https://doi.org:10.7554/eLife.11389

177 Penrose, L. S. The relative effects of paternal and maternal age in mongolism. *Journal of Genetics* **27**, 219-224 (1933). https://doi.org:10.1007/BF02984413
178 Chiang, T., Schultz, R. M. & Lampson, M. A. Age-dependent susceptibility of chromosome cohesion to premature separase activation in mouse oocytes. *Biol Reprod* **85**, 1279-1283 (2011). https://doi.org:10.1095/biolreprod.111.094094
179 Nakagawa, S. & FitzHarris, G. Intrinsically Defective Microtubule Dynamics Contribute to Age-Related Chromosome Segregation Errors in Mouse Oocyte Meiosis-I. *Curr Biol* **27**, 1040-1047 (2017). https://doi.org:10.1016/j.cub.2017.02.025
180 Mihajlovic, A. I., Haverfield, J. & FitzHarris, G. Distinct classes of lagging chromosome underpin age-related oocyte aneuploidy in mouse. *Dev Cell* **56**, 2273-2283 e2273 (2021). https://doi.org:10.1016/j.devcel.2021.07.022
181 Serebryannyy, L. A., Yuen, M., Parilla, M., Cooper, S. T. & de Lanerolle, P. The Effects of Disease Models of Nuclear Actin Polymerization on the Nucleus. *Front Physiol* **7**, 454 (2016). https://doi.org:10.3389/fphys.2016.00454
182 Mogessie, B. Advances and surprises in a decade of oocyte meiosis research. *Essays in Biochemistry* **64**, 263-275 (2020). https://doi.org:10.1042/ebc20190068
183 Yano, K. *et al.* Chemical zona pellucida thinning with acidified Tyrode's solution: comparison between partial and circumferential techniques. *J Assist Reprod Genet* **24**, 471-475 (2007). https://doi.org:10.1007/s10815-007-9131-z
184 Silva, M. C. C., Wutz, G., Tachibana, K. & Peters, J. M. Analysis of chromosomes from mouse oocytes and mammalian cultured cells by light microscopy. *Methods Cell Biol* **144**, 287-305 (2018). https://doi.org:10.1016/bs.mcb.2018.03.015
185 Huff, J. The Airyscan detector from ZEISS: confocal imaging with improved signal-to-noise ratio and super-resolution. *Nature Methods* **12**, i-ii (2015). https://doi.org:10.1038/nmeth.f.388
186 Schindelin, J. *et al.* Fiji: an open-source platform for biological-image analysis. *Nat Methods* **9**, 676-682 (2012). https://doi.org:10.1038/nmeth.2019
187 Schneider, C. A., Rasband, W. S. & Eliceiri, K. W. NIH Image to ImageJ: 25 years of image analysis. *Nat Methods* **9**, 671-675 (2012). https://doi.org:10.1038/nmeth.2089
188 Coelho, P. A. *et al.* Dual role of topoisomerase II in centromere resolution and aurora B activity. *PLoS Biol* **6**, e207 (2008). https://doi.org:10.1371/journal.pbio.0060207
189 Mogessie, B., Roth, D., Rahil, Z. & Straube, A. A novel isoform of MAP4 organises the paraxial microtubule array required for muscle cell differentiation. *Elife* **4**, e05697 (2015). https://doi.org:10.7554/eLife.05697
190 Dogterom, M. & Koenderink, G. H. Actin-microtubule crosstalk in cell biology. *Nat Rev Mol Cell Biol* **20**, 38-54 (2019). https://doi.org:10.1038/s41580-018-0067-1
191 Sandquist, J. C., Kita, A. M. & Bement, W. M. And the dead shall rise: actin and myosin return to the spindle. *Dev Cell* **21**, 410-419 (2011). https://doi.org:10.1016/j.devcel.2011.07.018
192 Margaron, Y., Fradet, N. & Cote, J. F. ELMO recruits actin cross-linking family 7 (ACF7) at the cell membrane for microtubule capture and stabilization of cellular protrusions. *J Biol Chem* **288**, 1184-1199 (2013). https://doi.org:10.1074/jbc.M112.431825
193 Jolly, A. L. *et al.* Kinesin-1 heavy chain mediates microtubule sliding to drive changes in cell shape. *Proc Natl Acad Sci U S A* **107**, 12151-12156 (2010). https://doi.org:10.1073/pnas.1004736107
194 Lancaster, O. M. *et al.* Mitotic rounding alters cell geometry to ensure efficient bipolar spindle formation. *Dev Cell* **25**, 270-283 (2013). https://doi.org:10.1016/j.devcel.2013.03.014
195 Forer, R. V. S.-G. a. A. Evidence that actin and myosin are involved in the poleward flux of tubulin in metaphase kinetochore microtubules of crane-fly spermatocytes. *Journal of Cell Science* **113**, 597-609 (2000).
196 Nair, U. B. *et al.* Crystal structures of monomeric actin bound to cytochalasin D. *J Mol Biol* **384**, 848-864 (2008). https://doi.org:10.1016/j.jmb.2008.09.082
197 Wallin, M. & Strömberg, E. in *International Review of Cytology* Vol. 157 (eds Kwang W. Jeon & Jonathan Jarvik) 1-31 (Academic Press, 1995).

198 Eot-Houllier, G. *et al.* Aurora A-dependent CENP-A phosphorylation at inner centromeres protects bioriented chromosomes against cohesion fatigue. *Nat Commun* **9**, 1888 (2018). https://doi.org:10.1038/s41467-018-04089-9
199 Santaguida, S., Tighe, A., D'Alise, A. M., Taylor, S. S. & Musacchio, A. Dissecting the role of MPS1 in chromosome biorientation and the spindle checkpoint through the small molecule inhibitor reversine. *J Cell Biol* **190**, 73-87 (2010). https://doi.org:10.1083/jcb.201001036
200 Clift, D. *et al.* A Method for the Acute and Rapid Degradation of Endogenous Proteins. *Cell* **171**, 1692-1706 e1618 (2017). https://doi.org:10.1016/j.cell.2017.10.033
201 Rhodes, D. A. & Isenberg, D. A. TRIM21 and the Function of Antibodies inside Cells. *Trends Immunol* **38**, 916-926 (2017). https://doi.org:10.1016/j.it.2017.07.005
202 Richter, J. D. & Lasko, P. Translational control in oocyte development. *Cold Spring Harb Perspect Biol* **3**, a002758 (2011). https://doi.org:10.1101/cshperspect.a002758
203 Holzinger, A. in *Cytoskeleton Methods and Protocols* (ed Ray H. Gavin) 71-87 (Humana Press, 2010).
204 Asbury, C. L., Gestaut, D. R., Powers, A. F., Franck, A. D. & Davis, T. N. The Dam1 kinetochore complex harnesses microtubule dynamics to produce force and movement. *Proc Natl Acad Sci U S A* **103**, 9873-9878 (2006). https://doi.org:10.1073/pnas.0602249103
205 Daum, J. R. *et al.* Ska3 is required for spindle checkpoint silencing and the maintenance of chromosome cohesion in mitosis. *Curr Biol* **19**, 1467-1472 (2009). https://doi.org:10.1016/j.cub.2009.07.017
206 Gaitanos, T. N. *et al.* Stable kinetochore-microtubule interactions depend on the Ska complex and its new component Ska3/C13Orf3. *Embo j* **28**, 1442-1452 (2009). https://doi.org:10.1038/emboj.2009.96
207 Grishchuk, E. L. *et al.* The Dam1 ring binds microtubules strongly enough to be a processive as well as energy-efficient coupler for chromosome motion. *Proc Natl Acad Sci U S A* **105**, 15423-15428 (2008). https://doi.org:10.1073/pnas.0807859105
208 Lampert, F., Hornung, P. & Westermann, S. The Dam1 complex confers microtubule plus end-tracking activity to the Ndc80 kinetochore complex. *J Cell Biol* **189**, 641-649 (2010). https://doi.org:10.1083/jcb.200912021
209 Powers, A. F. *et al.* The Ndc80 kinetochore complex forms load-bearing attachments to dynamic microtubule tips via biased diffusion. *Cell* **136**, 865-875 (2009). https://doi.org:10.1016/j.cell.2008.12.045
210 Schmidt, J. C. *et al.* The kinetochore-bound Ska1 complex tracks depolymerizing microtubules and binds to curved protofilaments. *Dev Cell* **23**, 968-980 (2012). https://doi.org:10.1016/j.devcel.2012.09.012
211 Umbreit, N. T. *et al.* Kinetochores require oligomerization of Dam1 complex to maintain microtubule attachments against tension and promote biorientation. *Nat Commun* **5**, 4951 (2014). https://doi.org:10.1038/ncomms5951
212 Volkov, V. A. *et al.* Long tethers provide high-force coupling of the Dam1 ring to shortening microtubules. *Proc Natl Acad Sci U S A* **110**, 7708-7713 (2013). https://doi.org:10.1073/pnas.1305821110
213 Welburn, J. P. *et al.* The human kinetochore Ska1 complex facilitates microtubule depolymerization-coupled motility. *Dev Cell* **16**, 374-385 (2009). https://doi.org:10.1016/j.devcel.2009.01.011
214 Westermann, S. *et al.* The Dam1 kinetochore ring complex moves processively on depolymerizing microtubule ends. *Nature* **440**, 565-569 (2006). https://doi.org:10.1038/nature04409
215 Drummond, D. R. & Cross, R. A. Dynamics of interphase microtubules in Schizosaccharomyces pombe. *Curr Biol* **10**, 766-775 (2000). https://doi.org:10.1016/s0960-9822(00)00570-4
216 Tran, P. T., Marsh, L., Doye, V., Inoué, S. & Chang, F. A mechanism for nuclear positioning in fission yeast based on microtubule pushing. *J Cell Biol* **153**, 397-411 (2001). https://doi.org:10.1083/jcb.153.2.397

217 Garzon-Coral, C., Fantana, H. A. & Howard, J. A force-generating machinery maintains the spindle at the cell center during mitosis. *Science* **352**, 1124-1127 (2016). https://doi.org:10.1126/science.aad9745
218 Georgatos, S. D., Pyrpasopoulou, A. & Theodoropoulos, P. A. Nuclear envelope breakdown in mammalian cells involves stepwise lamina disassembly and microtubule-drive deformation of the nuclear membrane. *J Cell Sci* **110 (Pt 17)**, 2129-2140 (1997). https://doi.org:10.1242/jcs.110.17.2129
219 Goldberg, D. J. & Burmeister, D. W. Microtubule-based filopodium-like protrusions form after axotomy. *J Neurosci* **12**, 4800-4807 (1992). https://doi.org:10.1523/jneurosci.12-12-04800.1992
220 Gerlitz, G., Reiner, O. & Bustin, M. Microtubule dynamics alter the interphase nucleus. *Cell Mol Life Sci* **70**, 1255-1268 (2013). https://doi.org:10.1007/s00018-012-1200-5
221 Mullins, R. D. & Pollard, T. D. Structure and function of the Arp2/3 complex. *Curr Opin Struct Biol* **9**, 244-249 (1999). https://doi.org:10.1016/s0959-440x(99)80034-7
222 Pimm, M. L. & Henty-Ridilla, J. L. New twists in actin-microtubule interactions. *Mol Biol Cell* **32**, 211-217 (2021). https://doi.org:10.1091/mbc.E19-09-0491
223 Farina, F. *et al.* The centrosome is an actin-organizing centre. *Nat Cell Biol* **18**, 65-75 (2016). https://doi.org:10.1038/ncb3285
224 Farina, F. *et al.* Local actin nucleation tunes centrosomal microtubule nucleation during passage through mitosis. *EMBO J* **38** (2019). https://doi.org:10.15252/embj.201899843
225 Inoue, D. *et al.* Actin filaments regulate microtubule growth at the centrosome. *Embo j* **38** (2019). https://doi.org:10.15252/embj.201899630
226 Inoue, D. *et al.* Actin filaments regulate microtubule growth at the centrosome. *EMBO J* **38** (2019). https://doi.org:10.15252/embj.201899630
227 Hauf, S. & Watanabe, Y. Kinetochore orientation in mitosis and meiosis. *Cell* **119**, 317-327 (2004). https://doi.org:10.1016/j.cell.2004.10.014
228 Kruger, A. N. & Mueller, J. L. Mechanisms of meiotic drive in symmetric and asymmetric meiosis. *Cell Mol Life Sci* **78**, 3205-3218 (2021). https://doi.org:10.1007/s00018-020-03735-0
229 Akera, T., Trimm, E. & Lampson, M. A. Molecular Strategies of Meiotic Cheating by Selfish Centromeres. *Cell* **178**, 1132-1144 e1110 (2019). https://doi.org:10.1016/j.cell.2019.07.001
230 Clark, F. E. & Akera, T. Unravelling the mystery of female meiotic drive: where we are. *Open Biol* **11**, 210074 (2021). https://doi.org:10.1098/rsob.210074
231 Barik, S. Expression and biochemical properties of a protein serine/threonine phosphatase encoded by bacteriophage lambda. *Proceedings of the National Academy of Sciences* **90**, 10633-10637 (1993). https://doi.org:doi:10.1073/pnas.90.22.10633
232 Kitajima, T. S. *et al.* Shugoshin collaborates with protein phosphatase 2A to protect cohesin. *Nature* **441**, 46-52 (2006). https://doi.org:10.1038/nature04663
233 Snider, J. *et al.* Intracellular actin-based transport: How far you go depends on how often you switch. *Proceedings of the National Academy of Sciences* **101**, 13204-13209 (2004). https://doi.org:doi:10.1073/pnas.0403092101
234 Khaitlina, S. Y. Intracellular transport based on actin polymerization. *Biochemistry (Moscow)* **79**, 917-927 (2014). https://doi.org:10.1134/S0006297914090089
235 Zielinska, A. P. *et al.* Meiotic Kinetochores Fragment into Multiple Lobes upon Cohesin Loss in Aging Eggs. *Curr Biol* **29**, 3749-3765 e3747 (2019). https://doi.org:10.1016/j.cub.2019.09.006
236 Scheffler, K. *et al.* Two mechanisms drive pronuclear migration in mouse zygotes. *Nat Commun* **12**, 841 (2021). https://doi.org:10.1038/s41467-021-21020-x
237 Fant, C. B. *et al.* TFIID Enables RNA Polymerase II Promoter-Proximal Pausing. *Mol Cell* **78**, 785-793 e788 (2020). https://doi.org:10.1016/j.molcel.2020.03.008
238 Zhou, C. J. *et al.* Loss of CENPF leads to developmental failure in mouse embryos. *Cell Cycle* **18**, 2784-2799 (2019). https://doi.org:10.1080/15384101.2019.1661173

239 Mehlmann, L. M., Uliasz, T. F. & Lowther, K. M. SNAP23 is required for constitutive and regulated exocytosis in mouse oocytesdagger. *Biol Reprod* **101**, 338-346 (2019). https://doi.org:10.1093/biolre/ioz106
240 Chen, X. *et al.* Degradation of endogenous proteins and generation of a null-like phenotype in zebrafish using Trim-Away technology. *Genome Biol* **20**, 19 (2019). https://doi.org:10.1186/s13059-019-1624-4
241 Weir, E., McLinden, G., Alfandari, D. & Cousin, H. Trim-Away mediated knock down uncovers a new function for Lbh during gastrulation of Xenopus laevis. *Dev Biol* **470**, 74-83 (2021). https://doi.org:10.1016/j.ydbio.2020.10.014
242 *IMARIS 9.2 Reference Manual*. (Bitplane AG An Oxford Instruments Company, 2018).
243 Evans, R. D. *et al.* Myosin-Va and dynamic actin oppose microtubules to drive long-range organelle transport. *Curr Biol* **24**, 1743-1750 (2014). https://doi.org:10.1016/j.cub.2014.06.019
244 Homchaudhuri, L., Sarma, N. & Swaminathan, R. Effect of crowding by dextrans and Ficolls on the rate of alkaline phosphatase–catalyzed hydrolysis: A size-dependent investigation. *Biopolymers* **83**, 477-486 (2006). https://doi.org:https://doi.org/10.1002/bip.20578
245 Yuan, J. M. *et al.* The effects of macromolecular crowding on the mechanical stability of protein molecules. *Protein Sci* **17**, 2156-2166 (2008). https://doi.org:10.1110/ps.037325.108
246 Monda, J. K. & Cheeseman, I. M. The kinetochore-microtubule interface at a glance. *J Cell Sci* **131** (2018). https://doi.org:10.1242/jcs.214577
247 Tolić, I. M. Mitotic spindle: kinetochore fibers hold on tight to interpolar bundles. *Eur Biophys J* **47**, 191-203 (2018). https://doi.org:10.1007/s00249-017-1244-4
248 Llano, E. *et al.* Shugoshin-2 is essential for the completion of meiosis but not for mitotic cell division in mice. *Genes Dev* **22**, 2400-2413 (2008). https://doi.org:10.1101/gad.475308
249 Salic, A., Waters, J. C. & Mitchison, T. J. Vertebrate shugoshin links sister centromere cohesion and kinetochore microtubule stability in mitosis. *Cell* **118**, 567-578 (2004). https://doi.org:10.1016/j.cell.2004.08.016
250 Colin, A., Singaravelu, P., Thery, M., Blanchoin, L. & Gueroui, Z. Actin-Network Architecture Regulates Microtubule Dynamics. *Curr Biol* **28**, 2647-2656 e2644 (2018). https://doi.org:10.1016/j.cub.2018.06.028
251 Woolner, S., O'Brien, L. L., Wiese, C. & Bement, W. M. Myosin-10 and actin filaments are essential for mitotic spindle function. *J Cell Biol* **182**, 77-88 (2008). https://doi.org:10.1083/jcb.200804062
252 Burdyniuk, M., Callegari, A., Mori, M., Nedelec, F. & Lenart, P. F-Actin nucleated on chromosomes coordinates their capture by microtubules in oocyte meiosis. *J Cell Biol* **217**, 2661-2674 (2018). https://doi.org:10.1083/jcb.201802080
253 Lee, J., Iwai, T., Yokota, T. & Yamashita, M. Temporally and spatially selective loss of Rec8 protein from meiotic chromosomes during mammalian meiosis. *J Cell Sci* **116**, 2781-2790 (2003). https://doi.org:10.1242/jcs.00495
254 Blom, H. & Widengren, J. Stimulated Emission Depletion Microscopy. *Chem Rev* **117**, 7377-7427 (2017). https://doi.org:10.1021/acs.chemrev.6b00653
255 Wassie, A. T., Zhao, Y. & Boyden, E. S. Expansion microscopy: principles and uses in biological research. *Nat Methods* **16**, 33-41 (2019). https://doi.org:10.1038/s41592-018-0219-4
256 Matsuda, Y. & Chapman, V. M. Application of fluorescence in situ hybridization in genome analysis of the mouse. *Electrophoresis* **16**, 261-272 (1995). https://doi.org:10.1002/elps.1150160142
257 Watkins, P. C., Tanzi, R. E., Cheng, S. V. & Gusella, J. F. Molecular genetics of human chromosome 21. *J Med Genet* **24**, 257-270 (1987). https://doi.org:10.1136/jmg.24.5.257
258 Miyanari, Y., Ziegler-Birling, C. & Torres-Padilla, M. E. Live visualization of chromatin dynamics with fluorescent TALEs. *Nat Struct Mol Biol* **20**, 1321-1324 (2013). https://doi.org:10.1038/nsmb.2680

259 Jagannathan, M., Cummings, R. & Yamashita, Y. M. A conserved function for pericentromeric satellite DNA. *eLife* **7**, e34122 (2018). https://doi.org:10.7554/eLife.34122
260 Myers, S. A. *et al.* Evaluation of Advanced Precursor Determination for Tandem Mass Tag (TMT)-Based Quantitative Proteomics across Instrument Platforms. *J Proteome Res* **18**, 542-547 (2019). https://doi.org:10.1021/acs.jproteome.8b00611
261 Virant-Klun, I. & Krijgsveld, J. Proteomes of animal oocytes: what can we learn for human oocytes in the in vitro fertilization programme? *Biomed Res Int* **2014**, 856907 (2014). https://doi.org:10.1155/2014/856907
262 Ruth, K. S. *et al.* Genetic insights into biological mechanisms governing human ovarian ageing. *Nature* **596**, 393-397 (2021). https://doi.org:10.1038/s41586-021-03779-7
263 Elie, A. *et al.* Tau co-organizes dynamic microtubule and actin networks. *Sci Rep* **5**, 9964 (2015). https://doi.org:10.1038/srep09964
264 Preciado Lopez, M. *et al.* Actin-microtubule coordination at growing microtubule ends. *Nat Commun* **5**, 4778 (2014). https://doi.org:10.1038/ncomms5778
265 Schaefer, A. W., Kabir, N. & Forscher, P. Filopodia and actin arcs guide the assembly and transport of two populations of microtubules with unique dynamic parameters in neuronal growth cones. *J Cell Biol* **158**, 139-152 (2002). https://doi.org:10.1083/jcb.200203038
266 Hu, J. *et al.* Septin-driven coordination of actin and microtubule remodeling regulates the collateral branching of axons. *Curr Biol* **22**, 1109-1115 (2012). https://doi.org:10.1016/j.cub.2012.04.019
267 Tsvetkov, A. S., Samsonov, A., Akhmanova, A., Galjart, N. & Popov, S. V. Microtubule-binding proteins CLASP1 and CLASP2 interact with actin filaments. *Cell Motil Cytoskeleton* **64**, 519-530 (2007). https://doi.org:10.1002/cm.20201
268 Kita, A. M. *et al.* Spindle-F-actin interactions in mitotic spindles in an intact vertebrate epithelium. *Mol Biol Cell* **30**, 1645-1654 (2019). https://doi.org:10.1091/mbc.E19-02-0126
269 Li, R. & Zhu, J. Effects of aneuploidy on cell behaviour and function. *Nat Rev Mol Cell Biol* **23**, 250-265 (2022). https://doi.org:10.1038/s41580-021-00436-9
270 Lopez-Otin, C., Blasco, M. A., Partridge, L., Serrano, M. & Kroemer, G. The hallmarks of aging. *Cell* **153**, 1194-1217 (2013). https://doi.org:10.1016/j.cell.2013.05.039
271 Macedo, J. C., Vaz, S. & Logarinho, E. in *Cell Division Machinery and Disease* (eds Monica Gotta & Patrick Meraldi) 153-188 (Springer International Publishing, 2017).
272 Macedo, J. C. *et al.* FoxM1 repression during human aging leads to mitotic decline and aneuploidy-driven full senescence. *Nat Commun* **9**, 2834 (2018). https://doi.org:10.1038/s41467-018-05258-6
273 Naylor, R. M. & van Deursen, J. M. Aneuploidy in Cancer and Aging. *Annu Rev Genet* **50**, 45-66 (2016). https://doi.org:10.1146/annurev-genet-120215-035303

Chapter 7 – Appendices

7.1 Supplementary figures

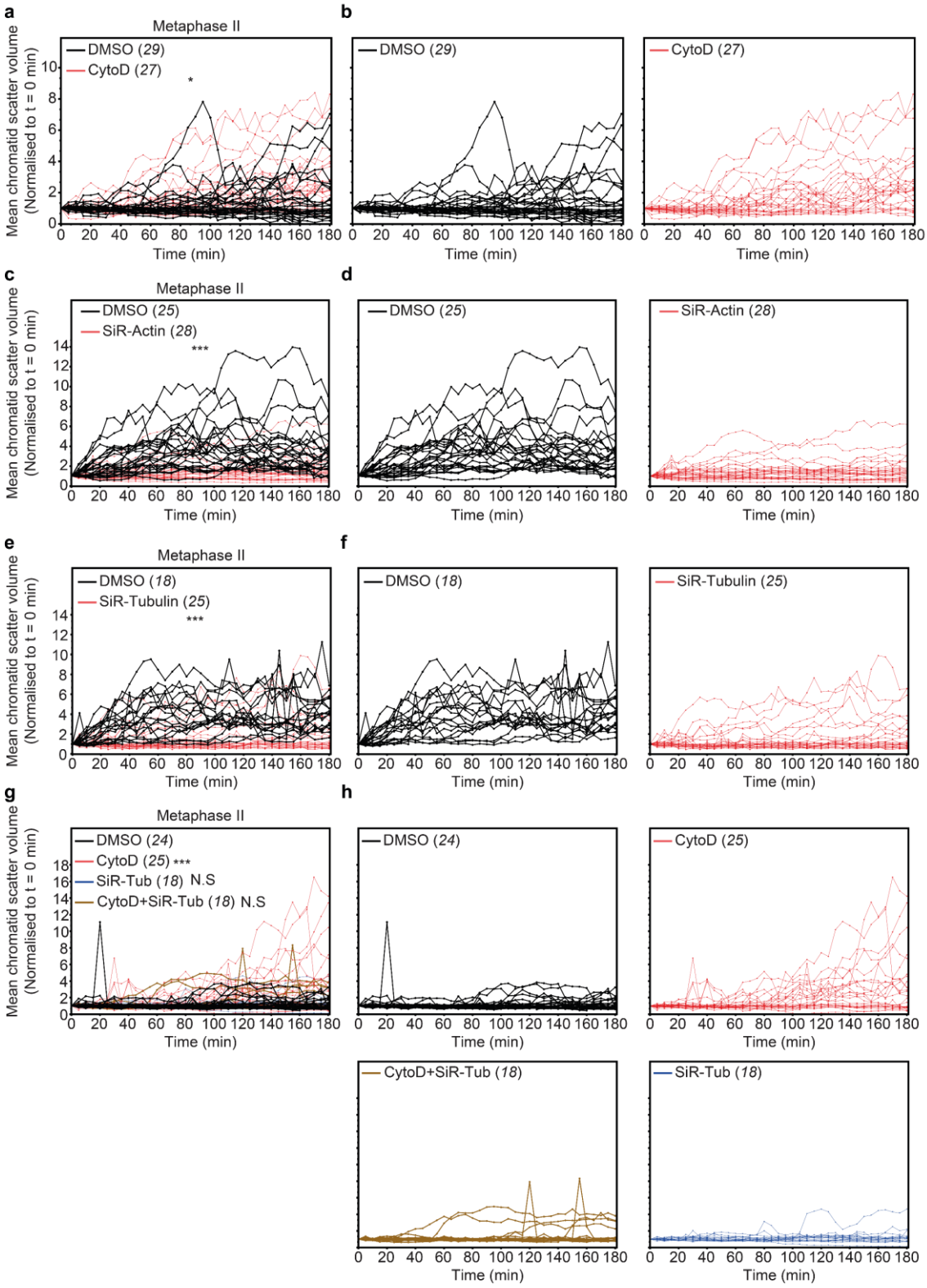

Figure 7.1 Normalized to T=0 Chromatid scatter volumes – Split figures (a) Normalised to T=0 mins chromatid scatter volumes measured over 3 hours in DMSO (black)- or Cytochalasin D-treated (red) metaphase II-arrested eggs with partially degraded Rec8. **(b)** Normalised to T=0 mins chromatid scatter volumes measured over 3 hours in DMSO (black)- or SiR-Actin-treated (red) metaphase II-arrested eggs with completely degraded Rec8. **(c)** Normalised to T=0 mins chromatid scatter volumes measured over 3 hours in DMSO (black)- or SiR-Tubulin-treated (red) metaphase II-arrested eggs with completely degraded Rec8. **(d)** Normalised to T=0 mins chromatid scatter volumes over 3 hours in DMSO- (black), Cytochalasin D- (red), SiR-Tubulin (blue)- or Cytochalasin D and SiR-Tubulin-treated (brown) metaphase II arrested eggs with partially degraded Rec8. Data are from 3 independent experiments, numbers in italics represent the number of eggs analysed per group. Statistical significance was evaluated using One-way ANOVA.

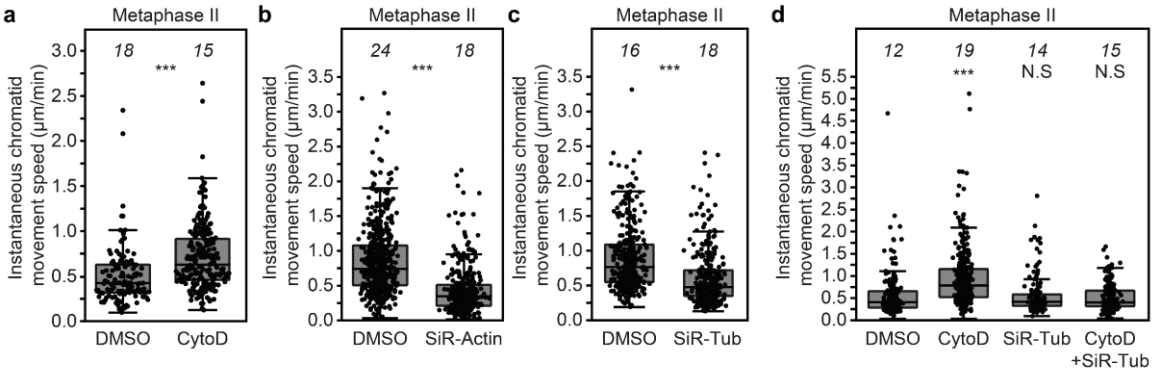

Figure 7.2 Instantaneous chromatid movement speeds – Box Blots (a) Distribution of instantaneous chromatid movement speeds (µm/min) in DMSO or Cytochalasin treated metaphase II-arrested eggs with partially degraded Rec8. Experimental design schematic. **(b)** Distribution of instantaneous chromatid movement speeds (µm/min) in DMSO or SiR-Actin-treated metaphase II-arrested eggs with completely degraded Rec8. **(c)** Distribution of instantaneous chromatid movement speeds (µm/min) in DMSO or SiR-Tubulin-treated metaphase II-arrested eggs with completely degraded Rec8. **(d)** Distribution of instantaneous chromatid movement speeds (µm/min) in DMSO- , Cytochalasin D- , SiR-Tubulin- or Cytochalasin D and SiR-Tubulin-treated metaphase II-arrested eggs with partially degraded Rec8. Data are from 3 independent experiments, numbers in italics represent the number of eggs analysed per group. Statistical significance for a,b,c was evaluated using Mann-Whitney t-test. Statistical significance for d was evaluated using One-way ANOVA.

7.2 Media and Buffers

7.2.1 M2 Medium

50 ml in embryo tested water (W1503, Sigma) pH 7.2 – 7.4 adjusted with 1 M NaOH (S2770, Sigma)

- 20 mL 10 mg/mL Bovine Serum Albumin (A3311-100G, Sigma)
- 5 mL Stock A
    - 55.5 mg/mL NaCl (S9888-1KG, Sigma)
    - 3.8 mg/mL KCl (529552, Sigma)
    - 1.74 mg/mL KH_2PO_4 (P0662, Sigma)
    - 0.67 mg/mL penicillin sodium salt (P3032, Sigma)
    - 31.4 mg/mL $MgSO_4$ (63136, Sigma)
    - 10.76 mg/mL glucose (49163, Sigma)
    - 0.54 mg/mL streptomycin sulfate (S1400000, Sigma)
    - 2.1% w/w sodium lactate (L7900-100ML, Sigma)
- 5 mL Stock B
    - 3.4 mg/mL $NaHCO_3$ (S6014, Sigma)
- 5 mL Stock C
    - 3.36 mM sodium pyruvate (P5280-25G, Sigma)
- 5 mL Stock D
    - 2.6 mg/mL $CaCl_2$ (902179, Sigma)
- 5 mL Stock E
    - 0.02 mg/mL phenol red (P3532, Sigma)
- 5 mL Stock F
    - 175.2 mM HEPES (H3375-25G, Sigma)

7.2.2 Immunofluorescence Fixative

- 470 µl Milli-Q water
- 100 µl 1M HEPES pH 7.0 (H3375-25G, Sigma)
- 200 µl 0.25M EGTA pH 7.0 (324626, Sigma)
- 10 µl 1M $MgSO_4$ (63136, Sigma)
- 200 µl 10% Formaldehyde (04018-1, Polysciences)
- 20 µl 10% Triton X-100 (2124-100, BioVision)

7.2.3 Extraction (Permeabilization) Buffer (PBT)

- 50 mL PBS (PD8117, Generon)
- 500 µl 10% Triton X-100 (2124-100, BioVision)

7.2.4 Blocking/Wash Buffer (3% PBT-BSA)

- 0.3 g BSA (BP1605-100, Fisher Scientific)
- 10 mL Extraction Buffer (PBT)

7.2.5 Spread Fixative Solution

pH 9.2 – 9.4 (adjusted with 1 M NaOH)

- 625 µl Formaldehyde (PI28906, Fisher Scientific)
- 30 µl DTT (10197777001, Millipore Sigma)
- 150 µl 10% Triton X-100 (2124-100, BioVision)
- 9.125 mL Milli-Q water

7.3 Plasmid maps

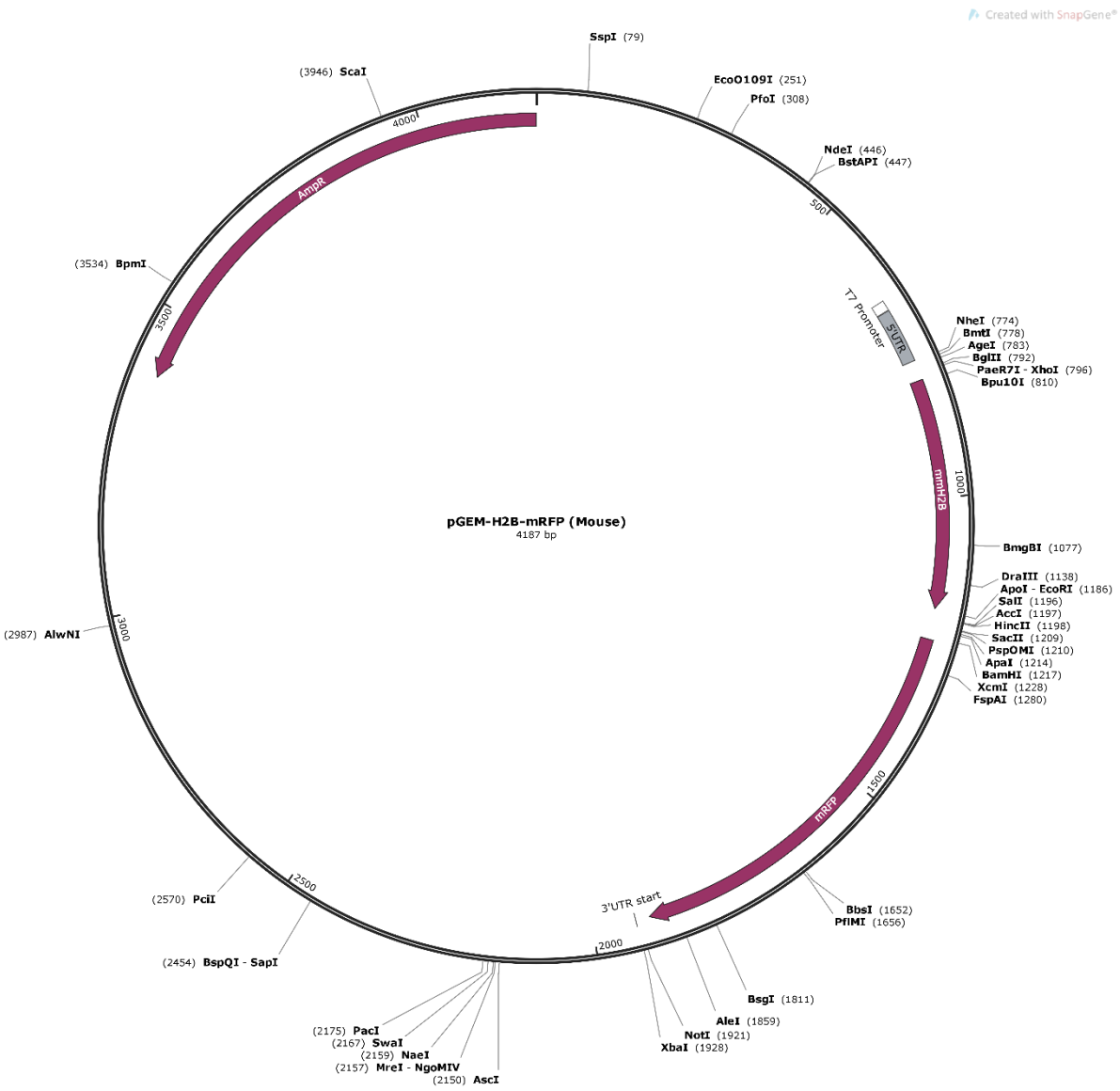

Figure 7.3 pGEM-H2B-mRFP(mouse) plasmid map Imported from SnapGene 5.1.7.

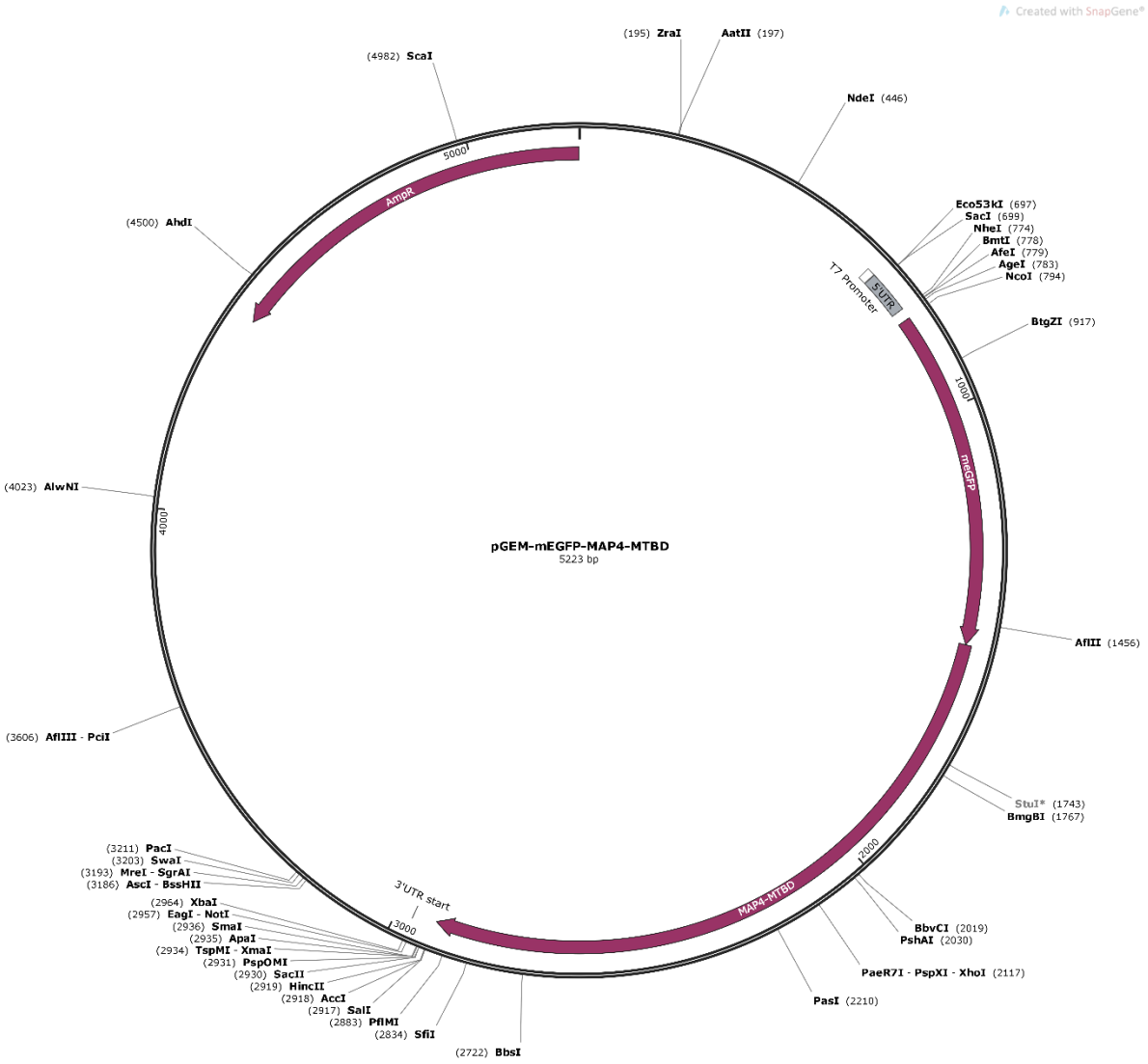

Figure 7.4 pGEM-mEGFP-MAP4-MTBD Imported from SnapGene 5.1.7.

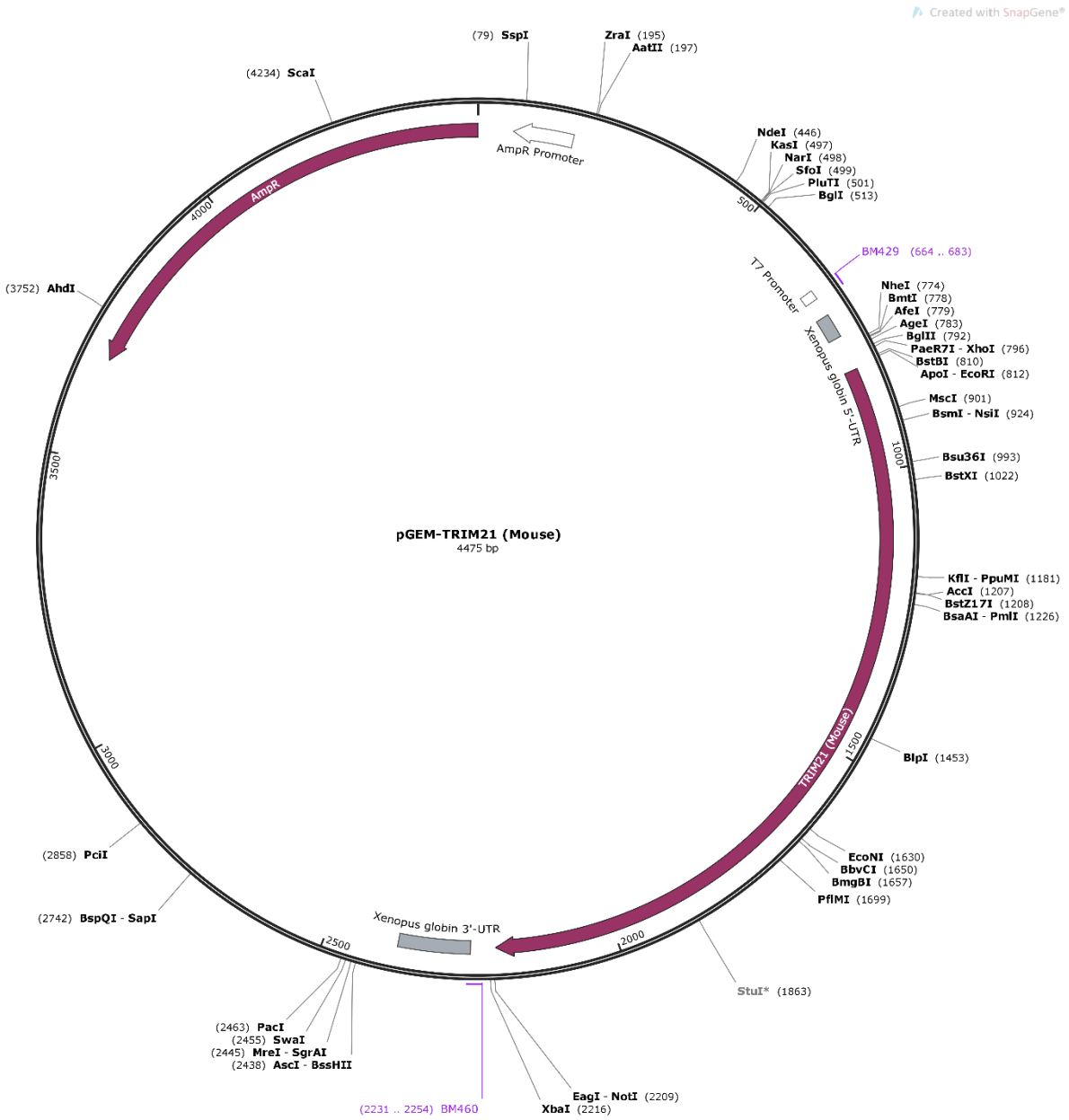

Figure 7.5 pGEM-TRIM21 (Mouse) Imported from SnapGene 5.1.7.

7.4 Equipment & Reagents

0.22 µm membrane filter - GSWP04700, MF-Millipore™

1 M NaOH - S2770

100x HCX PL APO CS oil immersion objective - 506211, Leica Microsystems

10x PBS Solution - PD8117

13 mm gauge hypodermic needles - BD303800, BD Microlance™

2-Propanol,BioReagent, for molecular biology, ≥99.5% - I9516-500ML

40x Apochromat 1.2 NA water immersion objective - 421767-9971-790, Zeiss

63x HC PL APO CS2 water immersion objective - 506361, Leica Microsystems

Alexa Fluor 488 Phalloidin - A12379

Anti-Topoisomerase II alpha + Topoisomerase II beta - ab109524

AscI - R0558L

Aspirator tube assemblies for calibrated microcapillary pipettes - A5177-5EA

Bovine Serum Albumin - A3311-100G

$CaCl_2$ – 902179

Calibrated 100ul glass capillary - pip3022

Capillary Tubes Glass 50µl volume 100mm length - 1-000-0500

Carl Zeiss™ Immersion medium Immersol W 2010, oiler 20 ml - 444969-0000-000

Cenp a (C51A7) Rabbit mAb (Mouse Specific) - 2048S

Centrifuge 5810R – 5811000360

Coplin jars - MIC6000

Corning® Primaria™ 35mm Easy Grip Style Cell Culture Dish – 353801

COVER SLIPS 22 X 22 MM - 631-0124

Cytochalasin D - C8273-1MG

Dextran, Alexa Fluor 488; 10,000 MW - D22910

Dimethyl sulfoxide (DMSO), Hybri-Max™ - D2650-5X5ML

Discovery V8 and Stemi 305 Stereomicroscopes – Carl Zeiss

DTT – 10197777001

EGTA- 324626

Embryo tested water -W1503

Eppendorf Centrifuge 5810 R, refrigerated, with Rotor A-4-62 - 4062-8168Q

Ethanol, Sigma - 32221-2.5L-PC-D

Falcon® 14mL Round Bottom High Clarity PP Test Tube – 352059

Formaldehyde, 10%, methanol free, Ultra-Pure - 04018-1

Gibson Assembly Master Mix - E2611L

Glass bottom imaging dishes - P35G-0-14-C

Glucose – 49163

Goat anti-Rabbit IgG (H+L) Secondary Antibody, Alexa Fluor 488 - A11034

Goat anti-Rabbit IgG (H+L) Secondary Antibody, Alexa Fluor 568 - A11011

Goat anti-Rabbit IgG (H+L) Secondary Antibody, Alexa Fluor 647 - A21244

Goat anti-Rat IgG (H+L) Secondary Antibody, Alexa Fluor 647 - A21247

H-1000 - VECTASHIELD Antifade Mounting Medium - H-1000-10

HEPES - H3375-25G

Hla / Terasaki Plates - 653180

Hoechst® 33342 Stain, 5 ml (20 mM) – 10150888

Human-Anti-Centromere (Kinetochore) - 15-234

Image J

Imaris 9.2 Bitplane

Invitrogen PureLink HiPure Plasmid Midiprep Kit - K210004

Invitrogen ambion Nuclease Free Water (not DEPC Treated) - AM9932

Invitrogen ambion Water Saturated Phenol, pH 6.6 - AM9710

KCl – 529552

KH_2PO_4 - P0662

Korasilon Paste - 0857.1

Lambda Protein Phosphatase - P0753S

Latrunculin B - 428020-1MG

Leica DMI6000 inverted widefield microscope

Leica SP8X confocal microscope

Mercury – 10119790

$MgSO_4$ – 63136

Milli-Q water

Mineral oil - M8410-100ML

mMESSAGE mMACHINE T7 Kit - AM1344

Mp Biomedicals Multitest Slides – 096041505

N6,2'-O-Dibutyryladenosine 3',5'-cyclic monophosphate sodium salt - D0627-100MG

NaCl - S9888-1KG

$NaHCO_3$ - S6014

NanoDrop Lite spectrophotometer- ND-LITE-PR

NEBuilder HiFi DNA Assembly Master Mix - E2621L

Nocodazole - 487928-10MG

Nunclon® Δ Multidishes – 10507591

Paclitaxel - T7191-1MG

PARAFFIN VISCOUS - 1.07160.1000

PBS - PD8117

PCR NUCLEOTIDE MIX – 11581295001

Penicillin sodium salt - P3032

Phenol - chloroform - isoamyl alcohol mixture, BioUltra - 77617-100ML

Phenol red - P3532

Phusion® High-Fidelity DNA Polymerase - M0530L

Pierce™ Methanol-free Formaldehyde Ampules 16% Formaldehyde (w/v) - PI28906

Pierce™ Surfact-Amps™ Detergent Solutions, Thermo Scientific, NP-40 – 85124

Prism software GraphPad

QIAprep Spin Miniprep Kit – 27106

QIAquick PCR Purification Kit – 28104

RAT ANTI TUBULIN ALPHA - MCA78G

rCutSmart™ Buffer - B6004S, NEB

Reversine - CAY10004412-5 mg

RNA loading dye - NEB N0362S

Sigmacote®, siliconizing reagent for glass and other surfaces - SIGMA SL2-100ML

SiR-Tubulin - 251SC002

Sodium hydroxide solution - 72068-100ML

Sodium lactate - L7900-100ML

Sodium pyruvate - P5280-25G

ssRNA Ladder - N0362S

ssRNA ladder -NEB N0362S

Streptomycin sulfate - S1400000

SYBR Safe DNA gel stain *10,000X concentrate in DMSO* - S33102

Syringe, Gastight; Hamilton Company; Model 1701; 10uL – 10271332

TBE Buffer, 10X Powder - BP1334-1

Thermo Scientific GeneRuler DNA Ladder Mix - SM0331

Thermoshaker Grant Instruments - PHMT-PSC24N

Triton® X-100, MegaPure™ Detergent, 10% Solution - 2124-100

Tyrode's Solution - T1788-100ML

Water for embryo transfer - W1503-500ML

Zeiss LSM 800 microscope

ZEN2 software Zeiss

7.5 bioRxiv preprint[3]

Dunkley, S. & Mogessie, B. **Actin limits egg aneuploidies associated with female reproductive aging**. bioRxiv, 2022.2005.2018.491967doi:10.1101/2022.05.18.491967 (2022).

Main Text:

Healthy mammalian embryo formation and development critically hinges on the accuracy of sister chromatid segregation in eggs (*1, 2*). Until fertilization occurs, a tight linkage between sister chromatids' centromeres resists their premature separation by microtubule fibers (*1, 2*). This association is predominantly achieved by Rec8-containing cohesin complexes that link sister chromatids centromeres (*1, 3-7*). Such tug-of-war between microtubule-based pulling forces and centromeric cohesion effectively generates tension between the sister chromatids' kinetochores (*8*). Unprogrammed cohesion loss can therefore cause premature sister chromatid separation and increase the likelihood of aneuploidy (*1, 9-11*). Indeed, gradual cohesin depletion in female reproductive aging (*1, 12, 13*) is considered a major cause of egg aneuploidies broadly associated with human infertility and genetic disorders (*1, 9, 14, 15*). However, such progressive cohesion loss does not satisfactorily explain the almost exponential increase in egg aneuploidy that is observed near the end of female reproductive life (*14, 15*). Since the actin cytoskeleton is a meiosis-specific functional component of the mammalian chromosome segregation machinery (*16-19*), we addressed whether its dysfunction in eggs could explain this striking reproductive aging phenomenon.

To examine the impact of reproductive aging on cellular F-actin integrity, we first applied quantitative super-resolution microscopy and visualized fluorescent Phalloidin labelled (*17*) actin structures in eggs isolated from reproductively young (6-12 weeks old) and aged (58-62 weeks old) mice. This revealed a significant reduction in spindle F-actin fluorescence intensity in aged eggs (Fig. 1, a and b, and Fig. S1a) that did not result from decreased spindle microtubule populations (Fig. S1, b and c). This analysis further showed that cytoplasmic F-actin network density was not disrupted in aged eggs (Fig. S1, d and e). Reproductive aging in females is therefore accompanied by meiotic spindle-specific disruption of F-actin in mammalian eggs.

To test whether F-actin loss can exacerbate egg aneuploidies that are generally caused by gradual cohesin depletion during aging, we visualized meiotic spindles, chromosomes, and centromeres in aged eggs – isolated from reproductively aged (35-39 weeks old) mice – by high-resolution 3D immunofluorescence microscopy. We then identified sister centromere pairs using automated spot detection in Imaris (Fig. 1c) and counted prematurely separated chromatids. Consistent with previous studies of aging-related centromeric cohesion loss (*10*), this approach revealed 10/26 of DMSO-treated control aged eggs had at least two prematurely separated chromatids (Fig. 1, d and e). By stark contrast, Cytochalasin D-mediated F-actin disruption (*16, 20*) caused untimely chromatid separation in 17/21 of aged eggs (Fig. 1, d and e). These data strongly suggested that F-actin limits the extent of chromatid separation in aged females, suggesting that it may mitigate the effects of age-related cohesion depletion.

To investigate the effect of F-actin removal on chromatid cohesion in young eggs, we performed similar analysis in eggs of reproductively younger (6-12 weeks old) mice. Compared to 2/20 of DMSO-treated control eggs, 12/25 of Cytochalasin D-treated young eggs displayed at least two prematurely separated chromatids (Fig. 1, d and e), which is notably comparable to incidence of chromatid separation in control aged eggs (Fig. 1e). Importantly, we were able to reproduce this high incidence of centromeric cohesion loss by treating metaphase II-arrested young eggs with Latrunculin B, a mechanistically distinct F-actin disrupting compound (*20-23*) (Fig. S2a). Similarly, quantification of chromatid linkage in independent chromosome spreads confirmed that F-actin removal predisposes eggs to centromeric cohesion loss (Fig. 1, f and g, and Fig. S2, b and c). Collectively, these results demonstrate that disruption of F-actin in young eggs is sufficient to induce a high incidence of premature sister chromatid separation similar to that seen in eggs from aged females. Notably, our quantitative immunofluorescence microscopy assays of oocyte meiosis I – when cohesion proteins can be more readily visualized along chromosome arms – did not reveal

decreased Rec8-containing cohesin complexes in Cytochalasin D-treated oocytes or their corresponding chromosomal spreads (Fig. S3, a to e, and movies S1 and S2). We therefore conclude that F-actin loss leads to chromatid separation without directly disrupting canonical chromosome cohesion pathways.

To uncover how F-actin disruption accelerates chromatid separation, we implemented the TRIM-Away system (*24-31*) (Fig. 2a) to artificially deplete Rec8 in young eggs. To induce aging-like sister chromatid separation via this approach, we microinjected control IgGs or low concentrations of Rec8 heavy-chain antibodies (to only partially degrade Rec8) into TRIM21-expressing, metaphase II-arrested young eggs. High-resolution live imaging of chromatids at 5-minute intervals showed that partial Rec8 depletion in this experimental system caused modest separation and dispersion of sister chromatids (Fig. 2b, Fig. S4a, and movie S3). To quantify this, we performed 3D iso-surface reconstruction (movie S4) and object-oriented bounding box analysis in Imaris software to identify the minimal cuboid volume that contained all chromatids at each live imaging timepoint (Fig. 2b). We then plotted this volume measurement over a three-hour observation time as readout for premature separation and scattering of sister chromatids. This analysis showed that partial Rec8 degradation in DMSO-treated control eggs caused gradual sister chromatid separation with most single chromatids remaining near the spindle equator during the three-hour observation time (Fig. 2, c and d, Fig. S4b, and movie S5), and with some dispersed chromatids often re-establishing alignment with the main chromosome mass (movie S6). By contrast, partial cohesion removal after F-actin disruption dramatically accelerated chromatid separation and caused persistent scattering of single chromatids in Cytochalasin D-treated eggs (Fig. 2, c and d, Fig. S4b, and movies S7 and S8). This finding demonstrated that aging-like centromeric cohesion depletion is more likely to cause extensive aneuploidies when F-actin is absent.

To test the effect of F-actin loss on chromatid motility, we tracked prematurely separated chromatids in 3D by high temporal resolution live imaging and measured their frame-to-frame displacement away from the metaphase II spindle equator. This analysis showed that most prematurely separated chromatids in Cytochalasin D-treated eggs migrated away from the spindle equator at significantly faster instantaneous speeds than in DMSO-treated control eggs that contained F-actin (Fig. 2e). This is consistent with a greater effect of chromatid-pulling microtubule forces when F-actin is disrupted. Importantly, ~62% of misaligned chromatids in control eggs became realigned at the spindle equator within the three-hours observation period (Fig. 2f). By contrast, only ~31% of previously scattered chromatids re-established correct alignment in the absence of F-actin (Fig. 2f). Persistently misaligned chromatids are more likely to be mis-segregated in anaphase II (*16*). We thus conclude that the actin cytoskeleton plays a critical, two-pronged role in the prevention of chromatid scattering: firstly, it acts as a brake against accelerated separation of sister chromatids by microtubules; secondly, it promotes the realignment of scattered single chromatids.

Having established that F-actin disruption predisposes weakly-linked sister chromatids to extensive separation (Fig. 1e), we tested whether it enrichment could help to keep them together in cohesin deficient eggs. We first stabilized F-actin in young eggs using high concentrations of SiR-Actin (*16, 17*), a fluorescence-labelled derivative of Jasplakinolide (*32*) that marks the actin cytoskeleton in living cells (*33*). We then fully degraded centromeric cohesin using highly concentrated Rec8 antibodies in our TRIM-Away strategy (Fig. 2a and movie S9). In DMSO-treated control eggs, this caused extensive separation and scattering of sister chromatids (Fig. 3, b and c, Fig. S4c, and movie S10), which is consistent with substantial depletion of cohesin from centromeric regions. In comparison, despite lack of robust cohesion, sister chromatids in SiR-Actin-treated eggs largely remained near the spindle equator during three hours of observation

(Fig. 3, b and c, Fig. S4c, and movie S11). Supporting our earlier conclusion that F-actin might act as a brake against their accelerated separation, most poleward migrating chromatids also moved at significantly slower speeds when F-actin was stabilized (Fig. 3d). These data therefore collectively define a new function of F-actin in restricting the poleward movement of prematurely separated chromatids in eggs with reduced centromeric cohesion (Fig. 3e).

Microtubules are well-established drivers of chromosomal separation during cell division (*18, 34*). Linking a decline in microtubule function with egg aneuploidy, defective microtubule dynamics were recently found to contribute to chromosomal abnormalities in aged eggs (*35*). We therefore asked whether microtubule dynamics also power chromatid movement in our experimental system of robust cohesion disruption. Consistent with earlier results, TRIM-Away-mediated acute depletion of Rec8 in DMSO-treated control eggs caused extensive dispersion of separated chromatids throughout the meiotic spindle (Fig. 3f, and movie S12). This was confirmed by bounding box analyses of chromatid mobility (Fig. 2b and 3g, and Fig. S4d). In contrast, blocking of microtubule dynamics prior to Rec8 degradation by treating eggs with high concentrations of SiR-Tubulin – a cell permeable and fluorogenic derivative of the microtubule stabilizing drug Docetaxel (*33, 36*) – significantly slowed down the movement of separated chromatids and restricted their mobility to only near the spindle equator (Fig. 3, f to h, Fig. S4d, and movie S13). These results demonstrated that microtubule dynamics drive the complete disengagement and scattering of sister chromatids following centromeric cohesion loss (Fig. 3i).

Spindle F-actin abundance directly impacts microtubule organization and dynamics in mouse eggs (*16*). To investigate whether more effective microtubule pulling in the absence of F-actin underpins chromatid separation in cohesion deficient eggs, we combined Cytochalasin D and SiR-Tubulin compounds in our experimental system of reproductive aging-like centromeric cohesion depletion (Fig. 2b). In line with our earlier data (Fig. 2, c to e), TRIM-Away-mediated partial Rec8

degradation caused rapid and extensive chromatid scattering only in eggs that did not contain F-actin (Fig. 4, a to c, Fig. S4e, and movies S14 and S15). Consistent with results showing that partial depletion of Rec8 causes only modest events of chromatid scattering (Fig. 2, c to e), SiR-Tubulin-mediated blocking of microtubule dynamics in these eggs had negligible effect on the dispersion of prematurely separated chromatids (Fig. 4, a and b, Fig. S4e, and movie S16). Similarly, the movement of unpaired chromatids was unaffected when microtubules were stabilized in eggs that were partially depleted of Rec8 (Fig. 4c). In striking contrast, blocking microtubule dynamics in eggs that did not contain F-actin – and thus experienced high incidence of chromatid scattering – significantly reduced both the extent of chromatid dispersion (Fig. 4, a and b, Fig. S4e, and movie S17) and speed of chromatid mobility (Fig. 4c). These data collectively indicate that pulling forces mediated by microtubule dynamics – normally insufficient to fully disengage weakly-bound chromatids – can cause complete chromatid separation when F-actin is lost (Fig. 4d).

Our findings indicate that spindle F-actin mitigates the effects of age-related cohesin depletion. Removal of F-actin in aged eggs with naturally reduced centromeric cohesion exacerbates premature chromatid separation. Consistently, experimentally reducing centromeric cohesion in young eggs only modestly causes untimely chromatid separation, unless F-actin is also disrupted. Because persistently misaligned chromatids in F-actin disrupted eggs are frequently mis-segregated in anaphase II (*16*), we propose that aging-related F-actin dysfunction can explain the sudden rise in embryo aneuploidy rate at advanced reproductive ages (*1, 14, 15*). This would be consistent with the spindle-specific physiological reduction of F-actin that we have identified in aged eggs.

Results from our combined cytoskeletal manipulation experiments indicate that F-actin exerts this previously unknown function by modulating microtubule dynamics. We previously showed that meiotic spindle F-actin stabilizes kinetochore-bound microtubules to promote accurate

chromosome segregation (*16*). Furthermore, increasing the F-actin content of meiotic spindles substantially limits microtubule dynamics and reduces chromosomal separation in mouse oocytes (*16*). Our new data are consistent with a model where spindle-associated actin filaments generally dampen forces generated by dynamic microtubules (Fig. 4e). In young eggs with strongly linked chromatids, this would supplement cohesion-mediated resistance to pulling forces exerted by dynamic microtubules, thus robustly generating inter-kinetochore tension. Such force limitation would more critically resist microtubule-based chromatid pulling in aged eggs where cohesion is depleted (Fig. 4e). This would explain why F-actin disruption in aged eggs leads to extensive separation of sister chromatids. Consistent with this model, female reproductive aging is accompanied by aberrant microtubule dynamics in mouse oocytes (*35*) that are proposed as a cohesion-independent cause of meiotic aneuploidy (*37*). Thus, our findings also define F-actin disruption as a new link between cohesion deterioration and microtubule dysfunction in aging eggs.

F-actin and its associated proteins promote microtubule stability and organization in various cellular contexts, including in female meiosis (*16, 38-43*). Moreover, recent findings show that F-actin is also a component of mitotic spindle machineries that separate sister chromatids (*44, 45*). Spindle-associated actin filaments might thus have similar roles in non-reproductive cell division where aging is also associated with aneuploidies (*46-50*).

References

1. M. Herbert, D. Kalleas, D. Cooney, M. Lamb, L. Lister, Meiosis and maternal aging: insights from aneuploid oocytes and trisomy births. *Cold Spring Harb Perspect Biol* **7**, a017970 (2015).
2. B. Mogessie, K. Scheffler, M. Schuh, Assembly and Positioning of the Oocyte Meiotic Spindle. *Annu Rev Cell Dev Biol* **34**, 381-403 (2018).

3. K. Tachibana-Konwalski *et al.*, Rec8-containing cohesin maintains bivalents without turnover during the growing phase of mouse oocytes. *Genes Dev* **24**, 2505-2516 (2010).
4. N. R. Kudo *et al.*, Resolution of chiasmata in oocytes requires separase-mediated proteolysis. *Cell* **126**, 135-146 (2006).
5. N. R. Kudo *et al.*, Role of cleavage by separase of the Rec8 kleisin subunit of cohesin during mammalian meiosis I. *J Cell Sci* **122**, 2686-2698 (2009).
6. K. Nasmyth, C. H. Haering, Cohesin: its roles and mechanisms. *Annu Rev Genet* **43**, 525-558 (2009).
7. K. I. Ishiguro, The cohesin complex in mammalian meiosis. *Genes Cells* **24**, 6-30 (2019).
8. S. Hauf, Y. Watanabe, Kinetochore orientation in mitosis and meiosis. *Cell* **119**, 317-327 (2004).
9. F. Pellestor, B. Andreo, F. Arnal, C. Humeau, J. Demaille, Maternal aging and chromosomal abnormalities: new data drawn from in vitro unfertilized human oocytes. *Hum Genet* **112**, 195-203 (2003).
10. Y. Yun, S. I. Lane, K. T. Jones, Premature dyad separation in meiosis II is the major segregation error with maternal age in mouse oocytes. *Development* **141**, 199-208 (2014).
11. R. Angell, First-meiotic-division nondisjunction in human oocytes. *Am J Hum Genet* **61**, 23-32 (1997).
12. L. M. Lister *et al.*, Age-related meiotic segregation errors in mammalian oocytes are preceded by depletion of cohesin and Sgo2. *Curr Biol* **20**, 1511-1521 (2010).
13. T. Chiang, F. E. Duncan, K. Schindler, R. M. Schultz, M. A. Lampson, Evidence that weakened centromere cohesion is a leading cause of age-related aneuploidy in oocytes. *Curr Biol* **20**, 1522-1528 (2010).

14. T. Hassold, P. Hunt, To err (meiotically) is human: the genesis of human aneuploidy. *Nat Rev Genet* **2**, 280-291 (2001).

15. S. I. Nagaoka, T. J. Hassold, P. A. Hunt, Human aneuploidy: mechanisms and new insights into an age-old problem. *Nat Rev Genet* **13**, 493-504 (2012).

16. B. Mogessie, M. Schuh, Actin protects mammalian eggs against chromosome segregation errors. *Science* **357**, (2017).

17. B. Mogessie, Visualization and Functional Analysis of Spindle Actin and Chromosome Segregation in Mammalian Oocytes. *Methods Mol Biol* **2101**, 267-295 (2020).

18. B. Mogessie, K. Scheffler, M. Schuh, Assembly and Positioning of the Oocyte Meiotic Spindle. *Annu Rev Cell Dev Biol*, (2018).

19. B. Mogessie, Advances and surprises in a decade of oocyte meiosis research. *Essays Biochem* **64**, 263-275 (2020).

20. K. Scheffler, F. Giannini, T. Lemonnier, B. Mogessie, The prophase oocyte nucleus is a homeostatic G-actin buffer. *J Cell Sci* **135**, (2022).

21. I. Spector, N. R. Shochet, Y. Kashman, A. Groweiss, Latrunculins: novel marine toxins that disrupt microfilament organization in cultured cells. *Science* **219**, 493-495 (1983).

22. M. Coue, S. L. Brenner, I. Spector, E. D. Korn, Inhibition of actin polymerization by latrunculin A. *FEBS Lett* **213**, 316-318 (1987).

23. W. M. Morton, K. R. Ayscough, P. J. McLaughlin, Latrunculin alters the actin-monomer subunit interface to prevent polymerization. *Nat Cell Biol* **2**, 376-378 (2000).

24. A. P. Zielinska *et al.*, Meiotic Kinetochores Fragment into Multiple Lobes upon Cohesin Loss in Aging Eggs. *Curr Biol* **29**, 3749-3765 e3747 (2019).

25. D. Clift *et al.*, A Method for the Acute and Rapid Degradation of Endogenous Proteins. *Cell* **171**, 1692-1706 e1618 (2017).

26. K. Scheffler *et al.*, Two mechanisms drive pronuclear migration in mouse zygotes. *Nat Commun* **12**, 841 (2021).

27. C. B. Fant *et al.*, TFIID Enables RNA Polymerase II Promoter-Proximal Pausing. *Mol Cell* **78**, 785-793 e788 (2020).

28. C. J. Zhou *et al.*, Loss of CENPF leads to developmental failure in mouse embryos. *Cell Cycle* **18**, 2784-2799 (2019).

29. L. M. Mehlmann, T. F. Uliasz, K. M. Lowther, SNAP23 is required for constitutive and regulated exocytosis in mouse oocytes. *Biol Reprod* **101**, 338-346 (2019).

30. X. Chen *et al.*, Degradation of endogenous proteins and generation of a null-like phenotype in zebrafish using Trim-Away technology. *Genome Biol* **20**, 19 (2019).

31. E. Weir, G. McLinden, D. Alfandari, H. Cousin, Trim-Away mediated knock down uncovers a new function for Lbh during gastrulation of Xenopus laevis. *Dev Biol* **470**, 74-83 (2021).

32. A. Holzinger, Jasplakinolide: an actin-specific reagent that promotes actin polymerization. *Methods Mol Biol* **586**, 71-87 (2009).

33. G. Lukinavicius *et al.*, Fluorogenic probes for live-cell imaging of the cytoskeleton. *Nat Methods* **11**, 731-733 (2014).

34. J. K. Monda, I. M. Cheeseman, The kinetochore-microtubule interface at a glance. *J Cell Sci* **131**, (2018).

35. S. Nakagawa, G. FitzHarris, Intrinsically Defective Microtubule Dynamics Contribute to Age-Related Chromosome Segregation Errors in Mouse Oocyte Meiosis-I. *Curr Biol* **27**, 1040-1047 (2017).

36. J. Dubois *et al.*, Fluorescent and biotinylated analogues of docetaxel: synthesis and biological evaluation. *Bioorg Med Chem* **3**, 1357-1368 (1995).

37. A. I. Mihajlovic, J. Haverfield, G. FitzHarris, Distinct classes of lagging chromosome underpin age-related oocyte aneuploidy in mouse. *Dev Cell* **56**, 2273-2283 e2273 (2021).

38. M. L. Pimm, J. L. Henty-Ridilla, New twists in actin-microtubule interactions. *Mol Biol Cell* **32**, 211-217 (2021).

39. A. Elie *et al.*, Tau co-organizes dynamic microtubule and actin networks. *Sci Rep* **5**, 9964 (2015).

40. M. Preciado Lopez *et al.*, Actin-microtubule coordination at growing microtubule ends. *Nat Commun* **5**, 4778 (2014).

41. A. W. Schaefer, N. Kabir, P. Forscher, Filopodia and actin arcs guide the assembly and transport of two populations of microtubules with unique dynamic parameters in neuronal growth cones. *J Cell Biol* **158**, 139-152 (2002).

42. D. Inoue *et al.*, Actin filaments regulate microtubule growth at the centrosome. *EMBO J* **38**, (2019).

43. A. Colin, P. Singaravelu, M. Thery, L. Blanchoin, Z. Gueroui, Actin-Network Architecture Regulates Microtubule Dynamics. *Curr Biol* **28**, 2647-2656 e2644 (2018).

44. M. Plessner, J. Knerr, R. Grosse, Centrosomal Actin Assembly Is Required for Proper Mitotic Spindle Formation and Chromosome Congression. *iScience* **15**, 274-281 (2019).

45. A. M. Kita *et al.*, Spindle-F-actin interactions in mitotic spindles in an intact vertebrate epithelium. *Mol Biol Cell* **30**, 1645-1654 (2019).

46. R. Li, J. Zhu, Effects of aneuploidy on cell behaviour and function. *Nat Rev Mol Cell Biol*, (2022).

47. C. Lopez-Otin, M. A. Blasco, L. Partridge, M. Serrano, G. Kroemer, The hallmarks of aging. *Cell* **153**, 1194-1217 (2013).

48. J. C. Macedo, S. Vaz, E. Logarinho, Mitotic Dysfunction Associated with Aging Hallmarks. *Adv Exp Med Biol* **1002**, 153-188 (2017).

49. J. C. Macedo *et al.*, FoxM1 repression during human aging leads to mitotic decline and aneuploidy-driven full senescence. *Nat Commun* **9**, 2834 (2018).

50. R. M. Naylor, J. M. van Deursen, Aneuploidy in Cancer and Aging. *Annu Rev Genet* **50**, 45-66 (2016).

51. M. Schuh, J. Ellenberg, Self-organization of MTOCs replaces centrosome function during acentrosomal spindle assembly in live mouse oocytes. *Cell* **130**, 484-498 (2007).

52. M. C. C. Silva, G. Wutz, K. Tachibana, J. M. Peters, Analysis of chromosomes from mouse oocytes and mammalian cultured cells by light microscopy. *Methods Cell Biol* **144**, 287-305 (2018).

Acknowledgments: We thank Mark Dodding for feedback on the manuscript; Kathleen Scheffler for feedback on the manuscript, cloning, advice, technical input, and TRIM-Away expertise; Michael Lampson (University of Pennsylvania) for a generous gift of Rec8 antiserum; and members of the Mogessie lab for discussions.

Funding: This work was supported by a Sir Henry Dale Fellowship jointly funded by the Wellcome Trust and the Royal Society [grant number 213470/Z/18/Z] to B.M. and a Wellcome Trust PhD studentship [grant number 220082/Z/20/Z] to S.D. For the purpose of open access, the corresponding author has applied a CC BY public copyright license to any Author Accepted Manuscript version arising from this submission.

Author contributions:

Conceptualization: BM

Methodology: BM, SD

Investigation: SD

Visualization: BM, SD

Supervision: BM

Writing – original draft: BM

Writing – review & editing: BM, SD

Competing interests: Authors declare that they have no competing interests.

Supplementary Materials

Materials and Methods

Supplementary Text

Figs. S1 to S4

References (*51–52*)

Movies S1 to S17

Materials and Methods

Mouse oocyte isolation, maturation, culturing, and microinjection

All animal work in this research was performed at the University of Bristol and approved by the institution's Animal Welfare and Ethical Review Body (AWERB). Mice were maintained in a pathogen-free environment in accordance with UK Home Office regulations under the guidelines of the University of Bristol Animal Services Unit. Oocytes were isolated from the ovaries of 8–12-week CD1 or C57BL/6 (young) or 8-9 months CD1 or 13-14 months C57BL/6 (aged) mice, cultured, and microinjected with 6-8 picolitres of *in vitro* transcribed mRNA as described in detail recently (*17*).

C57BL/6 mice were used for comparison of cytoplasmic and spindle F-actin populations between young and aged eggs as – owing to pandemic-associated supply chain failures – this was the only aged mouse strain commercially available to us in the early stages of the project.

Cytoskeletal drug addition experiments

Metaphase II-arrested eggs (at least 4 hours after polar body extrusion) were treated for 4 hours with: Cytochalasin D (C8273-1MG, Merck) at a final concentration of 5 µg/ml in M2 medium or Latrunculin B (428020-1MG, Merck) at a final concentration of 5 µM in M2 medium (to disrupt F-actin); SiR-Actin (SC001, Spirochrome) at a final concentration of 10 µM in M2 medium (to stabilize F-actin). In our initial experiments, we used optimized concentrations of the microtubule-stabilizing compound Taxol to effectively block microtubule dynamics in mouse eggs. However, combination of Taxol with Cytochalasin D invariably disrupted meiotic spindles. We therefore used the Docetaxel-derivative compound SiR-Tubulin (SC002, Spirochrome) at a final concentration of 1 µM in M2 medium to stabilize microtubules. In simultaneous F-actin disruption and microtubule stabilization experiments, eggs were treated with SiR-Tubulin (1 µM) for 2 hours then with a combination Cytochalasin D (5 µg/ml) and SiR-Tubulin (1 µM) for 2 hours. In TRIM-Away experiments, drug treatment was performed prior to antibody microinjection. All drugs were dissolved in DMSO (D2650-5X5ML, Merck). In control conditions, DMSO was diluted in M2 medium identically to corresponding experimental conditions.

Generation of expression constructs and mRNA synthesis

To label chromosomes, H2B-mRFP mRNA was transcribed from pGEM-H2B-mRP(*20*). To generate pGEM-SNAP-TRIM21 for TRIM-Away experiments, pGEM-N-SNAPf was first constructed by removing SNAPf from pSNAPf (NEB, N9183S) with AgeI-XhoI and inserting it into the AgeI-XhoI site of pGEM-HE (*51*). The coding sequence of mouse TRIM21 was then transferred from pGEM-EGFP-TRIM21 (*25*) into pGEM-N-SNAPf by Gibson assembly using

primers 5'TTAAACTCGAGCTCAAGCTTATGTCTCTGGAAAAGATG3' and 5' ATCCCGGGCCCGCGGTACCGTCACATCTTTAGTGGACAG3'.

Capped mRNAs were synthesized using a T7 polymerase (mMessage mMachine kit, Ambion). mRNA concentrations were measured using a Nanodrop spectrophotometer (Thermo Scientific).

Fixation and immunostaining of mouse oocytes and eggs

Cells were fixed in 100 mM HEPES, 10mM $MgSO_4$, 50mM EGTA, 0.5% Triton X-100 (v/v) and 2% formaldehyde (v/v) for 30 minutes at 37°C, then blocked at 4°C overnight in PBS containing 0.3% Triton X-100 (v/v) and 3% Bovine Serum Albumin (BSA) (w/v). In CENP-A immunostaining experiments, eggs were fixed at room temperature for 20 minutes, extracted in PBS containing 0.25% Triton X-100 (v/v) at room temperature for 10 minutes, and incubated in 3% BSA-PBS (w/v) at 4°C overnight. In Rec8 immunostaining staining experiments, the zona pellucida was removed before fixation by treating cells with Tyrode's acidic solution (Merck, T1788-100ML) as described previously (*52*). In both CENP-A and Rec8 immunostaining experiments, fixed cells were incubated with λ-phosphatase (NEB, P0753S) for 2 hours at 30°C prior to immunostaining. Primary antibodies were: Rec8 rabbit antiserum (gift from Michael Lampson produced as described previously (*13*); 1:2000 dilution); CENP-A (Cell Signalling Technology, 2048S; 1:200 dilution); Topoisomerase II (Abcam, ab52934; 1:200 dilution); Human Anti-Centromere Antibody (Antibodies Incorporated, 15-234; 1:200 dilution). Secondary antibodies and stains were: Alexa-Fluor-488-labelled anti-rabbit (Molecular Probes; 1:200 dilution); Alexa-488 phalloidin (Molecular Probes; 1:20 dilution) and 5μg/ml Hoechst 33342 (Molecular Probes).

Metaphase chromosomal spreading, fixation and immunostaining

To facilitate chromosomal spreading, the zona pellucida was removed from metaphase I oocytes or metaphase II-arrested eggs by washing cells through Tyrode's acid solution (Merck, T1788-

100ML) droplets covered with mineral oil (*52*). After washing out Tyrode's solution in M2 medium, cells were recovered from acid treatment for a minimum of 5 minutes at 37°C. To spread chromosomes, 2-3 cells were dropped by pipetting onto a well of 15-well Multitest slide (MP Biomedicals, 096041505) containing water-based spreading solution (1% paraformaldehyde (v/v); 0.15% Triton-X100 (v/v); 3mM DTT; pH 9.2-9.4)) and air-dried in a non-transparent humidified box. After incubation with λ-phosphatase (NEB, P0753S) for 2 hours at 30°C, spreads were blocked in 3% BSA (w/v) (Fisher Scientific, 11483823) in PBS. Immunostaining was performed by washing out blocking solution in PBS followed by sequential incubation with primary and secondary antibodies for 1.5 hours at 37°C. Primary antibodies were: Rec8 rabbit antiserum (as described above and produced previously(*13*); 1:2000 dilution); Human Anti-Centromere Antibody (15-234, Antibodies Incorporated, 1:200 dilution). Secondary antibodies and stains were Alexa-Fluor-488-labelled anti-rabbit (Molecular Probes; 1:200 dilution), Alexa-Fluor-488-labelled anti-human (Molecular Probes; 1:200 dilution), and 5µg/ml Hoechst 33342 (Molecular Probes). Slides were prepared for microscopy by covering wells were Vectashield antifade mounting medium (2B Scientific, H-1000-10), mounting with 22x22 mm glass coverslips (VWR, 631-0124) and sealing with nail varnish.

High-resolution confocal live microscopy

Confocal time lapse images of metaphase II-arrested mouse eggs were acquired using a Zeiss LSM 800 microscope equipped with an environmental chamber maintained at 37°C and a 40x C-Apochromat 1.2 NA water-immersion objective. Image acquisition using ZEN2 software (Zeiss) was performed at a temporal resolution of 5 minutes and with a Z-stack thickness of ~40 µm at 1.5 µm confocal sections. Eggs were imaged in M2 medium (with or without cytoskeletal drugs) under mineral oil as described previously (*17*).

Confocal, super-resolution and widefield immunofluorescence microscopy

Confocal immunofluorescence images were acquired using a Zeiss LSM 800 confocal microscope, equipped with a 40x C-Apochromat 1.2 NA water immersion objective. Z-stacks were acquired with a thickness of 2.5 µm at 0.5 µm confocal sections (for spindle microtubule fluorescence quantification), 15 µm at 0.3 µm confocal sections (for single chromatid quantification) or 30 µm at 0.5 µm confocal sections (for Rec8 fluorescence quantification).

For spindle F-actin imaging, super-resolution 3D images of fluorescent phalloidin-labelled F-actin structures were acquired at the middle of the meiotic spindle in 0.5 µm steps over a range of 2.5 µm using the Airyscan module on a Zeiss LSM 800 microscope and a 40x C-Apochromat 1.2 NA water immersion objective. Post-acquisition super-resolution images were obtained by 3D Airyscan processing of raw images in ZEN2 software (Zeiss).

For cytoplasmic F-actin imaging, single section super-resolution images of fluorescent phalloidin-labelled F-actin structures were acquired at hemispheric regions of each egg using the Airyscan module on a Zeiss LSM 800 microscope and a 40x C-Apochromat 1.2 NA water immersion objective.

3D Immunofluorescence images of metaphase chromosomal spreads were acquired at 0.5 µm steps covering 5 µm using a Leica DMI6000 inverted widefield microscope equipped with a 100x HCX PL APO CS oil immersion objective.

Images in control and experimental conditions were acquired using identical imaging settings. Eggs were imaged in M2 medium under mineral oil as described previously (*17*).

Fluorescence intensity quantification of Rec8

3D volumes of metaphase I chromosomes were reconstructed in Imaris software (Bitplane) using Hoechst 3342 immunofluorescence signal. Reconstructed surfaces were then used to mask

chromosomes, remove background, and measure the mean fluorescence intensity of Rec8 on individual chromosomes.

Rec8 fluorescence intensity in metaphase I chromosomal spreads was quantified from sum intensity projections of Z-stacks (ImageJ). Mean intensity measurements were performed in ImageJ by manually drawing a region of interest around each chromosome (Fig. S3g).

Mean fluorescence intensity measurements were normalized by dividing individual values in both control and experimental groups by the average of mean fluorescence intensity values in control groups.

Quantification of cytoplasmic and spindle F-actin fluorescence intensities in young and aged mouse eggs

The ratio of spindle F-actin to cytoplasmic F-actin fluorescence intensity was determined from sum intensity projected Z-stacks in ImageJ. Spindle F-actin fluorescence was measured by averaging the mean fluorescence intensities of 5 square regions of interest inside the spindle (Fig. S1a). Cytoplasmic F-actin fluorescence was measured by averaging the mean fluorescence intensities of 5 similarly sized square regions of interest in the area immediately surrounding the spindle (Fig. S1a). Ratios were obtained for each egg by dividing the average mean fluorescence intensity of spindle F-actin by the average mean fluorescence intensity of cytoplasmic F-actin.

Cytoplasmic F-actin fluorescence – not restricted to the region containing the meiotic spindle (Fig. S1e) – was measured in ImageJ by averaging the mean fluorescence intensities of 5 square regions of interest inside each egg. Background removal was performed by subtracting the average mean fluorescence intensity of 5 similarly sized square regions of interest – placed outside the image of the cell and in regions that did not contain any phalloidin signal – from the averaged mean fluorescence intensity of cytoplasmic F-actin (Fig. S1e). Mean fluorescence intensity

measurements were normalized by dividing individual values in both control and experimental groups by the average of mean fluorescence intensity values in control groups.

Quantification of spindle microtubule fluorescence intensity in young and aged mouse eggs

Spindle microtubule fluorescence was measured in ImageJ from sum intensity projected Z-stacks by averaging the mean fluorescence intensities of 5 square regions of interest inside the spindle (Fig. S1b). Background removal was performed by subtracting the average mean fluorescence intensity of 5 similarly sized square regions of interest – placed in cytoplasmic regions that did not contain any microtubule filament – from the averaged mean fluorescence intensity of spindle microtubules (Fig. S1b). Mean fluorescence intensity measurements were normalized by dividing individual values in both control and experimental groups by the average of mean fluorescence intensity values in control groups.

Identification and quantification of prematurely separated sister chromatids

Chromatids in metaphase II-arrested eggs were identified by reconstructing the 3D volume of Topoisomerase II immunofluorescence signal in Imaris software (Bitplane). Centromeres were then identified using CENP-A immunofluorescence signal for spot detection in Imaris. Lastly, neighboring centromeres were manually assigned as sisters using distance measurements and reconstructed chromatid volumes as reference. Chromatids containing centromeres for which no corresponding sisters were identified via this analysis were designated as prematurely separated chromatids (Fig. 1c). Single chromatids in metaphase II spreads were identified via Hoechst labelling and centromere distance measurements in combination with spot detection in Imaris using the immunofluorescence signal of human anti-centromere antibody.

Partial and complete targeted degradation of Rec8 in TRIM-Away experiments

In partial Rec8 degradation TRIM-Away experiments, TRIM21 expressing, metaphase II-arrested eggs were microinjected with 2-3 picolitres of Rec8 antiserum (*13*) (1:30-1:50 dilution) and Alexa

Fluor 488 Dextran 10,000 MW (to validate antibody microinjection by fluorescence imaging) (Molecular Probes, D22910; 1:40 dilution) in 0.05% (v/v) NP40-PBS. In complete Rec8 degradation TRIM-Away experiments, TRIM21 expressing, metaphase II-arrested eggs were microinjected with 2-3 picolitres of Rec8 antiserum (*13*) (1:2 dilution) and Alexa Fluor 488 Dextran 10,000 MW (Molecular Probes, D22910; 1:40 dilution) in 0.05% (v/v) NP40-PBS. In simultaneous Rec8 degradation and cytoskeletal manipulation experiments, all TRIM-Away microinjections were performed in M2 medium containing individual or a combination of cytoskeletal drugs as appropriate.

3D chromatid surface reconstruction and scattering volume measurement

Chromatid surfaces were reconstructed in 3D in Imaris (Bitplane) from high-resolution time lapse movies of H2B-mRFP. Object-oriented bounding box analysis was performed in Imaris to identify the minimal cuboid volume that enclosed all chromatids at each time point. This bounding box volume was defined as the chromatid scattering volume. For each egg, data normalization was performed by dividing measured values at each time point with the bounding box volume at the start of the live imaging experiment (t = 0 mins).

Quantification of 3D chromatid movement speed and realignment

To quantify chromatid mobility, the 3D volumes of chromatids were reconstructed in Imaris (Bitplane) from high-resolution live imaging datasets of H2B-mRFP. For chromatids that distinctly migrated away from the spindle equator in control and experimental conditions, frame-to-frame displacement was measured by tracking the position of chromatid leading ends via the Measurement Points function in Imaris. Displacement values (μm) were divided by the temporal resolution of live imaging experiments (5 minutes) to calculate instantaneous chromatid movement speeds.

Realignment of previously scattered single chromatids to the spindle equator was analyzed in 3D in Imaris. A realignment event was defined as the merging of a misaligned chromatid with the main chromosome mass for a duration of at least 10 minutes.

Statistical data analyses

Histograms, box plots and other graphs were generated using OriginPro (OriginLab) or Prism (GraphPad) software. Box plots show mean (line), 5^{th}, 95^{th} (Whiskers), 25^{th} and 75^{th} percentile (box enclosing 50% of the data) and are overlaid with individual data points. Statistical significance evaluations, one-way and two-way analyses of variance were performed in OriginPro or Prism software. Significance values are $*P<0.05$, $**P<0.005$ and $***P<0.0005$. Non-significant values are indicated as N.S.

Fig. 1

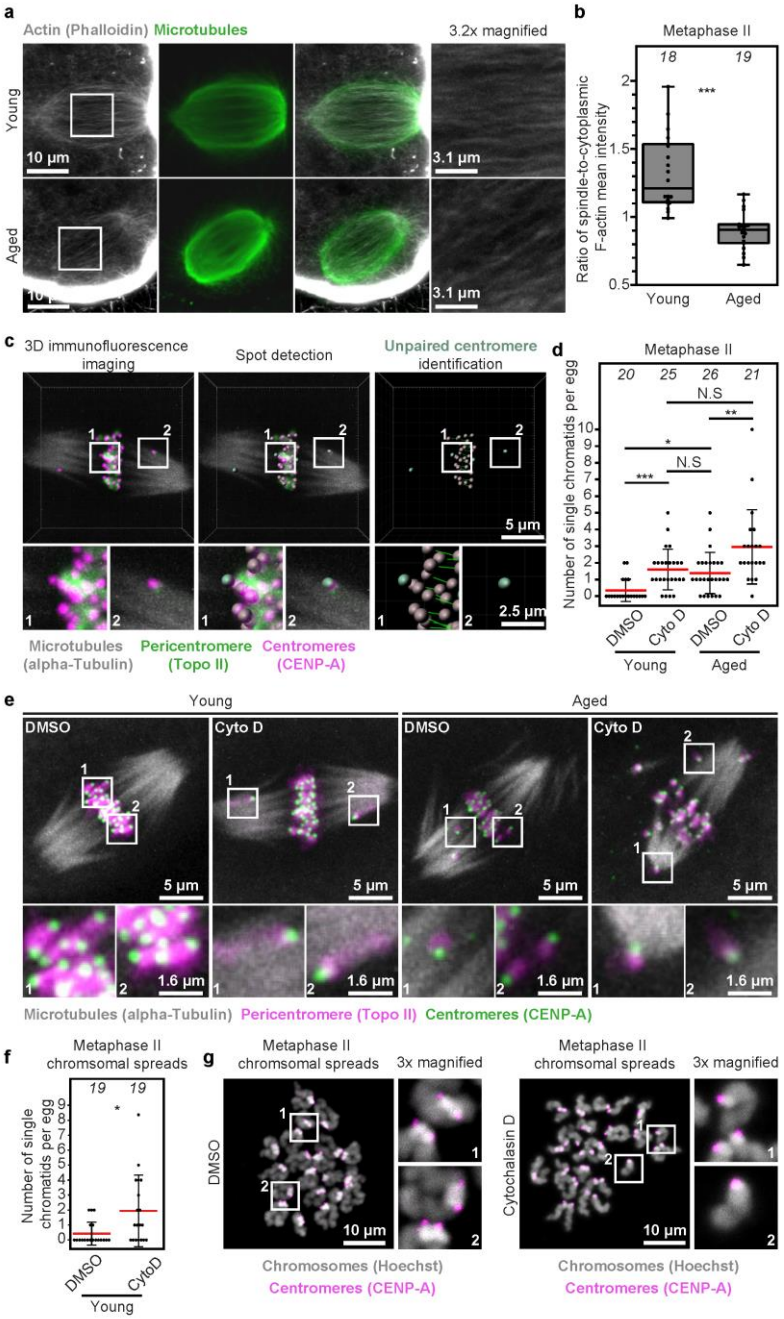

Fig. 1 F-actin loss exacerbates reproductive age-related premature chromatid separation in mammalian eggs

(a) Sum intensity projections of phalloidin labelled spindle F-actin and microtubules in young and aged metaphase II-arrested eggs. Boxes mark regions that are magnified in insets.

(b) Quantification of ratio of spindle-to-cytoplasmic F-actin mean fluorescence intensity in young and aged metaphase II-arrested eggs. Data are from 3 independent experiments.

(c) Unpaired chromatid identification pipeline from maximum intensity projected immunofluorescence images of CENP-A, Topoisomerase-II and microtubules in young and aged metaphase II-arrested eggs. CENP-A spots detection and inter-centromere distance measurements in Imaris were used to identify chromatids that did not contain two centromeres and assign them as single chromatids. Boxes mark regions that are magnified in insets.

(d) Quantification of the number of single chromatids (identified as in c) in DMSO- or Cytochalasin D-treated young and aged metaphase II-arrested eggs. Each filled black circle in graph represents a single egg and red bars represent mean values. Data are from 3 independent experiments.

(e) Representative maximum intensity projected immunofluorescence images of microtubules, centromeres, chromatid pairs and single chromatids in DMSO- or Cytochalasin D-treated young and aged metaphase II-arrested eggs. Boxes mark regions that are magnified in insets.

(f) Quantification of the number of single chromatids in metaphase II chromosomal spreads of DMSO- or Cytochalasin D-treated young eggs. Each filled black circle in graph represents chromosomal spread from a single egg and red bars represent mean values. Data are from 3 independent experiments.

(g) Representative maximum intensity projected immunofluorescence images of centromeres and chromatids in metaphase II chromosomal spreads of DMSO- or Cytochalasin D-treated young eggs. Boxes mark regions that are magnified in insets.

Statistical significance was evaluated using Mann-Whitney *t*-test (b and f) or Fisher's exact test (d).

Fig. 2

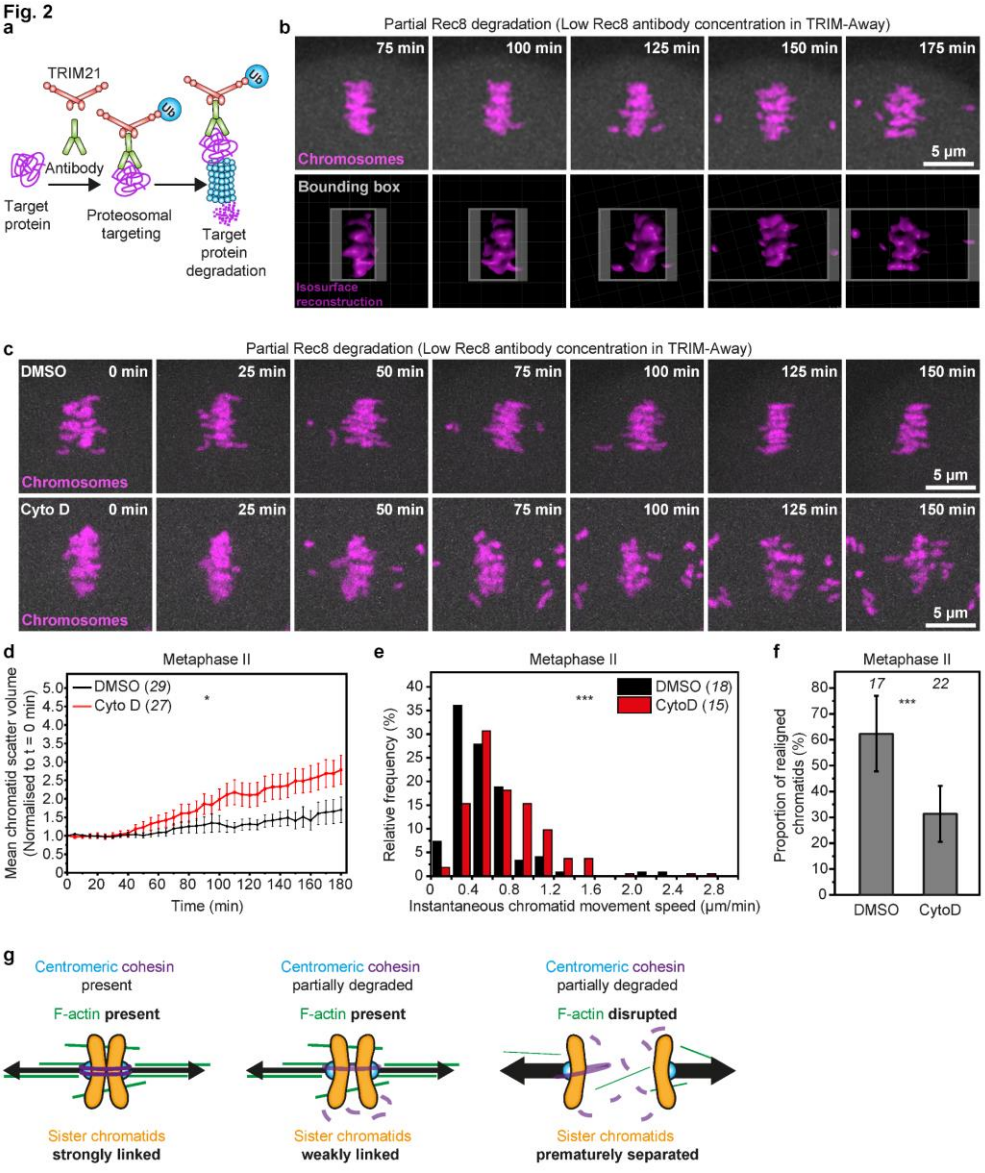

Fig. 2 F-actin disruption in young eggs accelerates aging-like premature chromatid separation

(a) The TRIM-Away system entails microinjection of antibodies against a protein of interest and transient expression of the E3 ubiquitin ligase TRIM21, which binds Fc domain of antibodies with high affinity. TRIM21 then recruits antibody-bound target proteins for degradation by the proteasome.

(b) Stills from time lapse movie of chromosomes (H2B-mRFP, top panel) and isosurface reconstructions (bottom panel) in a metaphase II-arrested egg with partially degraded Rec8. Pseudo object-orientated bounding box (grey, bottom panel) showing progressive increase in the minimal cuboid volume that encloses all chromatids as a measure of chromatid scattering.

(c) Stills from representative time lapse movies of chromosomes (H2B-mRFP) in DMSO- or Cytochalasin D-treated metaphase II-arrested eggs with partially degraded Rec8.

(d) Normalized chromatid scatter volumes measured as in b over 3 hours in DMSO- or Cytochalasin D-treated metaphase II-arrested eggs with partially degraded Rec8. Black and red lines represent mean values. Error bars represent S.E.M. Non-averaged individual measurements are provided in Fig. S3b. Data are from 3 independent experiments.

(e) Distribution of instantaneous chromatid movement speeds in DMSO- or Cytochalasin D-treated metaphase II-arrested eggs with partially degraded Rec8. Data are from 3 independent experiments.

(f) Proportion of scattered chromatids that re-established alignment to the spindle equator in DMSO- or Cytochalasin D-treated metaphase II-arrested eggs with partially degraded Rec8. Error bars represent S.D. Data are from 3 independent experiments.

(g) Graphical representation of the effect of F-actin loss on chromatid linkage in eggs containing partially reduced centromeric cohesion.

Statistical significance was evaluated using two-way ANOVA (d) or two-tailed Student's *t*-test (e and f).

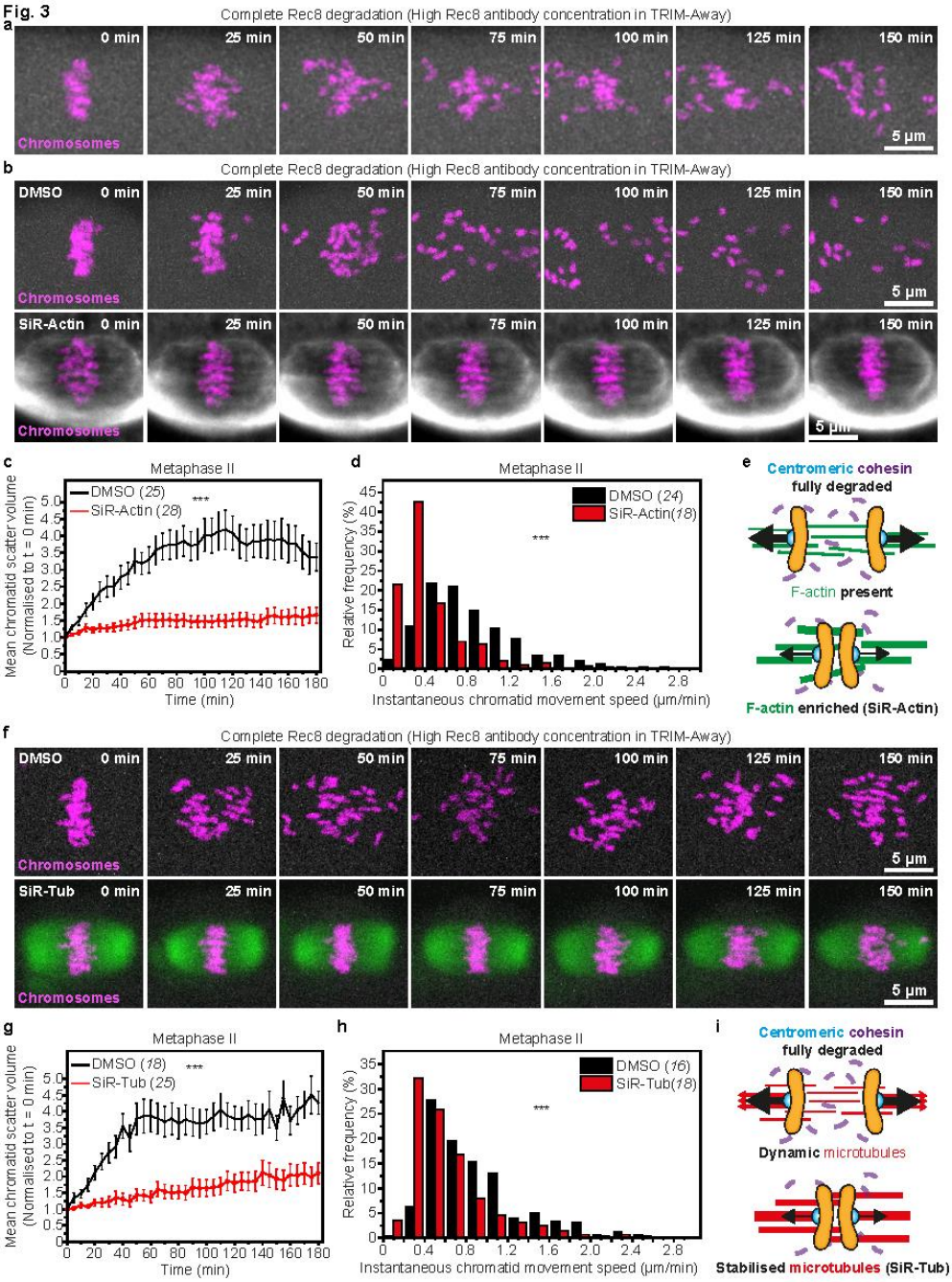

Fig. 3 F-actin enrichment or microtubule stabilization block premature chromatid separation in the absence of centromeric cohesion

(a) Stills from time lapse movie of chromosomes (H2B-mRFP) in a metaphase II-arrested egg with fully degraded Rec8.

(b) Stills from representative time lapse movies of chromosomes (H2B-mRFP) in DMSO- or SiR-Actin-treated (fluorescent F-actin shown in grey) metaphase II-arrested eggs with fully degraded Rec8.

(c) Normalized chromatid scatter volumes measured as in Fig. 2b over 3 hours in DMSO- or SiR-Actin-treated metaphase II-arrested eggs with fully degraded Rec8. Black and red lines represent mean values. Error bars represent S.E.M. Non-averaged individual measurements are provided in Fig. S3c. Data are from 3 independent experiments.

(d) Distribution of instantaneous chromatid movement speeds in DMSO- or SiR-Actin-treated metaphase II-arrested eggs with fully degraded Rec8. Data are from 3 independent experiments.

(e) Graphical representation of the effect of F-actin stabilization on chromatid linkage in eggs with fully disrupted centromeric cohesion.

(f) Stills from representative time lapse movies of chromosomes (H2B-mRFP) in DMSO- or SiR-Tubulin-treated (fluorescent microtubules shown in green) metaphase II-arrested eggs with fully degraded Rec8.

(g) Normalized chromatid scatter volumes measured as in Fig. 2b over 3 hours in DMSO- or SiR-Tubulin-treated metaphase II-arrested eggs with fully degraded Rec8. Black and red lines represent mean values. Error bars represent S.E.M. Non-averaged individual measurements are provided in Fig. S3d. Data are from 3 independent experiments.

(h) Distribution of instantaneous chromatid movement speeds in DMSO- or SiR-Tubulin-treated metaphase II-arrested eggs with fully degraded Rec8. Data are from 3 independent experiments.

(i) Graphical representation of the effect of blocking microtubule dynamics on chromatid linkage in eggs with fully disrupted centromeric cohesion.

Statistical significance was evaluated using two-way ANOVA (c and g) or two-tailed Student's *t*-test (d and h).

Fig. 4

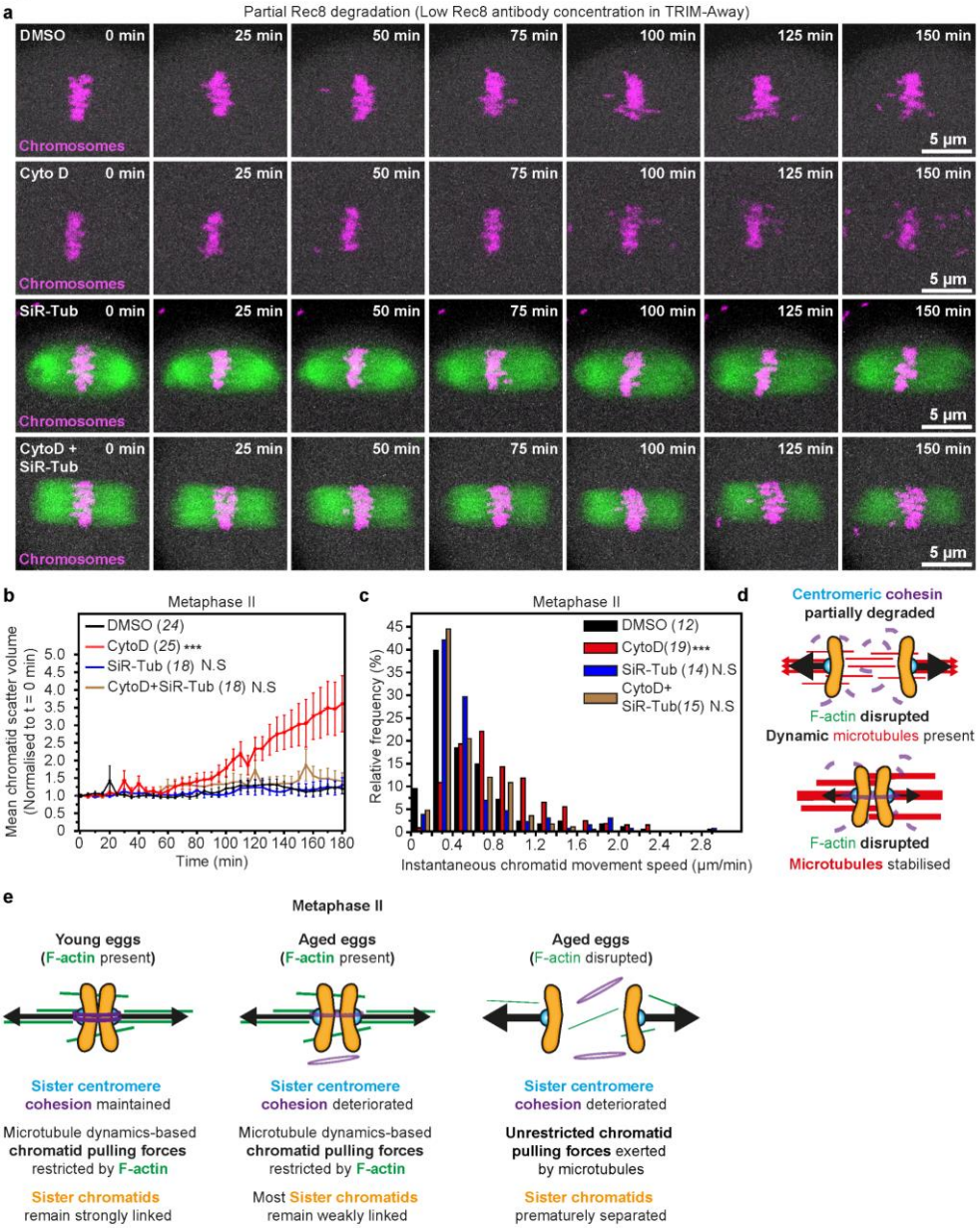

Fig. 4 F-actin dampens microtubule-based pulling forces to prevent aging-like premature chromatid separation

(a) Stills from representative time lapse movies of chromosomes (H2B-mRFP) in DMSO-, Cytochalasin D-, SiR-Tubulin- (fluorescent microtubules shown in green) or Cytochalasin D and SiR-Tubulin-treated metaphase II-arrested eggs with partially degraded Rec8.

(b) Normalized chromatid scatter volumes measured as in Fig. 2b over 3 hours in DMSO-, Cytochalasin D-, SiR-Tubulin- or Cytochalasin D and SiR-Tubulin-treated metaphase II-arrested eggs with partially degraded Rec8. Black, red, blue and brown lines represent mean values. Error bars represent S.E.M. Non-averaged individual measurements are provided in Fig. S3e. Data are from 3 independent experiments.

(c) Distribution of instantaneous chromatid movement speeds in DMSO-, Cytochalasin D-, SiR-Tubulin- or Cytochalasin D and SiR-Tubulin-treated metaphase II-arrested eggs with partially degraded Rec8. Data are from 3 independent experiments.

(d) Graphical representation of the effect of blocking microtubule dynamics on chromatid linkage in eggs devoid of F-actin and containing partially reduced centromeric cohesion.

(e) A model for a new function of F-actin in limiting microtubule-based chromatid pulling forces in eggs of reproductively young and older females. In young eggs containing full cohesin complement, F-actin reduces the effect of chromatid pulling forces resulting in strong sister chromatid linkage. When cohesin is partially depleted in reproductive aging, F-actin-mediated resistance to microtubule pulling forces maintains linkage between most sister chromatids. When F-actin is disrupted in eggs with further reproductive aging, pulling forces generated by dynamic microtubules more effectively and prematurely separate sister chromatids. Aging-related F-actin

disruption that proceeds cohesin depletion could therefore explain the dramatic rise in the incidence of egg aneuploidies near the end of female reproductive life.

Fig. S1

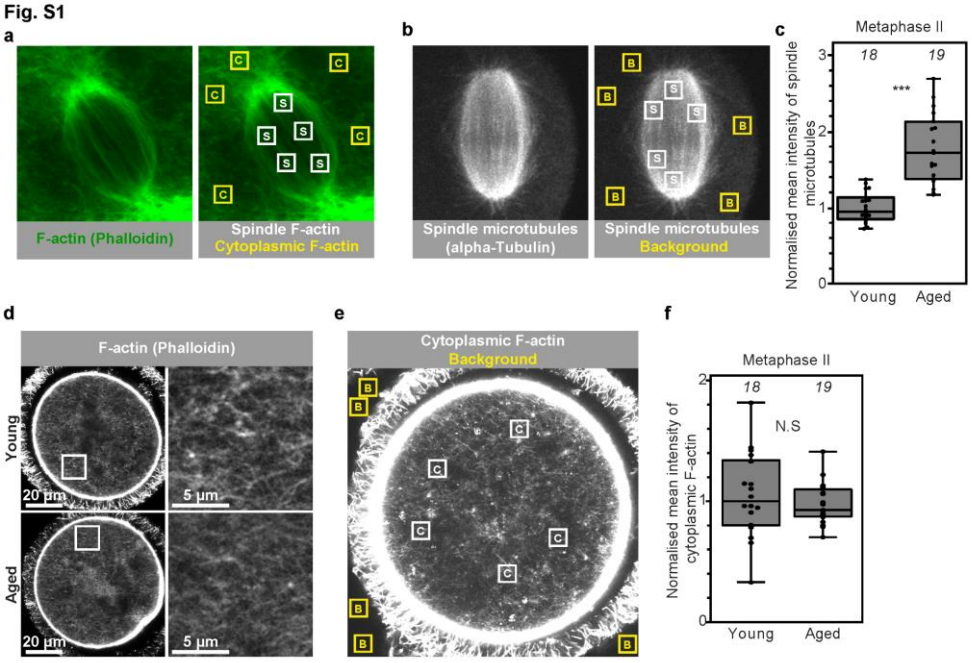

Fig. S1 Female reproductive aging is accompanied by spindle-specific F-actin loss in eggs.

(a) Method (described in Materials and Methods) for quantification of spindle-to-cytoplasmic F-actin mean fluorescence intensity ratio in metaphase II-arrested eggs of reproductively young or aged mice.

(b) Method (described in Materials and Methods) for quantification, background correction and normalization of spindle microtubule mean fluorescence intensities in eggs of reproductively young or aged mice.

(c) Normalized spindle microtubule mean fluorescence intensities in young and aged metaphase II-arrested eggs. Data are from 3 independent experiments.

(d) Representative single section Airyscan images of phalloidin labelled cytoplasmic F-actin structures in metaphase II-arrested eggs of reproductively young or aged mice. Boxes mark regions that are magnified in insets.

(e) Method (described in Materials and Methods) for quantification, background correction and normalization of cytoplasmic F-actin mean fluorescence intensities in eggs of reproductively young or aged mice.

(f) Normalized cytoplasmic F-actin mean fluorescence intensities in young and aged metaphase II-arrested eggs. Data are from 3 independent experiments.

Statistical significance was evaluated using Mann-Whitney *t*-test (c and f).

Fig. S2

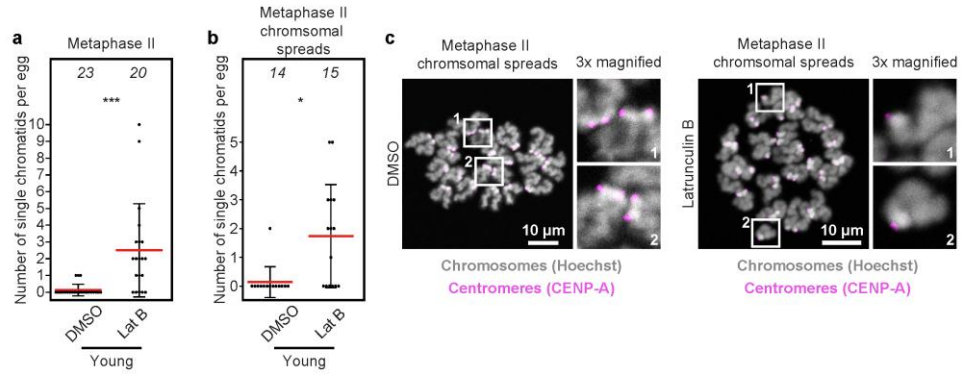

Fig. S2. F-actin disruption predisposes young eggs to premature sister chromatid separation

(a) Quantification of the number of single chromatids (identified as in Fig. 1c) in DMSO- or Latrunculin B-treated metaphase II-arrested eggs. Each filled black circle in graph represents a single egg and red bars represent mean values. Data are from 3 independent experiments.

(b) Quantification of the number of single chromatids in metaphase II chromosomal spreads of DMSO- or Latrunculin B-treated eggs. Each filled black circle in graph represents chromosomal spread from a single egg and red bars represent mean values. Data are from 3 independent experiments.

(c) Representative maximum intensity projected immunofluorescence images of centromeres and chromatids in metaphase II chromosomal spreads of DMSO- or Latrunculin B-treated young eggs. Boxes mark regions that are magnified in insets.

Statistical significance was evaluated using Mann-Whitney *t*-test (a and b).

Fig. S3

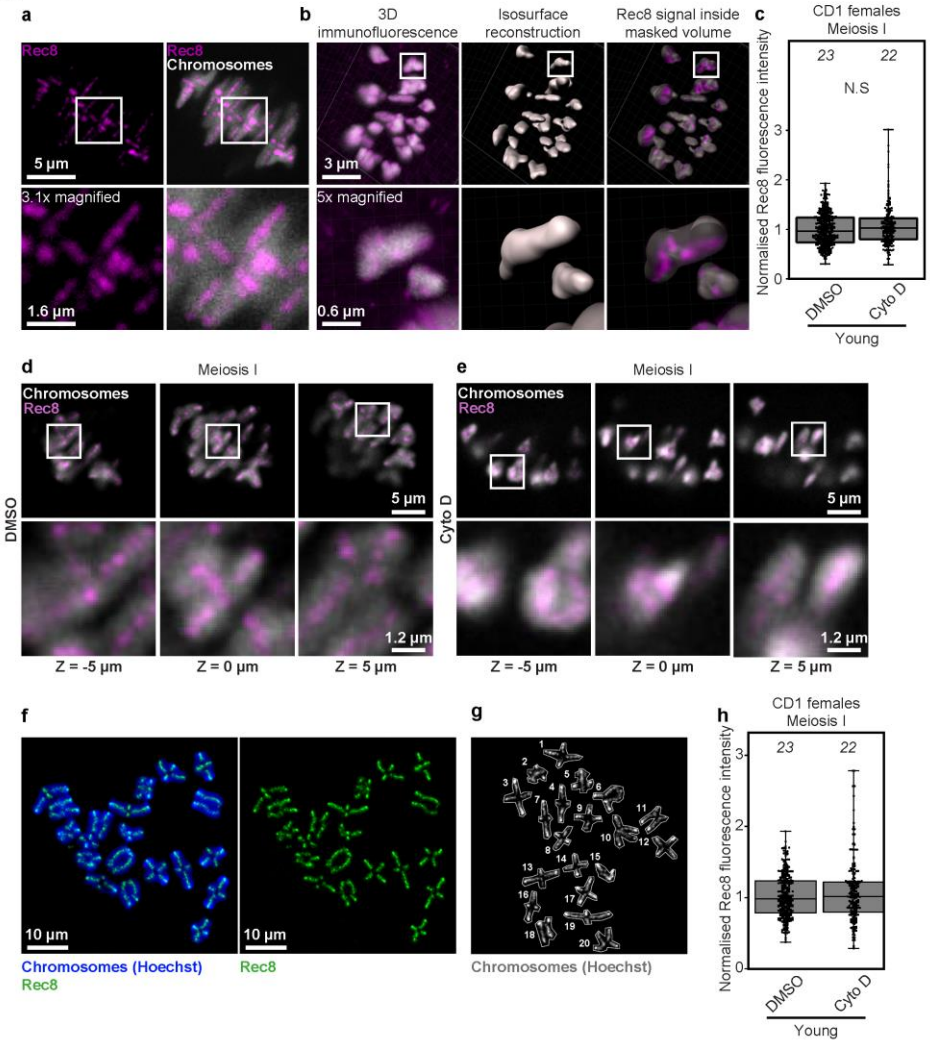

Fig. S3 F-actin disruption does not impact classical mechanisms of centromeric cohesion

(a) Maximum intensity projected high-resolution immunofluorescence images of Rec8 cohesin complexes and homologous chromosomes in a mouse oocyte. Boxes mark regions that are magnified in insets.

(b) Rec8 immunofluorescence intensity quantification pipeline. Individual chromosome volumes were reconstructed using the Surfaces module of Imaris. Mean Rec8 fluorescence intensity was then measured inside the masked volume each chromosome.

(c) Normalized Rec8 mean fluorescence intensities in DMSO- or Cytochalasin D-treated mouse oocytes. Data are from 3 independent experiments.

(d) Representative single confocal section immunofluorescence images of Rec8 and chromosomes – spaced 5 μm apart – in DMSO-treated mouse oocytes. Boxes mark regions that are magnified in insets.

(e) Representative single confocal section immunofluorescence images of Rec8 and chromosomes – spaced 5 μm apart – in Cytochalasin D-treated mouse oocytes. Boxes mark regions that are magnified in insets.

(f) Representative maximum intensity projected immunofluorescence images of Rec8 and chromosomes in metaphase I chromosomal spread of a mouse oocyte.

(g) Method (described in Materials and Methods) for quantification of Rec8 mean fluorescence intensity in metaphase I chromosomal spreads of mouse oocytes.

(h) Normalized Rec8 mean fluorescence intensities in metaphase I chromosomal spreads of DMSO- or Cytochalasin D-treated mouse oocytes. Data are from 3 independent experiments.

Statistical significance was evaluated using Mann-Whitney (c) and Welch's (h) *t*-test.

Fig. S4

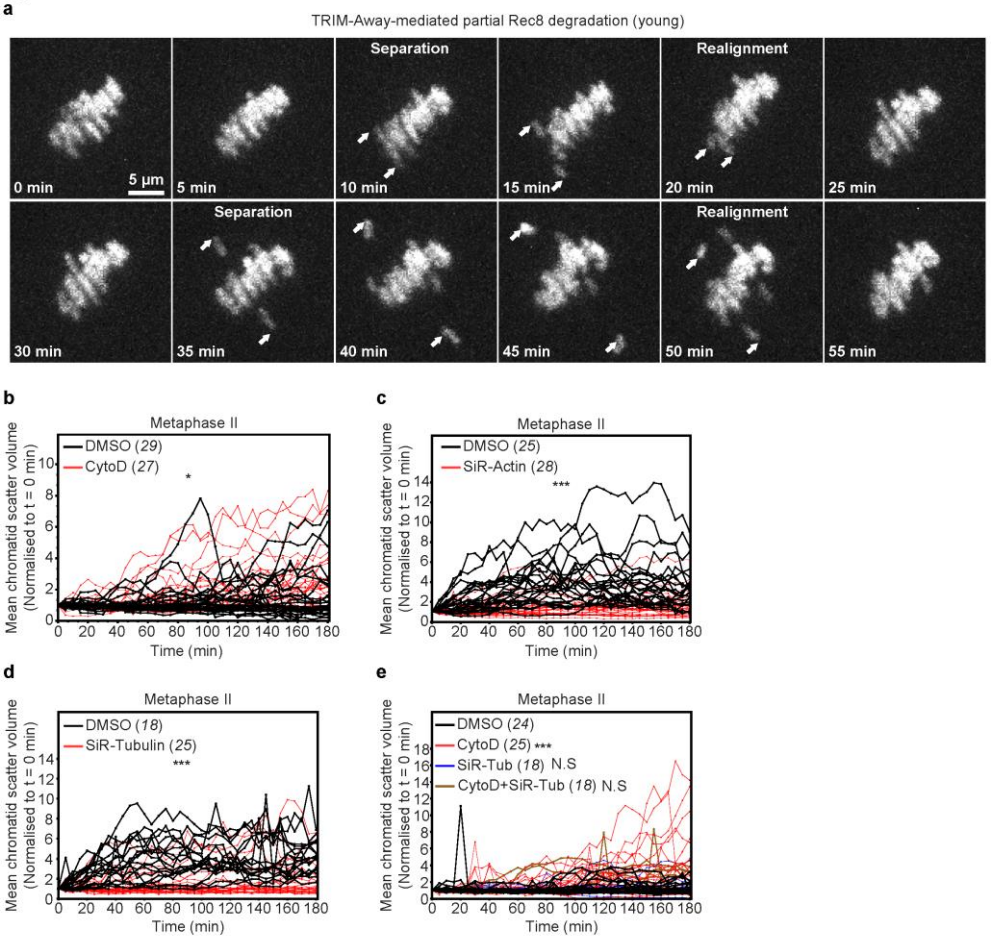

Fig. S4 F-actin limits aging-like premature chromatid separation by microtubule-based pulling forces

(a) Representative maximum intensity projected high-resolution confocal images of sister chromatids in a metaphase II-arrested mouse egg with partially degraded Rec8. Arrows indicate modest chromatid separation and subsequent realignment events.

(b) Normalized chromatid scatter volumes measured as in Fig. 2b over 3 hours in DMSO- or Cytochalasin D-treated metaphase II-arrested eggs with partially degraded Rec8. Each black and red line represents measurements from a single egg. Averaged measurements are presented in Fig. 2d. Data are from 3 independent experiments.

(c) Normalized chromatid scatter volumes measured as in Fig. 2b over 3 hours in DMSO- or SiR-Actin-treated metaphase II-arrested eggs with fully degraded Rec8. Each black and red line represents measurements from a single egg. Averaged measurements are presented in Fig. 3c. Data are from 3 independent experiments.

(d) Normalized chromatid scatter volumes measured as in Fig. 2b over 3 hours in DMSO- or SiR-Tubulin-treated metaphase II-arrested eggs with fully degraded Rec8. Each black and red line represents measurements from a single egg. Averaged measurements are presented in Fig. 3g. Data are from 3 independent experiments.

(e) Normalized chromatid scatter volumes measured as in Fig. 2b over 3 hours in DMSO-, Cytochalasin D-, SiR-Tubulin- or Cytochalasin D and SiR-Tubulin-treated metaphase II-arrested eggs with partially degraded Rec8. Each black and red line represents measurements from a single egg. Averaged measurements are presented in Fig. 4b. Data are from 3 independent experiments.

Movie S1. Navigation through single immunofluorescence confocal sections – spaced 0.5 µm apart – of Rec8 (magenta) and homologous chromosomes (grey) in a DMSO-treated mouse oocyte.

Movie S2. Navigation through single immunofluorescence confocal sections – spaced 0.5 µm apart – of Rec8 (magenta) and homologous chromosomes (grey) in a Cytochalasin D-treated mouse oocyte.

Movie S3. Time lapse movie of modest separation of chromatids (H2B-mRFP, magenta) in a metaphase II-arrested mouse egg with partially degraded Rec8.

Movie S4. 3D isosurface reconstruction (Imaris) of chromatids in movie 3 for bounding box analysis of chromatid scattering.

Movie S5. Time lapse movie of modest separation of chromatids (H2B-mRFP, magenta) in a DMSO-treated metaphase II-arrested mouse egg with partially degraded Rec8.

Movie S6. Time lapse movie of modest separation and subsequent realignment (indicated by write arrows) of chromatids (H2B-mRFP, magenta) in a DMSO-treated metaphase II-arrested mouse egg with partially degraded Rec8.

Movie S7. Time lapse movie of excessive separation and scattering of chromatids (H2B-mRFP, magenta) in a Cytochalasin D-treated metaphase II-arrested mouse egg with partially degraded Rec8 (example 1).

Movie S8. Time lapse movie of excessive separation and scattering of chromatids (H2B-mRFP, magenta) in a Cytochalasin D-treated metaphase II-arrested mouse egg with partially degraded Rec8 (example 2).

Movie S9. Time lapse movie of complete separation and scattering of chromatids (H2B-mRFP, magenta) in a metaphase II-arrested mouse egg with fully degraded Rec8.

Movie S10. Time lapse movie of complete separation and scattering of chromatids (H2B-mRFP, magenta) in a DMSO-treated (control for SiR-Actin treatment) metaphase II-arrested mouse egg with fully degraded Rec8.

Movie S11. Time lapse movie of restricted movement of chromatids (H2B-mRFP, magenta) in a SiR-Actin-treated metaphase II-arrested mouse egg with fully degraded Rec8. SiR-Actin fluorescence in shown in grey.

Movie S12. Time lapse movie of complete separation and scattering of chromatids (H2B-mRFP, magenta) in a DMSO-treated (control for SiR-Tubulin treatment) metaphase II-arrested mouse egg with fully degraded Rec8.

Movie S13. Time lapse movie of restricted movement of chromatids (H2B-mRFP, magenta) in a SiR-Tubulin-treated metaphase II-arrested mouse egg with fully degraded Rec8. SiR-Tubulin fluorescence in shown in green.

Movie S14. Time lapse movie of complete separation and scattering of chromatids (H2B-mRFP, magenta) in a DMSO-treated (control for Cytochalasin D + SiR-Tubulin treatment) metaphase II-arrested mouse egg with partially degraded Rec8.

Movie S15. Time lapse movie of excessive separation and scattering of chromatids (H2B-mRFP, magenta) in a Cytochalasin D-treated (control for Cytochalasin D + SiR-Tubulin treatment) metaphase II-arrested mouse egg with partially degraded Rec8.

Movie S16. Time lapse movie of restricted movement of chromatids (H2B-mRFP, magenta) in a SiR-Tubulin-treated (control for Cytochalasin D + SiR-Tubulin treatment) metaphase II-arrested mouse egg with partially degraded Rec8. SiR-Tubulin fluorescence in shown in green.

Movie S17. Time lapse movie of restricted movement of chromatids (H2B-mRFP, magenta) in a Cytochalasin D + SiR-Tubulin-treated metaphase II-arrested mouse egg with partially degraded Rec8. SiR-Tubulin fluorescence in shown in green.